



# Earthquake nucleation and recurrence

in laboratory, reservoir and  
tectonic settings

Meng Li

Earthquake nucleation and  
recurrence in laboratory, reservoir  
and tectonic settings

Meng Li

Utrecht Studies in Earth Sciences  
No. 315



**Composition of the Assessment Committee <sup>a</sup> and  
the Doctoral Examination Committee <sup>b</sup>:**

|                                              |                                                          |
|----------------------------------------------|----------------------------------------------------------|
| Prof. dr. J. -P. Ampuero <sup>ab</sup>       | <i>Université Côte d'Azur, France</i>                    |
| Prof. dr. J. -P. Avouac <sup>ab</sup>        | <i>California Institute of Technology, United States</i> |
| Prof. dr. D. R. Faulkner <sup>ab</sup>       | <i>University of Liverpool, United Kingdom</i>           |
| Dr. Y. Liu <sup>a</sup>                      | <i>McGill University, Canada</i>                         |
| Prof. dr. C. J. Spiers <sup>b</sup>          | <i>Universiteit Utrecht, Netherlands</i>                 |
| Dr. ir. F. C. Vossepoel <sup>b</sup>         | <i>Technische Universiteit Delft, Netherlands</i>        |
| Prof. dr. J. D. A. M. van Wees <sup>ab</sup> | <i>Universiteit Utrecht, Netherlands</i>                 |

Copyright © 2024 Meng Li. All rights reserved.

Cover image: The nucleation, coseismic, and postseismic phases of Earthquake #3 on a fault with heterogeneous normal stress, as shown in Figure 3.5, with colors representing the slip rate.

Printed by: Ipskamp Printing.

ISBN: 978-90-6266-688-1

DOI: <https://doi.org/10.33540/2400>

# Earthquake nucleation and recurrence in laboratory, reservoir and tectonic settings

Aardbevingsinitiatie en sequentie in laboratorium-,  
reservoir- en tektonische omgevingen

(met een samenvatting in het Nederlands)

## **Proefschrift**

ter verkrijging van de graad van doctor aan de  
Universiteit Utrecht,  
op gezag van de rector magnificus, prof. dr. H. R. B. M. Kummeling,  
ingevolge het besluit van het college voor promoties,  
in het openbaar te verdedigen op  
vrijdag 5 juli 2024 des ochtends te 10.15 uur

door

**Meng Li**

geboren op 16 juli 1995  
te Qinyang, China

**Promotor:**

Prof. dr. L. C. Matenco

**Copromotoren:**

Dr. Y. van Dinther

Dr. A. R. Niemeijer

**Beoordelingscommissie:**

Prof. dr. J. -P. Ampuero

Prof. dr. J. -P. Avouac

Prof. dr. D. R. Faulkner

Dr. Y. Liu

Prof. dr. J. D. A. M. van Wees

This research is part of the “InFocus: An Integrated Approach to Estimating Fault Slip Occurrence” project (grant number: DEEP.NL.2018.037) funded by the DeepNL programme of NWO (Dutch Research Council).

# Contents

|                                                                                                       |     |
|-------------------------------------------------------------------------------------------------------|-----|
| Summary                                                                                               | 1   |
| Samenvatting                                                                                          | 7   |
| 1 Introduction                                                                                        | 15  |
| 2 Characteristics of earthquake cycles: a cross-dimensional comparison of 0-D to 3-D numerical models | 41  |
| 3 Earthquake nucleation altered by stochastic normal stress heterogeneity                             | 85  |
| 4 Why induced earthquakes occur on conventionally stable faults: frictional healing explains          | 119 |
| 5 Earthquake nucleation and arrest in a heterogeneous earthquake sequence model for Groningen         | 153 |
| 6 Methods and code validation                                                                         | 173 |
| 7 Conclusions: summary and outlook                                                                    | 189 |
| Bibliography                                                                                          | 209 |
| Acknowledgements                                                                                      | 237 |
| Curriculum vitae                                                                                      | 241 |



# Summary

Numerical models play a crucial role in bridging the spatial and temporal scales between - and beyond - natural observations and laboratory experiments. Developing and applying numerical models provide a unique way to validate and generate scientific hypotheses that are not immediately demonstrable via observations. Recent advancements in instrumentation and methodologies have significantly improved the quantity and quality of natural and laboratory observations. Particularly, the rich observations in the Groningen gas field since the 2012 Huizinge earthquake (ML 3.6) have stimulated booming research on induced seismicity in this area. The dense geodetic and seismological networks improve the measurements of ground subsidence and earthquake source properties. The experiments conducted under in-situ conditions on samples collected from boreholes provide important information on the physical properties of all relevant geological layers. Given that numerical models are starting to master homogeneous model setups, the enriched observations provide us with an opportunity to develop and test models with more realistic heterogeneous setups. In this thesis, I aim to understand how earthquake nucleation and sequences are affected by heterogeneous material parameters and dimensions. To do so I further developed and validated (quasi-)dynamic earthquake sequence models from zero to three dimensions, from millions of years to sub-milliseconds, and from loading due to tectonic motions, gas extraction, poro-elastic reservoir compaction and fluid flow. I apply the necessary ingredients from these models to explore unique observations across a range of settings from small-scale laboratory experiments (Chapter 3) to large-scale tectonic environments (Chapter 2), and to human-induced earthquakes in the Groningen gas reservoir (Chapters 4 and 5).

A recurring concern among numerical modelers centers on determining the optimal model complexity to address their research objectives. The impact of spatial dimension reduction on results, both qualitatively and quantitatively, is a

common consideration. In Chapter 2, the first systematic examination of the advantages and limitations of simplifications that eliminate spatial dimensions in earthquake sequence models is presented. The quasi-dynamic analysis spans from 3-D models with a 2-D fault plane to 0-D or 1-D models with a 0-D fault point. While 2-D or 3-D models with quasi-periodic characteristic earthquakes exhibit qualitatively similar behavior to 0-D or 1-D models, dimension reduction quantitatively influences various outcomes. Notably, increased recurrence intervals, coseismic slip, peak slip velocities, and rupture speeds are observed. These changes stem from the elimination of velocity-strengthening patches, reducing interseismic stress rates and amplifying the slip deficit. A concise theoretical framework is developed to support this quantitative explanation. By introducing an equivalent stressing rate at the nucleation length  $h^*$  of 2-D and 3-D models, 0-D or 1-D models can effectively replicate the recurrence intervals and related source properties of higher-dimensional models. Additionally, it is highlighted that under the same resolution, 3-D models demand significantly longer computing times than lower-dimensional counterparts. A representative simulation in 0-D runs over a million times faster than in 3-D. Consequently, dimension reduction not only minimizes energy-consuming simulations but also enhances the efficiency of projects requiring repetitive forward models. Finally, this chapter provides qualitative and quantitative guidance on economical model design and interpretation of modeling studies.

Recent large-scale laboratory experiments exhibit varying nucleation locations with changing nucleation lengths, which is analogous to natural observations. It is hypothesized that heterogeneous normal stresses play an important role. Since fault stresses may vary significantly across variable lithologies in induced seismicity configurations (Chapter 5) and effective normal stress significantly impact fault strength and fracture energy, I systematically investigate the influence of normal stress heterogeneity on earthquake nucleation and the subsequent sequences in Chapter 3. Utilizing an earthquake sequence model featuring a stochastically variable, spatially heterogeneous normal stress field, analogous to a 2-meter scale laboratory experiment, I identify five regimes of earthquake nucleation and slip behaviors. These regimes are governed by the ratio of the heterogeneity wavelength ( $\lambda$ ) to the nucleation length ( $L_c$ ). First, full ruptures are observed when  $\lambda$  is significantly smaller than  $L_c$ , displaying slips and recurrence intervals akin to those on homogeneous faults with the same averaged normal stress (termed the homogenized nucleation regime). However,

frequent occurrences of slow slip events and partial ruptures prevail when  $\lambda$  is much larger than  $L_c$ , wherein each earthquake's nucleation length depends on the local stress level (localized nucleation regime). Between these end-member cases, when  $\lambda$  approaches the magnitude of  $L_c$ , nucleation locations migrate between low normal stress regions (LSR) and high normal stress regions (HSR). Specifically, when  $\lambda$  is larger than  $L_c$ , earthquakes nucleate in LSRs, and HSRs function as barriers (LSR-preferred nucleation regime). However, HSRs and LSRs exchange their roles when  $\lambda$  is smaller than  $L_c$  (HSR-preferred nucleation regime). Interestingly, nucleation location migrates from a LSR to its neighboring HSR in a single earthquake, when  $\lambda$  is between the minimum and maximum nucleation length of the heterogeneous fault (migratory nucleation regime). In this case, a large amount of aseismic slip and an associated stress drop are observed in the initial LSR, which can be linked to the migration of foreshocks documented in natural and laboratory observations. Notably, the study sheds light on the significance of effective normal stress in modifying the seismic potential of natural faults, especially in induced seismicity settings where human activities impact and even control the effective normal stress distribution. These results may be used to estimate fault stresses based on seismological and geodetic observations of fault slips, such as foreshocks and slow slips.

Current knowledge suggests that faults in the shallow subsurface should resist earthquake nucleation, because their frictional strength increases as slip accelerates. Yet, these supposedly stable faults frequently experience earthquakes induced by human exploration of the subsurface. In Chapter 4, I tackle this paradox of induced earthquakes by simulating earthquake sequences and *fault healing* governed by rate-and-state friction on a normal fault crosscutting a depleting gas reservoir. I demonstrate that single earthquakes can nucleate on velocity-strengthening faults following long-term fault healing over tectonic timescales. Subsequent slip on ruptured segments remains stable and aseismic. On our human lifetimes, these ruptured segments thus form a barrier repressing future, larger, and more destructive earthquakes. The frictional healing mechanism during the period of tectonic inactivity increases fault strength. In this way, the subsequent fault failure caused by induced stress accumulation could obtain fast slips due to an adequate stress drop. The healing mechanism, governed by the evolution parameter  $b$  in rate-and-state friction, emphasizes the potential seismicity of conventionally stable faults, challenging previous assumptions. I quantify the corresponding potential of any fault to experience induced seis-



micity in terms of the required healing time to achieve a sufficient slip rate upon fault reactivation. With a geological timescale of healing, the conventional divide between seismogenic and non-seismogenic frictional properties at velocity-neutral ( $a/b = 1$ ) is shifted substantially to the velocity-strengthening side:  $a/b = 1.3$ , and at most  $a/b = 1.7$  when dynamic weakening in form of flash heating is considered. The nucleation characteristics on velocity-strengthening faults and velocity-weakening faults also show similarities in terms of nucleation length and slip acceleration. I update the theoretical nucleation length calculation to include the contribution of healing time. My quantification emphasizes that rock layers previously deemed safe in sustainable explorations can unexpectedly host earthquakes, making them potentially riskier than previously presumed. My finding illustrates the importance of a better understanding and quantification of healing rate and healing time globally towards correctly assessing induced seismic hazard in all traditional and sustainable settings. Better understanding and accounting for fault healing when assessing induced seismic hazards may contribute to safer exploration of the shallow subsurface and assist in our transition towards a society driven by sustainable energy.

I extend these generalized simulations with global relevance to build a more realistic earthquake sequence model of the Groningen gas reservoir in Chapter 5. This model features lithology-dependent friction and elastic parameters obtained from laboratory experiments and seismic inversions. Combining my findings in Chapter 4 with experimental output suggests a velocity-weakening Basal Zechstein layer in the overburden is potentially seismogenic, whereas the velocity-strengthening Slochteren sandstone reservoir becomes seismogenic upon healing over geological times. Other over- and underburden layers are expected to remain non-seismogenic due to their low or even negative rate-and-state  $b$  parameter. This suggestion raises critical questions about which layers will be able to nucleate earthquakes and whether the seismic rupture can propagate into other layers. Despite highly dense recordings, seismological observations fail to sufficiently answer questions on earthquake nucleation and slip locations due to measurement and inversion uncertainties. My simulations feature induced earthquakes nucleating within the velocity-strengthening sandstone reservoir, mostly from the top end, and rupturing across its entire width. However, compared to the homogeneous model used in Chapter 4, a larger pore pressure change is required due to the less efficient loading resulting from heterogeneous elastic properties. Notably, no evidence of earthquakes

nucleating within the velocity-weakening Basal Zechstein layer is found, nor does this layer rupture seismically. Moreover, all ruptures I have simulated do not extend into the underburden, represented by a non-healing, velocity-strengthening Carboniferous shale layer. I find that the pore pressure change outside the reservoir is minimal, such that the stress state at the fault is far from critical. This strong stress valley forms an efficient barrier inhibiting propagation to larger depths. On top of that, the fault segments that are velocity-strengthening do not exhibit healing and thus did not build up strength during the geological timescale, which is required to trigger an adequate stress drop upon activation. Consequently, earthquake nucleation is not expected, and dynamic rupture is arrested in these areas, restricting rupture propagation mostly within the reservoir. This reduced possibility of propagation into the under- and overburden reduces the total seismic energy release and the anticipated moment magnitude. These findings have substantial implications for estimating maximum earthquake magnitude and defining seismic hazards in Groningen. Given the uncertainties in parameters and fault geometry, I will build on my current model sets to test whether other factors, such as reservoir thickness and fault offset, will allow seismic propagation into the underburden.

Lastly, the development and validation of the two code packages used in this thesis are introduced in Chapter 6. I used *Garnet* in Chapters 2 and 3. This code library has been validated in a series of benchmark problems, which compare my simulations of fully dynamic and quasi-dynamic sequences of earthquakes and aseismic slip in 2D and 3D to those of others in the community. Besides these developments based on the existing code package *Garnet* to model various dimensions, scales, fluid diffusion and heterogeneous fault stress, a completely new MATLAB code is developed from scratch to accurately accommodate the dipping fault used in Groningen. This code is used in Chapters 4 and 5. My code features heterogeneous stress states, frictional properties and mechanical properties, along with the implementation of frictional healing and controlled pore pressure change due to gas production. In summary, I provide the community with open access codes that simulate nucleation and dynamic earthquake ruptures, reservoir geomechanics and fluid-induced (a-)seismic slips.

Overall, these chapters collectively contribute to our understanding of earthquake nucleation, propagation and arrest and provide valuable insights for refining seismic hazard assessments across different scales and tectonic settings.

In Chapter 7, I summarize the main findings and discuss potential implications and applications of my findings across natural, induced and laboratory settings. My forward models are also used to provide the physics-based input for the assimilation of limited and uncertain observations, such that both earthquakes and slow slip events can be better forecast in synthetic studies. Finally, I propose future research avenues and challenges that require community attention.

# Samenvatting

Numerieke modellen spelen een cruciale rol in het overbruggen van de ruimtelijke en temporele schalen tussen - en voorbij - natuurlijke waarnemingen en laboratoriumexperimenten. Het ontwikkelen en toepassen van numerieke modellen biedt een unieke manier om wetenschappelijke hypothesen te valideren en te genereren die niet direct aantoonbaar zijn via waarnemingen. Recente ontwikkelingen in instrumentatie en methodologieën hebben de kwantiteit en kwaliteit van natuurlijke en laboratoriumwaarnemingen aanzienlijk verbeterd. Met name de rijke waarnemingen in het Groningen gasveld sinds de Huizinge aardbeving in 2012 (ML 3.6) hebben intens onderzoek naar geïnduceerde seismiciteit in dit gebied gestimuleerd. De dichte geodetische en seismologische netwerken verbeteren de nauwkeurigheid van grondverzakingsmetingen en de bepaling van bron karakteristieken van de aardbeving, zoals hypocenterlocatie. De experimenten uitgevoerd onder in-situ omstandigheden op monsters verzameld uit boorgaten informeren ons over de fysische eigenschappen van de verschillende gesteentes. Gezien het feit dat numerieke modellen beginnen te domineren in homogene modelopstellingen, bieden de verrijkte waarnemingen ons een kans om modellen te ontwikkelen en te testen met meer realistische heterogene opstellingen. In deze scriptie streef ik ernaar te begrijpen hoe aardbevingsnucleatie en sequenties worden beïnvloed door heterogene materiaalparameters en dimensies. Om dit te doen, heb ik (quasi-)dynamische aardbevingssequentie modellen verder ontwikkeld en gevalideerd, van nul tot drie dimensies, van miljoenen jaren tot sub-milliseconden, en van belasting als gevolg van tektonische bewegingen, gaswinning, poro-elastische reservoircompactie en vloeistofstroming. Ik pas de nodige elementen uit deze modellen toe om unieke waarnemingen te verkennen in een serie omgevingen van kleinschalige laboratoriumexperimenten (Hoofdstuk 3) tot grootschalige tektonische omgevingen (Hoofdstuk 2), en tot door de mens geïnduceerde aardbevingen in het Groningen gasreservoir (Hoofdstukken 4 en 5).

Een terugkerende zorg onder numerieke modelleers is het bepalen van de optimale modelcomplexiteit om hun onderzoeksdoelen te bereiken. De impact van ruimtelijke dimensiereductie op de resultaten, zowel kwalitatief als kwantitatief, is een veelvoorkomende overweging. In Hoofdstuk 2 wordt het eerste systematische onderzoek gepresenteerd naar de voordelen en beperkingen van vereenvoudigingen die ruimtelijke dimensies elimineren in aardbevingssequentie modellen. De quasi-dynamische analyse varieert van 3D-modellen met een 2D-breukvlak tot 0D- of 1D-modellen met een 0D-breukpunt. Terwijl 2D- of 3D-modellen met quasi-periodieke karakteristieke aardbevingen kwalitatief vergelijkbaar gedrag vertonen met 0D- of 1D-modellen, beïnvloedt dimensiereductie kwantitatief verschillende uitkomsten. Met name verhoogde herhalingsintervallen, coseismische verschuiving, piekschuifsnelheden en breuksnelheden worden waargenomen. Deze veranderingen zijn het gevolg van de eliminatie van snelheidsversterkende patches, waardoor de interseismische snelheid van spanningslading afnemen en het schuiftekort toeneemt. Ik heb een beknopt theoretisch kader ontwikkeld om deze kwantitatieve verklaring te ondersteunen. Door een equivalente snelheid van spanningstoename te introduceren op de nucleatielengte  $h^*$  van 2D- en 3D-modellen, kunnen 0D- of 1D-modellen effectief de herhalingsintervallen en gerelateerde bron-eigenschappen van modellen met hogere dimensies repliceren. Daarnaast wordt benadrukt dat bij dezelfde resolutie 3D-modellen aanzienlijk langere rekentijden vereisen dan modellen met lagere dimensies. Een representatieve simulatie in 0D draait meer dan een miljoen keer sneller dan in 3D. Als gevolg hiervan vermindert dimensiereductie niet alleen energieverblindende simulaties, maar verbetert het ook de efficiëntie van projecten die repetitieve voorspellende modellen vereisen. Tot slot biedt dit hoofdstuk kwalitatieve en kwantitatieve richtlijnen voor economisch modelontwerp en de interpretatie van modelleringstudies.

Recente grootschalige laboratoriumexperimenten vertonen variërende nucleatielocaties met veranderende nucleatielengtes, wat analoog is aan natuurlijke waarnemingen. Er wordt verondersteld dat heterogene normale spanningen een belangrijke rol spelen. Aangezien breukspanningen significant kunnen variëren over verschillende lithologieën in geïnduceerde seismiciteitsconfiguraties (Hoofdstuk 5) en effectieve normale spanning de breuksterkte en breukenergie significant beïnvloeden, onderzoek ik systematisch de invloed van heterogeniteit in normale spanning op aardbevingsnucleatie en de daaropvolgende sequenties in Hoofdstuk 3. Ik heb een aardbevingssequentie model met

een stochastisch variabel, ruimtelijk heterogeen normaal spanningsveld, ontwikkeld dat analoog aan een laboratoriumexperiment op schaal van 2 meter. Daarin identificeer ik vijf regimes van aardbevingsnucleatie en schuifgedrag. Deze regimes worden bepaald door de verhouding van de heterogeniteitsgolflengte ( $\lambda$ ) tot de nucleatielengte ( $L_c$ ). Ten eerste worden volledige breuken waargenomen wanneer  $\lambda$  aanzienlijk kleiner is dan  $L_c$ , waarbij verschuivingen en herhalingsintervallen worden weergegeven die vergelijkbaar zijn met die op homogene breuken met dezelfde gemiddelde normale spanning (genoemd het gehomogeniseerde nucleatieregime). Echter, frequente voorkomens van trage verschuivingen en gedeeltelijke breuken prevaleren wanneer  $\lambda$  veel groter is dan  $L_c$ , waarbij de nucleatielengte van elke aardbeving afhangt van het lokale spanningsniveau (gelokaliseerd nucleatieregime). Tussen deze extreme gevallen, wanneer  $\lambda$  de grootte van  $L_c$  nadert, migreren nucleatielocaties tussen lage normale spanningsgebieden (LSR) en hoge normale spanningsgebieden (HSR). Specifiek, wanneer  $\lambda$  groter is dan  $L_c$ , nucleëren aardbevingen in LSR's, en fungeren HSR's als barrières (LSR-voorkeursnucleatieregime). Echter, HSR's en LSR's wisselen hun rollen wanneer  $\lambda$  kleiner is dan  $L_c$  (HSR-voorkeursnucleatieregime). Interessant genoeg migreert de nucleatielocatie van een LSR naar een aangrenzende HSR in een enkele aardbeving, wanneer  $\lambda$  zich bevindt tussen de minimale en maximale nucleatielengte van de heterogene breuk (migrerend nucleatieregime). In dit geval wordt een grote hoeveelheid aseismische verschuiving en een bijbehorende spanningsafname waargenomen in de initiële LSR, wat kan worden gekoppeld aan de migratie van voorschokken die zijn gedocumenteerd in natuurlijke en laboratoriumwaarnemingen. Deze studie benadrukt het belang van effectieve normale spanning bij het wijzigen van het seismische potentieel van natuurlijke breuken, vooral in geïnduceerde seismiciteitsomgevingen waar menselijke activiteiten de verdeling van effectieve normale spanning beïnvloeden en zelfs beheersen. Deze resultaten kunnen worden gebruikt om breukspanningen te schatten op basis van seismologische en geodetische waarnemingen van breukverschuivingen, zoals voorschokken en langzame verschuivingen.

De huidige kennis suggereert dat breuken in de ondiepe ondergrond aardbevingsnucleatie zouden moeten weerstaan, omdat hun wrijvingssterkte toeneemt naarmate verschuiving versnelt. Toch ervaren deze ogenschijnlijk stabiele breuken vaak aardbevingen die worden geïnduceerd door menselijke exploratie van de ondergrond. In Hoofdstuk 4 behandel ik deze paradox van geïnduceerde

aardbevingen door aardbevingssequenties en *breukgenezing* of versterking over duizenden tot miljoenen jaren te simuleren. Dit wordt beschreven door de wrijvingsweerstand afhankelijk van schuifsnelheid en een evoluerende breuk toestand te maken - zogenaamde *rate-and-state friction* - en die toe te passen op een afschuivende breuk die een leeglopend gas reservoir doorkruist. Ik toon aan dat enkele aardbevingen kunnen nucleëren op snelheidsversterkende breuken na breukgenezing over tektonische tijdschalen. Vervolgens kan dat stuk geen aardbevingen meer genereren en alleen nog maar heel erg langzaam over miljoenen jaren schuiven. Over verscheidene mensenlevens vormen deze gebroken stukken dus een barrière die toekomstige, grotere en schadelijkere aardbevingen onderdrukt. Tijdens de periode van tektonische inactiviteit versterkt de breuk dankzij wrijvingsgenezing. Op deze manier kan de daaropvolgende aardbeving veroorzaakt door geïnduceerde spanningsopbouw snelle verschuivingen verkrijgen vanwege een adequate spanningsafname. Het genezingsmechanisme, beheerst door de evolutieparameter  $b$  in *rate-and-state friction*, benadrukt het potentiële seismische risico van conventioneel stabiele breuken. Dit staat in contrast tot eerdere aannames. Ik kwantificeer het bijbehorende potentieel van elke breuk om geïnduceerde seismiciteit te ervaren in termen van de vereiste genezingstijd om een schuifsnelheid te kunnen genereren die seismische golven zal uitzenden. Met een geologische tijdschaal van genezing wordt de conventionele scheidslijn tussen seismogene en niet-seismogene wrijvingseigenschappen aanzienlijk verschoven van snelheidsneutraal ( $a/b = 1$ ) naar snelheidsversterkend ( $a/b = 1.3$ ), en maximaal  $a/b = 1.7$  wanneer extreme dynamische verzwakking in de vorm van *flash heating* wordt meegenomen. De nucleatiekenmerken op snelheidsversterkende breuken en snelheidsverzwakkende breuken vertonen ook overeenkomsten in termen van nucleatielengte en schuifversnelling. Ik pas de theoretische nucleatielengteberekening aan om de bijdrage van genezingstijd mee te nemen. Mijn kwantificering benadrukt dat gesteentelagen die voorheen als veilig werden beschouwd in duurzame exploraties onverwachts aardbevingen kunnen veroorzaken. Hierdoor zijn deze gesteentes potentieel riskanter dan eerder aangenomen. Mijn bevindingen illustreren het belang van een beter begrip en kwantificering van genezingsnelheid en genezingsstijd om de gevaren van geïnduceerde seismische wereldwijd correct in te schatten in zowel traditionele als duurzame exploratie omgevingen. Door rekening te houden met breuk genezing kan geïnduceerde seismiciteit beter geminimaliseerd worden. Hierdoor kan de ondiepe

ondergrond veiliger gebruikt worden om een overgang naar een samenleving gedreven door duurzame energie te versnellen.

Ik breid deze gegeneraliseerde simulaties met mondiale relevantie uit om een realistischer aardbevingssequentiemodel van het Groningen gasreservoir te bouwen in Hoofdstuk 5. Dit model bevat lithologie-afhankelijke wrijvings- en elastische parameters, die verkregen zijn uit laboratoriumexperimenten en geofysische observaties. Experimentele resultaten en mijn bevindingen in Hoofdstuk 4 suggereren dat een snelheidsverzwakkende Basal Zechstein-laag boven het reservoir potentieel seismogeen is, terwijl het snelheidsversterkende Slochteren zandsteenreservoir pas seismogeen wordt na genezing over geologische tijdschalen. Ik verwacht dat aardbevingen niet kunnen ontstaan in andere boven- en onderlagen vanwege hun lage of zelfs negatieve rate-and-state evolutie parameter  $b$ . Deze bevindingen roepen kritische vragen op over in welke lagen in Groningen de aardbevingen ontstaan en of de aardbevingen zich ook in andere lagen zullen voortplanten. Ondanks zeer dichte opnamen kunnen seismologische waarnemingen deze belangrijke vragen niet voldoende beantwoorden vanwege meet- en inversieonzekerheden en kunnen deze waarnemingen ook niet in de toekomst kijken. Mijn simulaties genereren geïnduceerde aardbevingen die nucleëren binnen het snelheidsversterkende zandsteenreservoir, meestal vanaf de bovenkant, en die breken vervolgens de gehele reservoir breedte. Echter, in vergelijking met het homogene model uit Hoofdstuk 4, is een grotere drukverandering in de poriën vereist vanwege de minder efficiënte lading als gevolg van heterogene elastische eigenschappen. Opmerkelijk is dat er geen bewijs is van aardbevingen die nucleëren binnen de snelheidsverzwakkende Basal Zechstein-laag, noch dat deze laag met seismische snelheden geactiveerd kan worden. Bovendien breiden alle aardbevingen die ik heb gesimuleerd zich niet uit naar de onderlaag, vertegenwoordigd door een niet-genezende, snelheidsversterkende Carboon schalielaag. Ik observeer dat de drukverandering in de poriën buiten het reservoir minimaal is, waardoor de spanning op de breuk net onder het reservoir verre van kritisch is en een sterke barrière vormt. Bovendien vertonen deze stukken van de breuk die snelheidsversterkend zijn geen genezing en bouwen ze dus geen sterkte op over geologische tijdschalen. Hierdoor kan ook mijn alternatieve manier om aardbevingen te genereren geen adequate spanningsafname veroorzaken bij activering. Als gevolg hiervan wordt aardbevingsnucleatie niet verwacht en wordt de dynamische aardbeving in deze gebieden snel gestopt, zodat de aardbeving zich



voornamelijk binnen het reservoir voortplant. Deze verminderde mogelijkheid van voortplanting naar de onder- en bovenlagen vermindert de totale seismische energievrijgave en de verwachte grootte van een aardbeving aanzienlijk. Deze bevindingen hebben belangrijke implicaties voor het schatten van de maximale aardbevingsmagnitude en het definiëren van seismische gevaren in Groningen. Gezien de onzekerheden in parameters en breukgeometrie, zal ik voortbouwen op mijn huidige modelsets om te testen of andere factoren, zoals reservoirdikte en geologisch verschoven breuk afstand, seismische voortplanting naar de onderlaag mogelijk maken.

Ten slotte worden de ontwikkeling en validatie van de twee codepakketten die in deze scriptie worden gebruikt, geïntroduceerd in Hoofdstuk 6. Ik gebruikte *Garnet* in Hoofdstukken 2 en 3. Deze bibliotheek met codes is succesvol gevalideerd in een reeks benchmarkproblemen, die mijn simulaties van volledig dynamische en quasi-dynamische sequenties van aardbevingen en aseismische verschuiving in 2D en 3D vergelijken met codes van anderen in de wetenschappelijke gemeenschap. Naast mijn werk om met een bestaande code verschillende dimensies, tijd en ruimte schalen, vloeistof diffusie en heterogene breukspanningen te modelleren, heb ik een geheel nieuwe MATLAB code van de grond af ontwikkeld om de dippende breuk in Groningen nauwkeurig te kunnen beschrijven. Deze code wordt gebruikt in Hoofdstukken 4 en 5. Mijn code bevat heterogene spanningsstaten, wrijvings- en mechanische eigenschappen, samen met de implementatie van wrijvingsgenezing en gecontroleerde poriedrukverandering als gevolg van gasproductie. Samengevat, voorzie ik de gemeenschap van publiek te gebruiken codes die de tektonische lading, nucleatie, voortplanting en de stop van series van aardbevingen, reservoirgeomechanica en door vloeistof geïnduceerde (a-)seismische verschuiving simuleren.

Over het geheel genomen dragen deze hoofdstukken gezamenlijk bij aan ons begrip van het ontstaan, voortplanten en eindigen van aardbevingen, en bieden ze waardevolle inzichten voor het verfijnen van seismische risicobeoordelingen op verschillende schalen en tektonische omgevingen. In Hoofdstuk 7 vat ik de belangrijkste bevindingen samen en bespreek ik de potentiële implicaties en toepassingen van mijn bevindingen over en voor natuurlijke, geïnduceerde en laboratorium aardbevingen. Mijn voorwaartse modellen worden ook gebruikt om de fysica-gebaseerde invoer te leveren voor de assimilatie van beperkte en onzekere waarnemingen, zodat zowel aardbevingen als trage verschuivin-

gen beter voorspeld kunnen worden in synthetische studies. Ten slotte stel ik toekomstige onderzoeksmogelijkheden en uitdagingen voor die de aandacht van de gemeenschap vereisen.



# 1

Introduction

Earthquakes, among nature's most formidable phenomena, have reshaped landscapes and societies through their immense power and devastating consequences. The 2004 Sumatra (Indonesia) earthquake, registering a staggering 9.1 in moment magnitude, generated a massive tsunami that devastated populations along coastlines in multiple countries. Similarly, the 2008 Wenchuan (China) earthquake, though of lower magnitude, resulted in significant casualties and widespread destruction due to its shallow depth and proximity to densely populated areas. The 2011 Tohoku (Japan) earthquake, a magnitude 9.0 event, demonstrated the multifaceted hazards associated with seismic activity. Beyond the intense ground shaking, the subsequent tsunami wreaked havoc on coastal regions, triggering nuclear emergencies and exposing the vulnerabilities of critical infrastructure.

Meanwhile, regions far away from plate boundaries are suffering from emerging induced seismicity: earthquakes triggered by human activities, such as extraction of gas from or injecting of fluids into the subsurface [Segall, 1989; McGarr *et al.*, 2002; Ellsworth, 2013]. An example is the Groningen gas field in the Netherlands, where on August 16, 2012, at 22:31 local time, an earthquake of magnitude ML 3.6 occurred near the village of Huizinge (Fig 1.1). This earthquake resulted from gas extraction from the Groningen gas field, Europe's largest gas field, located at 3 km depth within the Groningen province. While not the first recorded earthquake in the area, it was the most powerful one up to now, causing damage to buildings and spreading fear among locals [Dost and Kraaijpoel, 2013]. The Groningen gas field was discovered in 1959 and soon became one of the largest onshore reservoirs in the world [de Jager and Visser, 2017]. Production started in 1963 and the first earthquake was recorded in 1991 with a magnitude of 2.5. While earthquakes had been infrequent, their frequency and size began to rise since 2003 (Fig 1.1) [van Thienen-Visser and Breunese, 2015]. The increasing number of earthquakes felt a decade ago marked a turning point in the public perception of induced seismicity in the Netherlands. It altered the future of Dutch gas production. Before the Huizinge earthquake, the earthquake statistics showed that the maximum earthquake magnitude in the gas fields would remain small, but the earthquake showed otherwise, causing a reevaluation of gas production and the potential risks associated. Following the Zeerijp earthquake in 2018 (ML 3.4), the Dutch government decided to completely halt gas production by 2030,

later moving up the timeline to 2022. However, the public concern about induced seismicity, perhaps even after field closure, remains unsettled. Not restricted to Groningen, induced earthquakes, sometimes reaching magnitudes as high as 5.5, have occurred in various regions globally. These events have been documented in several countries, including the United States, Switzerland, South Korea and China [Hough, 2014; Li *et al.*, 2007; Diehl *et al.*, 2017]. Both traditional and novel usage of the underground, such as in geothermal energy and CO<sub>2</sub> storage, are being challenged.

These natural and induced earthquakes stand as stark reminders of the catastrophic hazards associated with seismic activity, highlighting the critical need for comprehensive risk mitigation methodologies. Current hazard mitigation strategies include increasing the preparedness from civil engineering and scientific perspectives, which both depend on a reliable understanding of where, when, why and how earthquakes take place in both long-term and short-term time scales. However, earthquake forecasting remains an elusive pursuit due to the inherent complexities and uncertainties surrounding earthquakes and faults [Geller *et al.*, 1997]. Advancements in probabilistic seismic hazard assessments (PHSA) offer insights into the likelihood of earthquakes occurring within specified time frames and regions, and thus provide guidance on urban planning and risk mitigation without precisely predicting the exact timing or magnitude of an event. While significant progress has been made in understanding earthquake processes in the past decades, accurate short-term earthquake forecasting remains a scientific challenge. Seismologists pin their hope on precursory phenomena such as foreshocks and precursory slips, changes in groundwater level and underground gas release, and gravitational and electromagnetic anomalies [Reasenber, 1999; Jordan *et al.*, 2011; Pritchard *et al.*, 2020]. However, these signals still lack consistent correlation with imminent seismic events, not to mention that their physical basis is yet to be verified. Emerging technologies like machine learning and big data analysis are gaining scientists' attention. By analyzing vast datasets and patterns, these approaches aim to discern precursory signals from being immersed in noises. Nevertheless, these data-dense methodologies intentionally or unintentionally overlook the fundamental physics of earthquake processes. Despite the inherent complexities and uncertainties, I believe that understanding earthquake physics plays a fundamental role towards earthquake forecasting. Combining physics-based numerical modeling of earthquake sequences and seismological and geodetic observa-

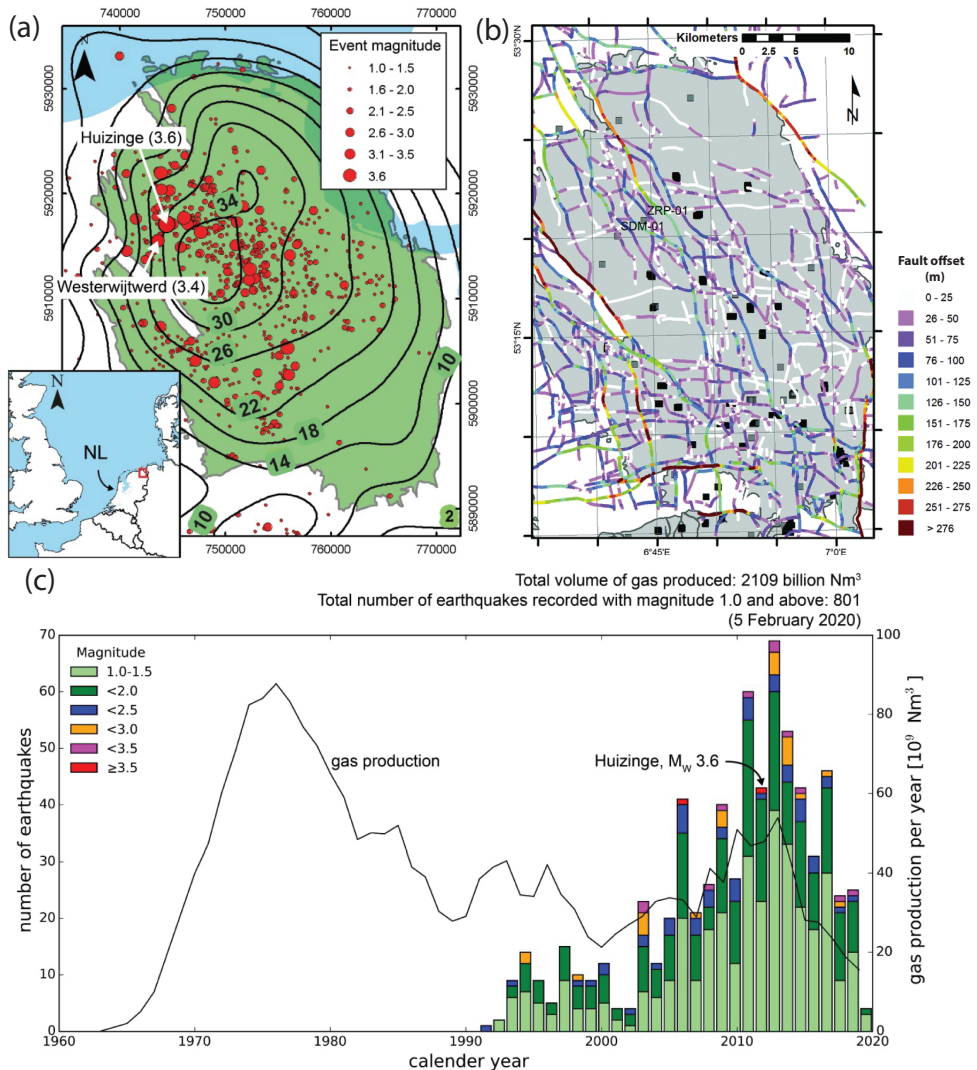


Figure 1.1: *Spatial and temporal distribution of Groningen seismicity. (a) Spatial distribution of induced earthquakes (magnitude above 1.0) and surface subsidence (black contour lines, cm). The location of Groningen field in Europe is shown in the bottom-left inset. The locations of the 2012 Huizinge earthquake (ML 3.6) and the 2019 Westerwijtwerd earthquake (ML 3.4) are labeled, adopted from [Hunfeld, 2020]. (b) Faults in the Groningen field (grey) colored by fault offset. Black and gray squares indicate producing and closed-in wells, with the Stedum 1 (SDM-1) well and the Zeerijp 1 (ZRP-1) labeled. The fault offset is colored. Data from NAM ([www.nam.nl](http://www.nam.nl)), adopted from [Buijze et al., 2017]. (c) The number of induced earthquakes (magnitude above 1.0) and the gas production per calendar year. The data are derived from <https://www.nam.nl/feiten-en-cijfers>, adopted from [Hunfeld, 2020].*

tional data will lead to a better estimate of fault evolution. Within the DeepNL InFocus project my collaborators and I adopt ensemble data assimilation methods to achieve this [Van Dinther *et al.*, 2019a; Diab-Montero *et al.*, 2023]. In this thesis, I start from utilizing numerical models to simulate earthquake processes, quantify seismic hazard halfway through, and conclude with a forward-looking exploration of earthquake forecastability. In this opening chapter, I will begin by outlining the essential aspects of the Groningen gas field, covering its geological and seismological attributes. Next, I will elaborate on the critical processes I aim to explore concerning both earthquake and aseismic sequences, along with the most impactful factors influencing these processes. I will provide a summary of previous research and my current comprehension, emphasizing the novelty brought by my PhD work. Lastly, I will articulate the motivation behind this work and lay out its objectives, concluding with an outline of how the thesis is structured.

## 1.1 Induced earthquakes in Groningen

### 1.1.1 Geological, geodetic and seismological observations

#### Lithology and faulting

The Groningen gas field occupies a roughly 30 km by 30 km region in the North-east of the Netherlands and is one of the largest onshore gas fields in the world (Fig 1.1) [de Jager and Visser, 2017]. Seismological studies and well logs have provided us with an unprecedented resolution of the subsurface (Fig 1.2). The gas extraction from the Groningen field primarily targets the Slochteren formation within the upper Rotliegend group of Permian age. This geological layer is predominantly composed of fluvial and aeolian sandstones characterized by porosities ranging from 10% to 24% and permeabilities from 1 to 1000 mD [de Jager and Visser, 2017]. The reservoir's depth varies across the field, lying at about 2400 m in the southern region and deepening to approximately 2900 m towards the northern areas [de Jager and Visser, 2017]. The reservoir also thickens northward, ranging from around 50 m to exceeding 300 m [de Jager and Visser, 2017]. Overlying the Slochteren Formation is the Ten Boer Claystone, part of the upper Rotliegend group, with a thickness varying from several tens of meters to over 80



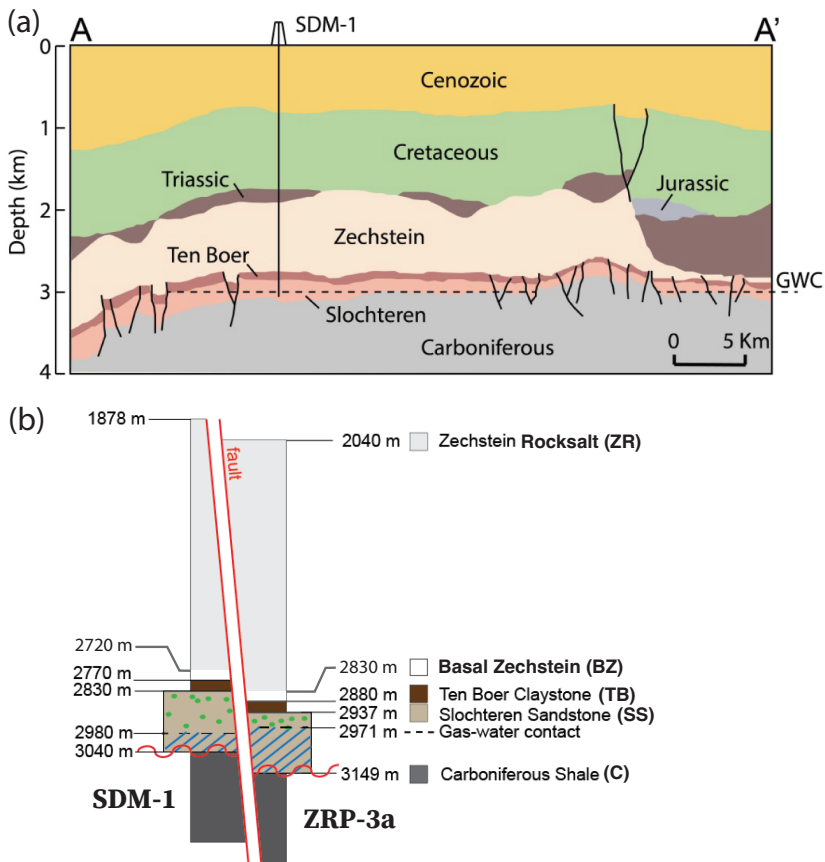


Figure 1.2: *Stratigraphy of the subsurface in Groningen.* (a) A cross-section of the Groningen field showing the rock formations with faults, adopted from [Hunfeld et al., 2021]. (b) Stratigraphy of the Groningen field at the SDM-1 and ZRP-3a wells. The data are from <https://www.nlog.nl/datacenter/brh-overview>, adapted from [Pijnenburg et al., 2019].

m. Further above lies the Triassic Zechstein formation, characterized by a 50-m thick basal sequence of anhydrite and carbonates known as the Basal Zechstein formation, overlain by a rocksalt (Halite) formation spanning 100-1000 meters in thickness. Beneath the Slochteren Reservoir lies the Carboniferous underburden, consisting of siltstones and shales.

In the Slochteren Formation, an extensive network of over a thousand normal faults has been identified through 3D seismic interpretations [Kortekaas and Jaarsma, 2017]. The primary fault trend within the Groningen gas field predominantly follows an NNW-SSE orientation, complemented by additional fault trends aligned in an east-west (E-W) and north-south (N-S) direction. Typically, these faults exhibit a steep dip, ranging from 60 to 80 degrees, within the Slochteren reservoir [Wentinck, 2016]. These faults are characterized by offsets typically ranging between 20 to 100 meters and occasionally up to around 300 meters, resulting in the juxtaposition of various stratigraphic units (Fig 1.2). They have been imaged to extend more than 1000 m downdip into the Carboniferous underburden, while their upper extents stop at the Basal Zechstein. The ductile Zechstein rocksalts inhibit brittle deformation, such that faults typically do not crosscut the rocksalt [Kortekaas and Jaarsma, 2017]. The origin of the faults can be traced back to the Late Jurassic to Early Cretaceous rifting period and the faults were reactivated during the Late Cretaceous to Early Tertiary inversion associated with the Alpine orogeny [de Jager and Visser, 2017].

### Reservoir compaction

Prior to gas production, the vertical stress at the reservoir depth was approximately 65 MPa due to the 3 km overburden. The minimum horizontal stress was approximately 43 MPa. The gas pressure before production was around 35 MPa [Breckels and Van Eekelen, 1982]. The field's gas production began in 1963 and surged to a peak annual production exceeding 80 BCM (billion cubic meters) in 1976, after which it gradually stabilized to 40 BCM per year for three decades. Following the Huizinge earthquake in 2012, gas production was further restricted to mitigate seismic risks, and finally phased out. Consequently, the reservoir pressure has significantly decreased to 8 MPa at the present day [van Oeveren et al., 2017]. This pressure decline has been relatively uniform across different reservoir compartments, indicating a high permeability of the reservoir faults. Additionally, pressure measurements reveal that the overlying Ten

Boer Claystone is undergoing pore pressure depletion, although it lags behind the depletion observed in the sandstone layer [Burkitov *et al.*, 2016].

The principal process that leads to fault activation and induced earthquakes in Groningen is the differential loading on the fault due to reservoir compaction, which is the consequence of the pore pressure reduction [Van Wees *et al.*, 2014; Van Eijs, 2015]. This mechanism will be further explained in the next section. Reservoir compaction leads to subsidence at the surface that can be measured by geodetic instruments and techniques, such as GNSS and InSAR. Since a few years after the start of gas production, the Groningen field has experienced accelerated surface subsidence. Currently, the subsidence has reached approximately 35 cm in the central part of the field, coinciding with the areas of highest porosity, while the peripheral regions have subsided less (Figure 1.1a). The compaction is also monitored with in-situ measurements using distributed strain sensing [Cannon and Kole, 2017]. The measured reservoir compaction rate in 2016 is about 25  $\mu\epsilon/\text{yr}$  (microstrain per year). The same study also measured compaction of 10  $\mu\epsilon/\text{yr}$  in the overburdening Ten Boer claystone, in agreement with the pore pressure measurement at the same layer.

## Earthquakes

The recent advancements in the seismological instrumentation network in the Groningen field have significantly enhanced earthquake location accuracy [Dost *et al.*, 2017]. Prior to 2014, limited station coverage and reliance on a 1D velocity model led to large uncertainties in earthquake locations, with horizontal uncertainties of 0.5 to 1 km and vertical uncertainties exceeding 1 km. However, improvements in the seismic network since 2014 and the introduction of a 3D velocity model by NAM in 2017 reduced these uncertainties to 0.1 to 0.3 km horizontally and 0.3 km vertically [Dost *et al.*, 2017]. The relocation of seismic events between 2014 and 2016 highlighted two key observations: the relocated events often clustered around known faults, and a majority occurred within the reservoir formation [Spetzler and Dost, 2017; Willacy *et al.*, 2019]. This aligns with data from deep borehole arrays [Zhou and Paulssen, 2020] and waveform inversion results. Moment tensor inversions of larger events, such as the 2012 Huizinge, and 2018 Zeerijp earthquakes, indicated a dominant normal faulting mechanism on NW-SE faults, consistent with the regional stress field where the maximum horizontal stress aligns NNW-SSE [Van Eijs, 2015]. This result also agrees with full

waveform modeling using data from deep and shallow boreholes [Willacy *et al.*, 2019].

Adopting the Brune source model, which assumes a circular rupture area, the rupture radius, slip, and stress drop associated with the aforementioned earthquakes can be estimated [Kraaijpoel and Dost, 2013]. For example, the 2012 Huizinge earthquake had a rupture radius of about 390 m, a stress drop of 2.5 MPa, and an average slip of 50 mm. It should be noted that these computations rely on assumptions regarding rupture shape and kinematics. To avoid making large assumptions about the source behaviors, I model earthquakes and aseismic slips in sequence from millions of years ago and into the future. My simulations resolve and focus on the entire earthquake process.

## 1.2 Modeling of earthquake and aseismic slip

### 1.2.1 “Earthquake cycle”

*Earthquake cycle* is a widely accepted term describing the (quasi-)recurring pattern of loading, release and relaxation of fault stress. The associated fault slips encompass a broad spectrum from aseismic creep, slow slip events to earthquakes, which are observed in both natural and induced scenarios [Dragert *et al.*, 2001; Eyre *et al.*, 2022]. While *cycle* may suggest a repetitive sequence of comparable or characteristic events, it is essential to note that real fault behavior often deviates from a perfectly predictable cycle. Understanding the earthquake cycle involves exploring the various phases of fault activity that span across many time and slip rate scales. Generally, an earthquake cycle can be divided into four phases:

1. **Interseismic phase:** This phase is characterized by a period of relative fault quiescence where stress gradually accumulates along the fault. The fault is locked in some regions (asperities) so that strain energy builds up at the transitions between the locked and creeping regions. This phase can last from years to centuries, with slip velocities that are far below the tectonic loading rate, or practically zero ( $<1$  nm/s).

2. **Nucleation phase:** As stress accumulates, there is a point where slip begins to accelerate. This phase represents the preparation for the coming earthquake, with slip velocities still relatively low ( $<1$  mm/s). During this phase, the activated fault patch progressively grows until it reaches a critical length scale, the nucleation length  $L_c$ . With further acceleration, the slip goes from aseismic to seismic, which is reflected in the fast slip rate and rupture speed. The slip rate usually goes beyond 1 mm/s and the rupture speed goes to the order of km/s at the end of this phase (Fig 1.3).

3. **Coseismic phase:** This is the phase where an earthquake occurs. Rapid slip along the fault generates seismic waves, releasing accumulated stress and strain energy. Slip velocities during this phase can be extremely high, reaching speeds of 1 m/s or higher, and continue for milli-seconds to minutes. This is the period when faults show various dynamic behaviors depending on the earthquake magnitude, among others. Earthquakes can propagate at different slip rates and rupture speeds, producing different stress drops and ground motions, depending on the nature and the history of the fault [Perrin *et al.*, 2016].

4. **Postseismic phase:** Following the main shock, the fault continues to adjust and relax, resulting in decelerating slip velocities. The fault in this phase still slips at rates ranging from 1 mm/s to 1 nm/s, as the fault settles back to a more stable state and finally becomes re-locked. This phase can last for years, sometimes even decades, after an event.

Research into fault properties and fault evolution is fundamental for understanding the kinetic and dynamic aspects of earthquake ruptures. It aids in seismic hazard assessment by predicting potential earthquake behavior and assessing associated risks. Improved simulations of fault processes can enhance earthquake forecasting capabilities and contribute to various fields like the safe use of the subsurface for sustainable energy production and storage, hydrology, and civil engineering, where knowledge of faults is essential for resource exploration, water management, and infrastructure stability.

In this work, I center my investigation on the whole sequence of recurring earthquakes and aseismic slips particularly on the nucleation phase, employing numerical models to understand if, why, and how slow slips finally escalate into earthquakes. The nucleation phase primarily comprises two fundamental mechanisms: fault failure and fault weakening. Nucleation starts with

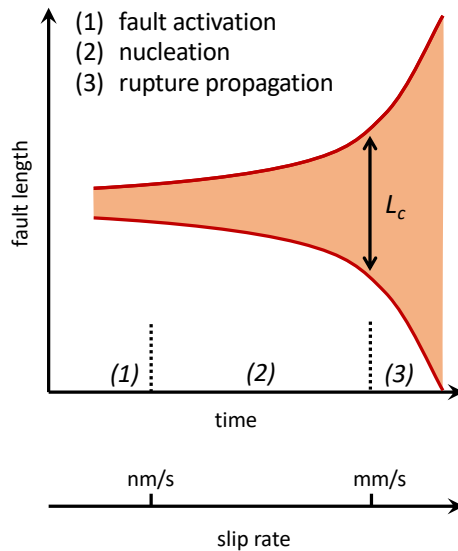


Figure 1.3: **Earthquake nucleation.** Schematic illustration of the growth of the rupture zone. The colored region shows a symmetrical growth of the nucleation zone to reach the nucleation length  $L_c$ . The three stages match the first three phases in an earthquake cycle. The evolution of the slip rate at the rupture tip is shown at the bottom.

fault failure, which marks the moment when faults start to deviate from elastic deformation and slip initiates. Yet, the continuation of nucleation and the following coseismic rupture demand continuous fault weakening, which can be in the form of slip-weakening, velocity-weakening, and various forms of dynamic weakening.

## 1.2.2 Fault as a frictional interface

Until now I have not defined what a fault is, which is necessary to benefit the coming mathematical descriptions. From a seismological perspective, faults are localized deformation zones where unstable energy release, i.e. earthquakes, can take place. Earthquakes are considered as a fracture process, a frictional process, or a combination of the two. Fracture mechanics treats earthquakes as a growing fracture or crack, and focuses on understanding the stability of cracks under stress. It offers a structured approach to analyzing the behavior of materials near the tips of pre-existing cracks, providing insights into fracture initia-

tion, propagation, and failure. As one of the prevalent branches, linear elastic fracture mechanics (LEFM) establishes critical concepts such as stress intensity factors, fracture toughness, and crack propagation criteria [Freund, 1979]. Stress intensity factors quantify the stress state near a crack tip and determine the likelihood of crack growth under the applied loading conditions. Fracture toughness represents a material's resistance to crack propagation and is crucial in assessing its ability to withstand fracture. Additionally, Griffith's energy balance defines the conditions under which cracks propagate, providing critical insights into material failure mechanisms. In practice, using the concept of the crack tip as an analog to the rupture tip has been proven to be a successful estimate for describing the behavior of the dynamic rupture front [Kammer *et al.*, 2015; Weng and Ampuero, 2022].

Frictional description of earthquakes and faults treats the inelastic fault slip as a frictional process. This theory is rooted in the observation that earthquakes predominantly occur along pre-existing fault lines, often sealed within the Earth's crust. Shear stress accumulates along locked faults until it surpasses the *frictional* strength, resulting in sudden fault slip and the release of stored energy as seismic waves. Empirical friction laws, established on the basis of laboratory experiments, establish relationships between shear stress on the fault and normal stress, slip velocity, and slip history. Notably, the rate-and-state phenomenology, pioneered by Dieterich [1979] and Ruina [1983], presents a framework that describes the multi-faceted shear stress evolution using simple empirical parameters. This formulation has successfully included the time-dependent fault strength recovery and the dependency of fault strength on slip rate. In particular, as the slip rate increases fault strength may decrease (velocity-weakening) or increase (velocity-strengthening). The rate-and-state frictional response is influenced by factors such as mineralogy, pressure, temperature, fault microstructure, and other environmental conditions. Different from fracture mechanics, this frictional model predicts a smooth transition of stable, aseismic slip to unstable, seismic slip. Despite being based on different assumptions, some parallels may be drawn between the fracture and the friction descriptions. Both demonstrate a mechanism of stress drop at the rupture tip and an associated energy release. The analogy of breakdown energy results in a comparable length scale requirement for unstable deformation, i.e., the characteristic length of the process zone in the fracture model and the nucleation length in the frictional model. Recently, increased attention has been given to a combi-

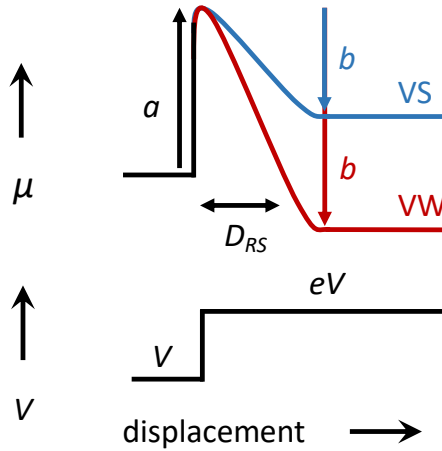


Figure 1.4: *Rate-and-state friction*. Schematic diagram showing the evolution of friction coefficient after a velocity step and corresponding rate-and-state parameters. Scenarios of velocity-strengthening and velocity-weakening friction are shown in blue and red, respectively.

nation of the two descriptions to better accommodate the on-fault and off-fault ruptures in a single framework. In this thesis, I employ the rate-and-state frictional description of faults and discuss fault failure and weakening in this context.

### 1.2.3 Rate-and-state friction

The rate-and-state dependent friction (RSF) formulation is mainly derived based on two types of laboratory experiments, the velocity-step experiments and the slide-hold-slide experiments (reviews by *Dieterich and Kilgore [1996]*; *Marone [1998]*). The classical expression has the form [*Dieterich, 1979*; *Ruina, 1983*]

$$\mu = \mu_0 + a \ln \left( \frac{V}{V_0} \right) + b \ln \left( \frac{V_0 \theta}{D_{RS}} \right) \quad (1.1)$$

where:

- $\mu$  represents the coefficient of friction defined as  $\mu = \tau/\sigma$ , with  $\tau$  being the fault shear stress and  $\sigma$  the fault normal stress;
- $V$  is the slip rate;
- $\theta$  is the state variable;



- $\mu_0$  represents the coefficient of friction at a reference velocity  $V_0$ ;
- $a$  and  $b$  are experimentally determined dimensionless constants, linked respectively to the rate and state dependence of friction; and
- $D_{RS}$  denotes a critical slip distance.

The rate parameter  $a$ , also known as the direct effect, dictates the immediate response in frictional behavior corresponding to a change in sliding velocity and is always in the same direction as the velocity step (i.e.  $a$  is always positive). The state parameter  $b$ , also known as the evolution effect, characterizes the extent of the evolution of frictional properties in response to the change in sliding velocity. These parameters can be determined from velocity-step experiments (Fig 1.4). Imagine a fault is sheared at a constant slip rate  $V$  and reaches a steady state. The slip rate is then suddenly increased to  $eV$  and the friction has to evolve to reach a new steady state. During this process, the friction first increases transiently by a magnitude of  $a$  before any fault slip. Then it gradually drops by a magnitude of  $b$  over a certain amount of slip. The final steady-state friction differs from the initial state by  $(a-b)$ . If  $a-b > 0$ , fault resistance becomes stronger upon slip acceleration (velocity-strengthening, VS), and stable slip is favored [Rice and Ruina, 1983]. Conversely,  $a-b < 0$  represents velocity-weakening friction (VW), favoring fault acceleration and an instability can emerge. Thus, these friction parameters are critical in determining conditions suitable for the growth of a nucleation patch. Laboratory experiments demonstrate that the RSF framework effectively describes fault sliding behaviors at low velocities across a diverse range of geological materials, subject to factors including temperature, composition, gouge thickness, and slip rate [Marone, 1998]. The usage of the value of  $(a-b)$  as an indicator for fault stability has gained success when applied to nature [Dieterich, 1992; Rubin and Ampuero, 2005; Kaneko et al., 2008]. However, this convention is challenged by the emergence of induced earthquakes. They are observed at shallow depths where most fault rocks consistently exhibit velocity-strengthening behavior in low temperature and pressure experiments [Marone and Scholz, 1988; Scholz, 2019; Kang et al., 2019; Ruggieri et al., 2021; Miyamoto et al., 2022; Zhong et al., 2023]. The Groningen earthquakes strengthen this paradox. I will propose a new mechanism inside the rate-and-state framework to solve the paradox.

The critical slip distance  $D_{RS}$  is often interpreted as the distance over which the state variable  $\theta$  evolves in order to reach a new steady state upon alteration

in sliding conditions. It is suggested to reflect the renewal of the population of frictional contacts during slip progression in the microscopic sense [Marone and Kilgore, 1993]. Various formulations have been proposed to model the evolution of the state variable based on experimental observations and interpretations [Dieterich, 1979; Ruina, 1983; Beeler et al., 1994; Kato and Tullis, 2001; Tullis and Goldsby, 2003]. Two prevalent state evolution laws include the Dieterich-Ruina aging law [Dieterich, 1979]

$$\dot{\theta} = 1 - \frac{V\theta}{D_{RS}} \quad (1.2)$$

and the Ruina-Dieterich slip law [Ruina, 1983]

$$\dot{\theta} = -\frac{V\theta}{D_{RS}} \ln \left( \frac{V\theta}{D_{RS}} \right). \quad (1.3)$$

The aging law matches better with data from slide-hold-slide experiments, while the slip law matches better with velocity-step experiments. More complicated laws combining the two and accounting for the rate-dependence of the parameters include the *Kato-Tullis law* [Kato and Tullis, 2001; Tullis and Goldsby, 2003] and microphysics-based models such as the *Chen-Niemeijer-Spiers model* [Chen and Spiers, 2016] or the *Aharonov & Scholz model* [Aharonov and Scholz, 2018].

In summary, the RSF framework serves as a robust mathematical tool for modeling earthquake cycles, aiding in inferences about earthquake nucleation processes and earthquake cycles [Lapusta et al., 2000; Lapusta and Rice, 2003; Rubin and Ampuero, 2005; Kaneko et al., 2008]. Despite the lack of microphysical understanding of rate-and-state friction being addressed with the microphysics-based models, questions about parameter scaling and the effects of natural fault heterogeneity remain inadequately understood, which I will introduce shortly after.

## 1.3 Mechanisms and models for induced seismicity in Groningen

This section summarizes the physical mechanisms and models proposed for the induced earthquakes in Groningen. Modeling of Groningen seismicity includes the works that focus on seismicity rates in the fault network in response to Coulomb stress changes [Bourne and Oates, 2017; Candela et al., 2019, 2022;

*Smith et al.*, 2022; *Heimisson et al.*, 2022; *Acosta et al.*, 2023]. *Candela et al.* [2019, 2022] explored the non-linear relation between stressing rate and seismicity rate in Groningen using a Coulomb rate-and-state approach. A similar Coulomb rate-and-state approach is adopted in *Acosta et al.* [2023] while this work also reveals the role nucleation time plays in the characteristics of seismicity at various timescales. *Bourne and Oates* [2017]; *Heimisson et al.* [2022]; *Smith et al.* [2022] updated the Coulomb criterion by adding a failure threshold to explain the lagged response of Groningen seismicity to production. Their model reproduced a better seismicity rate profile in Groningen than using a static Coulomb failure criterion.

Other works focus on modeling the time-dependent stress change on a single fault and the induced fault failure [*Van Wees et al.*, 2014, 2017; *van Wees et al.*, 2018; *Jansen et al.*, 2019; *Jansen and Meulenbroek*, 2022; *Cornelissen and Jansen*, 2023]. *Jansen et al.* [2019]; *Jansen and Meulenbroek* [2022]; *Cornelissen and Jansen* [2023] derived analytical and semi-analytical expressions of the fluid-induced stress changes on displaced vertical and inclined faults and the associated aseismic slips. *Van Wees et al.* [2017]; *van Wees et al.* [2018] combines the semi-analytical approach with a finite element method to solve the stress change during and after gas production.

More works focus on modeling the earthquake processes of a single earthquake using quasi-dynamic or dynamic approaches [*Zbinden et al.*, 2017; *Buijze et al.*, 2019; *Buijze*, 2020; *Weng et al.*, 2021; *Ruan et al.*, 2023]. *Buijze et al.* [2019]; *Buijze* [2020] used a 2-D quasi-static reservoir depletion model to simulate until fault activation coupled to a dynamic rupture model for the subsequent dynamic rupture. In their simulations, most seismic ruptures remain confined to the reservoir interval, but may propagate into the underburden in conditions such as small fault offset, large stress drop, small fracture energy, and critical in situ stress. *Ruan et al.* [2023] applied a similar approach in 3-D and confirmed the aforementioned findings. They add that whether the induced earthquakes nucleate from the top, middle, or bottom of the reservoir could be related to the angle at which a secondary fault branches out, which is commonly seen in the Groningen fault network. A report by *Weng et al.* [2021] estimated the maximum earthquake magnitude in Groningen in their 2.5-D model using the concept of fracture energy derived in linear elastic fracture mechanics (LEFM).

In the following subsections, I will first introduce the mechanism in these cur-

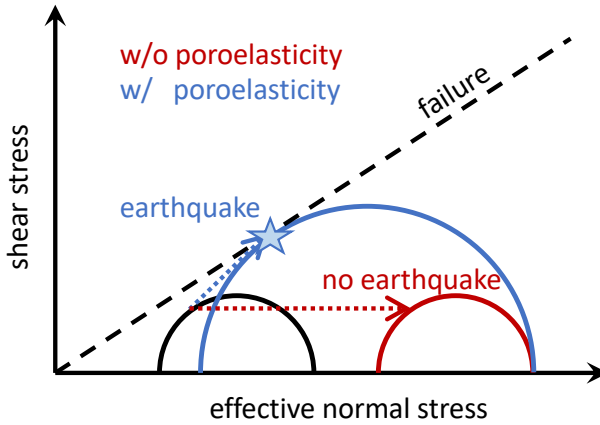


Figure 1.5: *Mohr diagram showing the effect of pore pressure change on a normal fault. The initial stress state is shown in black. The red line shows the possible stress change due to a decrease in pore pressure without consideration of the poroelastic effect. The blue line shows the possible stress change accounting for the poroelastic effect. The dashed arrows show the changes in normal and shear stress on a fault with a fixed strike and dip angle with respect to the principal stress direction. The blue star indicates the earthquake when the poroelastic effect is accounted for.*

rent models characterized by a combination of a Mohr-Coulomb failure criterion and a linear slip-weakening friction formulation. Then I will motivate my shift towards utilizing the rate-and-state friction framework to describe fault failure and the subsequent weakening. Frictional healing is inherent in this formulation, allowing for a unified modeling of all phases in a whole earthquake sequence.

### 1.3.1 Fluid extraction induces fault failure

Specific to the induced earthquakes during fluid extraction, fault failure is triggered by reservoir compaction resulting from the pressure drop and the associated poroelastic effect. The mechanism of such earthquakes is distinct from natural earthquakes. On a fault near plate boundaries, the stress accumulation is the result of plate tectonics, where plates move at rates ranging from millimeters to centimeters per year. This gradual stress buildup can lead to either the faulting of initially intact rocks or the reactivation of pre-existing, optimally oriented faults. In the case of the activation or reactivation of a fault in a reservoir

context, however, the stress can be altered by the direct mechanical impact of pore fluid pressure, associated poroelastic effects, and even thermal effects.

This poroelastic effect is especially relevant during fluid extraction. This is different from the mechanism in a fluid injection scenario where the pore pressure increase causes a substantial reduction in the effective normal stress and thus a reduction in fault strength. Reservoir depletion, specifically the decrease in pore fluid pressure  $\Delta P$ , induces stress alterations in several ways. These stress changes collectively determine whether fault failure occurs. First, pore pressure reduction increases the effective normal stresses both within the reservoir and those acting on faults. If this increase in effective normal stresses is isotropic, the fault will experience an increase of the same magnitude in its normal stress, while the fault shear stress does not change. That means an increase in fault strength with unchanged stress. In the Mohr diagram, the Mohr circle, representing the stress state, is moved rightwards and becomes far away from the failure criterion (red circle in Fig 1.5). However, assuming linear poroelasticity, pore pressure reduction in a reservoir rock also induces a contraction inducing negative volumetric strain [Geertsma, 1973]. For laterally extensive reservoirs, this effect results in an additional reduction in horizontal stress while the effective vertical stress change is not affected. In the context of normal faulting regimes ( $\sigma_v > \sigma_h$ ) and considering that the principal stresses  $\sigma_1$  and  $\sigma_3$  are vertical and horizontal, reservoir depletion results in an increase in differential stress  $\sigma_1 - \sigma_3$ . In other words, the radius of the Mohr circle increases at the same time (blue circle in Fig 1.5). In this case, the fault stress can either converge towards or deviate from the failure criterion (blue dashed line in Fig 1.5). It is suggested that a shallower dip angle and a lower Poisson's ratio help the fault stress to converge towards failure [Geertsma, 1973; Hettema et al., 2000]. The third and probably the strongest effect is the stress concentration due to limited reservoir thickness and the offset of reservoir compartments by the fault. Both geometrical factors induce displacement gradients across the discontinuity, which generate pronounced local stress concentrations that encourage fault (re)activation. Jansen et al. [2019] derived an analytical solution of the stress change on faults with offsets in a homogeneous medium, which justified this hypothesis. In particular, the stress concentration at the edges where mechanically contrasting formations juxtapose is substantial [Buijze et al., 2019].

### 1.3.2 Frictional healing controls fault strength

Numerous numerical studies have been employing the standard Mohr-Coulomb criterion, either in combination with a linear slip-weakening or a rate-and-state friction formulation, to investigate fault (re)activation due to gas production in Groningen [Zbinden *et al.*, 2017; van Wees *et al.*, 2018; Jansen *et al.*, 2019; Buijze *et al.*, 2019; Candela *et al.*, 2022]. However, such criterion cannot account for the change in fault strength due to frictional healing. Healing is a well-established phenomenon describing the time-dependent recovery of fault strength between earthquakes or during tectonic inactivity. This phenomenon is globally observed in slide-hold-slide experiments using various rocks, where the peak stress of the subsequent slip ('slide') after fault reactivation increases with the time of inactivity ('hold') [Beeler *et al.*, 1994; Olsen *et al.*, 1998; Marone, 1998; Nakatani and Scholz, 2004; Chen *et al.*, 2015; Carpenter *et al.*, 2016]. In this way larger stress drops are obtained after a longer healing period. The observed strength increase originates from the microphysical growth of grain contacts (asperities) as well as the development of cohesion [Tenthorey and Cox, 2006]. Processes such as cementation are evidenced to be involved in cohesion development by microscopic imaging [Hunfeld *et al.*, 2017]. This behavior is confirmed also for the specific lithologies in Groningen [Hunfeld *et al.*, 2020]. Rate-and-state friction inherently includes the description of healing. Nakatani [2001] derived the expression of *interface strength*  $\Psi = \mu_0 + b \ln \frac{V_0 \theta}{D_{RS}}$ , which is equivalent to the strength used in Mohr-Coulomb failure criterion, but not static. This expression comes from a reformulation of the RSF

$$\frac{V}{V_0} = \exp \left[ \frac{\frac{\tau_s}{\sigma'_n} - \left( \mu_0 + b \ln \frac{V_0 \theta}{D_{RS}} \right)}{a} \right]. \quad (1.4)$$

In this expression, the slip rate is defined by the relative amplitude of the applied shear force  $\frac{\tau_s}{\sigma'_n}$  compared to a state-dependent variable  $\Psi = \mu_0 + b \ln \frac{V_0 \theta}{D_{RS}}$ . When the shear force is much higher than  $\Psi$ , a high slip rate is achieved, simulating the coseismic phase. If the shear force is much lower, a locked phase is simulated with a near-zero slip rate. Therefore, the term  $\Psi$  in the equation behaves just as well as a description of the fault strength. Its dependence on the state variable  $\theta$  indicates that the fault strength in rate-and-state friction is time-dependent.

Healing is especially relevant for induced earthquakes as the research regions have been tectonically inactive for millions of years before human activities,

such as Groningen [*van Oeveren et al.*, 2017]. Recent work by *Bourne and Oates* [2017]; *Heimisson et al.* [2022]; *Smith et al.* [2022] updated the Coulomb criterion by adding a failure threshold. Their model reproduced a better seismicity rate profile in Groningen than using a static Coulomb failure criterion and explained the lagged response of Groningen seismicity to production. The threshold used in their works can be justified by healing. Even though healing is inherent in rate-and-state friction, this work is the first to adopt this concept to explain the occurrence of induced earthquakes, and illustrate the nucleation process on velocity-strengthening faults.

### 1.3.3 A single friction formulation for healing, loading, and sequences of slip

Besides the frictional healing, utilizing rate-and-state friction also allows for a unified approach to modeling of all phases in a whole earthquake sequence, especially the simulation of the continuous nucleation process. This friction formulation is popular in modeling natural earthquakes [*Lapusta et al.*, 2000; *Kaneko et al.*, 2008], but has not been applied to the Groningen field. Instead, a *Mohr-Coulomb criterion + slip-weakening law* is utilized [*Zbinden et al.*, 2017; *Buijze et al.*, 2019], which ignores the velocity-dependence of friction and thus cannot simulate a continuous nucleation process between interseismic and seismic phases. Nucleation in these models is mostly simulated in an artificial manner, either using a prescribed overstressed asperity as the nucleation zone or a small over-stress at the first location of failure as initiation to trigger the formation of the nucleation zone. The absence of frictional healing and the artificial nucleation suggest that these models lack the ability to simulate the whole earthquake sequence.

In fact, it is worth noting that the RSF inherently includes the requirements for both fault failure and weakening. In other words, it replaces the *Mohr-Coulomb criterion + slip-weakening law* combination in prevalent geomechanical models (Fig 1.4). The static Mohr-Coulomb failure point is replaced by the interface strength  $\psi$ . The fault weakening is not purely a linear slip weakening, as seen in Fig 1.4, but the slope of the weakening curve to a large content follows  $k_{sw} = -b/D_{RS}$  [*Liu and Rice*, 2007]. This is the first work applying rate-and-state friction to explain the Groningen seismicity: why earthquakes take



place in Groningen; where they could nucleate; and how far they could rupture. This work focuses on unraveling these mechanisms and addressing these questions.

### 1.3.4 Heterogeneities on the fault

Faults are heterogeneous not only due to their roughness but also the various physical processes thereon. As is seen in Groningen, highly variable lithological layers in a narrow depth interval with offset caused by tectonic faulting millions of years ago have resulted in heterogeneous fault stress and strength conditions. Generally speaking, fault heterogeneity emerges from diverse processes in the shear zone, such as the variation in material strengths due to different lithologies and their mixtures following geological movements [Ben-Zion and Sammis, 2003; Huang, 2018; Bedford *et al.*, 2022], a heterogeneous local stress field due to fluid presence and the slip of historical earthquakes [Duan and Oglesby, 2006; Hillers and Miller, 2007; Behr and Bürgmann, 2021], the complex and sometimes random fracture growth [Preuss *et al.*, 2020]. These factors result in spatially variable stress, strength and frictional properties, if faults are considered as infinitely thin interfaces [Yamashita *et al.*, 2018; Gounon *et al.*, 2022; Morad *et al.*, 2022]. Fault geometry and roughness, formed during shear localization, additionally influence the heterogeneous stress, strength and friction. Laboratory experiments reveal distinctive features of earthquake sequences on rough faults, showcasing irregular rupture events with low repeatability [Yamashita *et al.*, 2018; Morad *et al.*, 2022]. Furthermore, earthquakes on rough faults can more readily attain supershear rupture speed [Xu *et al.*, 2023], a phenomenon where the rupture speed surpasses the seismic shear wave velocity. Numerical simulations corroborate these findings. Research indicates that smoother faults tend to generate larger earthquakes compared to rougher faults [Zielke *et al.*, 2017]. The amplitude of roughness significantly impacts the nucleation length, as highlighted by Tal *et al.* [2018]. Additionally, studies like Cattania and Segall [2021] delineate the correlation between foreshock and aseismic slip migration and the distribution of fault roughness. Overall, these multi-faceted studies underscore the intricate relationship between fault heterogeneity and the diverse seismic behaviors exhibited by faults, contributing significantly to our understanding of earthquake mechanics and hazard assessment.



Among heterogeneous physical variables, effective normal stress gains significant attention for its expected variability and its pivotal role in initiating earthquakes. The heterogeneity in effective normal stress arises from multiple factors such as fault geometry, roughness, variations in pore pressure, and the growth of damage zones [Duan and Oglesby, 2006; Hillers and Miller, 2007; Huang, 2018; Cattania and Segall, 2021]. Laboratory experiments have demonstrated the generation of diverse slip behaviors by manipulating effective normal stress [Passetlègue et al., 2020]. Models incorporating even a singular anomaly in effective normal stress can yield a spectrum of seismic slip behaviors: from slow slip events (SSEs) to earthquakes, from subshear to supershear ruptures [Weng et al., 2015], and the transformative role of seamounts in subduction zones shifting from barriers to seismogenic sources [Yang et al., 2012; Dong et al., 2022]. Heterogeneous normal stress models contribute to explaining empirical scaling relationships observed in seismic events. For example, linear scaling of magnitude and duration for SSEs has been linked to third-order scaling for larger earthquakes through models incorporating fault geometry and stress heterogeneity [Weng and Ampuero, 2022]. Moreover, these models aid in creating earthquakes akin to natural observations, providing insights into the dynamics and behaviors of seismic events [Tang et al., 2021; Zhang et al., 2022; Taufiqurrahman et al., 2023]. These studies underscore the intricate relationship between heterogeneous stress distributions and the diverse spectrum of earthquake behaviors, shedding light on the underlying mechanics of earthquake initiation and propagation. Building on these previous contributions, this thesis further explores the effect of normal stress heterogeneity by focusing on its stochastic nature. The nucleation behavior altered by the interplay between the heterogeneity wavelength and the nucleation length will be investigated.

## 1.4 Numerical modeling bridging experiments and observation

Directly observing the recurrence of significant, damaging earthquakes in nature remains a rare phenomenon, despite that some intermediate to large earthquakes have been observed to revisit the same fault [Segall and Harris, 1987; Chlieh et al., 2004; Prawirodirdjo et al., 2010]. However, these natural observations are primarily constrained to the Earth's surface, distant from the earthquake

source. As a result, these observations often necessitate inverse modeling techniques for interpretation due to their indirect nature. To our rescue, laboratory experiments that generate earthquakes in a quasi-periodic manner have been proposed [Fukuyama *et al.*, 2003; Rosenau *et al.*, 2009; Corbi *et al.*, 2013; McLaskey and Lockner, 2014; McLaskey, 2019]. However, these experiments operate within a confined millimeter to meter scale, posing challenges in extrapolating their findings to a larger, natural scale. To complement these observations, a quantitative understanding of the complex, multi-physics, multi-scale processes driving fault slip is imperative. Numerical models serve as a bridge to overcome the spatial and temporal limitations inherent in both natural and experimental observations. With the ability to thoroughly explore the parameter space, numerical models also play a role in isolating the roles of processes and parameters in a systematic manner. These models play a crucial role in enhancing our comprehension of earthquake sequences and ultimately aid in refining long-term seismic hazard assessments. By simulating fault behaviors under various conditions, numerical models contribute significantly to our insights into earthquake dynamics, bridging the gap between laboratory experiments and natural occurrences.

However, numerical models often face challenges in tremendous time and energy costs, giving rise to various justified and unjustified simplifications and assumptions. These simplifications include using lower dimensional models to replace 3-D models and employing the quasi-dynamic (QD) approximation instead of modeling the wave propagation (fully dynamic models, FD). This need becomes even more urgent when monotonous repetition of those forward models is required, for example, for inversion, data assimilation, physics-based deep learning, uncertainty quantification, and when dealing with probabilities, such as for probabilistic seismic hazard assessment [e.g., Weiss *et al.*, 2019; Van Dinther *et al.*, 2019a]. Therefore, it becomes a common concern to what extent lower dimensional models can reproduce nature when compared to 3-D models. How are the observed differences in results attributed to the corresponding dimension reduction? And under what circumstances is this simplification justified? These questions have not yet been systematically addressed. Without answering these questions, the designers could not justify a simplified model, and the users could not interpret the model output. I will perform a systematic investigation of the limitations and advantages of models with different dimensions and inertia approximations simulating earthquake sequences, both qualitatively and

quantitatively.

## 1.5 Thesis objectives and structure

Motivated by natural observations and laboratory experiments, this thesis addresses how earthquake nucleation and recurrence are affected by heterogeneous material parameters and dimensions. To address this, I study earthquake sequences in the laboratory, in the reservoir, and in tectonic settings. I employ numerical models to bridge the spatial and temporal scales between natural observations and laboratory experiments, and use the knowledge acquired from different scales to help improve the understanding of one another. For example, I extrapolate the observed frictional healing phenomenon in laboratory experiments to explain induced seismicity on velocity-strengthening faults in Groningen. Additionally, findings related to migrated nucleation locations in laboratory-scale heterogeneous models inform the identification of potential precursory signals in natural settings. The modeling of induced earthquakes in the heterogeneous Groningen setup, in turn, underscores the necessity for laboratory experiments to investigate the frictional properties of material mixtures. These achievements are made possible by the two numerical codes I developed: one integrated into the code package *Garnet* [Pranger, 2020] and another entirely original.

I address the following thesis objectives in a dedicated chapter each:

### 1. Develop and validate 1-D to 3-D earthquake sequence models

The results in this thesis are obtained through developing, validating and applying two code packages. In Chapters 2 and 3, I developed my models using the code package *Garnet*. In Chapters 4 and 5, I employed a MATLAB code that I developed from scratch for induced seismicity. I validate *Garnet* for the simulation of fully dynamic and quasi-dynamic sequences of earthquakes and aseismic slips in 2D and 3D, which may also involve fluid diffusion along the fault. The validation is published in two co-authored papers, whereas a third co-authored paper about fluid diffusion is submitted. Jiang *et al.* [2022] validates the quasi-dynamic model in 3-D and Erickson *et al.* [2023] validates the dynamic earthquake rupture model in 2-D. These are described in Chapter 6, along with methodological information on the developments of my new code.

## 2. Explain the impact of reducing spatial dimensions in earthquake sequence models

I systematically study the advantages and limitations of simplifications that eliminate spatial dimensions in quasi-dynamic earthquake sequence models, from 3-D models with a 2-D fault plane down to 0-D or 1-D models with a 0-D fault point. Given the computational efficiency of lower-dimensional models that run more than a million times faster, I also provide qualitative and quantitative guidance on economical model design and interpretation of modeling studies. This chapter 2 is published as *Li, M., Pranger, C., & van Dinther, Y. (2022). Characteristics of earthquake cycles: A cross-dimensional comparison of 0-D to 3-D numerical models. Journal of Geophysical Research: Solid Earth, 127(8), e2021JB023726.*

## 3. Understand how normal stress heterogeneity affects earthquake nucleation and earthquake sequence

I use a stochastically variable, spatially heterogeneous normal stress, analogous to a 2-m scale laboratory experiment, to quantitatively understand its impact on earthquake nucleation and the following earthquake sequence. I identify five regimes of earthquake nucleation and slip behaviors, controlled by the ratio of the heterogeneity wavelength over the nucleation length. This chapter 3 is submitted to *Journal of Geophysical Research: Solid Earth*.

## 4. Explain the occurrence of induced earthquakes on stable faults

Earthquakes are hardly ever expected on velocity-strengthening faults, because they are conventionally considered stable. Paradoxically, they are often observed. I explore the conditions under which earthquakes might nucleate by highlighting the significance of fault healing. By assessing the potential of any fault to host induced seismicity, I urge a re-evaluation of the seismic potential in tectonically inactive regions for safe exploitation of the subsurface for applications such as geothermal energy production and energy storage. This chapter 4 is in review at *Nature Communications* and preprinted on *Research Square*.

## 5. Understand earthquake nucleation and arrest in the Groningen gas field

I apply the theory of Chapter 4 to the case of the Groningen field, using lithology-specific parameters obtained from in-situ and laboratory measurements for each geological layer. I reproduce induced earthquakes that match geophysical observations. Furthermore, I examine in which layer earthquakes nucleate in

Groningen and how far the rupture propagates. These are not well constrained by current seismological inversions. This chapter 5 will be submitted to *Solid Earth* after more extensive parameter investigations.

The thesis is concluded in chapter 7 with a summary and an outlook to future works. In the outlook I will illustrate and discuss earthquake forecasting using my forward models that provide the physics-based input for the assimilation of limited and uncertain observations. This work is also part of NWO's DeepNL project InFocus, which aims at (i) building physics-based forward models and understanding the physics of earthquakes in Groningen and in the laboratory, and (ii) building and testing data assimilation tools to forecast laboratory earthquakes. My TU Delft collaborator Hamed Diab-Montero shows that by using data assimilation techniques to combine my physics-based models with observations, we can obtain a better forecastability of earthquakes and slow slip events. In a published, co-authored paper we demonstrate this in a perfect model test in 1-D [*Diab-Montero et al., 2023*]. I also built 2-D and 3-D earthquake sequence models of a meter-scale laboratory setup to assimilate the real data collected in the experiments. This is made possible for the first time in a meter scale apparatus. These are currently being used for evaluating the performance of ensemble-based data assimilation in forecasting laboratory earthquakes. Finally, I make suggestions on future numerical, experimental, and observational works that can help improve the understanding of earthquake processes and provide better constraints for numerical models.

# 2

## Characteristics of earthquake cycles: a cross-dimensional comparison of 0-D to 3-D numerical models

*Meng Li<sup>1</sup>, Casper Pranger<sup>2,3</sup>, and Ylona van Dinther<sup>1</sup>*

<sup>1</sup>Utrecht University, Netherlands, <sup>2</sup>LMU Munich, Germany, <sup>3</sup>ETH Zurich, Switzerland

Published as: Li, M., Pranger, C., & van Dinther, Y. (2022). Characteristics of earthquake cycles: A cross-dimensional comparison of 0-D to 3-D numerical models. *Journal of Geophysical Research: Solid Earth*, 127(8), e2021JB023726.

## Abstract

High-resolution computer simulations of earthquake sequences in three or even two dimensions pose great demands on time and energy, making lower-cost simplifications a competitive alternative. We systematically study the advantages and limitations of simplifications that eliminate spatial dimensions in quasi-dynamic earthquake sequence models, from 3-D models with a 2-D fault plane down to 0-D or 1-D models with a 0-D fault point. We demonstrate that, when 2-D or 3-D models produce quasi-periodic characteristic earthquakes, their behavior is qualitatively similar to lower-dimension models. Certain coseismic characteristics like stress drop and fracture energy are largely controlled by frictional parameters and are thus largely comparable. However, other observations are quantitatively clearly affected by dimension reduction. We find corresponding increases in recurrence interval, coseismic slip, peak slip velocity, and rupture speed. These changes are to a large extent explained by the elimination of velocity-strengthening patches that transmit tectonic loading onto the velocity-weakening fault patch, thereby reducing the interseismic stress rate and enhancing the slip deficit. This explanation is supported by a concise theoretical framework, which explains some of these findings quantitatively and effectively estimates recurrence interval and slip. Through accounting for an equivalent stressing rate at the nucleation size  $h^*$  into 2-D and 3-D models, 0-D or 1-D models can also effectively simulate these earthquake cycle parameters. Given the computational efficiency of lower-dimensional models that run more than a million times faster, this paper aims to provide qualitative and quantitative guidance on economical model design and interpretation of modeling studies.

## 2.1 Introduction

Destructive earthquakes every so often take us by surprise, because observations reveal a complex and opaque pattern of earthquake recurrence. Unraveling this pattern is challenging as the recurrence of large destructive earthquakes in nature is hardly observed. Some intermediate to large size earthquakes are observed to revisit the same fault [e.g., *Segall and Harris, 1987; Chlieh et al., 2004; Prawirodirdjo et al., 2010*]. However, despite limited borehole data, these and most other natural observations are largely confined to the earth's surface, such that they remain indirect and at a distance to the hypocenter and thus often require inverse modeling to interpret. Earthquakes can also be generated quasi-periodically in large-scale laboratory experiments [e.g., *Rosenau et al., 2009; McLaskey and Lockner, 2014*] while these experiments are restricted to their millimeter to meter scale, such that they require a challenging upscaling step to interpret their findings. To complement our observations in nature and in laboratories, we need a quantitative description of the multi-physics, multi-scale processes governing fault slip. Numerical models are well-suited to overcome these spatial-temporal limitations and are thus important to improve our understanding of earthquake sequences and ultimately help to better estimate long-term seismic hazard assessment.

Numerical models featuring different degrees of complexity in different dimensions have been used to simulate earthquake cycles. A fault can be modeled as simple as a single block slider connected to a spring. The spring provides the slider above the fault with a direct elastic response that mimics the response of the surrounding medium. We call this a zero-dimensional (0-D) model with a 0-D fault point [e.g., *Gu and Wong, 1991; Madariaga, 1998; Erickson et al., 2008; Ohtani et al., 2020*]. Similarly but more accurately, a fault can be modeled as a series of sliders connected to a series of springs in a row. This is a one-dimensional (1-D) model with a 1-D fault line [*Burridge and Knopoff, 1967; Petrillo et al., 2020*]. In both models the medium response is integrated directly onto the fault. However, it is also possible and common to mesh and model the surrounding medium explicitly, such that a rheologically more accurate and/or more heterogeneous response of the medium can be realized. A two-dimensional (2-D) model is required for a 1-D fault line in this case [e.g., *Lapusta et al., 2000; Van Dinther et al., 2013b; Herrendörfer et al., 2018; Barbot, 2019; Cattania, 2019*]. To accommodate more on- and off-fault complexity, including variations in fault



properties or geometry along strike, a three-dimensional (3-D) model with a 2-D fault plane is also prevalent [e.g., *Okubo, 1989; Lapusta and Liu, 2009; Barbot et al., 2012; Erickson and Dunham, 2014; Chemenda et al., 2016; Jiang and Lapusta, 2016*]. In certain scenarios a so-called 2.5D model is used for the sake of affordable computational cost, which approximately accounts for the effect of a finite fault width [e.g., *Lapusta, 2001; Weng and Ampuero, 2019; Preuss et al., 2020*]. To do better justice to the large amount of earthquake cycle papers, we refer the reader to a white paper on future challenges for earthquake modeling [*Lapusta et al., 2019*] and an overview of benchmarked modeling codes provided in *Erickson et al. [2020]* and *Jiang et al. [2022]* for 2-D anti-plane and 3-D settings, respectively. Generally, 3-D models will produce results most representative for nature. However, given that they are still very time and energy consuming [*Uphoff et al., 2017*], simplified model setups are still largely adopted by many researchers and may be a very good choice to answer specific research questions [e.g., *Allison and Dunham, 2018; Cattania, 2019; Van Dinther et al., 2019b; Sathiakumar et al., 2020; Romanet et al., 2020*]. A key reason for the need of such simplifications is the extremely high resolution required in both space and time, while at least exploring sensitivities in forward modeling studies [*Lambert and Lapusta, 2021*]. On top of that, computational speed is particularly critical in situations where monotonous repetition of those forward models is required, for example, for inversion, data assimilation, physics-based deep learning, uncertainty quantification, and when dealing with probabilities, such as for probabilistic seismic hazard assessment [e.g., *Weiss et al., 2019; Van Dinther et al., 2019a*]. However, also when trying to understand coupled multi-physics or multi-scale feedback these approximations can be really useful [e.g., *Van Dinther et al., 2013a; Allison and Dunham, 2018; Lotto et al., 2019; Ohtani et al., 2019; Petrini et al., 2020*]. To optimize computing resources, researchers have to define suitable model complexities before and during their numerical simulations. Therefore it becomes a common concern to what extent lower dimensional models can reproduce nature when compared to 3-D models. How are the observed differences in results attributed to the corresponding dimension reduction? And under what circumstances is this simplification justified?

These questions have not yet been systematically addressed. Nonetheless, several papers considered various aspects of this problem, especially via the comparison between 2-D and 3-D models. *Lapusta and Rice [2003]; Kaneko et al. [2010]; Chen and Lapusta [2019]* suggested ways to interpret their 2-D results in

more realistic 3-D situations, such that they could be directly compared to 3-D results. By doing this, they could compare velocity-strengthening (VS) barrier efficiency in rupture propagation, seismic moment, and the scaling law for earthquake recurrence interval and seismic moment between 2-D and 3-D models in their studies. For the coseismic phase alone, the dynamic rupture community, conducting simulations with dynamic rupture models of one single earthquake, compared 2-D and 3-D results for benchmarking purposes. *Harris et al.* [2011] introduced two benchmark problems for dynamic rupture modelers where 3-D simulations produced smaller ground motions (peak ground velocities) than in 2-D simulations, in both elastic and elasto-plastic scenarios. Similar 2-D vs. 3-D comparisons focusing on coseismic rupture behavior as well as earthquake recurrence have also been made in the earthquake cycle community [e.g., *Chen and Lapusta*, 2009, 2019] where qualitative differences in earthquake magnitude and recurrence interval are discussed. However, these findings are not systematic and occasionally lack necessary theoretical support. Here we fill this gap by comparing earthquake cycle results across all dimensions from 0-D to 3-D, which includes comparisons for all phases of the earthquake cycle, i.e., interseismic, nucleation, coseismic and postseismic phases.

We perform a systematic investigation of the limitations and advantages of models with different dimensions simulating cycles of characteristic earthquakes. By doing so, we compare physical characteristics and importance of different physical processes across dimensions both qualitatively and quantitatively. The aim of this paper is to serve as guidelines for modelers designing models and for all researchers interpreting results developed under necessary limitations. We first introduce the numerical method and the model setup of a strike-slip fault under rate-and-state friction. The code package is validated and benchmarked by Southern California Earthquake Center (SCEC) Sequences of Earthquakes and aseismic slip (SEAS) benchmark problems BP1-QD [*Erickson et al.*, 2020] and BP4-QD [*Jiang et al.*, 2022] (see Chapter 6). Next, we systematically compare interseismic and coseismic characteristics of our models from 1-D to 3-D, summarizing and quantifying their advantages and shortcomings. The numerical results are explained and supported by a series of theoretical calculations. Finally, the computational cost is compared. In the discussions, we first discuss under what conditions 2-D models can substitute 3-D models. Related issues on the model choices of this research, limitations and future improvements as well as possible applications are also discussed.

## 2.2 Methods

We exploit the flexibility of *Garnet*, a recently developed code library for the parallel solution of coupled non-linear multi-physics problems in earth sciences [Pranger, 2020]. *Garnet* enables its users to formulate problems in a largely dimension-independent way by defining a generic set of symbolic differential operators such as `div` and `grad`, which are then realized at compile-time in the appropriate number of dimensions as concrete and performant compute kernels. *Garnet* implements the classical second-order accurate staggered grid finite difference discretization of PDEs in space, and adaptive time stepping schemes of various orders of accuracy and other characteristics, all based on the linear multistep family of time discretizations. The library interfaces to PETSc [Balay et al., 1997, 2019a,b] for linear and nonlinear solvers and preconditioners, to MPI [MPI Forum, 2015] for coarse scale distributed memory parallelism and intermediate scale shared memory parallelism, and to Kokkos [Edwards et al., 2014] (and in turn OpenMP, POSIX threads, or CUDA) for fine scale concurrency. In this section we further introduce the equations and algorithms that define our study.

### 2.2.1 Physics

Under the assumption of static stress transfer, the momentum balance equation reads

$$\nabla \cdot \boldsymbol{\sigma} = 0, \quad (2.1)$$

where  $\boldsymbol{\sigma}$  is the Cauchy stress tensor whose component  $\sigma_{ij}$  denotes the stress acting along the  $x_j$  axis on the plane that is normal to the  $x_i$  axis ( $i, j = 1, 2, 3$ ). Both gravity and inertia are ignored in our models. Hooke's law relates stress rate  $\dot{\boldsymbol{\sigma}}$  to strain rate  $\dot{\boldsymbol{\epsilon}}$  by

$$\dot{\boldsymbol{\sigma}} = 2G\dot{\boldsymbol{\epsilon}} + \lambda \text{Tr}(\dot{\boldsymbol{\epsilon}})\mathbf{I} \quad (2.2)$$

with bulk modulus  $K$ , shear modulus  $G$ , Lamé's constant  $\lambda := K - 2G/3$  and  $\mathbf{I}$  identity tensor.  $\text{Tr}(\dot{\boldsymbol{\epsilon}}) := \dot{\epsilon}_{kk}$  is the matrix trace. We assume infinitesimal strain rate  $\dot{\boldsymbol{\epsilon}}$  as defined by

$$\dot{\boldsymbol{\epsilon}} = \frac{1}{2} (\nabla \mathbf{v} + \mathbf{v} \nabla), \quad (2.3)$$

where  $\mathbf{v}$  is the material velocity whose component  $v_i$  denotes the velocity in the direction  $x_i$  ( $i = 1, 2, 3$ ). We use  $(x_1, x_2, x_3)$  and  $(x, y, z)$  to refer to the three axes interchangeably.

For a fault with unit normal vector  $\hat{\mathbf{n}}$ , the (scalar) normal stress  $\sigma_n$  (positive in compression) is given by the projection  $\sigma_n = -\hat{\mathbf{n}} \cdot \boldsymbol{\sigma} \cdot \hat{\mathbf{n}}$ , the shear traction vector  $\boldsymbol{\tau}_s$  by the projection  $\boldsymbol{\tau}_s = \boldsymbol{\sigma} \cdot \hat{\mathbf{n}} + \sigma_n \hat{\mathbf{n}}$ , the scalar shear traction  $\tau_s$  by the Euclidean norm  $\tau_s = \|\boldsymbol{\tau}_s\|$ , and finally the unit fault tangent  $\hat{\mathbf{t}}$  (which defines the orientation of the scalar fault slip  $V$ ) by the normalization  $\hat{\mathbf{t}} = \boldsymbol{\tau}_s / \tau_s$ , such that  $\tau_s = \hat{\mathbf{t}} \cdot \boldsymbol{\sigma} \cdot \hat{\mathbf{n}}$ . Further following *Jiang et al.* [2022], the fault is assumed to be governed by the rate-and-state friction law, which was initially proposed based on laboratory friction experiments by *Dieterich* [1979]; *Ruina* [1983]. We employ a regularization near zero slip velocity according to *Rice and Ben-Zion* [1996] and *Ben-Zion and Rice* [1997], so that the friction law that defines the relation between shear stress  $\tau_s$  and normal stress  $\sigma_n$  on the fault is given by

$$\tau_s = a\sigma_n \operatorname{arcsinh} \left\{ \frac{V}{2V_0} \exp \left[ \frac{\mu_0}{a} + \frac{b}{a} \ln \left( \frac{\theta V_0}{L} \right) \right] \right\} + \eta V. \quad (2.4)$$

The “state”  $\theta$  in turn is governed by the evolution equation

$$\dot{\theta} = 1 - \frac{V\theta}{L}, \quad (2.5)$$

corresponding to the so-called “aging law” [*Ruina*, 1983]. Symbols used in (2.4) and (2.5) include the reference friction coefficient  $\mu_0$ , the reference slip rate  $V_0$ , the characteristic slip distance  $L$ , and the parameters  $a$  and  $b$  that control the relative influence of direct and evolutionary effects, respectively. The fault is velocity-weakening (VW) and potentially frictionally unstable when  $a - b < 0$ , and velocity-strengthening (VS) and generally frictionally stable when  $a - b > 0$ . Finally, the parameter  $\eta$  used in (2.4) refers to the “radiation damping term” used in the quasi-dynamic (QD) approximation of inertia [e.g., *Rice*, 1993; *Cochard and Madariaga*, 1994; *Ben-Zion and Rice*, 1995; *Liu and Rice*, 2007; *Crupi and Bizzarri*, 2013], which is employed in earthquake cycle simulations to reduce the computational costs. However, this is known to introduce qualitative and quantitative differences compared to fully dynamic (FD) modeling results [*Thomas et al.*, 2014]. The damping viscosity  $\eta = G/(2c_s)$  is equal to half the shear impedance of the elastic material surrounding the fault.

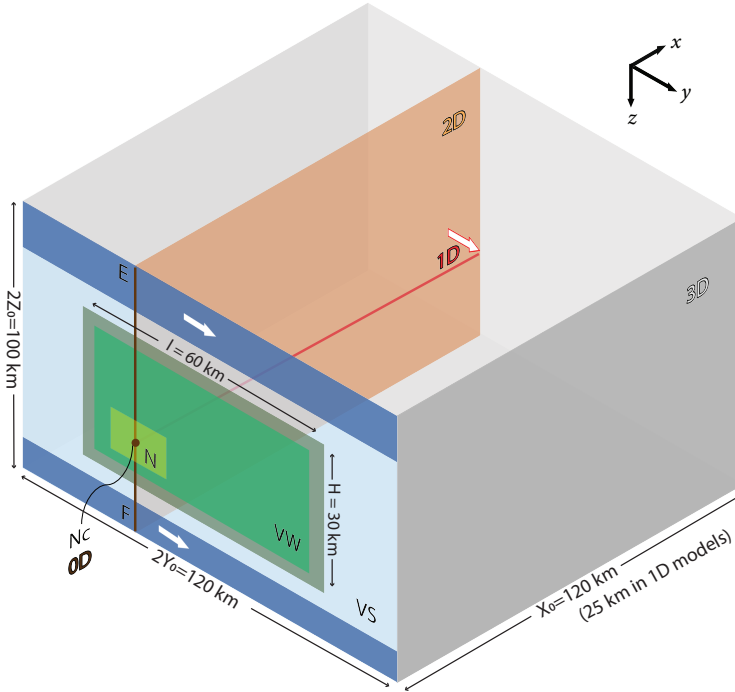


Figure 2.1: Numerical model setup of a vertical strike-slip fault embedded in an elastic medium: 3-D setup of SEAS benchmark BP4-QD and its simplification to 2-D, 1-D and 0-D. Only one side of the fault (half space  $x \geq 0$ ) is shown and modeled due to symmetry. “VW” and “VS” denotes the VW (light green) and VS (light blue) patches, respectively. The transition between VW and VS patches is shown in dark green. Tectonic loading regions at the top and bottom of the fault (dark blue) are subjected to constant velocities (white arrows). “N” denotes the predefined nucleation zone (yellow) with higher initial slip rate and shear stress, whose center is denoted as “Nc”. “EF” denotes a vertical line through “Nc”. Computational domain in 2-D is reduced to  $xz$ -plane (orange) with 1-D fault line “EF” (brown). Computational domain in 1-D is reduced to the  $x$ -axis (red) with a 0-D fault point “Nc” (brown). In this case tectonic loading is applied at the far-away end with constant velocity (white arrow with red frame). Computational domain in 0-D is fault point “Nc” without medium extent.

### 2.2.2 Model setup

Over the last decade, the SCEC has supported various code comparison projects to verify numerical simulations on dynamic earthquake ruptures [e.g. *Harris et al., 2009, 2018*]. The SEAS benchmark project [*Erickson et al., 2020; Jiang et al., 2022*], launched in 2018, is an extension to evaluate the accuracy of numerical models simulating earthquake cycles. We use this benchmark initiative to successfully verify the earthquake cycle implementation in *Garnet*, which is demonstrated in Chapter 6 and *Jiang et al. [2022]*. To allow for a comparison with other existing and established implementations that are commonly used, we build our models based on the setup of SEAS benchmark problem BP4-QD.

The BP4-QD describes a planar vertical fault embedded in a homogeneous, isotropic linear elastic medium, observing the physics described in section 2.2.1 (Fig. 2.1). The  $x, y, z$  axes are directions perpendicular to the fault plane, along the strike and along the dip, respectively. Following *Jiang et al. [2022]*, the fault condition is prescribed at  $x = 0$ . The central part of the fault is assumed to follow the rate-and-state friction formulation where a VW region is surrounded by a VS region. The top and bottom parts of the fault are not governed by rate-and-state friction and are instead subjected to a constant fault-parallel loading velocity  $V_p/2$ . The inherited frictional parameters  $a, b, L$  lead to a large nucleation size ( $\sim 12$  km), such that it facilitated benchmarking under low resolution (500 - 1000 m) with a reasonable computational load (see Chapter 6 for the benchmarking). We are aware that this setup allows for simple periodic earthquakes instead of smaller irregular ones, but this simple earthquake sequence also facilitates the comparison over dimensions and make quantitative comparisons of some characteristic observations possible.

Due to the symmetry respective to the fault plane and the resulting anti-symmetry of fault-parallel motion, the motion at the fault is taken to be relative to a fictitious oppositely moving domain that is not modeled. The computational domain is thus limited to the half space  $x \geq 0$ . Since this still proposes an infinitely large half space, the computational domain needs to be truncated to a finite domain when using a volumetric discretization. We use the computational domain  $\Omega(x, y, z) = [0, X_0] \times [-Y_0, Y_0] \times [-Z_0, Z_0]$  (Fig. 2.1), where  $X_0, Y_0, Z_0$  are chosen sufficiently large to have negligible impact on the fault behavior [*Jiang et al., 2022*]. The top and bottom boundaries  $z = \pm Z_0$  are pre-

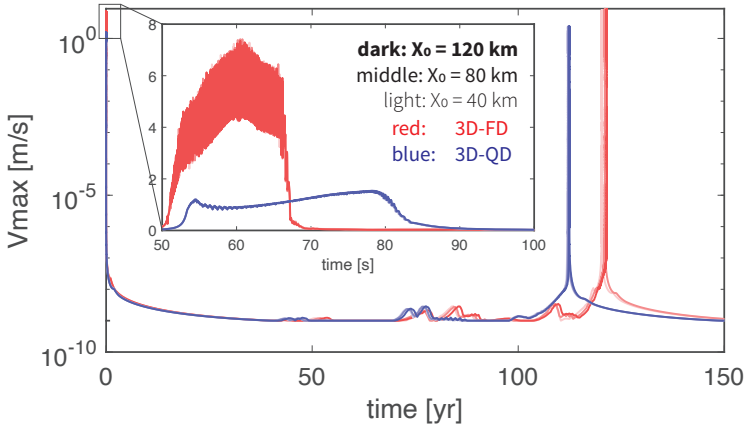


Figure 2.2: Influence of computational domain size: comparison of long-term and coseismic maximum slip velocity with various medium thickness  $X_0$  choices in 3-D models. The inner panel shows the coseismic zoom-in to the first earthquake event.

scribed to move at the same constant loading velocity  $V_p/2$ . The remaining three boundaries  $x = X_0, y = -Y_0, y = Y_0$  mimic the conditions at infinity and are set to be traction-free. We show that the simulated earthquake sequences are converging in both interseismic and coseismic phases upon enlarging the medium thickness  $X_0$  and the difference is negligible when  $X_0 > 40$  km (Fig. 2.2). The same parameter study is also implemented for  $Y_0$  and  $Z_0$  to achieve convergence (Table 2.1).

The initial conditions are chosen to allow the fault to creep at the imposed slip velocity  $V_p$  in a steady state at  $t = 0$  [Jiang et al., 2022], namely

$$\theta(t = 0) = \frac{L}{V_p}, \quad (2.6)$$

and

$$\begin{aligned} \tau_s(t = 0) \\ = a\sigma_n \operatorname{arcsinh} \left\{ \frac{V_p}{2V_0} \exp \left[ \frac{\mu_0}{a} + \frac{b}{a} \ln \left( \frac{V_0}{V_p} \right) \right] \right\} + \eta V_p. \end{aligned} \quad (2.7)$$

We additionally define a highly stressed zone “N” in the VW patch with higher initial slip velocity  $V_i$  (Fig. 2.1) to ensure the first earthquake nucleates at that location when the computation starts. In this zone, the state variable  $\theta$  keeps

unchanged to achieve the high pre-stress, namely

$$\begin{aligned} \tau_s((y, z) \in N, t = 0) \\ = a\sigma_n \operatorname{arcsinh} \left\{ \frac{V_i}{2V_0} \exp \left[ \frac{\mu_0}{a} + \frac{b}{a} \ln \left( \frac{V_0}{V_p} \right) \right] \right\} + \eta V_i. \end{aligned} \quad (2.8)$$

This helps us to better compare the coseismic behavior across dimensions. All physical and numerical parameters are summarized in Table 2.1.

### 2.2.3 Model simplification by progressive elimination of dimensions

In this work we take a structured approach to dimension reduction, eliminating first the lateral along-strike dimension, then the vertical dimension, and finally the fault-perpendicular dimension. Each of these steps are illustrated in Fig. 2.1. For clarity, the assumptions and variables concerned in each dimension are summarized in Table 2.2.

In 2-D, the model is simplified by excluding the along-strike fault direction (denoted in orange in Fig. 2.1). This means that the material and frictional properties, boundary and initial conditions are assumed to be homogeneous in this direction. That assumption thus omits the along-strike heterogeneity introduced by the bounding VS patches as well. In this way, any half plane cutting the fault vertically may be taken as representative of the the entire model. The computational domain can thus be reduced to  $\Omega(x, z) = [0, X_0] \times [-Z_0, Z_0]$ . Furthermore, we omit the along-dip motion  $v_z$  and only model the anti-plane motion. As a consequence, only the  $\sigma_{xy}$  and  $\sigma_{yz}$  components of the stress tensor are required to be evaluated in this anti-plane strain model. To allow a coseismic comparison we keep there the highly stressed nucleation zone defined in 3-D and choose to model the plane cutting across this zone. The fault is collapsed to the line “EF” (denoted in red in Fig. 2.1). Another common 2-D perspective that models a horizontal plane cutting the fault includes the in-plane strain assumption. While this configuration models a more complete set of momentum balance and elastic constitutive equations than the anti-plane configuration we have chosen, the differences are only expected to manifest as a slightly modified elastic loading and corresponding changes in friction and nucleation size. We therefore choose



Table 2.1: *Physical and numerical parameters*

| Parameter                               | Symbol     | Value                     |
|-----------------------------------------|------------|---------------------------|
| Density                                 | $\rho$     | 2.670 g/cm <sup>3</sup>   |
| Shear wave speed                        | $c_s$      | 3.464 km/s                |
| Poisson ratio                           | $\nu$      | 0.25                      |
| Shear modulus                           | $G$        | 32.0 GPa                  |
| Bulk modulus                            | $K$        | 53.4 GPa                  |
| Normal stress                           | $\sigma_n$ | 50 MPa                    |
| Plate rate                              | $V_p$      | 10 <sup>-9</sup> m/s      |
| Width of rate-and-state fault           | $W_f$      | 80 km                     |
| Length of uniform VW region             | $l$        | 60 km                     |
| Width of uniform VW region              | $H$        | 30 km                     |
| Width of VW-VS transition zone          | $h$        | 3 km                      |
| Reference friction coefficient          | $\mu_0$    | 0.6                       |
| Reference slip rate                     | $V_0$      | 10 <sup>-6</sup> m/s      |
| Characteristic slip distance            | $L$        | 0.04 m                    |
| Rate-and-state direct effect            | $a$        |                           |
| - VW                                    |            | 0.0065                    |
| - VS                                    |            | 0.025                     |
| Rate-and-state evolution effect         | $b$        | 0.013                     |
| Width of predefined nucleation zone "N" | $w_i$      | 12 km                     |
| Distance of nucleation zone to boundary | $h_i$      | 1.5 km                    |
| Initial slip rate                       |            |                           |
| - inside nucleation zone                | $V_i$      | 10 <sup>-3</sup> m/s      |
| - outside nucleation zone               | $V_p$      | 10 <sup>-9</sup> m/s      |
| Medium extent perpendicular to fault    | $X_0$      | 40/80/120 <sup>a</sup> km |
| Half fault extent along strike          | $Y_0$      | 60/90 <sup>a</sup> km     |
| Half fault extent along dip             | $Z_0$      | 50/60 <sup>a</sup> km     |
| Grid size                               | $\Delta x$ | 500/1000 <sup>a</sup> m   |

<sup>a</sup> Numbers in italic are used in parameter studies.

to use the vertical 2-D configuration that keeps the top/bottom loading regions for better comparison.

The simplified physical equations (2.1)-(2.3) in 2-D read:

$$\begin{aligned}\dot{\sigma}_{xy} &= G \frac{\partial v_y}{\partial x}, \\ \dot{\sigma}_{yz} &= G \frac{\partial v_y}{\partial z}, \\ \frac{\partial \sigma_{xy}}{\partial x} + \frac{\partial \sigma_{yz}}{\partial z} &= 0.\end{aligned}\tag{2.9}$$

In 1-D, we further simplify the model by setting all variables invariant along dip in which case only the shear stress component  $\sigma_{xy}$  and the velocity component  $v_y$  remain. We thus lose the possibility to model spatial variations of frictional properties as the fault reduces to a 0-D point at  $x = 0$  in the computational domain  $\Omega(x) = [0, X_0]$ . We choose the fault “point” to be velocity-weakening, corresponding to a location inside the predefined nucleation zone at “Nc” (denoted in red in Fig. 2.1) to facilitate coseismic comparison. Furthermore, without an along-dip fault extent, the original on-fault tectonic loading from the top and bottom is no longer possible. Instead, it is added at the far-away boundary through a constant creeping rate there. To achieve a comparable interseismic stress rate inside the VW patch across dimensions, we adjust the domain size  $X_0$  so that the shortest distance between the VW patch and the creeping boundary is the same as in higher dimensional models. Namely, we set  $X_0$  equal to  $(W_f - H)/2$ .

The simplified physical equations in 1-D read:

$$\begin{aligned}\dot{\sigma}_{xy} &= G \frac{\partial v_y}{\partial x}, \\ \frac{\partial \sigma_{xy}}{\partial x} &= 0.\end{aligned}\tag{2.10}$$

In 0-D, both the medium and the fault become the same point by eliminating the fault-perpendicular dimension. In this model without medium extent, physical loading is impossible at any medium boundaries. Therefore a “driving force” that can be chosen arbitrarily (equivalent to loading at the fault point) has to be added to the system instead.

Table 2.2: Simplifications in different dimensional models

| Model | Fault | Unknowns                                                                                                      | Simplifications                            |
|-------|-------|---------------------------------------------------------------------------------------------------------------|--------------------------------------------|
| 3-D   | 2-D   | $V, \theta; v_x, v_y, v_z,$<br>$\sigma_{xx}, \sigma_{xy}, \sigma_{xz}, \sigma_{yy}, \sigma_{yz}, \sigma_{zz}$ | No fault opening                           |
| 2-D   | 1-D   | $V, \theta; v_y, \sigma_{xy}, \sigma_{yz}$                                                                    | + strike-slip only, along-strike invariant |
| 1-D   | 0-D   | $V, \theta; v_y, \sigma_{xy}$                                                                                 | + along-dip invariant                      |
| 0-D   | 0-D   | $V, \theta$                                                                                                   | + integral perpendicular to fault          |

The simplified physical equation in 0-D reads:

$$\dot{\sigma}_{xy} = -kV + \dot{f}_d \quad (2.11)$$

where  $k$  is the stiffness of the system and  $\dot{f}_d$  is the applied driving force. This model will be further discussed in section 2.4.2 where the equivalence of 1-D and 0-D models will be illustrated.

## 2.2.4 Numerical algorithm

The nonlinear friction law (2.4) and evolution law (2.5) are solved in a point-wise fashion using a Newton-Raphson iteration for the slip rate  $V$  at a given stress  $\sigma$ , given initial conditions (2.6)-(2.8) (algorithm flowchart in Fig. 6.1). The medium is closed with an essential velocity boundary condition  $\mathbf{v} = V\hat{\mathbf{t}}/2$  on the fault ( $x = 0$ ) and the remaining boundary conditions given in the two sections above.

We choose a spatial discretization that ensures that the smallest physical length scale in the rate-and-state friction model – the cohesive zone size  $\Lambda$  – is always well resolved. This cohesive zone size  $\Lambda$  [Rubin and Ampuero, 2005; Day et al., 2005] is given by

$$\Lambda = \Lambda_0 \sqrt{1 - \frac{V_r^2}{c_s^2}} \quad (2.12)$$

$$\Lambda_0 = \frac{9\pi}{32} \frac{GL}{b(1-\nu)\sigma_n},$$

where  $V_r$  is the rupture speed and  $c_s$  is the shear wave speed.  $\Lambda_0$  is the upper limit of the cohesive zone size when  $V_r \rightarrow 0$ . The dynamic cohesive zone size

$\Lambda$  shrinks with increasing rupture speed  $V_r$ . We find that a high resolution is required for the seismogenic domain and its neighboring off-fault area, while it is not required at medium to large distances to the fault. We improve computational efficiency by considering a grid that is statically refined (ie. remaining fixed over time) near the VW zone. Refinement is realized by designing an orthonormal rectilinear (but not Cartesian) coordinate system that measures Euclidean space, and sampling this deformed coordinate system, rather than the Cartesian reference frame itself, at regular intervals. Differential operators are expressed in a general curvilinear coordinate system [see e.g. *Simmonds, 1994*] before discretization, a procedure that preserves the 2<sup>nd</sup>-order accuracy of the numerical method [*Pranger, 2020*].

We use adaptive time stepping to deal with the strong variation of the slip velocity and state variables in between interseismic and coseismic phases. The critically resolvable time scale is according to the evolution of the friction law (Eq. 2.5). Following *Lapusta et al. [2000]*, we let the time step  $\Delta t$  be given by

$$\Delta t = \min \left\{ \zeta \frac{L}{V_{\max}}, (1 + \alpha)\Delta t_{\text{old}}, \Delta t_{\max} \right\}. \quad (2.13)$$

where  $\zeta$  is a factor controlled by the material and frictional parameters [see calculation method in *Lapusta et al., 2000*]. We also require the next time step not to be larger than  $(1+\alpha)$  times the former time step  $\Delta t_{\text{old}}$  to avoid instability in the postseismic phase. A maximum time step size  $\Delta t_{\max}$  is further added to keep resolving the interseismic period in sufficient detail. We use  $\alpha = 0.2$  and  $\Delta t_{\max} = 10^8$  s.

## 2.3 Results and Analysis

Following the simplifications summarized in Table 2.2 and Fig. 2.1, this section compares and analyzes the 3-D to 2-D and 1-D results, where the fault is modeled in 2-D, 1-D and 0-D, respectively.

### 2.3.1 Interseismic phase

Regardless of dimension, we observe quasi-periodic earthquake sequences (Fig. 2.3). In one earthquake cycle, shear stress is first accumulated from min-

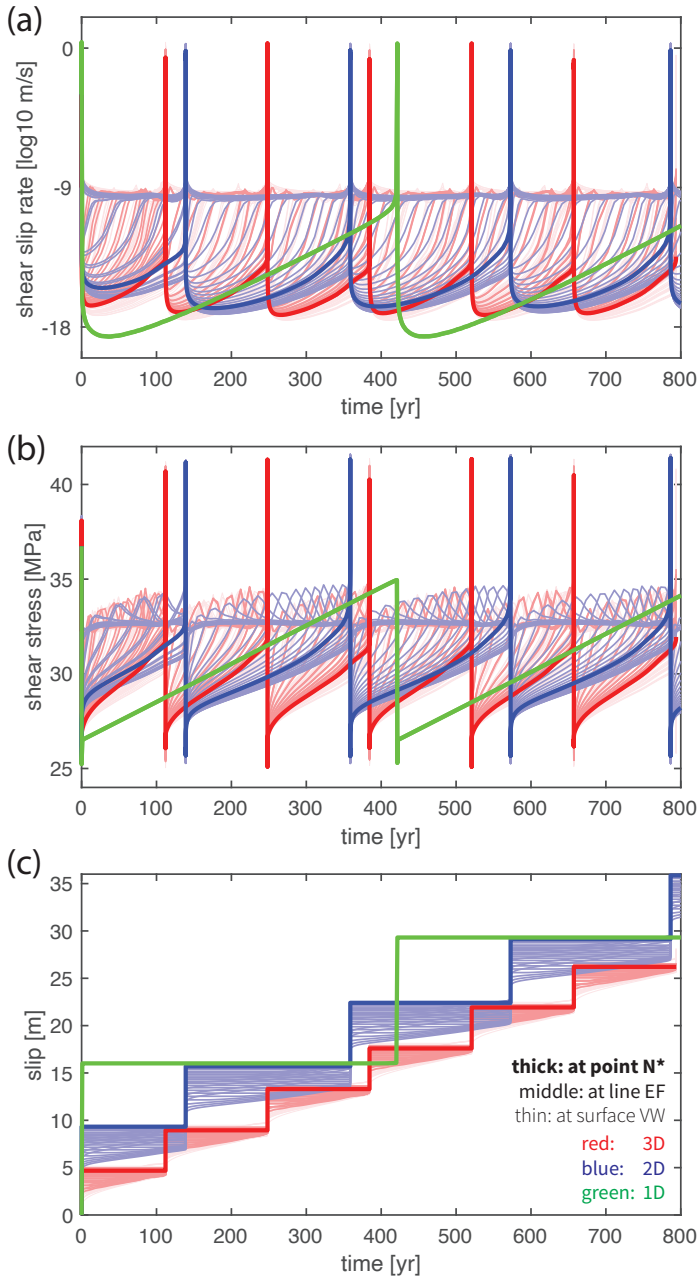


Figure 2.3: Comparison of the long-term time series of (a) slip rate, (b) stress and (c) accumulated slip in 1-3-D models. The lines with different thicknesses and degrees of transparency are recorded at different locations on the fault, where the thick lines are recorded at the rim of the nucleation zone “N\*” of the sixth earthquake, the semi-thick lines along the line “EF” cutting across “N\*” vertically and the thin lines elsewhere in the VW patch (see Fig. 2.7).

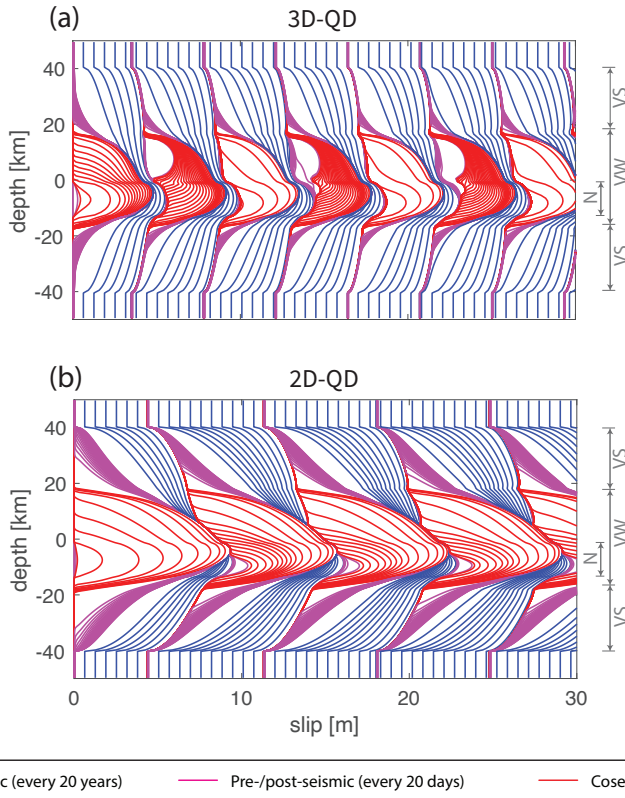


Figure 2.4: Cross-dimensional comparison of cumulative seismic and aseismic slip. The cumulative slip profile of (a) the 3-D model and (b) the 2-D model, along the dip direction “EF” cutting across the predefined nucleation zone “N” (see Fig. 2.1). “VW”, “VS”, “N” label the range of VW, VS and predefined nucleation zone. The interseismic phase is plotted every 20 years (blue), the pre- and post-seismic phase every 20 days (magenta) and the coseismic rupture every two seconds (red). Note that the slip contour distortions around a depth of -1.5 km and -13.5 km are introduced into these cumulative patterns by the predefined nucleation zone, whose properties increased the amount of slip in that zone for the first earthquake only.

imum 25 MPa to maximum 35-42 MPa during the interseismic phase and then released in an earthquake (Fig. 2.3b). Accordingly, slip velocity also increases from locked rates of  $10^{-17}$  m/s in 2-D and 3-D and  $10^{-20}$  m/s in 1-D to seismic rate  $10^0$  m/s at the same time (Fig. 2.3a). This similarity indicates the possibility of using lower dimensional models to substitute higher dimensional ones in earthquake cycle modeling.

By dimension reduction, simulated earthquakes become more characteristic (Fig. 2.3, 2.4). In 3-D, all simulated earthquakes nucleate from one corner of the rectangular VW zone and rupture throughout it until the rupture front reaches the transition to the VS zone. However, not all earthquakes initiate from the same nucleation zone, as is suggested by the slip profile (Fig. 2.4a). Rather, the nucleation location alternates between the top-left and bottom-right corners, resulting in a periodic cycle of two earthquakes with slightly different slip and recurrence interval. Similar results in 3-D of two or more characteristic earthquakes repeating as a group have also been reported by *Barbot [2019]*, where several possible mechanisms are suggested for this poorly understood phenomenon, including near-stable condition, large geometrical aspect ratio and velocity-strengthening/-weakening region interaction [see also *Chen and Lapusta, 2019; Cattania, 2019*]. In 2-D, earthquakes are more periodic because they all nucleate from the same down-dip limit of the VW patch and rupture towards the up-dip limit, instead of alternately nucleating from the top and bottom sides (Fig. 2.4b). The earthquake size is also more identical with same recurrence interval. In 1-D, we observe purely periodic, characteristic earthquakes of the same size (Fig. 2.3). This trend is because with fewer dimensions, the interseismic loading pattern to the VW patch becomes simpler, so that the potential nucleation locations are also reduced. Earthquakes can potentially nucleate from four corners of the VW patch in 3-D, but it reduces to two (top and bottom) in 2-D and one in 1-D. This demonstrate that as spatial dimensions are eliminated, the simulated results typically exhibit a simpler spatio-temporal behavior.

From a quantitative point of view, simulated earthquakes reach larger slip and longer recurrence interval by dimension reduction (Fig. 2.4). To quantify the difference in slip we compare the total slip (i.e., seismic slip + aseismic slip), because it is largely constant throughout the fault plane in one earthquake cycle. Total slip is also equal to the maximum coseismic slip, since the maximum is only achieved where the fault portion is fully locked in the interseismic pe-

riod. This makes it, together with earthquake recurrence interval, good long-term earthquake cycle characteristics. In 3-D, we observe earthquakes with average total slip of  $\sim 4.5$  m and recurrence interval of  $\sim 135$  yr (Fig. 2.4a). In 2-D, fault slips  $\sim 6.8$  m every  $\sim 215$  yr, about 50% larger than in 3-D (Fig. 2.4b). In 1-D, fault slips  $\sim 13.3$  m every  $\sim 420$  yr, about three times as large as the 3-D results and twice the 2-D results (Fig. 2.3c). Note that in calculation of these numbers we excluded the slightly larger first earthquake that initiated at the predefined nucleation zone.

We contribute the larger earthquakes simulated in lower dimensional models largely to a lower interseismic stress rate. During the interseismic phase, the VS patches are creeping at the plate rate so they do not accumulate stress. They only play a role in transferring the tectonic loading from the loading boundaries into the VW patch they surround. In other words, the VW patch is loaded directly by its surrounding VS patches rather than the loading boundaries, whether the bulk medium is simulated explicitly or not. This clarification is fundamental because in this way the VW patch in 3-D is loaded from four sides, rather than only from the top/bottom where tectonic loading regions are located. While the VW patch in 2-D is loaded from two sides, resulting in slower interseismic stress rate inside the VW patch and hence a longer period before the next earthquake can nucleate (thickest lines in Fig. 2.3b). Given that the constant creeping rate in the VS patches is unchanged, the resulting larger slip deficit in the VW patch has to be made up by an earthquake with more slip. This is why larger earthquake slips are observed in lower dimensional models. Therefore these interseismic differences are largely explained by the reduced presence of VS patches due to dimension reduction. Quantitative calculations based on theoretical considerations, supporting the analysis above, will follow in section 2.3.5.

That clarification also implies that the interseismic stress rate in the VW patch does not depend on the size of the VS patches  $W_f$  or the distance of the loading boundaries  $(W_f - H)/2$ , but on the size of the VW patch itself. The smaller the VW patch is, on average the faster the loading will be. This is because the average distance from a portion of the VW patch to the VW-VS boundary is shorter. This explains why larger slip and longer recurrence interval are still observed in 1-D even though the distance between the VW fault and the far-away loading boundary  $X_0$  is already chosen to be  $(W_f - H)/2$ , the same as in higher dimensions (in section 2.2.3). Using this concept we aimed to make the stress rate di-



rectly caused by the loading boundaries comparable to that in 2-D and 3-D models, but the actual stress rate proved to be inadequate. Therefore  $X_0$  has to be shortened to obtain higher stress rate, and finally to achieve similar earthquake slip and recurrence interval. Based on this idea and further theoretically considerations (section 2.3.5) we propose a revised formulation of  $X_0$  in section 2.4.2, where more similar results as in higher dimensional models are achieved.

### 2.3.2 Coseismic rupture of the first earthquake

For the first earthquake (Fig. 2.5a, c, e), the source time function at all locations within the VW patch takes the shape of Kostrov's classic self-similar crack solution [Kostrov and Das, 1988] with a short rise time and relatively long deceleration tail. As dimensions are reduced, the duration of the rise time decreases while the duration of the deceleration increases. The deceleration in 1-D is the slowest, since the rupture does not interact with patches of different stress or strength properties that could decelerate it. For the same reason, it is impossible to observe rupture reflections in 1-D. While the rupture reflection from the VW-VS boundary in 3-D is clearly observable as a second slip velocity peak (Fig. 2.5a).

Despite this qualitative similarity, we compare slip velocity, rupture speed and stress drop for their quantitative differences across dimensions. Peak slip velocity and rupture speed are important earthquake characteristics that reflect the dynamic characteristics of a fracture. We observe that peak slip velocities reach the same order of magnitude of around  $10^0$  m/s regardless of dimension, but they do increase by tens of percent in lower dimensional models (Fig. 2.5a). In 3-D, the peak slip velocity is initially  $\sim 0.8$  m/s in the predefined nucleation zone and gradually increases to its maximum of  $\sim 1.5$  m/s. In 2-D, the peak slip velocity starts around  $\sim 1.6$  m/s and gradually increases up to  $\sim 2.0$  m/s. In 1-D, the maximum slip velocity is  $\sim 2.4$  m/s. We connect this increase again to the reduced presence of VS patches due to dimension reduction. In 2-D models, the 1-D fault "line" represents a 2-D fault plane in which the VW patch is extended infinitely long along strike in a 3-D perspective [e.g., Andrews *et al.*, 2007], whereas in 1-D models the 0-D fault "point" represents an infinitely large, fully-VW 2-D fault plane. In other words, the VS patches are removed from the dimensions that is not explicitly simulated, which would originally absorb energy from the

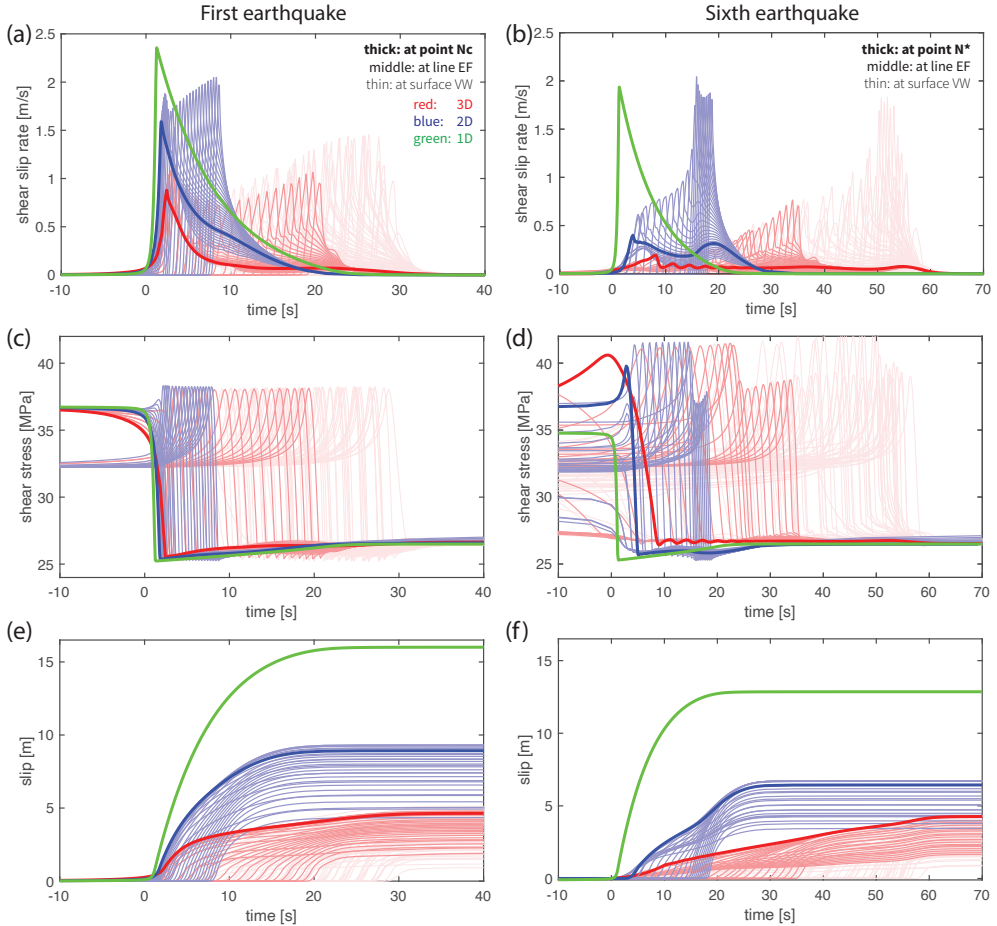


Figure 2.5: Comparison of the coseismic time series of (a, b) slip rate, (c, d) stress and (e, f) accumulated slip in 1-3-D models. The first earthquake is shown in (a, c, e), and the sixth earthquake is shown in (b, d, f), where origin time is set at the onset of the respective earthquake. The lines with different thicknesses and degrees of transparency are recorded at different locations on the fault, where the thick lines are recorded at the nucleation location “Nc” (the first earthquake) or “N\*” (the sixth), the semi-thick lines along the line “EF” cutting across it vertically and the thin lines elsewhere in the VW patch (see Fig. 2.7a, c).

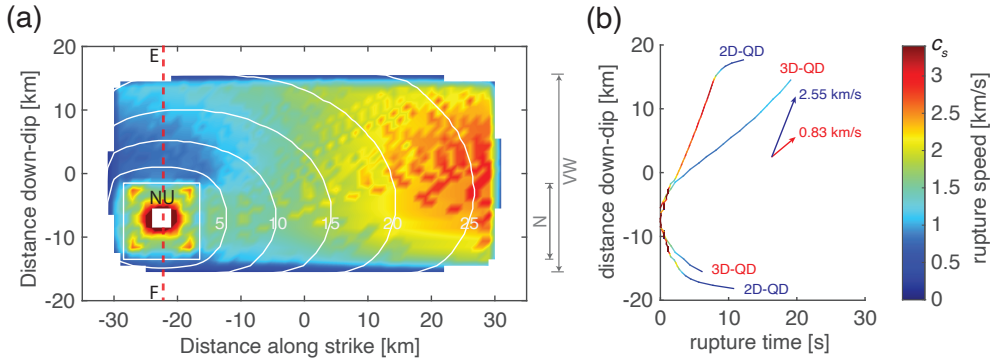


Figure 2.6: Comparison of coseismic rupture propagation. (a) The coseismic rupture speed of the first earthquake in 3-D. The arrival time of the coseismic rupture front, which is measured when slip velocity reaching the seismic limit, is plotted every five seconds as contours. The central part of the fault plane is shown where white color means no seismic slip is observed. The red dashed line labels the observation line “EF” introduced in Fig. 2.1. Note that no reliable rupture speed is measured at rupture onset (left white near “Nc”). (b) The coseismic rupture front arrival time along the vertical line “EF” in 2-D and 3-D. The line color indicates the rupture speed under the same color scale as (a). Lines end at where slip rates drop below seismic threshold. The average rupture speed in the middle of propagation (i.e., except during nucleation and arrest) is measured as stated.

rupture if the rupture would interact with them. More importantly, every portion of the fault along the not explicitly simulated direction ruptures at the same time as its simulated counterpart. Thus no fracture energy is consumed in those directions. The energy that is not consumed in these ways can instead be used to achieve higher slip velocities, as evident from the earthquake energy budget considerations in *Kanamori and Rivera [2006]*.

Rupture speed across different dimensional models shows larger variation than peak slip velocity. In 3-D, the total coseismic rupture lasts for  $\sim 30$  s. Rupture propagates faster in the horizontal direction than in the vertical direction and it experiences an acceleration in the last  $\sim 10$  s to reach near-shear speed (Fig. 2.6a). The rupture front takes  $\sim 20$  s to propagate along the vertical line “EF”, at a near-constant speed of  $\sim 0.83$  km/s, except for the first several seconds and the arrest. In 2-D, the rupture takes only  $\sim 10$  s to reach the up-dip limit, starting from the same nucleation region (Fig. 2.6b). Accordingly, the rupture speed of the stable part is  $\sim 2.55$  km/s, almost twice higher than in 3-D. To explain these differences in rupture speed, the same considerations used to explain the differences in peak slip velocities are applied. In 2-D models, no frac-

ture energy needs to be overcome to rupture into the strike direction and hence more energy can be directed along dip, which allows the rupture to achieve higher speeds. This also shortens the rupture duration and leads to ruptures that propagate deeper into the surrounding VS patches compared to 3-D models (Fig. 2.6b). Given that the difference between 2-D and 3-D models occurs in the horizontal direction while the vertical direction remains identical, our results suggest that the (in)existence of the horizontal VS patches has influence on the coseismic rupture behavior inside the VW patch, even in the vertical direction. This is confirmed in additional models where a second rupture deceleration can be observed if the length of the VW patch is shortened to one fourth (see section 2.4.1, Fig. 2.10).

Given the same initial condition, the stress drop and fracture energy of the first earthquake are comparable in all dimensional models, both inside and outside the pre-stressed zone (Fig. 2.7b). The stress drop  $\Delta\tau$ , i.e., the stress difference between the start and the end of an earthquake, and the fracture energy  $G_c$ , i.e., the surface area below the stress w.r.t slip profile, are important earthquake parameters (see Fig. 2.7b for more definitions of stresses and stress drops used below). Regardless of dimension and at all VW locations we first observe the shear stress increasing up to the yield stress and then it drops to a constant level corresponding to dynamic friction (Fig. 2.5c). Both the yield stress and the dynamic stress are comparable across dimensions. Therefore the difference between the two (so-called breakdown stress drop  $\Delta\tau_b$ , i.e., strength excess + stress drop) is also similar. Notice that the initial stress increase is not as large when getting close to the nucleation zone and it is nearly zero inside it (thickest line in Fig. 2.5c). This shows that the nucleation zone has to reach its yield stress before the coseismic phase, which is usually lower comparing to the maximum achievable yield stress elsewhere. After the stress drop, an immediate small stress increase is observed that is also similar in size across dimensions (Fig. 2.5c). It is worth noting that the stress drop at different locations is achieved within a similar amount of slip (Fig. 2.7b), regarded as the characteristic slip weakening distance  $D_c$  in a linear slip-weakening friction formulation. After this distance, coseismic slip continues to accumulate until the earthquake arrests. The critical slip-weakening distance varies from 0.8 m to 1.1 m from 3-D to 1-D. Given the similar size of stress drop and slip-weakening distance, the fracture energy  $G_c \approx \Delta\tau_b D_c / 2$  (Fig. 2.7b) is also found to be comparable across dimensions and at all VW locations (with a minor increase from 1-D to 3-D).

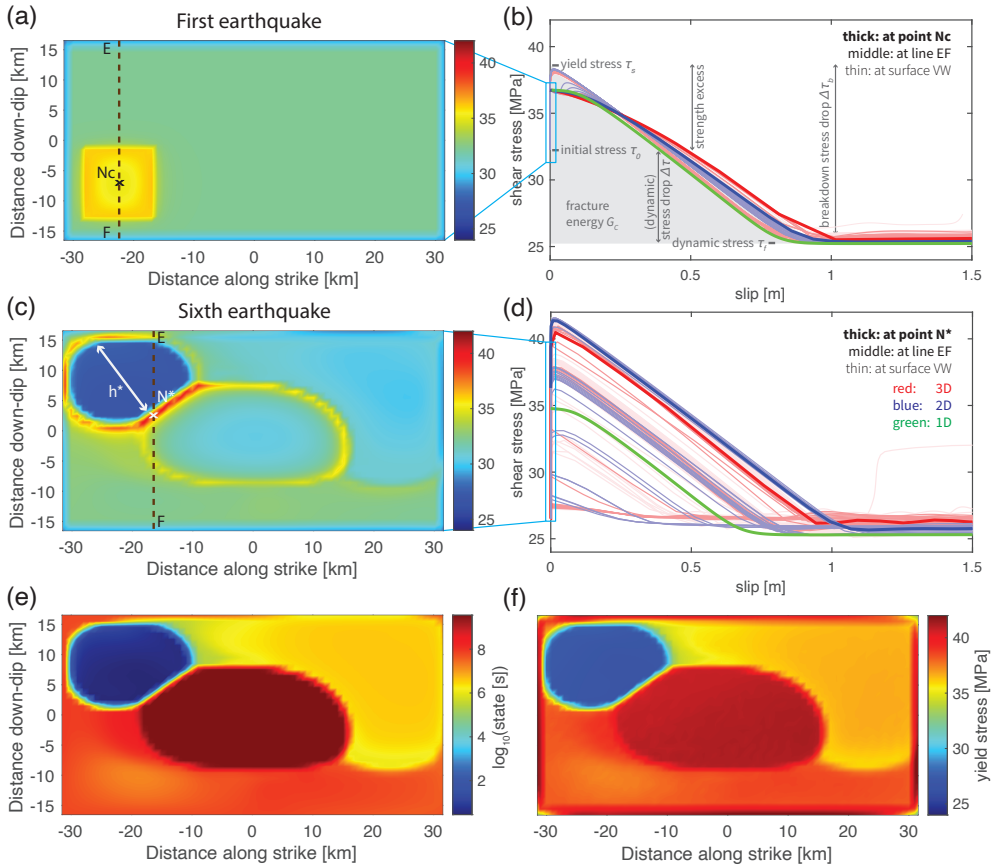


Figure 2.7: Cross-dimensional comparison of (a, c) the initial stress and (b, d) the coseismic stress evolution w.r.t. slip in 1-3-D models for (a, b) the first earthquake and (c, d) the sixth earthquake. (a, c) The initial stress is measured when the maximum slip velocity reaches the seismic threshold. The nucleation size is denoted as  $h^*$ . Due to the high prestress, the coseismic slip of the first earthquake begins from the center of the nucleation zone (denoted as “Nc”). Whereas the coseismic slip of the sixth earthquake begins at the rim of the nucleation zone (denoted as “N\*”). (b, d) The lines with different thicknesses and degrees of transparency are recorded at different locations on the fault, where the thick lines are recorded at point “Nc” (the first earthquake) or “N\*” (the sixth), the semi-thick lines along the vertical line “EF” through it and the thin lines elsewhere in the VW patch (see panels a, c, respectively). (e) The initial state of the sixth earthquake. (f) The yield stress of the sixth event. The definitions of stresses and stress drops used in the text are labeled in panel (b).

The differences in stress drop and fracture energy across dimensions are minor. This is in line with expectations, since these earthquake parameters are considered to be largely controlled by the frictional properties and the normal stress [e.g., *Rubin and Ampuero, 2005*] that are homogeneous in this model. However, the modest systematic differences in, for example, the critical slip weakening distance that becomes shorter at lower dimensions, still indicates that the dynamics on the fault play a role in redistributing the earthquake energy budget, so that the stress drop and the slip weakening distance can change accordingly. This is more evident when the fault is shorted to one fourth its width where yield stress is observed decreasing while rupture propagates (see section 2.4.1, Fig. 2.10).

### 2.3.3 Nucleation phase

A spontaneous nucleation phase is observed in later earthquakes that experience tectonic loading. To understand cross-dimensional differences under more realistic initial conditions prevalent after the first earthquake, we also analyze the sixth earthquake. This earthquake is representative since earthquakes are essentially characteristic from the second onward.

Earthquake initiation somewhat differs across dimensions in how much aseismic slip is accumulated prior to nucleation and in the nucleation size  $h^*$ . To understand this and to understand which fault plane locations are most comparable, we analyze interseismic slip velocity and shear stress evolution patterns (Fig. 2.3). These patterns that depend on the distance between the observation point and the VS patches are qualitatively similar in all dimensional models. Faster loading occurs near the VS-VW transition and these regions start to creep at plate rate the earliest. Slip becomes unstable when the creeping front propagates into the locked region up to the nucleation size  $h^*$ . Nucleation then occurs in one of the four corners in the VW patch in 3-D or one of the two ends in 2-D. The nucleation size is observed to be roughly twice as large in 3-D compared to the size in 2-D (Fig. 2.4). At the rim of this nucleation zone, highest shear stress is achieved due to the largest velocity gradient between creeping and locked zones. In the meantime, the inner nucleation zone yields and accelerates, which is accompanied by stresses dropping back to their steady-state (Fig. 2.7c). Based on whether the observation point is inside the nucleation zone, at the nucleation

rim (e.g., point “N\*” in Fig. 2.7c) or outside the nucleation zone, similar loading and nucleating behavior is shared across dimensions, respectively (Fig. 2.3). Inside the nucleation zone, faster slip velocity and stress accumulation rates are observed, both with a plateau at steady-state before earthquake starts (middle to thin lines that are to the left and above the thickest line in Fig. 2.3a, b). Outside the nucleation zone, at a point closer to the central VW patch that experiences slower loading, slip velocity and shear stress increase more slowly. This fault portion remains locked before the start of the next earthquake, i.e., slip velocity is always below plate rate and shear stress below the aforementioned steady-state stress level (middle to thin lines that are to the right and below the thickest line in Fig. 2.3a, b). Only at the rim of the nucleation zone, can slip velocity and shear stress increase at a unique rate that allows for the earthquake to occur as soon as the plate rate and the fault strength are reached at the same time (e.g., thickest lines in Fig. 2.3a, b). Since the seismic rate is achieved instantaneously, no aseismic slip is accumulated at this location during nucleation.

In 1-D models with a 0-D fault “point”, slip also immediately becomes seismic as soon as the shear stress reaches the interface strength and thus does not accumulate preceding aseismic slip. Therefore, such models mimic the rim of the nucleation zone in higher dimensional models (thickest lines in Fig. 2.3). This is because, as we discussed above, the 0-D fault “point” represents an infinite fully-VW fault plane from a 3-D perspective, on which earthquakes nucleate simultaneously at all locations as yield stress is reached at the same time. This location is where simulation results are best compared across dimensions and are further explored in theoretical calculations (section 2.3.5).

### 2.3.4 Coseismic phase of later earthquakes

An important consequence of interseismic loading is that it reshapes the initial stress (stress at the beginning of coseismic phase) and initial state to be heterogeneous (Fig. 2.7c, e, also refer to panel b for the definition of below-mentioned stress, stress drop and energy). Due to the variable distances to the VS patches and the nucleation process, different locations in the VW patch are loaded to a spatially variable level of initial stress and initial state. The nucleation zone has the lowest initial stress, whereas its rim has the highest values close to the yield stress (Fig. 2.7c). The same holds for initial state except that a high state variable



is also achieved in the center of the VW patch (Fig. 2.7e). This is because during the preceding interseismic phase the central VW patch remains locked. According to *Nakatani* [2001]'s definition of interface strength ( $\sigma_n \left[ \mu_0 + b \ln \left( \frac{\theta V_0}{L} \right) \right]$ ), this region is healed to a much higher interface strength than its surrounding. Consequently, the subsequent coseismic phase exhibits characteristics that the first earthquake did not show.

Our dimensional comparison of the first earthquake regarding the rupture speed and slip velocity remains qualitatively valid (Fig. 2.5b, d, f vs. a, c, e) for the coseismic phase of later earthquakes. However, it is worth pointing out that the rupture speed is overall about 50% slower than the first earthquake, resulting in twice as long rupture duration in both 2-D and 3-D models (Fig. 2.5b vs. a). The peak slip velocity grows slowly at the beginning when the rupture is propagating into the central VW patch. The high interface strength suppresses its propagation into this patch and thus limits both rupture speed and peak slip velocity. Only once the rupture front has passed and is closer to the VW-VS transition do the rupture speed and peak slip velocity increase sharply. Combining lower slip velocity and longer coseismic duration, the accumulated seismic slip is smaller in latter earthquakes than for the first earthquake (Fig. 2.4, 2.5f vs. e). Smaller seismic slip is thus a result of the lower average initial stresses (and lower slip deficit) for spontaneously loaded earthquakes with respect to the highly stressed nucleation zone predefined for the first earthquake.

Given the same level of dynamic stress after the earthquake, the nonuniform initial stress field also results in a nonuniform stress drop  $\Delta\tau$  (Fig. 2.7d). Additionally, the yield stress is spatially variable, making the breakdown stress drop  $\Delta\tau_b$  nonuniform as well (Fig. 2.7d, f, also clearly visible in 2.5d). The stress-slip profile and fracture energy are thus no longer near-identical throughout the VW patch as they are in the first event (Fig. 2.7d vs. b). Compared to the first earthquake, the yield stress becomes higher near the central VW patch and lower closer to the VW-VS transition, making it lower when averaged over the whole seismogenic zone (Fig. 2.7f). Fracture energy  $G_c$  varies accordingly: it increases near the center, decreases closer to the transition, and decreases on average. This illustrates the importance of tectonic loading for the coseismic rupture, as it modifies the initial stress, yield stress and energy profiles. Yield stress can thus no longer be simply defined by the frictional properties.

The 1-D models, lacking the space for nucleation and dynamic rupture, never



reach the initial and yield stress level higher dimensional models achieve in later earthquakes (Fig. 2.5d). This makes them quantitatively dissimilar to 2-D or 3-D simulations in the coseismic phase, even from the aspect of mimicking the nucleation rim (thickest lines in Fig. 2.5b, d, f vs. a, c, e).

### 2.3.5 Theoretical considerations

To better analyze the similarities and understand the differences across dimensions, we utilize theoretical calculations that can estimate the aforementioned characteristic observables to the first order.

#### Earthquake cycle parameters

We estimate earthquake recurrence interval and total slip (i.e., aseismic + seismic slip, maximum coseismic slip) by extending the 3-D theoretical formulation in *Chen and Lapusta* [2019] to all other dimensions using the analytical crack models of *Knopoff* [1958] and *Keilis-borok* [1959]. Earthquake recurrence interval  $T$  can be estimated when it is known how much stress is accumulated and what the interseismic stress rate is, namely  $T = \Delta\tau/\dot{\tau}$ . Maximum coseismic slip  $D$ , which equals to the interseismic slip deficit, can be estimated from the aseismic slip accumulated on the surrounding creeping VS patches during the interseismic phase, namely  $D = V_p T$ .

To provide a reliable estimate of the interseismic stress rate and its maximum it is important to know which fault location is most representative for this purpose. This is important because the stress accumulation pattern is non-linear and spatially variable (Fig. 2.3), as explained in the description of the nucleation phase (section 2.3.3). Give the nonuniform initial stress  $\tau_i$  (Fig. 2.7c) and the generally uniform dynamic stress  $\tau_f$  as a starting level, the interseismic stress that needs to be accumulated  $\Delta\tau = \tau_i - \tau_f$  is thus not uniform. A similar spatial variation holds for the interseismic stress rate  $\dot{\tau}$  (Fig. 2.3b). Interestingly, the stress accumulates at an approximately linear rate at the rim of the nucleation zone, e.g., at location “N\*” in Fig. 2.7c. Additionally, this location does not experience aseismic creep during the nucleation phase, as the slip becomes seismic

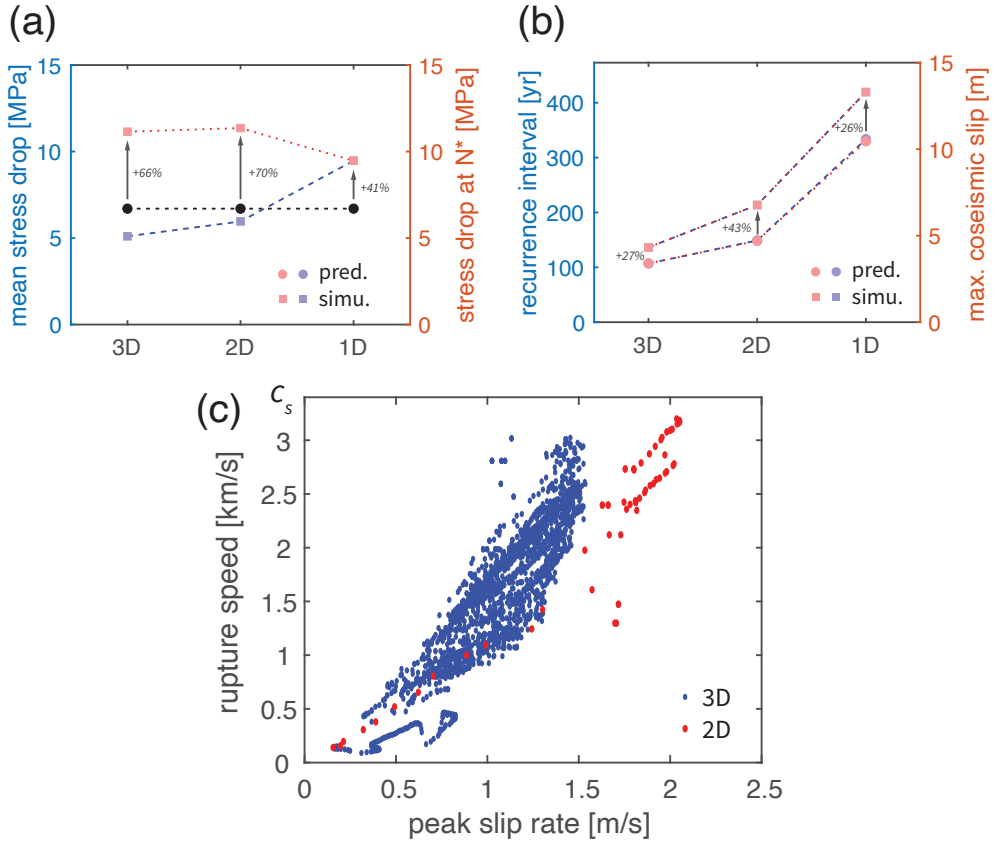


Figure 2.8: Comparison between theoretical predicted and numerically simulated results. (a) Comparison between theoretically predicted (circle) and numerically simulated (square) average stress drop (blue) and stress drop at location "N\*" (red). The prediction is shared by both axis quantities and colored in black. The difference (in percentage) between calculated and simulated stress drop at location "N\*" is labeled aside. (b) Comparison between theoretically predicted (circle) and numerically simulated (square) recurrence interval (blue) and maximum coseismic slip (red). Same labels as in (a). Note that the markers in blue and red are largely overlapped in this panel. (c) Interrelation between rupture speed and peak slip velocity in 3-D (blue) and 2-D (red) models. The local values are measured at different locations inside the VW patch.

immediately. These two observations make a straight-forward theoretical calculation to estimate both recurrence interval  $T$  and maximum coseismic slip  $D$  feasible by analyzing the stress accumulation at location “N\*”.

This location is at the distance of  $h^*$  inside the VW patch since an earthquake can only nucleate when the creep penetrates this distance into the VW patch, where  $h^*$  is the nucleation size. First, the interseismic stress accumulation is estimated by the stress drop  $\Delta\tau_{\text{dyn}}$ , which is approximated from the stress difference between the two steady-state friction level during the interseismic and coseismic phase [Cocco and Bizzarri, 2002]

$$\begin{aligned}\Delta\tau_{\text{dyn}} &\approx \tau(V_p) - \tau(V_{\text{dyn}}) \\ &\approx \sigma[\mu_0 + (a - b)\ln(V_p/V_0)] \\ &\quad - \sigma[\mu_0 + (a - b)\ln(V_{\text{dyn}}/V_0)] \\ &= \sigma(b - a)\ln(V_{\text{dyn}}/V_p),\end{aligned}\tag{2.14}$$

where dynamic slip velocity  $V_{\text{dyn}}$  is approximated as 1 m/s for simplicity. Second, the stress rate is calculated at the desired location that is at the distance of  $h^*$  inside the VW patch [in 2-D and 3-D models, respectively, Rubin and Ampuero, 2005]

$$\begin{aligned}h_{2-D}^* &= \frac{2GLb}{\pi\sigma(b - a)^2} \\ h_{3-D}^* &= \frac{\pi^2}{4}h_{2-D}^* = \frac{\pi GLb}{2\sigma(b - a)^2}\end{aligned}\tag{2.15}$$

for mode III deformation in our models. The factor  $\pi^2/4$  comes from the stress intensity factor (SIF) that is different for different rupture front curvatures in 2-D and 3-D [Tada et al., 1973]. The stress rate  $\dot{\tau}_{h^*}$  at this location can be expressed as [Chen and Lapusta, 2019; Keilis-borok, 1959; Knopoff, 1958]

$$\dot{\tau}_{h^*} = C \frac{GV_p}{\sqrt{r^2 - (r - h^*)^2}}.\tag{2.16}$$

For a fault segment of half-width  $r$  in 2-D models or a circular fault of radius  $r$  in 3-D models it has the same form with  $C$  a dimension-dependent constant being either  $C_{3-D} = \frac{\pi(2-\nu)}{8(1-\nu)} = 7\pi/24$  [Keilis-borok, 1959] or  $C_{2-D} = 1/2$  [Knopoff, 1958]. This expression is directly applicable to our 2-D models with  $r = H/2$ . While in 3-D models, taken into consideration that the width of VW patch  $H$  is shorter than its length  $l$ , we apply this expression to our rectangular fault by assuming

$r \approx H/2$ . In 1-D, the tectonic loading is applied from the far-away boundary. In this case we replace the whole denominator  $\sqrt{r^2 - (r - h^*)^2}$  by  $X_0$ , the distance between fault and the far-away loading boundary, with  $C_{1-D} = 1$ . Third, by combining the interseismic stress rate and coseismic stress drop together we approximate the recurrence interval  $T$  by

$$T = \Delta\tau_{\text{dyn}}/\dot{\tau}_{h^*} = \frac{(b-a)\sigma}{CGV_p} \sqrt{r^2 - (r - h^*)^2} \ln \frac{V_{\text{dyn}}}{V_p}. \quad (2.17)$$

Finally, the total slip  $D$ , or the maximum coseismic slip, is estimated by

$$D = V_p T = \frac{(b-a)\sigma}{CG} \sqrt{r^2 - (r - h^*)^2} \ln \frac{V_{\text{dyn}}}{V_p}. \quad (2.18)$$

The theoretically predicted recurrence interval and maximum coseismic slip values systematically underestimate the numerical simulations by about 30% but there is yet a qualitative agreement to simulations across all dimensions (Fig. 2.8b). Especially, the theoretical prediction successfully captured the observed trend of increasing recurrence interval and coseismic slip a result of dimension reduction, with accurate relative changes from 3-D to 2-D and 1-D. This agreement suggests that the essence of the cause is already captured in the simpler theoretical considerations and justifies our explanation that the larger coseismic slip is caused by the larger slip deficit during longer recurrence interval and the longer recurrence interval is caused by the lower interseismic stress rate. Furthermore, we notice that the relative difference is nearly identical between the recurrence interval and the total slip, indicating that the error in slip calculation (2.18) may be directly inherited from the recurrence interval calculation (2.17). The underestimation of the stress drop at location “N\*” by stress drop  $\Delta\tau_{\text{dyn}}$  is a main contributor to this error (Fig. 2.8a). Our simulations show that for the locations at the nucleation rim (point “N\*” in Fig. 2.7c) initial stress  $\tau_i$  is notably higher than its surrounding. However, we notice that this underestimation of the accumulated stress is stronger than the underestimation of the final values (Fig. 2.8a), indicating that the interseismic stress rate  $\dot{\tau}$  is underestimated as well. This is due to the increased stress rate at the beginning and the end of the interseismic phase. At the beginning of the interseismic phase, it is increased by the effect of the postseismic slip. While near the end of the nucleation phase it is due to the expanding nucleation zone that creeps, introducing additional slip gradient (Fig. 2.3b). Despite the errors, these theoretical

considerations well explained the simulated earthquake cycle parameters and their trend with dimension reduction as a first order approximation.

### Coseismic rupture parameters

Unlike the recurrence interval and total slip, coseismic rupture parameters such as rupture speed and slip velocity vary across the fault. Our theoretical calculations cannot provide an absolute estimate of the rupture speed. However, both laboratory experiments [Ohnaka *et al.*, 1987] and theoretical considerations [Ida, 1973; Ampuero and Rubin, 2008] suggest that the peak slip velocity  $V_{\text{peak}}$  and the rupture speed  $V_r$  are interrelated by

$$V_r = \alpha_r V_{\text{peak}} \frac{G}{\Delta\tau_b}, \quad (2.19)$$

where  $\alpha_r$  is a factor on the order of 1. This positive correlation is confirmed by our simulations (Fig. 2.8c). We measured on average  $\alpha_r$  of 0.82 in 3-D and 0.65 in 2-D for the first earthquake respectively, which is similar to what Hawthorne and Rubin [2013] measured (0.50-0.65) in their 2.5D simulations. The lower value of  $\alpha_r$  in 2-D suggests that with dimension reduction higher slip velocity can be achieved under the same rupture speed.

Whereas the calculated stress difference from rate-and-state friction between the two steady states in the interseismic and coseismic phase (2.14) is independent of dimension and location, the stress drop  $\Delta\tau$  is not uniform across the simulated VW patch. Therefore that theoretical prediction only provides an estimation of the average stress drop [Chen and Lapusta, 2019]

$$\overline{\Delta\tau} \approx \Delta\tau_{\text{dyn}} \approx \sigma(b-a) \ln(V_{\text{dyn}}/V_p). \quad (2.20)$$

The calculated average stress drop is slightly higher than the simulated results in 2-D and 3-D (Fig. 2.8a). However, it is still satisfying as a first order approximation for both models given that the contribution of the changing state has been ignored. It is noticed that the 1-D model has a higher simulated average stress drop. This is because the “average” loses its meaning in this case and the simulated value only represents where the earthquake nucleates in higher dimensional models (point “N\*”). It is well expected that higher stress drop is achieved here following the explanation in section 2.3.3 and the subsection above.

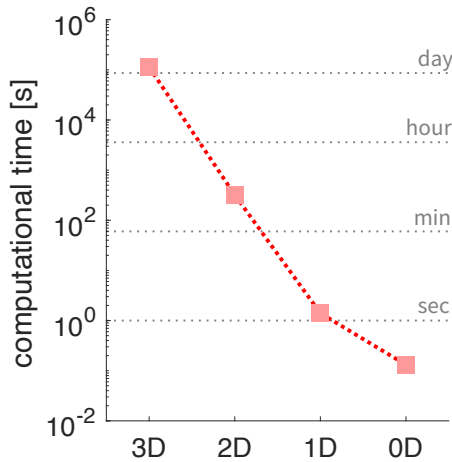


Figure 2.9: *The average computational time of one earthquake cycle in 0-D to 3-D models, under the same resolution and domain size, with 12 CPUs Kokkos level parallelization.*

### 2.3.6 Computational efficiency

Lower dimensional models are computationally more efficient without losing the qualitative characteristics and the ability to estimate certain earthquake parameters such as maximum slip velocity, maximum or average stress drop, and fracture energy. To evaluate the computational efficiency of each model we measure the average computational time per earthquake cycle (Fig. 2.9). The 3-D model takes  $10^3$  times longer time than 2-D and  $10^5$  times longer than 1-D. In the following discussions we will see that the 1-D model can be further simplified to its 0-D equivalent by removing the medium content (the  $x > 0$  axis in 1-D models). The 0-D model will again save more than 90% running time compared to 1-D, making it more than a million times faster than 3-D models. Note that these computations do not use distributed memory and therefore ignore related parallel scaling issues.

## 2.4 Discussions

We are the first to systematically study and quantify similarities and differences in how models in different dimensions simulate earthquake sequences. While

large-scale parallel computing can be exploited to reduce the time to solution of 3-D applications, this does not significantly lower the power consumption and consequently the monetary and environmental burden. Moreover, we find that the orders of magnitude difference of speed-up by dimensional reduction are so large (Fig. 2.9), and can be even larger when higher resolution is necessary, that they readily make the difference between being feasible for scientific and exploratory research or not. Hence lower dimensional models will likely remain essential for scientific exploration in the coming decades [Lapusta *et al.*, 2019]. Especially when the researcher's objectives fall into the scope of what the lower dimensional models can handle, they are encouraged to use them as they could be hundreds to millions times faster than a 3-D model with the same resolution.

However, we should also acknowledge that there are research questions whose answers inherently require higher-dimensional spatial or geometrical complexity. For example, rupture arrest in the missing dimension can never be captured in lower-dimensional models, no matter if it is self-arrested or due to the presence of VS patches. Temporally complex patterns of earthquake occurrence as well as partial ruptures reduce their existence at the same time. We are not aiming at finding substitutes for such cases but rather to present the essential differences that are apparent in the simplest setup. The differences between models of different dimensions presented in this paper will have no reason to disappear when more complicated setups are adopted. On the other hand, although 3-D models are necessary for certain studies [e.g., Galvez *et al.*, 2014; Ulrich *et al.*, 2019; Wollherr *et al.*, 2019; Madden *et al.*, 2021], simpler models can always be a useful starting point of an exploration. These results should also serve as guidelines as to how to interpret the lower-dimensional modeling results with their limitations ready in hand, rather than being regarded solely as restricting model simplifications to being adopted.

#### 2.4.1 Under what conditions can 2-D models substitute 3-D models?

We have summarized model similarities over dimensions as well as analyzed how model discrepancies due to dimension reduction explain the resulting differences. It is worth further exploring in which situations dimension reduction

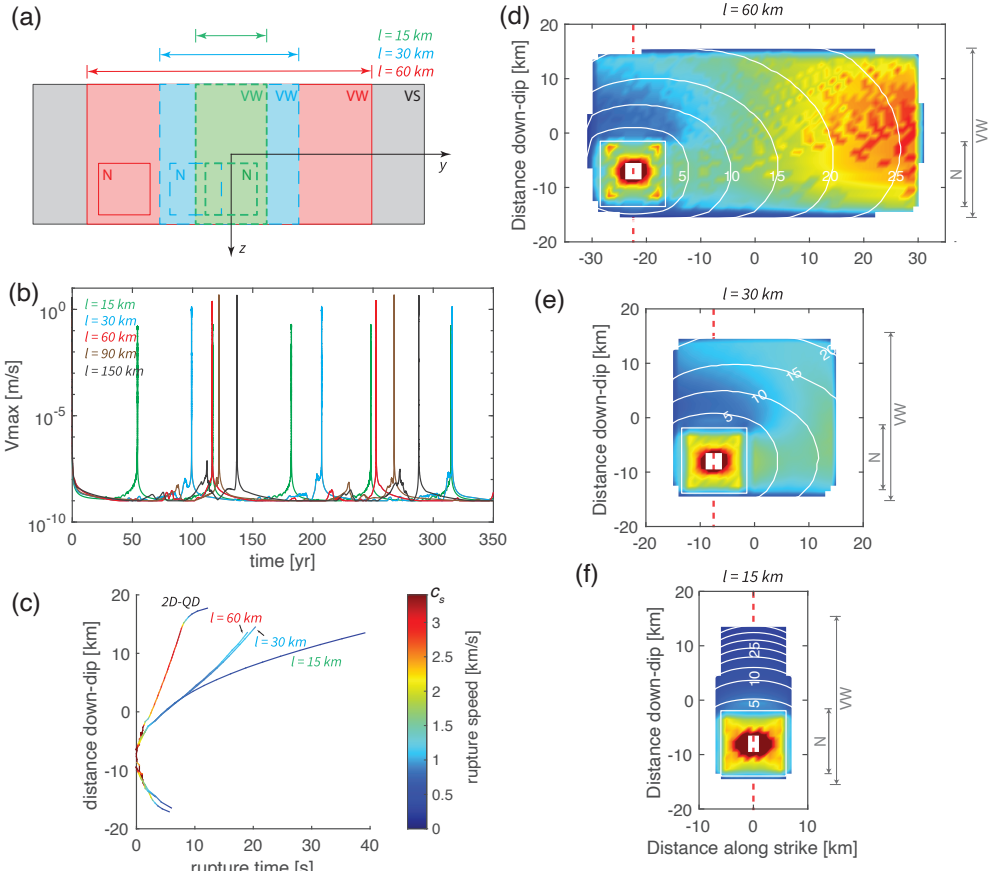


Figure 2.10: Comparison of the effects of fault length  $l$  (15 - 150 km) in 3-D models: (d, g, j) 60 km, (e, h, k) 30 km, and (f, i, m) 15 km. (a) The varied VW patch sizes and varied locations of the predefined nucleation zone in three testing models with  $l$  from 15 km to 60 km. (b) The maximum slip velocity in multiple earthquake cycles for models with  $l$  from 15 km to 150 km. (d-f) The arrival time of the coseismic rupture front of the first earthquake, which is measured when slip velocity reaching the seismic limit. Only the central part of the fault plane is shown, where white color means no seismic slip is observed. Contours are plotted every five seconds. The red dashed line labels the observation line “EF” introduced in Fig. 2.1. (c) The coseismic rupture front arrival time along the vertical line “EF” under the same color scale. Lines end at where no seismic slip is observed. The rupture time of the corresponding 2-D model is plotted as reference. (Continuing next page.)



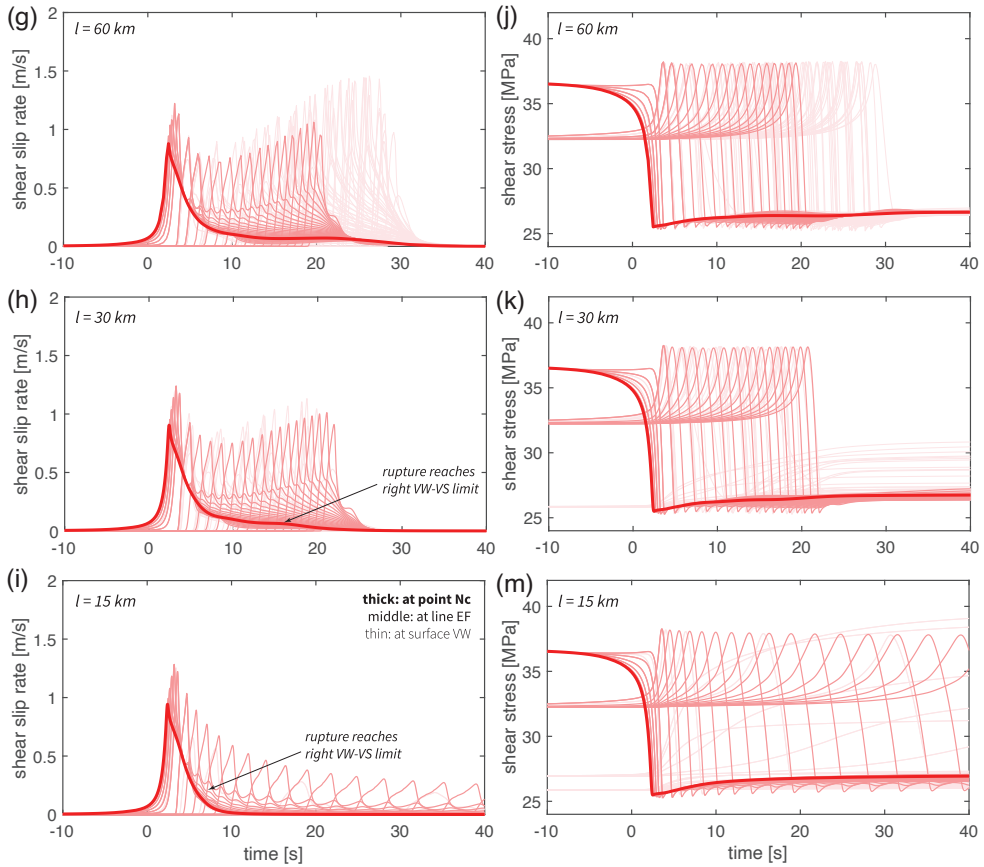


Figure 2.10: (Following previous page.) (g-i) The time series of slip velocity in the coseismic phase of the first seismic event, in which origin time is set at the onset of this event. The lines with different thicknesses and degrees of transparency are recorded at different locations on the fault, where the thick lines are recorded at point “Nc”, the semi-thick lines along the line “EF” and the thin lines elsewhere (see Fig. 2.1). (j-m) The time series of shear stress in the coseismic phase of the first seismic event, with the same line property.

can be used without considerable side effects or when it should be avoided even if computational efficiency is a factor. To simplify the question, we restrict ourselves to the most common discussion point: under what conditions can a 3-D model be substituted by a 2-D model? Since along-strike heterogeneities are ignored in the given dimension reduction assumption (section 2.2.3), 3-D models with different along-strike features are simplified to the same 2-D model. However, they originally simulate different earthquake sequences. We have chosen the VW patch length as one common along-strike heterogeneity to analyze the role of this reduced dimension. We vary the VW patch length  $l$  and keep the VW patch width  $H$  fixed. By varying the VW patch length from 150 km to 15 km, we change the aspect ratio from 5:1 to 0.5:1 (Fig. 2.10). The fault (VW+VS patches) size and the computational domain ( $X_0, Y_0, Z_0$ ) are kept unchanged as well as the predefined nucleation zone as an initial condition, which is always set at the left bottom corner with fixed distance  $h_i$  to the VW-VS boundary (Fig. 2.10a). This configuration benefits the coseismic comparison along the vertical line “EF” crossing this zone (Fig. 2.10c-m) to our 2-D simulations (Fig. 2.5, 2.6).

In the long term, longer VW patches result in longer recurrence intervals (Fig. 2.10b). This is because the stress rate at the nucleation zone is lower comparing to a fault with a shorter VW patch. Given that the nucleation always starts from a corner of the rectangular VW patch, the nucleation zone in a longer VW patch is mainly loaded from three directions as the tectonic loading from the other horizontal direction is farther away. This is also supported by our theoretical considerations (see section 2.3.5) where we assumed circular fault geometry in 3-D and infinitely long fault in 2-D. The elongated fault geometry deviates from the 3-D assumption but is closer to the 2-D one. Therefore longer recurrence intervals are to be expected. Consequently, by prolonging the VW patch length, we achieve longer recurrence intervals to fit better what is observed in 2-D. In other words, higher aspect ratio faults in 3-D are better represented by 2-D models in the long term. However, even extending the 3-D patch to 150 km still leads to shorter recurrence intervals comparing to what is observed in 2-D (Fig. 2.3), as interseismic loading remains more effective from three lateral sides than two.

On the other hand, a longer VW patch requires longer rupture propagation time along strike and thus longer coseismic duration, if the rupture speed remains unvaried (Fig. 2.10d-e). As explain before, 2-D models can be seen as 3-D mod-

els where theoretically no time is required to rupture along strike. In this sense, a longer VW patch length is not preferred to fit the short coseismic duration observed in 2-D. However, even the shortest coseismic duration, observed with aspect ratio 1:1, is still about 50% longer than 2-D due to its low rupture speed. The rupture propagation time is not further shortened when the fault becomes even shorter. On the contrary, rupture speed is even largely decreased in the case with aspect ratio 0.5:1, resulting in a fairly long coseismic duration (Fig. 2.10c, f). This speed change happens after the rupture front reaches the horizontal VW-VS transition, confirming again that horizontal VW-VS interaction can change vertical rupture speed. Accompanying the rupture speed reduction, the slip velocity and the stress drop are reduced at the same time (Fig. 2.10g-m). This is dissimilar to the observations in 2-D (Fig. 2.5a, c). From this aspect, a shorter VW patch length is not favored either. In other words, medium aspect ratio (close to 1:1) fault is better represented by 2-D models in the coseismic phase. Additionally, if only what happens along the vertical line “EF” in 3-D is taken into consideration when compared to 2-D, then all models with aspect ratio higher than 1:1 can be accepted. This is because we notice that the rupture propagation along the vertical line “EF” does not change much with respect to the fault length when the aspect ratio is larger than 1:1 (Fig. 2.10c). Nor do the slip velocity and coseismic slip change along this line (Fig. 2.10d-e, g-h, j-k).

To summarize, 2-D models can better represent high aspect ratio faults in 3-D for long-term observations and medium-to-high aspect ratio faults for coseismic observations. Whereas for coseismic observations there are definitely inevitable qualitative differences in between. Our conclusion suggests that when using empirical scaling relations to interpret 2-D results to a 3-D perspective, it is crucial to assume a suitable aspect ratio according to the corresponding research objective. This geometrical effect is especially relevant for very large earthquakes and for induced ruptures constrained by reservoir thickness, where the large aspect ratio of the seismogenic zone has an impact on the energy release rate and the related scaling laws [Weng *et al.*, 2021]. Wesnousky [2008] summarized 36 historical natural earthquakes and found that they have similar rupture width but varied rupture length, resulting in varied aspect ratio from 0.7 to 12. The analysis in this study, covering the range 0.5 - 5, can therefore be useful to refer to when comparing or validating 2-D simulations to 3-D natural observations.

## 2.4.2 Implication of reducing models to 1-D or 0-D

Our results and theoretical calculations suggest that 1-D models reflect some key characteristics and thus can be used well to understand and quantify earthquake sequences under specific circumstances, which we discuss here. These implications from 1-D models also hold for 0-D models due to their mathematical equivalence. Since physical tectonic loading has to be removed in 0-D models, an arbitrary “driving force” has to be added to the system instead (section 2.2.3). To facilitate comparison, we can integrate the strain rate along the  $x$  direction in 1-D models and use it to drive the 0-D system. This is how the well-known “spring-slider” model is built [Burridge and Knopoff, 1967]. Such a 0-D model is mathematically equivalent to the 1-D model. This is because the static momentum balance equation in 1-D gives homogeneous shear stress in the medium. Combined with the boundary conditions, the time derivative of stress is given by

$$\dot{\sigma}_{xy} = G \frac{V_p - V}{X_0} . \quad (2.21)$$

Since this is an analytical derivation, the resulting model behavior is to remain the same. In this case we recommend replacing 1-D models with 0-D models, because they are more computationally efficient (Fig. 2.9). Nevertheless, the explanation above no longer holds when the governing equation (2.10) does not establish, including when heterogeneity, in-elasticity and/or inertia are considered. In these more complex cases 1-D models prevail in the ability of describing such physics [e.g., Pranger et al., 2022].

The domain size  $X_0$  in 1-D and the arbitrary driving force  $f_d^i$  in 0-D can be flexibly adapted to fit the earthquake cycle parameters. We have noted that setting the distance between the VW patch and the loading boundary  $X_0$  in 1-D to be the same as in higher dimensions  $(W_f - H)/2$  provides inadequate interseismic stress rate (section 2.3.1). This is because tectonic loading is realized at the VW-VS transition and it is neither dependent on  $W_f$  nor  $H$ . Relevant observations (section 2.3.3) and theoretical considerations (section 2.3.5) confirm that the 0-D fault point mimics the nucleation rim in higher dimensional models that is located at a distance  $h^*$  from the VW-VS transition. By using the calculated stress rate (2.16) in 2-D and 3-D as the 0-D “driving force”  $f_d^i$  in (2.11), recurrence intervals of about 133 yr and 250 yr are obtained. These are about 1.5% and 16%

different from the real 3-D and 2-D simulations, respectively. This minor difference suggests that 0-D and 1-D models can be used to estimate both interseismic (e.g., earthquake recurrence interval) and coseismic (e.g., maximum coseismic slip) characteristics.

The commonly observed periodic slow slip events cannot be reproduced in 1-D models with classical rate-and-state friction, as suggested by our explanation to the coseismic rupture characteristics (section 2.3.2). In 1-D the nucleation zone suddenly becomes infinitely large as soon as the 0-D fault point starts to nucleate. This instability unavoidably leads to an earthquake (i.e., slip at seismic rate) instead of slow slip events. This inference is supported by a parameter study of hundreds of models in which no suitable frictional parameters could be found [Diab-Montero *et al.*, 2021]. Slow-slip events are only observed (slowly) decaying when the system stiffness is close to but smaller than the critical stiffness. Using the consideration that 0-D fault point represents an infinitely large fully-VW 2-D fault, the infinite ratio of VW patch size ( $H$ ) over nucleation size ( $h^*$ ) is known to lead to seismic slip rates [Liu and Rice, 2007; Rubin, 2008; Herrendörfer *et al.*, 2018]. To produce slow-slip events in 1-D, additional damping needs to be present via, e.g., rate-dependent rate-and-state parameters [Im *et al.*, 2020], two-state variable rate-and-state friction behavior and/or additional spatio-temporal complexities [Leeman *et al.*, 2018]. Not only slow-slip events, any earthquake sequences including earthquakes that are not periodic, characteristic are hardly possible to be produced in 0-D and 1-D models, although they are to be expected most of the time in nature. The feature of the infinite VW fault dimension in 0-D and 1-D should be the first criterion to decide whether one should run a simulation in higher dimensions or not.

### 2.4.3 Implications for other model setups

Our model was designed according to the SEAS benchmark BP4-QD [Jiang *et al.*, 2022] to maximize comparability, interpretability and reproducibility with a common setup featuring a simple recurrence pattern of a single earthquake rupturing the entire seismogenic zone instead of smaller ones with complex temporal patterns [Cattania, 2019; Barbot, 2019; Chen and Lapusta, 2019]. Here we discuss several model setup adjustments, which largely shows that the conclusions drawn from our simulations can be generalized to a broader context.

Table 2.3: Influence of tectonic loading realization: Recurrence interval (yr) under different tectonic loading conditions and computational domain size in 2-D QD model.

| Medium extent $X_0$ | Loading condition (a) | (b)   | (c)   |
|---------------------|-----------------------|-------|-------|
| 80 km               | 104.0                 | 125.5 | 104.0 |
| 40 km               | 104.0                 | 128.0 | 104.0 |
| 20 km               | 101.5                 | 118.5 | 101.0 |
| 10 km               | 103.0                 | 87.5  | 86.0  |

(a) only on fault surface at top/bottom region with fixed fault width,

(b) only on far-away boundary surface,

(c) both (a) and (b).

We have investigated the similarities and differences in models of different dimensions using a fully dynamic (FD) approach to extend the applicability of our statements. Our conclusions still largely hold with minor quantitative variations. However, we also found qualitative differences in coseismic characteristics that demand a deeper discussion via the comparison between QD vs. FD models, which we for clarity referred to a follow-up paper [Li *et al.*, 2021].

Tectonic loading is typically applied in two different ways: directly on the fault plane [e.g., Kaneko *et al.*, 2011] or indirectly at the far-away boundaries [e.g., Herrendörfer *et al.*, 2018]. Both types have been adopted by studies for different research purpose. We adopted tectonic loading at the top/bottom of the fault plane for 2-D and 3-D models following BP4-QD, but at the far-away boundary for 1-D models due to dimensional restriction. To test the influence in the interseismic phase we applied tectonic loading conditions (a) only on fault surface at top/bottom region with fixed fault width, (b) only on far-away boundary surface, (c) both (a) and (b). We modeled in 2-D with gradually enlarged computational domain (Table. 2.3). We find that the recurrence interval converges to a set value as the computational domain is enlarged and is hardly affected by the type of loading when the computational domain is large enough. This invariance with respect to loading condition is supported by our theoretical calculations (section 2.3.5). Because there we explained that the main loading force to the locked VW patch is from its surrounding creeping VS patches. No matter which type of loading is applied, the stress rate inside the VW patch is largely defined by its own dimension and independent of the size of the VS patches or the fault as a whole (Eq. 2.16). Naturally the velocity gradient perpendicular to

the fault contributes to the loading process as well, but it is minimized for large enough computational domain where on-fault loading becomes dominant. During the coseismic period, the way in which tectonic loading is applied does not influence results because of the short duration. Therefore both the interseismic and coseismic characteristics are not sensitive to what kind of loading boundary condition is applied. Comparison in the SEAS benchmark BP4-QD of different modeling groups demonstrated the same idea: numerical results generally agreed with each other when computational domain was large enough, where for the numerical method's convenience, either stress-free or constant-moving boundary condition is chosen at far-away boundaries [Jiang *et al.*, 2022].

As for the initial condition, we have adopted a predefined highly stressed zone within the VW patch following BP4-QD. Since the later earthquakes do not necessarily occur from the same location, this predefined zone facilitated the quantitative coseismic comparison across dimensions by forcing the first earthquake to nucleate from this same region. It is suggested by some former studies that initial conditions have little effect on subsequent earthquakes [e.g., Takeuchi and Fialko, 2012; Allison and Dunham, 2018], therefore this special initial condition should not harm our findings in terms of earthquake cycle characteristics as well as nucleation behavior. In this study we did notice that the accumulative slip contour distortions around a depth of -1.5 km and -13.5 km are introduced by the predefined nucleation zone, whose properties increased the amount of slip in that zone for the first earthquake (Fig. 2.4). However, for non-accumulative variables no influence from the initial condition is observed in later earthquakes. Nevertheless, the first earthquake is not completely characteristic in an earthquake cycle even though some qualitative characteristics are still shared by later earthquakes. This also becomes apparent in the comparison to the sixth earthquake.

## 2.5 Conclusions

In this paper, we addressed a common concern of numerical modelers: how complex should my model be to answer my research question? Will dimension reduction qualitatively and quantitatively affect my results? And how? For this purpose, we have systematically investigated different dimensional models from 0-D to 3-D in terms of their interseismic and coseismic characteris-

tics and computational time for earthquake sequences and individual quasi-dynamic ruptures.

Our results demonstrate that, when 2-D or 3-D models produce quasi-periodic characteristic earthquakes, their behavior is qualitatively similar to lower-dimension models. The stress accumulation pattern is much the same when observed at the rim of the nucleation zone. As for the earthquake cycle parameters, lower dimensional models produce longer recurrence intervals and hence larger coseismic slip. This trend is supported by our theoretical calculations where the effect of dimension reduction is well quantified. We observe that the VS patches play a crucial role in causing differences in the interseismic phase, because tectonic loading is effectively realized at the VW-VS transition by the velocity contrast between the creeping VS patches and the locked VW patch. As VS patches are removed when fault dimension is reduced, their absence reduces the interseismic stress rate inside the VW patch and thus increases the recurrence interval. The larger slip deficit built in this period leads to a larger coseismic slip.

In the coseismic phase, we find that certain earthquake parameters such as the stress drop and fracture energy can be accurately reproduced in each of these simpler models, because they are mainly governed by material frictional parameters. This finding is especially valid for the first earthquake without physical tectonic loading. For later earthquakes, the statement is only true on average of the VW patch. This is because the initial stress, yield stress and effective slip weakening distance can change due to tectonic loading and earthquake history. For the coseismic rupture parameters, lower dimensional models generally produce higher maximum slip velocities and higher rupture speeds in lower dimensional models. Furthermore, we demonstrate that the interaction at the VW-VS transition can modify rupture speed, which is another crucial role the VS patches play in the coseismic phase. We find that the vertical rupture speed along the vertical direction in 3-D is slower compared to 2-D. It can be further slowed down when the fault length is shortened even more, suggesting that the vertical rupture behavior is influenced by horizontal frictional properties.

The aforementioned findings are supported by our theoretical calculations, which confirm that geometric differences due to dimension reduction influence the interseismic loading and finally affect the subsequent coseismic phase. Through accounting for an equivalent stressing rate at the nucleation size  $h^*$



into 2-D and 3-D models, 0-D and 1-D models can also effectively estimate earthquake cycle parameters such as recurrence interval and total slip. These theoretical considerations can be generally applied to other earthquake cycle models as well.

Based on these differences and similarities, we have analyzed under what condition 3-D models can be substituted by 2-D models by focusing on the aspect ratio of the VW patch. Our results present that 3-D models with longer fault length have longer recurrence interval, which fits better 2-D observations in the long term. On the other hand, shorter fault length requires shorter rupture propagation time along strike, which fits better 2-D observations in the coseismic phase.

Finally, we highlight the power of lower dimensional models in terms of their computational efficiency. We find that under the same (relatively low) resolution 3-D models require  $10^3$  times longer computational time than 2-D,  $10^5$  times longer than 1-D and  $10^6$  times longer than 0-D models. Therefore dimension reduction can not only relieve the heavy energy-consuming simulations, but also improve the efficiency of projects that require monotonous repetitions of forward models. This paper may serve as guidelines to check in simplified models what results can be expected to be accurately modeled as well as what physical aspects are missing and how they are related to the discrepancies observed in the results.

# 3

## Earthquake nucleation altered by stochastic normal stress heterogeneity

Submitted as: Li, M., Niemeijer, A. R., & van Dinther, Y. (2024). Earthquake nucleation altered by stochastic normal stress heterogeneity. *Journal of Geophysical Research: Solid Earth*.

## Abstract

In recent laboratory experiments, varying nucleation locations of accelerating slip with changing nucleation lengths were observed. Spatial variations in effective normal stress, due to the controlling influence on fault strength and fracture energy, play an important role. We quantitatively explain how spatially heterogeneous effective normal stresses affect earthquake nucleation and slip behavior. We simulate a meter-scale laboratory experiment in a numerical earthquake sequence model with stochastically variable normal stresses. We identify five regimes of earthquake nucleation and slip behaviors, controlled by the ratio of the heterogeneity wavelength ( $\lambda$ ) to the nucleation length ( $L_c$ ). When  $\lambda$  is much smaller than  $L_c$ , full ruptures are observed. Slip rates and recurrence intervals are similar to those on homogeneous faults with comparable averaged normal stress. When  $\lambda$  is much larger than  $L_c$ , slow slip events and partial ruptures occur frequently and the nucleation length of each earthquake depends on the local stress level. We find locations of nucleation and arrest in both low and high normal stress regions (LSR and HSR, respectively) when  $\lambda$  and  $L_c$  are of the same magnitude. When  $\lambda$  is larger than  $L_c$ , earthquakes nucleate in LSRs, and arrest in HSRs. However, HSRs and LSRs switch these roles when  $\lambda$  is smaller than  $L_c$ . Interestingly, we observe that nucleation migrates from an LSR to its neighboring HSR in one earthquake, when  $\lambda$  is between the minimum and maximum local nucleation lengths. We observe a large amount of aseismic slip and associated stress drop in the initial LSR, which might be linked to the migration of foreshocks as documented in natural and laboratory observations. This improved understanding of earthquake nucleation is important in estimating the seismic potential of different fault patches for natural and induced seismicity.

## 3.1 Introduction

Earthquakes are suggested to start with a slow preparation phase instead of as a sudden surprise, as evidenced by natural [Ellsworth and Beroza, 1995; Abercrombie and Mori, 1996; Helmstetter and Sornette, 2003; Kato et al., 2016; Ellsworth and Bulut, 2018] and laboratory observations [Dieterich, 1978; Nielsen et al., 2010; Latour et al., 2013; McLaskey, 2019]. The so-called nucleation phase, which begins long before the dynamic rupture, exhibits diverse slip behaviors such as foreshocks and slow-slip events (SSEs). These possible earthquake precursors recently received a lot of scientific attention due to their link with the timing and magnitude of the coming mainshock [Dieterich, 1978; Wyss, 1991; Sykes et al., 1999; Obara and Kato, 2016; Bedford et al., 2020; Pritchard et al., 2020]. The hope is that they can assist in earthquake early warning and ultimately earthquake prediction. However, reliable field observations have proven difficult and whether - and in which cases - a robust connection to the mainshock exists remains unclear. Laboratory and numerical simulations suggest two end-member nucleation types, the “preslip” model and the “cascade” model. The preslip model describes earthquake nucleation as a slow, continuously accelerating aseismic fault slip that eventually reaches a critical size and transitions to dynamic rupture [Dieterich, 1978; Latour et al., 2013; McLaskey and Kilgore, 2013]. The cascade model suggests that a large earthquake is triggered by a series of small foreshocks, triggering each other [Helmstetter and Sornette, 2003; McLaskey and Lockner, 2014; Wang et al., 2023]. In both models, fault heterogeneity is believed to be essential for generating the diverse spectrum of precursory slip and thus is decisive in earthquake generation.

Fault heterogeneity exists in different perspectives and originates from different sources. It could originate from background physical processes. This includes the variation in material strengths due to different lithologies and their mixtures following geological movements [Ben-Zion and Sammis, 2003; Fagereng and Sibson, 2010; Huang, 2018; Behr and Bürgmann, 2021; Bedford et al., 2022; Arts et al., 2024], a heterogeneous local stress field due to topography, fluid presence and pressure, and the slip of previous earthquakes [King et al., 1994; Kilb et al., 2002; Tabrez et al., 2008; Catalli et al., 2013; Behr and Bürgmann, 2021]. The complex and sometimes random fracture structure is both a consequence of such heterogeneity and an origin of future rupture complexity [Mitchell and Faulkner, 2009; Perrin et al., 2016; Preuss et al., 2019]. Even if a fault is taken as a discrete

surface, heterogeneity on this fault still arises from geometrical roughness as well as the spatial variability in strength and frictional properties [Candela *et al.*, 2012; Yamashita *et al.*, 2018; Gounon *et al.*, 2022; Morad *et al.*, 2022]. Fault geometry and roughness, as a primary result of shear localization, often excise a secondary effect on the heterogeneous strength and friction. Laboratory experiments reveal that earthquake sequences on rough faults contain more irregular rupture events with low repeatability [Yamashita *et al.*, 2018; Morad *et al.*, 2022], and earthquakes can reach supershear rupture speed more readily on rough faults [Xu *et al.*, 2023]. Numerical simulations support these findings. Zielke *et al.* [2017] indicates that smoother faults generate larger earthquakes than rougher faults. Tal *et al.* [2018] shows that roughness introduces local barriers that complicate the nucleation process and increase the nucleation length. Cattania and Segall [2021] relates the temporal and spatial migration of foreshocks and aseismic slips to the fault normal stress distribution. Heimisson [2020] describes how the roughness wavelength influences seismicity statistics and the transition from crack to pulse-like rupture. Similar findings have been obtained on smooth faults with heterogeneous fault friction. Periodic heterogeneous faults are adopted in Gounon *et al.* [2022]’s laboratory experiments and Luo and Liu [2021]’s numerical simulations to generate the full spectrum from partial rupture to full rupture, and from SSEs to earthquakes. Both studies reveal the influence of frictional heterogeneity on slip diversity.

Among the heterogeneous physical variables, effective normal stress receives the most attention due to its anticipated variation and its controlling role in earthquake initiation. Effective normal stress is in most cases heterogeneous due to e.g., fault geometry, roughness, pore pressure variation, and damage zone growth [Duan and Oglesby, 2006; Hillers and Miller, 2007; Huang, 2018; Cattania and Segall, 2021]. Laboratory experiments generate diverse slip spectra by varying effective normal stress [Passelègue *et al.*, 2020]. Models with one single anomaly in effective normal stress can already produce variable slip behaviors: a spectrum of SSEs and earthquakes [Dong *et al.*, 2022], a transition from subshear to supershear rupture [Weng *et al.*, 2015], and a transformation from a seismogenic zone to a rupture barrier [Yang *et al.*, 2012] are generated numerically. Models with heterogeneous normal stress are also used to explain the linear scaling of magnitude and duration for SSEs and its relation to the third-order scaling for large earthquakes [Weng and Ampuero, 2022]. A combination of fault geometry and heterogeneous stresses are used to obtain sequences compa-

rable to natural observations in earthquake sequence models [Tang *et al.*, 2021; Zhang *et al.*, 2022; Taufiqurrahman *et al.*, 2023].

However, an enhanced comprehension of how heterogeneous normal stress systematically affects earthquake nucleation and slip behaviors is missing. One of the reasons is that the normal stress distribution used in numerical models is frequently not in reasonable agreement with natural or laboratory observations (Fig. 3.1c). Many studies for simplicity restrict themselves to a single asperity or two [Yang *et al.*, 2012; Weng *et al.*, 2015; Cebry *et al.*, 2022; Dong *et al.*, 2022], while others use periodic asperities [Luo and Liu, 2021; Gounon *et al.*, 2022]. These studies lack the ability to understand the role of the randomness displayed in observations of normal stress in nature and experiments. Especially the inherent length scale, which might be potentially involved in the nucleation process of earthquakes and aseismic slips, has been ignored [Renard and Candela, 2017; Romanet *et al.*, 2020]. Here, we present a study using generated heterogeneous normal stress fields to understand their impact on earthquake nucleation and recurrence behaviors. We use normal stress fields stochastically generated from Gaussian random distributions with different wavelengths to represent the multi-scale randomness in observations [Renard and Candela, 2017]. We compare the results to a reference homogeneous model to explain how heterogeneity alters the recurrence of earthquakes and aseismic slips, as well as the location and length of the nucleation zones. We use this to develop a conceptual model and discuss how this relation between stress heterogeneity and slip can help with earthquake forecasting using precursory slips.

## 3.2 Methods

### 3.2.1 Numerical model

In this study, we build numerical models inspired by laboratory experiments. These laboratory-scale models will be upscaled for comparison to natural observations in the discussion. We model the planar fault setup in the National Research Institute for Earth Science and Disaster Resilience (NIED, Japan) laboratory (Fig. 3.1) [Yamashita *et al.*, 2018]. The model has two sandstone blocks, one on top of the other, constructing a horizontal fault interface of 2 m long.

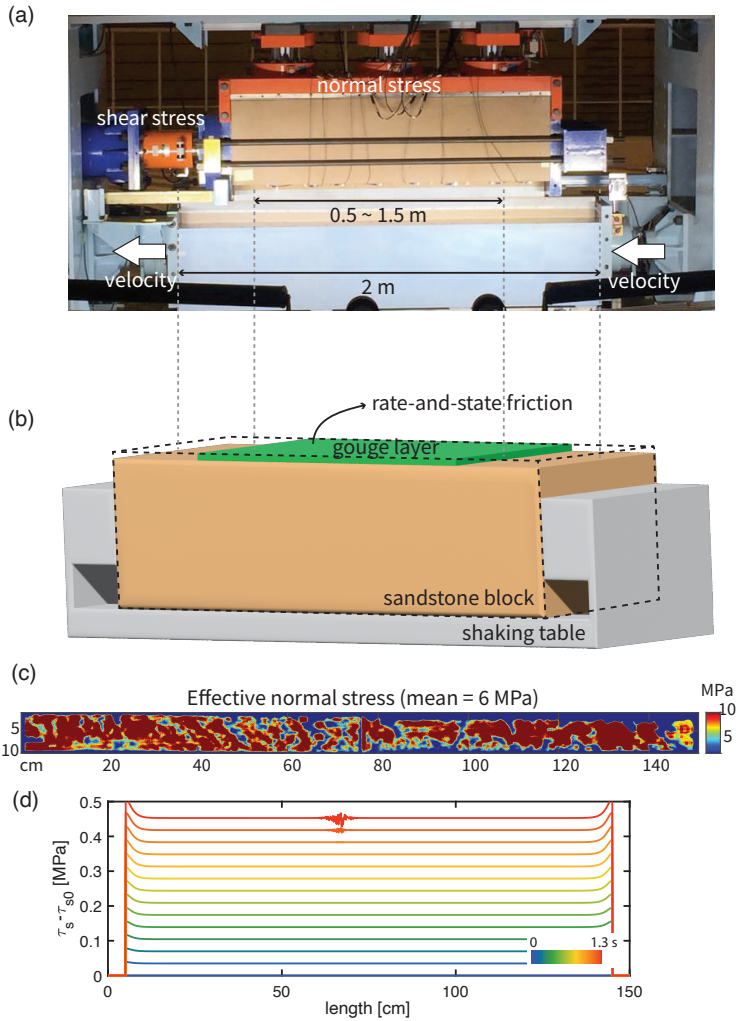


Figure 3.1: **Laboratory experiment and numerical model setup.** (a) The meter-scale fault model in the NIED laboratory in Japan [Ji et al., 2023]. Fine-ground material (gouge) is spread between two sandstone blocks to simulate a gouge layer, with a variable extent between 0.5 and 1.5 m. (b) Numerical model simulating the laboratory experiment. We only model the bottom half of the experimental setup in (a) while taking the system stiffness into account. The dashed framework (black) shows the volume being modeled. The gouge layer is assumed to deform elastically with its infinitely thin surface following rate-and-state friction. (c) An example of normal stress distribution, obtained through a measurement using a pressure sheet at the beginning of the laboratory experiment in (a), with an average normal loading of 6 MPa from the top. The measurement saturates at a maximum of 10 MPa. (d) An example of interseismic shear stress increase on a fault with heterogeneous normal stress, from numerical modeling. Lines showing the difference between current shear stress ( $\tau_s$ ) and the shear stress at a reference time  $t_0$  ( $\tau_{s0}$ ) are color-coded and plotted with an interval of 0.1 s.

The bottom block is mounted to a shaking table, which moves at an assigned velocity. The top block is pushed down from the top using three hydraulic jacks, applying a constant normal force which is measured using serially connected load cells. The top block is held with a metal bar from the left side, which is connected to an unmovable wall. A load cell in-line with the metal bar is used to measure shear stress. Fine-ground material is distributed between the rocks to simulate a gouge layer, which accommodates most of the deformation during fault slip. In the laboratory experiments, the length of the gouge layer is shorter than the rock dimension, with a variable length between 0.5 m and 1.5 m.

We assume elasticity in the rock blocks and ignore the inelastic deformation there. The apparatus, including the shaking table and the hydraulic cylinders, is not modeled explicitly but its configuration is used to specify the boundary conditions. To avoid modeling of the spreading plastic deformation throughout the gouge layer, we separate plastic and elastic strains into different locations. Plastic deformation is only assumed on an infinitely thin horizontal plane at the center of the gouge layer and is assumed to follow a rate-and-state friction formulation [*Dieterich, 1979; Ruina, 1983*]. The remainder of the gouge layer is assumed to deform elastically, the same as the rock blocks, albeit with a different density and elastic modulus. This assumption allows us to change the gouge thickness easily and model the laboratory experiments with and without a gouge layer in the same way. The regions outside of the gouge extent are filled with air, whose low elastic modulus approximates a free surface at the ends of the gouge. The interseismic shear stress increase on the gouge layer is close to uniform, which precludes the impact of heterogeneous loading in our study (Fig 3.1d).

To improve computational efficiency without losing characteristic features, we introduce additional symmetry to the laboratory setup respective to the fault plane and simulate only the bottom half numerically (as shown in Fig. 3.1b). Due to the introduced symmetry and the resulting anti-symmetry of fault-parallel motion, the motion at the fault is taken to be relative to a fictitious oppositely moving domain that is not modeled. In this way, the top boundary of the numerical model is regulated by rate-and-state friction. The front and back boundaries are free of normal and shear stress. The left, right, and bottom boundaries are the shaking table and are thus prescribed to move at the same constant loading velocity.

The initial conditions are chosen to allow the fault to slip at the imposed ini-



tial velocity  $V_i$  in a steady state manner before the experiment. We then switch to a new loading velocity  $V_p$  at  $t = 0$ , following the procedure of velocity-step experiments in the laboratory.

### 3.2.2 Physical equations and length scales

We use the code library *Garnet* [Pranger, 2020], which has been validated in a series of benchmark problems regarding seismic and aseismic slips, developed by the Statewide California Earthquake Center [Jiang et al., 2022; Li et al., 2022; Erickson et al., 2023]. Benefiting from the fact that *Garnet* allows users to formulate problems in a largely dimension-independent way, we establish our numerical model in both 2D and 3D to balance efficiency and details. Given the narrow width of the fault compared to its length, our 2D and 3D results do not show distinct deviations. We present results from both models and direct the readers to our work summarizing the characteristics of modeling outputs at different dimensions from 0D to 3D [Li et al., 2022]. We solve the momentum conservation equation inside the bottom rock and the gouge in a quasi-dynamic fashion, thus ignoring inertia [Rice, 1993]

$$\nabla \cdot \boldsymbol{\sigma} = 0, \quad (3.1)$$

where  $\boldsymbol{\sigma}$  is the Cauchy stress tensor. This equation solves the stress field inside the medium with a given set of boundary conditions. The elastic constitutive equation relates stress rate  $\dot{\boldsymbol{\sigma}}$  to strain rate  $\dot{\boldsymbol{\epsilon}}$  by

$$\dot{\boldsymbol{\sigma}} = 2G\dot{\boldsymbol{\epsilon}} + \lambda \text{Tr}(\dot{\boldsymbol{\epsilon}})\mathbf{I} \quad (3.2)$$

with bulk modulus  $K$ , shear modulus  $G$ , Lamé's constant  $\lambda = K - 2G/3$  and  $\mathbf{I}$  identity tensor. Poisson's ratio is defined as  $\nu = \lambda/(2\lambda + 2G)$ . The rock and gouge samples used in the experiments were taken from a borehole drilled into the Groningen gas reservoir in the Netherlands. We take their mechanical parameters from the seismological studies of the same region [Lele et al., 2015] (Table 3.1).  $\text{Tr}(\dot{\boldsymbol{\epsilon}}) = \dot{\epsilon}_{kk}$  is volumetric strain rate. We assume infinitesimal strain rate  $\dot{\boldsymbol{\epsilon}}$  defined as

$$\dot{\boldsymbol{\epsilon}} = \frac{1}{2} (\nabla \boldsymbol{v} + \boldsymbol{v} \nabla), \quad (3.3)$$

where  $\boldsymbol{v}$  is the velocity vector. The deformation inside the medium is obtained by solving the three equations together.

The infinitely thin plane at the center of the gouge layer, featuring the fault, is assumed to follow the rate-and-state friction formulation [Dieterich, 1979; Ruina, 1983]. We use the regularized version as proposed by Rice and Ben-Zion [1996] and Ben-Zion and Rice [1997]

$$\tau_s = a\sigma_n \operatorname{arcsinh} \left\{ \frac{V}{2V_0} \exp \left[ \frac{\mu_0}{a} + \frac{b}{a} \ln \left( \frac{\theta V_0}{D_{RS}} \right) \right] \right\} + \eta V \quad (3.4)$$

where  $\tau_s$  and  $\sigma_n$  are the shear and normal stress on the fault,  $V$  the slip rate and  $\theta$  the state variable. The reference friction coefficient  $\mu_0$  at the reference slip rate  $V_0$ , the characteristic slip distance  $D_{RS}$ , and the parameters  $a$  and  $b$  that control the relative influence of direct and evolutionary effects are also used in the expression. We take these frictional parameters from the laboratory experiments using the same rock sample [Hunfeld *et al.*, 2017] (Table 3.1). In the quasi-dynamic approximation, the radiation damping term  $\eta V$  is used to account for the wave-radiated energy loss [Rice, 1993], which aims to reduce computational costs. The damping viscosity  $\eta = G/(2c_s)$  is equal to half the shear impedance of the rock. Friction on the fault weakens as a function of slip velocity, i.e., “velocity-weakening” (VW), when  $a - b < 0$ , and strengthens with slip velocity, i.e., “velocity-strengthening” (VS), when  $a - b > 0$ . In this study, we only consider VW faults and adopt homogeneous friction parameters following the laboratory experiments. We use the aging description of the state variable [Ruina, 1983]

$$\dot{\theta} = 1 - \frac{V\theta}{L}. \quad (3.5)$$

The slip rate  $V$  is equal to the difference of the material velocity  $\mathbf{v}$  at two sides of the fault, thus they are related by

$$\hat{\mathbf{t}}V = [\mathbf{v} - \mathbf{v} \cdot \hat{\mathbf{n}}]_{\Gamma^+} - [\mathbf{v} - \mathbf{v} \cdot \hat{\mathbf{n}}]_{\Gamma^-} \quad (3.6)$$

where  $\hat{\mathbf{n}}$  is the unit fault normal,  $\hat{\mathbf{t}}$  is the unit fault tangent in the direction of the slip rate. Subscripts  $\Gamma^+$  and  $\Gamma^-$  refer to the two sides of the fault. Assuming symmetry, this boundary condition is simplified to

$$\hat{\mathbf{t}}V/2 = [\mathbf{v} - \mathbf{v} \cdot \hat{\mathbf{n}}]_{\Gamma^+}. \quad (3.7)$$

The fault stress  $\tau_s$  and  $\sigma_n$  are equal to the projection of the stress field  $\boldsymbol{\sigma}$  at the fault plane, thus they are related by

$$\begin{aligned} \sigma_n &= -[\hat{\mathbf{n}} \cdot \boldsymbol{\sigma} \cdot \hat{\mathbf{n}}]_{\Gamma^+} \\ \tau_s &= [\hat{\mathbf{t}} \cdot \boldsymbol{\sigma} \cdot \hat{\mathbf{n}}]_{\Gamma^+}. \end{aligned} \quad (3.8)$$

The first equation has a negative sign because we adopt positive compressive normal stress convention.

Spatial and temporal resolutions must be guaranteed to obtain accurate and reliable results. We choose a spatial discretization that resolves the minimum nucleation length  $L_b$  (also called the cohesive length)

$$L_b = \frac{GD_{RS}}{b\sigma_n(1-\nu)} \quad (3.9)$$

with  $\sim 10$ -1000 grid cells [Lapusta *et al.*, 2000; Rubín and Ampuero, 2005]. At the same time, we use adaptive time stepping to restrict the time step size. By using a time step size that is inversely proportional to the maximum slip rate  $V_{\max}$  [Lapusta *et al.*, 2000], the computational cost in the interseismic phase is reduced, i.e.,

$$\Delta t = \zeta \frac{D_{RS}}{V_{\max}} \quad (3.10)$$

where  $\zeta$  is a factor controlled by the material and frictional parameters as defined and derived in Lapusta *et al.* [2000].

Following energy balance, a critical size of an aseismic slip region needs to be reached before dynamic slip begins, which is the so-called nucleation length [Rubín and Ampuero, 2005]

$$L_c = \frac{bGD_{RS}}{\pi(b-a)^2\sigma_n(1-\nu)}. \quad (3.11)$$

This classical definition assumes a circular nucleation zone and calculates its radius (half-width). It is more convenient to use the full width of the nucleation zone  $2L_c$  in this study. Both  $L_b$  and  $L_c$  have been calculated based on the assumption of a planar homogeneous fault. However, we can take them as a point-wise function and extend their applicability to heterogeneous faults. When the normal stress or the frictional parameters are variable on the fault, both length scales become a spatially variable function. The actual nucleation length is no longer obtained from the analytical solutions shown above but must be calculated with spatial convolution. A combined model of both analytical and numerical approaches is developed by Lebihain *et al.* [2021] using linear slip-weakening friction to understand the homogenized instability behavior on faults with heterogeneous weakening rates. However, such calculations are challenging to implement theoretically with rate-and-state friction. Recent analytical works

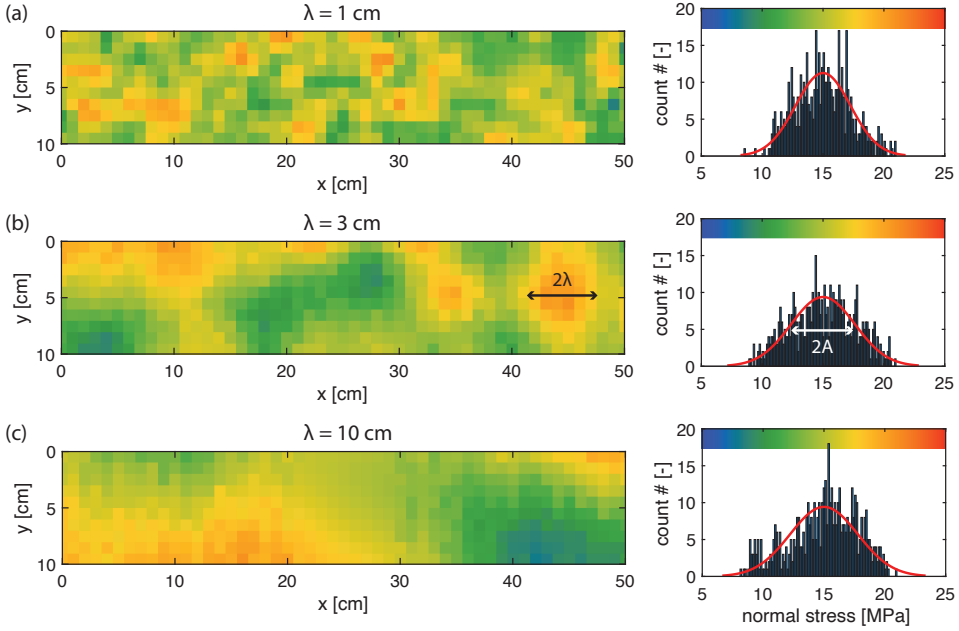


Figure 3.2: *Stochastic normal stress field examples.* (a) Stochastically generated normal stress field realization ( $\bar{\sigma}_n = 15$  MPa,  $A = 2$  MPa,  $\lambda = 1$  cm) (left) with the corresponding probability distribution (right). (b) Same as (a) but with  $\lambda = 3$  cm. (c) Same as (a) but with  $\lambda = 10$  cm. Note that when  $\lambda$  is in the same order as the domain dimension or larger, the probability distribution of the generated realization may strongly deviate from the applied Gaussian distribution.

by [Ray and Viesca \[2017\]](#) using sinusoidal heterogeneities claimed that heterogeneous properties shall lead to a finite number of candidates for nucleation: maxima, minima, and between them, but whether these candidates will become preferred nucleation locations or not will be determined by the specific heterogeneous distribution. Hence, we aim to clarify the nucleation and slip behavior on heterogeneous faults from a purely numerical perspective. We still use the formula of  $L_c$  (Eq. 3.11) as a first-order approximation to the local nucleation length  $L_c^{loc}$  to compare our results with, with its deviation from the actual nucleation length acknowledged. If the average normal stress on the heterogeneous fault is  $\bar{\sigma}_n$ , the average nucleation length is approximated by the nucleation length on a homogeneous fault with uniform normal stress  $\bar{\sigma}_n$  as

$$L_c^{homo} = \frac{bGD_{RS}}{\pi(b-a)^2\bar{\sigma}_n(1-\nu)}. \quad (3.12)$$

### 3.2.3 Stochastic stress generation

We define the normal stress heterogeneity in a stochastic way. We generate random normal stress distributions with an isotropic stationary Gaussian-type probability density function

$$p(\sigma_n) = \frac{1}{\sqrt{(2\pi)^d A^2}} \exp \left[ -\frac{1}{2} \left( \frac{\sigma_n - \bar{\sigma}_n}{A} \right)^2 \right] \quad (3.13)$$

where  $\bar{\sigma}_n$  is the mean normal stress,  $A$  is the standard deviation.  $d$  is the dimension of the fault surface, e.g.,  $d = 2$  for a 2D fault in a 3D model. To generate a spatial distribution requires defining a spatial correlation function, which we also assume isotropic and stationary and follow

$$\text{cor}(r) = \exp \left[ -\frac{\pi}{4} \left( \frac{r}{\lambda} \right)^2 \right] \quad (3.14)$$

where  $r = |\mathbf{x}_1 - \mathbf{x}_2|$  is the distance between two arbitrary locations  $\mathbf{x}_1$  and  $\mathbf{x}_2$ ,  $\lambda$  is the correlation length. We only consider the isotropic case where  $\lambda$  is a scalar. When  $\lambda = 0$ , there is no correlation between the normal stress states at any two spatial locations. This random field is extremely heterogeneous and is also called “white noise”. When  $\lambda \rightarrow \infty$ , the correlation function obtains a constant value of one independent of  $r$ . In this case, the random field is completely homogeneous. We therefore use  $A$  and  $\lambda$  as the amplitude and the wavelength of the normal stress field, respectively. A higher  $A$  and/or a smaller  $\lambda$  indicate a more heterogeneous stress field.

Figure 3.2 shows several generated realizations with the same amplitude  $A$  and increasing wavelength  $\lambda$ . The size of generated asperities increases with increasing  $\lambda$ . When the domain size is much larger than  $\lambda$ , every generated realization approximates the applied Gaussian probabilistic density function (Eq. 3.13) (Fig 3.2a, b). In particular, the generated stress field resembles white noise when the correlation size is equal to or below the grid size (Fig 3.2a). However, when  $\lambda$  is in the same order as the domain size or larger, the probability distribution of the generated realization may strongly deviate from the applied Gaussian distribution, despite that the collective of all realizations still approximates the same Gaussian distribution (Fig 3.2c). For this reason, we only look at the collective behavior of a large number of realizations when we investigate the long-term earthquake recurrence behavior. To find robust features in the nucleation process, we require the heterogeneity wavelength to be much smaller

than the domain size to allow enough asperities on the simulated fault. Large-scale heterogeneities that are mostly accounted for by large-scale mechanics, such as overburden gravity, tectonic folding and bending, and stress perturbation due to large seismic slips, are out of the scope of this study. They are better measured and studied in a deterministic fashion [Yang *et al.*, 2012; Michel *et al.*, 2021; Taufiqurrahman *et al.*, 2023].

Physical and numerical parameters used in this work are summarized in Table 3.1. The mechanical parameters are taken from the laboratory experiments using the same sandstone sample [Hunfeld *et al.*, 2017]. The frictional and statistical parameters are based on the laboratory measurements [Ji *et al.*, 2023] but extended to a broader range to investigate the multi-scale randomness of fault heterogeneity.

### 3.3 Results and Analysis

We study how earthquake nucleation and slip behavior are affected by normal stress heterogeneity characterized by different wavelengths (Fig 3.3). This is realized by using the same mean stress  $\bar{\sigma}_n$  and standard deviation  $A$  in the Gaussian probabilistic density function (Eq. 3.13), while changing the correlation length  $\lambda$  in the spatial correlation function (Eq. 3.14). We identified five regimes of earthquake nucleation behaviors controlled by the ratio of the heterogeneity wavelength and the nucleation length. We first introduce two end-member cases with extremely short or extremely long wavelengths ( $\lambda$ ) compared to the nucleation length ( $L_c$ ). In the former case, the normal stress field is extremely heterogeneous but the nucleation process depends on the homogenized fault properties at length scale  $2L_c$ . In the latter case, nucleation is dependent on the local fault properties. We call these “homogenized” and “localized” nucleation regimes, respectively. We then identify three regimes between the end-member cases, when the heterogeneity wavelength is comparable to the nucleation length. In these cases, regions with low effective normal stress (LSR) and regions with high effective normal stress (HSR) are preferred nucleation locations. Note that the LSR and HSR used here are not strictly defined terms, but rather used to refer to the local minima/maxima and their vicinity in the effective normal stress profile. Roughly speaking, they concern a region with a radius

Table 3.1: *Physical and numerical parameters*

| Parameter                            | Symbol     | Value                   |
|--------------------------------------|------------|-------------------------|
| Sandstone                            |            |                         |
| Density                              | $\rho_r$   | 2.450 g/cm <sup>3</sup> |
| Poisson ratio                        | $\nu_r$    | 0.16                    |
| Young's modulus                      | $E_r$      | 20.51 GPa               |
| Width                                | $W$        | 10 cm                   |
| Length                               | $L$        | 200 cm                  |
| Height                               | $H$        | 50 cm                   |
| Gouge                                |            |                         |
| Density                              | $\rho_g$   | 2.000 g/cm <sup>3</sup> |
| Poisson ratio                        | $\nu_g$    | 0.16                    |
| Young's modulus                      | $E_g$      | 4 GPa                   |
| Width                                | $w$        | 10 cm                   |
| Length                               | $l$        | 40 or 140 cm            |
| Height                               | $h$        | 0.5 cm                  |
| Normal stress: Gaussian random field |            |                         |
| mean                                 | $\sigma_n$ | 15 MPa                  |
| standard variance                    | $A$        | 2, 4, or 8 MPa          |
| correlation length                   | $\lambda$  | 0.3-100 cm              |
| Reference friction coefficient       | $\mu_0$    | 0.671                   |
| Reference slip rate                  | $V_0$      | 10 <sup>-4</sup> m/s    |
| Characteristic slip distance         | $D_{RS}$   | 0.1-100 $\mu$ m         |
| Rate-and-state direct effect         | $a$        | 0.0024                  |
| Rate-and-state evolution effect      | $b$        | 0.0047                  |
| Loading rate $t < 0$                 | $V_i$      | 10 <sup>-4</sup> m/s    |
| Loading rate $t \geq 0$              | $V_p$      | 10 <sup>-5</sup> m/s    |

<sup>a</sup> Entries with multiple values are specified in the corresponding figure captions.

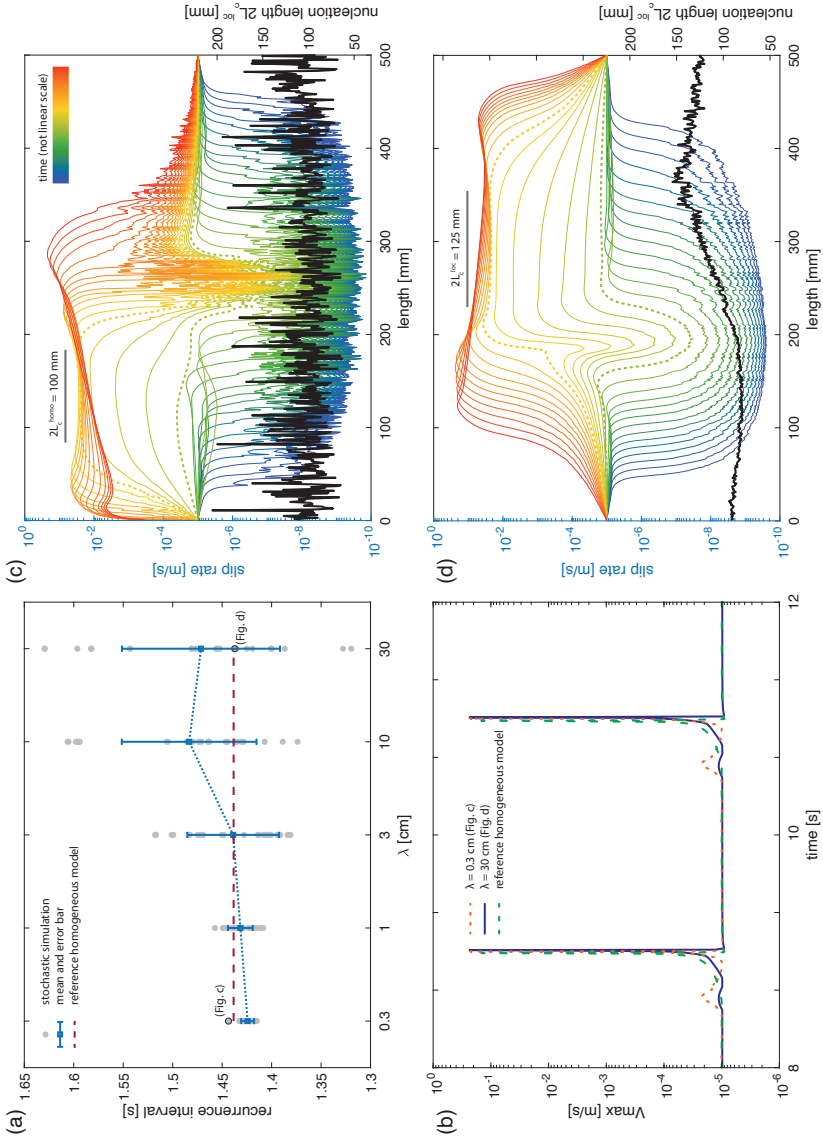


Figure 3.3: (Caption next page.)



Figure 3.3: (Previous page.) **Earthquake sequence characteristics for variable wavelengths of normal stress heterogeneity.** (a) Simulated recurrence intervals from models with heterogeneity wavelengths  $\lambda$  between 0.3 and 30 cm. At each wavelength, we generated 32 realizations stochastically (gray dots). The realizations shown in (c) and (d) are highlighted with black rims. The mean and standard deviation of these realizations are labeled in blue. The recurrence interval measured from a reference model with homogeneous normal stress equal to the average normal stress  $\bar{\sigma}_n$  is shown in red. (b) A representative earthquake sequence of two heterogeneous models with  $\lambda = 0.3$  cm and 30 cm. An earthquake sequence in the homogeneous model is shown for reference. (c, d) The nucleation process of the first earthquake in the two heterogeneous models as shown in (a), respectively. The interseismic and nucleation phases are plotted in blue and yellow, with a gradual transition to the coseismic phase in red. The start and end of the nucleation phase are highlighted with dotted lines. The plotted lines are not in regular time intervals. The black line shows the theoretically calculated nucleation length  $2L_c^{loc}$  (Eq. 3.11). The gray bars indicate the nucleation length at the center of the nucleation zone.

of  $\lambda$ , or a width of  $2\lambda$  (Fig 3.2b). Therefore, the ratio of  $2L_c$  and  $2\lambda$  becomes decisive in determining the location of nucleation. Depending on  $\lambda/L_c$ , nucleation either prefers LSRs or HSRs, or migrates from the former to the latter in a single earthquake. We call these “LSR-preferred”, “HSR-preferred” and “migratory” nucleation regimes.

### 3.3.1 Two end-member cases: $\lambda \ll L_c$ and $\lambda \gg L_c$

#### $\lambda \ll L_c$ : homogenized nucleation regime

We first focus on the recurrence of earthquakes and aseismic slips in a sequence when the fault normal stress is extremely heterogeneous. We elaborate on a scenario where the average nucleation length  $2L_c^{homo}$  is about 10 cm, using the analytical solution of Eq. 3.12. For a fault of 50 cm in length, this allows us to observe characteristic repeating earthquakes. Earthquakes nucleate close to the center of the fault and rupture the whole fault. We increase the wavelength from 0.3 cm to 30 cm and measure the recurrence interval of the characteristic earthquakes under these conditions (Fig 3.3a). To obtain reasonable statistics, we generate 32 stochastic stress realizations at each wavelength. When the wavelength is much smaller than the nucleation length (e.g.,  $\lambda = 0.3$  cm), all the randomly generated scenarios simulate nearly identical characteristic earthquake sequences. Sequences exhibit almost identical recurrence intervals, nucleation

lengths, and magnitudes. Their recurrence interval also resembles what is measured in a reference model with homogeneous normal stress equal to the average normal stress used in the stochastic generation (Fig 3.3b). Increasing the wavelength introduces fluctuations in the measured recurrence intervals for different realizations, which is reflected by the increase in the standard deviation of the ensemble. The mean value also shows a subtle increase, which remains within a few percent from the reference homogeneous model.

We analyze the two end-member cases of  $\lambda = 0.3$  cm and 30 cm further (as labeled in Fig 3.3a) and plot the earthquake sequence of one representative realization in each case (Fig 3.3b). For robust comparison, we select the realization with the average recurrence interval closest to the reference homogeneous model. The same maximum slip rate is achieved in the coseismic phase, but differences appear in the aseismic slip during the nucleation phase (Fig 3.3c, d). A smooth and steady acceleration of slip rate before the coseismic phase is observed in the homogeneous model. However, it is replaced with a small secondary peak and a subsequently sharper acceleration in the heterogeneous models. The secondary peak can be either an aseismic event or part of the nucleation process. This peak has a higher magnitude in more heterogeneous cases and reflects the minor failures taking place at local asperities (Fig 3.3c).

#### $\lambda \gg L_c$ : localized nucleation regime

Comparison of the nucleation process reveals more differences in the two end-member cases (Fig 3.3c, d). When the heterogeneity wavelength is much smaller than the nucleation length, the nucleation requires the activation of a collection of asperities before an instability can occur (Fig 3.3c). This condition is satisfied at the theoretical length scale  $2L_c^{homo}$  calculated with the average normal stress. In this case, the effective fault properties are the homogenized fault properties at the length scale of  $2L_c^{homo}$ , which are essentially homogeneous. This explains why the earthquake sequences and the recurrence intervals observed in each realization are highly identical and close to the reference homogeneous model. Nevertheless, the minor failures indicated by secondary slip rate peaks demonstrate the impact of the asperities. When the wavelength increases, fewer asperities need to be activated to satisfy the nucleation length. In this case, the homogenization at length scale  $2L_c^{homo}$  becomes less effective, thus the variation within the stochastic ensemble is amplified (Fig 3.3a). Simulated earthquakes still show a regular recurrence for each random normal stress realization (Fig

3.3b), because the earthquakes nucleate from the same location close to the center of the fault and rupture the whole fault (Fig 3.3d). However, each realization in the ensemble has a different nucleation location and a slightly different actual nucleation length  $2L_c$ . They hence have varying recurrence interval. If the wavelength is increased further to become comparable to or larger than  $2L_c^{homo}$ , the homogenized nucleation length will finally approach the value determined by the local stress level  $2L_c^{loc}$  (Fig 3.3d).

Figure 3.3 only shows characteristic earthquake sequences due to the restricted fault length. We therefore extend the fault length and reduce the nucleation length to study the influence of heterogeneity wavelength when the slip behavior is more than periodic full ruptures (Fig 3.4). When the heterogeneity wavelength is much larger than the nucleation length, earthquakes can nucleate at any location. In this end-member case, nucleation completes in a single asperity. Slow slips and partial ruptures become prevalent. At the beginning of the simulation, regions with low effective normal stress (LSR) reach their yield point first. Therefore the first earthquake takes place at the location of the minimum normal stress and the following earthquakes at the locations of other local minima (Fig 3.4a, events #1 and #2). The high stress regions (HSR) remain locked until they are activated later (event #3). After this “warm-up” period, the earthquake sequence becomes quasi-periodic. A number of partial earthquakes, each rupturing a fault portion, form a “supercycle” (similar as simulated in *Barbot [2019]*). Generally, the earthquakes occurring at HSRs reach higher slip rates, compared to those occurring at LSRs. At some LSRs, slow slips gradually replace normal earthquakes (e.g., locations of events #1 and #2). As aforementioned, the actual nucleation length is essentially equal to  $2L_c^{loc}$ , controlled by the local normal stress level. Earthquakes with nucleation in HSRs (Fig 3.4b, event #3) thus have a shorter nucleation length than those in LSRs (events #1 and #2).

### 3.3.2 Nucleation location altered by heterogeneity when $\lambda \sim L_c$

#### $\lambda \gtrsim L_c$ : LSR-preferred nucleation regime

Earthquake nucleation location and the associated slip behavior exhibit more complexity when the nucleation length and the wavelength of the stress heterogeneity are around the same magnitude. To vary  $\lambda/L_c$ , we modify the nucleation

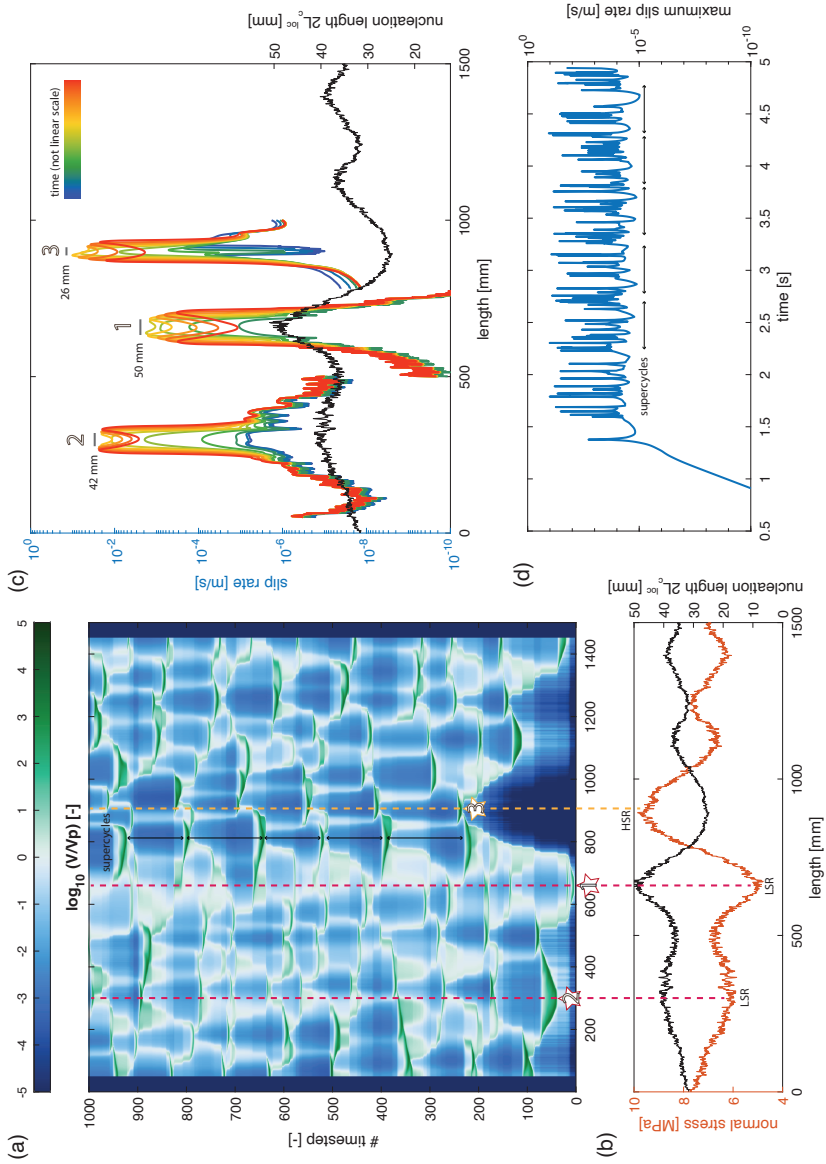


Figure 3.4: (Caption next page.)

Figure 3.4: (Previous page.) *Earthquake sequence under localized nucleation regime* ( $\lambda \gg L_c$ ). (a) Simulated earthquake sequence with nucleation length much smaller than the heterogeneity wavelength ( $\lambda = 100$  mm). Colors indicate the relative magnitude of slip rate  $V$  over loading rate  $V_p$ . For better visualization, it is plotted at a fixed time step interval instead of a fixed time interval. A “supercycle” of partial earthquakes is indicated with black arrows. (b) The normal stress distribution along the fault (left, orange) and the corresponding theoretical nucleation length  $2L_c^{loc}$  (right, black). Three earthquakes shown in (c) are denoted with stars. Dashed lines highlight their relation to local minima and maxima of the normal stress, referred to as low stress regions (LSRs) and high stress regions (HSRs). (c) The nucleation processes of the three earthquakes denoted in (a). The interseismic and nucleation phases are plotted in blue and yellow, with a gradual transition to the coseismic phase in red. The plotted lines are not in regular time intervals. The three sets of lines are independent, and we have only plotted a fault portion for each event. The black line shows the theoretically calculated nucleation length  $2L_c^{loc}$ . The gray bars indicate the nucleation lengths  $2L_c^{loc}$  at the center of each nucleation zone. (d) Time series of the maximum slip rate. The “supercycle” shown in (a) is indicated with black arrows.

length by modifying the elastic modulus and the rate-and-state frictional parameters, while keeping the normal stress fixed (Fig 3.5). When the heterogeneity wavelength is larger than the maximum nucleation length on the fault, the nucleation process could be completed in any single asperity (Fig 3.5a). Since LSRs are weaker than HSRs, earthquakes usually nucleate at the locations of local normal stress minima (locations A, C, E), starting from the global minimum. After failure at one location, its surrounding regions start to slip aseismically and this slipping region expands until the required nucleation length is achieved (e.g., location E in event #1). At this point, slip accelerates to rates above the seismic rate ( $V_{seis} = a\sigma_n/\eta \approx 0.037$  m/s as defined in *Rubin and Ampuero [2005]*) and propagates outwards. Its closest neighboring HSRs function as barriers to arrest the earthquake (location B in event #4). Alternatively, an HSR can be activated by the rupture and coalesce into a larger event (locations B and D in event #3). Even if that is not achieved, the activated HSR starts to slip and will accommodate the nucleation of the next event (location F in event #2).

#### $L_c(HSR) < \lambda < L_c(LSR)$ : migratory nucleation regime

When the heterogeneity wavelength becomes shorter than the local nucleation length, nucleation cannot be completed within a single LSR (Fig 3.5c). For a direct comparison with the case above, we keep using the same normal stress distribution. To vary  $\lambda/L_c$ , we increase the frictional parameter  $D_{RS}$  to increase the nucleation length instead. Since the theoretical nucleation length is inversely

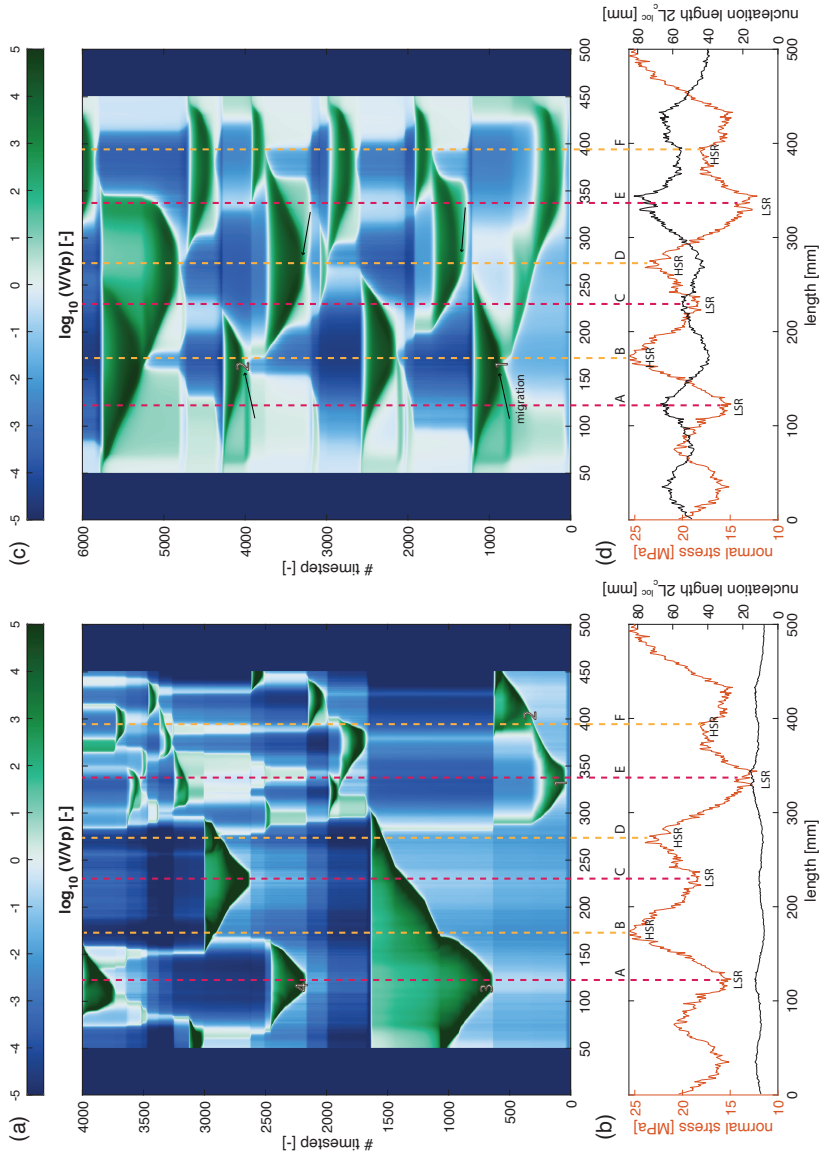


Figure 3.5: (Caption next page.)

Figure 3.5: (Previous page.) **Earthquake sequences under LSR-preferred ( $\lambda \gtrsim L_c$ ) and migratory nucleation regime ( $L_c(\text{HSR}) < \lambda < L_c(\text{LSR})$ ).** (a) Simulated earthquake sequence with nucleation length smaller than the heterogeneity wavelength ( $\lambda = 3$  cm). Colors indicate slip rate  $V$  normalized by loading rate  $V_p$ . For better visualization, it is plotted at a fixed time step interval instead of a fixed time interval. (b) The normal stress distribution along the fault (left, orange) and the corresponding theoretical nucleation length  $2L_c^{\text{loc}}$  (right, black). Dashed lines highlight several LSRs (purple) and HSRs (yellow). (c) Simulated earthquake sequence with nucleation length comparable to the heterogeneity wavelength. The same normal stress field as (a) is used ( $\lambda = 3$  cm). We have changed the value of the rate-and-state frictional parameter  $D_{RS}$  in (a) to five times larger to increase the nucleation length. The heterogeneity wavelength is between the nucleation lengths of HSRs and LSRs. The migratory nucleation locations are indicated by arrows. (d) Same as (b).

proportional to the normal stress (Eq. 3.11), shorter nucleation lengths should be expected in HSRs. Therefore it is possible that nucleation can still be completed within a single HSR, when the nucleation length there is shorter than the heterogeneity wavelength. In this case, LSRs are still activated to slip first (e.g., locations A and E), but a complete nucleation process is not observed. The surrounding regions start to slip as before, but the nucleation center moves away as the activated regions expand (from location A to B in events #1 and #2). A complete nucleation process is finally realized in the neighboring HSR instead. During the whole process, the slip rate in the LSR first increases above the loading rate and then decreases, and finally increases again when the rupture front arrives (location B in event #1). In this scenario, in contrast to expectations, earthquake nucleation is almost always observed in HSRs. While most of the time LSRs coalesce into the event (location A in event #1 and #2, as also can be seen in Fig 3.6a), sometimes an LSR can function as a barrier to arrest the event and then accommodate the initial slipping of the following event (location C in event #2).

The migration of nucleation locations has consequences for the stress drop and slip accumulation patterns (Fig 3.6). During the initial nucleation phase, which takes less than 2 s to complete, slip rate increases to around 100 times the loading rate in the activated LSR (location A, Fig 3.6a). The nucleation length of  $\sim 65$  mm follows the theoretical prediction  $2L_c^{\text{loc}}$  at this location. The friction coefficient (the ratio between shear stress and effective normal stress) decreases from 0.678 to 0.666, which is equivalent to a stress drop of 0.19 MPa for the average normal stress of 16 MPa at this location (Fig 3.6b). The maximum accumulated aseismic slip is about 0.2 mm (Fig 3.6c). The nucleation location then migrates

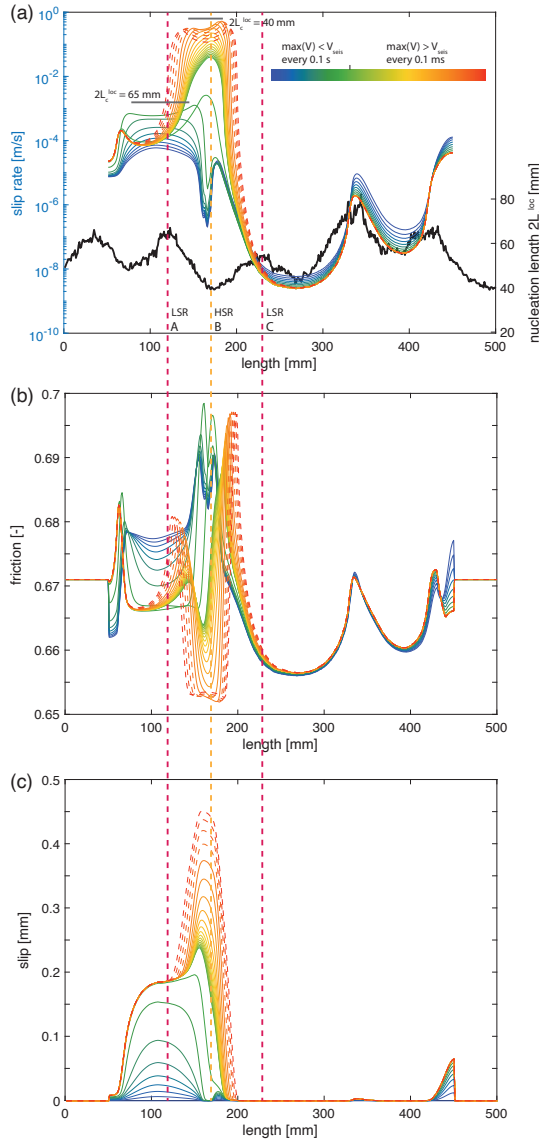


Figure 3.6: **Earthquake nucleation with migrated location** ( $L_c(HSR) < \lambda < L_c(LSR)$ ). (a) The nucleation processes of earthquake #2 in Fig 3.5c. The interseismic and nucleation phases are plotted in blue and green, with a gradual transition to the coseismic phase in red. The coseismic phase is plotted using dashed lines. The evolution with the maximum slip rate below the seismic rate  $V_{seis}$  is plotted every 0.1 s, the evolution above  $V_{seis}$  is plotted every 0.1 ms. The black line shows the theoretically calculated nucleation length  $2L_c^{loc}$ . The gray bars indicate the nucleation lengths  $2L_c^{loc}$  at locations A and B. The labels “A”, “B” and “C” refer to the same locations as in Fig 3.5. (b, c) The evolution of (b) frictional coefficient and (c) slip for the same earthquake. The same color scale applies.



to the neighboring HSR (location B) with a sharp increase in slip rate to beyond the seismic threshold. It takes about 0.2 s (10% time compared to the initial nucleation at the LSR) to complete the nucleation, with a nucleation length of  $\sim 40$  mm, same as the theoretical prediction  $2L_c^{loc}$  at this location. During this period, the friction coefficient drops further to 0.652. This is equivalent to an additional stress drop of 0.35 MPa using the average normal stress of 25 MPa at this location. This HSR did not slip in the initial nucleation phase. About 0.25 mm aseismic slip and 0.2 mm seismic slip are accumulated during the secondary nucleation (location B, Fig 3.6b, c). That means, different from non-migratory nucleation, the initial nucleation at the LSR produces about one-third of the total stress drop and half of the total slip. We will discuss later whether such large portions of aseismic slip could potentially be linked to observable precursory signals. The final nucleation at the HSR is followed by double-sided rupture propagation (dashed lines in Fig 3.6). The leftward-traveling rupture increases the slip rate of the already unlocked LSR to above the seismic threshold and is arrested at the left boundary. The rightward-traveling rupture is arrested at the neighboring LSR (location C, can be seen in Fig 3.5c).

#### $\lambda \lesssim L_c$ : HSR-preferred nucleation regime

When the heterogeneity wavelength is shorter than the minimum nucleation length, the nucleation cannot be completed in any single asperity (Fig 3.7). In this case, nucleation is observed to start in HSRs (locations B and D). Even in these regions, the nucleation process has to extend to the surrounding regions to satisfy the nucleation length. The consequent earthquakes often have lower slip rates compared to simulations with smaller nucleation lengths (Fig 3.5). Some of them are even close to slow slip events. LSRs sometimes coalesce into the nucleation or rupture process, as they did in the migratory regime (location C), while at other times they function as a barrier to arrest ruptures (location E). In the latter case, the LSR is barely re-locked during the interseismic phase and remains slipping at around the loading rate. Note that here the terms HSRs and LSRs are rather used to refer to the absolute normal stress levels at these locations, instead of referring to the local minima or maxima. For example, location F is a local maximum but aseismic slips are predominantly observed. This is because this location and its surroundings actually have low stress and are thus barely locked.

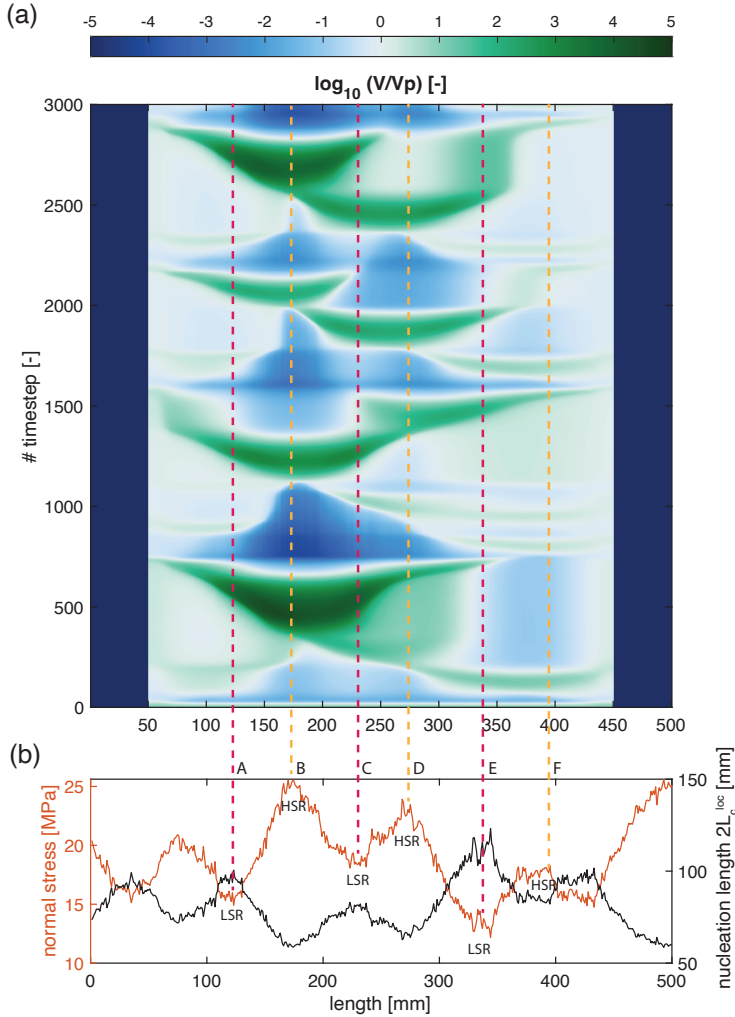


Figure 3.7: *Earthquake sequences in the HSR-preferred nucleation regime ( $\lambda \lesssim L_c$ ).* (a) Simulated earthquake sequence with nucleation length larger than the heterogeneity wavelength ( $\lambda = 3$  cm). Colors indicate slip rate  $V$  normalized by loading rate  $V_p$ . For better visualization, it is plotted at a fixed time step interval instead of a fixed time interval. (b) The normal stress distribution along the fault (left, orange) and the corresponding theoretical nucleation length  $2L_c^{loc}$  (right, black). Dashed lines highlight several LSRs (purple) and HSRs (yellow).

## 3.4 Discussion

### 3.4.1 The role of normal stress heterogeneity in earthquake nucleation

#### Switching of the locations of nucleation and arrest

Earthquake slip is controlled by the stress and strength on the fault. Classical studies use a “Coulomb criterion” to define strength, which is the stress level where the fault fails, while using a “slip-weakening friction formulation” to define how the fault weakens after failure. Using the rate-and-state friction formulation, which provides a unified expression of the two concepts, we studied how the nucleation process is altered by a spatially heterogeneous distribution of effective normal stress. In this formulation, both stress and strength are dependent on the slip rate. On the one hand, strength is proportional to normal stress  $\sigma'_n$ , so that increasing normal stress moves the fault away from failure. On the other hand,  $(b - a)\sigma'_n$  defines the stress drop and thus the frictional energy. Increasing normal stress thus also promotes instabilities instead of stable slips after failure. This consequence is also reflected in the reduction of the nucleation length  $L_c$  with increased  $\sigma'_n$  (Eq. 3.11).

Given the opposite effects of the two controlling processes, earthquake nucleation becomes complicated when the normal stress is heterogeneous. We propose a conceptual model with five regimes to provide an overview summarizing the contrasting roles (Fig 3.8). We have seen that the LSRs are activated earlier due to their low strength, while their larger nucleation length makes it harder for them to reach the critical length and thus they require a longer loading phase. HSRs behave opposite; they remain locked for a longer time, but need a shorter nucleation time after being activated. Consequently, depending on the length scale of the asperities (equivalent to the wavelength of the heterogeneity we use), HSRs and LSRs switch their roles as nucleation and barrier locations (Fig 3.8). In the two end-member cases, i.e., when  $\lambda \ll L_c$  or  $\lambda \gg L_c$ , both HSRs and LSRs are involved in the nucleation process (Fig 3.8a, e, 3.3, 3.4). When  $\lambda \ll L_c$ , the nucleation requires activating a collection of asperities to reach  $L_c$ . Therefore, the fault properties are homogenized at this length scale (homogenized nucleation regime, Fig 3.8a). When  $\lambda \gg L_c$ , earthquakes can

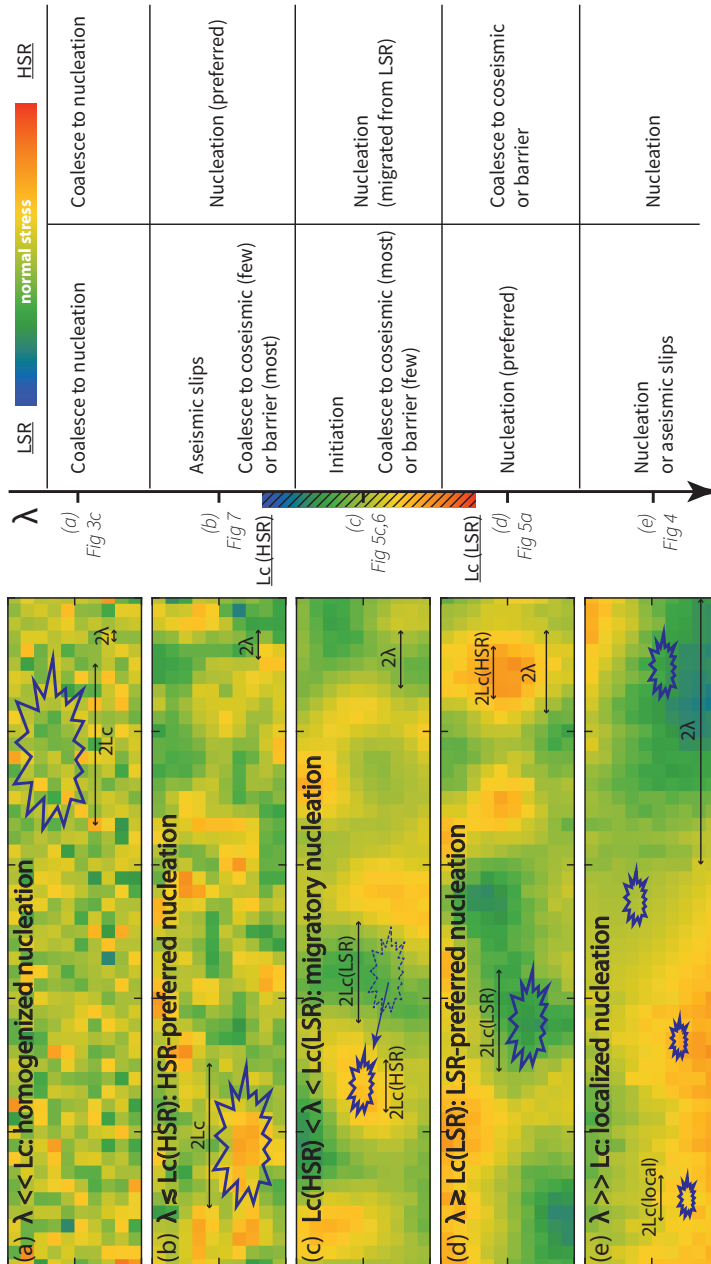


Figure 3.8: A *conceptual model of earthquake nucleation on heterogeneous faults*. (a-e) Earthquake nucleation patterns in five regimes exemplified by representative scenarios with different heterogeneity wavelength  $\lambda$ . Each explosion shape indicates a possible nucleation location and the corresponding nucleation length. The roles of HSRs and LSRs in these scenarios are summarized on the right.

nucleate at any single asperity, regardless of the stress. The nucleation length depends on the local stress level (localized nucleation regime, Fig 3.8e). However, when  $\lambda \sim L_c$ , HSRs and LSRs behave either as a location for nucleation or arrest, dependent on the ratio of  $\lambda$  and  $L_c$  (Fig 3.8b, c, d, 3.5, 3.7). When  $\lambda \gtrsim L_c$ , earthquakes nucleate in LSRs while HSRs function as barriers (LSR-preferred nucleation regime, Fig 3.8b). However, HSRs and LSRs switch their roles when  $\lambda \lesssim L_c$  (HSR-preferred nucleation regime, Fig 3.8d). An interesting fifth regime is found when  $L_c(\text{HSR}) < \lambda < L_c(\text{LSR})$ , we find that nucleation initiates in LSRs but migrates to neighboring HSRs and complete there (migratory nucleation regime, Fig 3.8c, 3.5b).

### Transition from “preslip” to “cascade” model

Along with the migration of nucleation location, our results show a trend transitioning from the “preslip model” [Dieterich, 1978; Latour *et al.*, 2013; McLaskey and Kilgore, 2013] to the “cascade model” [Helmstetter and Sornette, 2003; McLaskey and Lockner, 2014; Wang *et al.*, 2023] as heterogeneity wavelength increases. When  $\lambda \ll L_c$ , earthquake nucleation requires the activation of a collection of asperities before instability (homogenized regime). After these asperities are activated, their slip rates remain at the background loading rate until the length of the collection reaches the required nucleation length (Fig 3.3c). This observation of a growing slipping region during nucleation fits the description of the “preslip model” [McLaskey and Kilgore, 2013]. When  $\lambda \lesssim L_c$ , most LSRs continue to slip at the loading rate during interseismic phase (HSR-preferred regime, Fig 3.7). The preslip in these regions loads the locked HSRs. When  $\lambda$  is increased such that  $L_c(\text{HSR}) < \lambda < L_c(\text{LSR})$ , our results exhibit features from both nucleation models (migratory regime, Fig 3.5b). First, nucleation initiates with preslips in an LSR, as the “preslip model” describes. Then it triggers a second nucleation in the neighboring HSR. If we take the initial nucleation in the LSR as a separate process that triggers a subsequent earthquake in the HSR, the observation fits the “cascade model” description [McLaskey and Kilgore, 2013]. This triggering becomes even more evident in the HSR-preferred and localized nucleation regimes (e.g., Fig 3.4a). In the latter case, although we do not identify mainshocks and foreshocks, the recurrence of a series of events that form a “supercycle” is apparent.

The migration of nucleation location in the migratory nucleation regime is different from what *McLaskey* [2019] observed as earthquake “ignition”. The final nucleation location is termed the “ignition” by these authors, such that it can be separated from the location of the preslip. Based on experimental results, they claimed that the ignition takes place in strong locations (HSRs in this study) when  $2L_c$  is much larger than the asperity size (fig 13 in *McLaskey* [2019]). In that scenario, they claimed that the normal stress heterogeneity should be mild enough so that there is little overall variation in  $L_c^{loc}$ . We used a different methodology such that we do not have physical asperities on our simulated faults. A simple approximation could be treating HSRs as asperities because they remain locked when their surrounding LSRs are activated to slip. Then  $2\lambda$  would be the approximate asperity size. The scenario *McLaskey* [2019] talked about is equivalent to our HSR-preferred and localized nucleation regimes. Our results thus support their statement but suggest further that their additional assumption of mild heterogeneity is not necessary (Fig 3.7). On the contrary, slipping behavior is promoted in LSRs even with strong heterogeneity that changes  $L_c^{loc}$  significantly. Moreover, such “ignition” in HSRs can already happen when the asperity size is just above the minimum nucleation length, which is the  $L_c^{loc}$  at HSRs (migratory regime, Fig 3.5c). In this case, the LSRs are not only slipping at the background slip rate but go beyond it to attempt nucleation. *McLaskey* [2019] observed similar slip behavior but claimed that  $L_c$  loses its function as the critical length scale because the stress concentration at the HSR/LSR boundary becomes critical. In this case, nucleation length is not regulated in their work (fig 14 in *McLaskey* [2019]). However, our simulations reveal that the theoretically calculated nucleation length  $L_c$  is respected in all scenarios (Fig 3.8). Even in the migratory nucleation regime, the local nucleation lengths at both the old and the new locations still follow the theoretical predictions (Fig 3.6a). This is because the nucleation length reflects the energy balance during the nucleation process and our simulations suggest that this rule should still be satisfied after nucleation migration.

### Combination with frictional heterogeneity

We observed that preferred nucleation and barrier locations are swapped when normal stress heterogeneity changes wavelength. We attribute the swap to the controlling role normal stress plays in both fault strength and nucleation

length. Both LSRs and HSRs become good candidate nucleation locations. Similar observations are expected when heterogeneities in frictional parameters are present. Analytical derivations in *Ray and Viesca [2017]* suggest that both local minima and maxima of  $(a - b)$  are preferential nucleation locations. Whether the maxima or minima become unstable then also depends on the distribution of  $(a - b)/b$ . The answer perhaps only becomes simpler when only a heterogeneous  $D_{RS}$  is present. Nucleation then starts from the location of the lowest  $D_{RS}$  (equivalent to the lowest  $L_c$ ) because in this scenario fault strength is homogeneous, as observed in the simulations in *Selvadurai et al. [2023]*. However, since it is commonly thought that fault roughness can result in heterogeneities in normal stress,  $(a - b)$ , and  $D_{RS}$  at the same time [*Yamashita et al., 2018; Gounon et al., 2022; Morad et al., 2022*], their impacts can hardly be disentangled.

### 3.4.2 Preslip during nucleation migration: evidence and implication

In the scenario when  $L_c(HSR) < \lambda < L_c(LSR)$  (migratory nucleation regime, Fig 3.8c), abundant aseismic slips at sub-seismic rates are observed in LSRs before the nucleation location migrates (Fig 3.6). This process takes more than 90% of the nucleation duration and produces one-third of the total stress drop, indicating a distinct amount of energy release over a relatively long time. Such slips in the preparation phase can take the form of tremors, VLFs, foreshocks, and other forms of precursory signals in the real world. Natural signatures are captured by geodetic observations before large earthquakes, such as the 2011 Mw 9.0 Tohoku-oki earthquake [*Mavrommatis et al., 2014*], 2014 Mw 8.1 Iquique earthquake [*Socquet et al., 2017*] and 2014 Mw 7.3 Papanoa earthquake [*Radigue et al., 2016*]. Understanding the mechanism of the precursors contributes to detecting the preparation phase of large earthquakes, and finally contributes to earthquake early warning and forecasting. Recent observations of ice-quakes within the west Antarctica ice sheet suggest abundant and predominant migratory precursory slip, whereas self-nucleation is nearly absent [*Barcheck et al., 2021*]. However, it is not yet known how frequent nucleation location migrates in tectonic settings when compared to other nucleation regimes. Our results indicate that these precursors could exist in low-stress regions (Fig 3.5c). This finding suggests a re-examination of natural observations (such as GPS data) of

low stress regions at a distance from the epicenter area. By mapping the spatial distribution of such signals and the migration of foreshock and aftershock hypocenters, we could identify migratory nucleation and thus infer which nucleation regime is dominant in nature. On the other hand, these observations will in turn inform us about the characteristics of the on-fault stress distribution. Fault stress depends on multiple factors such as the local stress field and fault geometry and thus still remains largely unknown for most fault systems around the world. We probably only have a better knowledge of the effective normal stress distribution in induced seismicity settings, where human activities affect and even control pore pressure changes. There could we inspect if our proposition is effective or not.

### 3.4.3 Heterogeneity statistics and its deviation from Gaussian

Since we generated continuous heterogeneity instead of binary series flipping properties, the impact of wavelengths and amplitudes of the spatial distribution is convoluted. Generally, an increase in amplitude shrinks the available space for potential nucleation around a local stress peak. Yet a decrease in wavelength has the same effect. In this study, we mainly focused on the influence of the heterogeneity wavelength, but the role of the amplitude can be investigated in the same manner. For example, in the homogenized regime, increasing amplitude also promotes slow slip events and partial ruptures before the mainshocks. Previous studies using binary or periodic heterogeneity formulations have proposed to use the ratio between amplitude and wavelength (in their case the length of each flip) as the heterogeneity indicator. However, this parameter has a potential problem if we notice that  $L_c$  is inversely proportional to normal stress (Eq. 3.11). Modifying the amplitude of a Gaussian-type stress heterogeneity has an asymmetric effect on the probability density distribution of  $L_c$ . The long-tail feature of the inverse Gaussian distribution of  $L_c$  amplifies the variation at the low-stress end and suppresses variations at the high-stress end. Not to mention that this issue becomes even more difficult to tackle when we consider more complicated heterogeneity formulations that give a better description to fit the observations [Chen et al., 2020; Selvadurai et al., 2023].

Laboratory measurements reveal that fault roughness often deviates from a Gaussian distribution [Chen et al., 2020]. Selvadurai et al. [2023] suggests a bi-



modal Gaussian distribution of fault roughness. This distribution, featuring two characteristic roughness scales, is supported in the tribology community due to its fitting description of the wear process during friction [Adachi and Kato, 2000; Hu *et al.*, 2019]. Depending on the relative sizes of the two roughness scales, their interaction with the nucleation length might behave as a mixture of the modes introduced in Figure 3.8. Moreover, recent research based on natural observations suggests other correlation functions could be used, such as power-law and fractal distributions [Brown and Scholz, 1985; Okubo and Aki, 1987; Ohnaka, 2003; Candela *et al.*, 2012]. These correlation functions have richer structures at small wavelengths, especially as a length scale is absent when the random field becomes fractal [Ide and Aochi, 2005]. The influence of having multiscale heterogeneities on the interaction of the length scales needs further confirmation. However, the overall philosophy of our conceptual model might still persist when accounting for multi-scale structures.

### 3.5 Conclusions

We build an earthquake sequence model to quantitatively understand the impact of heterogeneous effective normal stress on earthquake nucleation and the associated slip behavior. Our model features a stochastically variable, spatially heterogeneous normal stress distribution, analogous to a meter-scale laboratory experiment. We identify five regimes of earthquake nucleation and slip behaviors, governed by the ratio of the heterogeneity wavelength ( $\lambda$ ) to the nucleation length ( $L_c$ ). First, full rupture events are observed when  $\lambda$  is significantly smaller than  $L_c$ , displaying slips and recurrence intervals akin to those on homogeneous faults with the same averaged normal stress (termed the homogenized nucleation regime). Nucleation requires the failure of a collection of asperities (locked patches), the total length of which reaches  $L_c$ . Thus, the fault property is homogenized at length scale  $L_c$ . However, frequent occurrences of slow slip events and partial ruptures prevail when  $\lambda$  is much larger than  $L_c$ . In that localized nucleation regime, each earthquake's nucleation length depends on the local stress level. Between these end-member cases, when  $\lambda$  approaches the magnitude of  $L_c$ , locations of earthquake nucleation and arrest switch between low normal stress regions (LSR) and high normal stress regions (HSR). When  $\lambda$  is larger than  $L_c$ , nucleation can be completed in a single asperity. In

this case, the weaker LSRs fail first (LSR-preferred nucleation regime). HSRs function as barriers, but can also be activated by a dynamic rupture and coalesce into a large event. Otherwise, the activated HSRs become the nucleation location of the next event. However, HSRs and LSRs switch their roles when  $\lambda$  is smaller than  $L_c$  (HSR-preferred nucleation regime). Whereas nucleation prefers HSRs, LSRs are barely re-locked and remain slipping at around the loading rate. Between these regimes, there is a regime when  $\lambda$  is between the minimum and maximum local nucleation lengths, which are located at the HSRs and LSRs, respectively. We find that nucleation location regularly migrates from an LSR to its neighboring HSR in a single earthquake (migratory nucleation regime). We still observe LSR being activated first, but the nucleation cannot be completed. The final nucleation thus takes place in its neighboring HSR and the activated LSR becomes a barrier for rupture propagation. In this case, a large amount of aseismic slip and an associated stress drop are observed in the initial LSR, which might be linked to the migration of foreshocks documented in natural and laboratory observations. Notably, this study sheds light on the significance of effective normal stress in modifying the seismic potential of natural faults, especially in induced seismicity settings where human activities impact and even control the effective normal stress distribution. In the future, these results may be used to estimate fault stresses based on seismological and geodetic observations of fault slips such as foreshocks and preslips.



# 4

## Why induced earthquakes occur on conventionally stable faults: frictional healing explains

*Meng Li, André R. Niemeijer, and Ylona van Dinther*

Under review at Nature Communications. Preprinted as: *Li, M., Niemeijer, A., & Van Dinther, Y. (2023). Why induced earthquakes occur on conventionally stable faults: frictional healing explains*, available at Research Square.

<https://doi.org/10.21203/rs.3.rs-3317840/v1>

## Abstract

Conventional studies suggest that faults in the shallow subsurface should be resistant to earthquake nucleation, because their frictional strength increases as slip accelerates. Yet, such faults frequently exhibit earthquakes induced by human intervention. Here we explain this paradox by showing, through numerical simulation using rate-and-state friction, that single earthquakes can nucleate on velocity-strengthening faults, following fault “healing” over thousands to millions of years. Fault strength gained during fault healing allows for adequate stress drop in an induced earthquake. However, subsequent slip on human lifetimes is stable and aseismic. We apply our approach to assess the potential of any velocity-weakening or velocity-strengthening fault to host induced seismicity, in terms of the healing time needed to produce sufficient stress drop and fast slip upon fault reactivation. This demonstration of how healing promotes induced earthquakes instead of aseismic events is critical for correctly assessing which sites can be safely targeted in exploiting the subsurface for applications such as geothermal energy production and energy storage.

## 4.1 Introduction

Following the boom of subsurface exploitation to meet our increasing energy demand, induced earthquakes gained significant societal and scientific attention. However, these earthquakes, induced by human activities such as fossil fuel production and underground sustainable energy production and storage, are “unexpected” in several aspects. First, they show a distinctly different global spatial distribution from natural seismicity (Fig. 4.1A). Such induced earthquakes mostly take place in intraplate regions where tectonic loading rate is low or near-zero [Magnani *et al.*, 2017]. Human-induced stress perturbations are the drivers for the failure of pre-existing faults. In this way, earthquakes occur on inactive faults that lack historical seismicity and where consequently people are more at risk as infrastructure has not been built to withstand earthquakes. Moreover, these earthquakes generally occur at depths close to human activities, i.e., within the shallow few kilometers, which is considerably shallower than most natural earthquakes (Fig. 4.1B). Therefore, they can be more hazardous and cause more ground shaking [Atkinson *et al.*, 2020]. In most cases, source properties of induced earthquakes, such as moment tensor and energy spectrum, are also different from natural earthquakes [Cesca *et al.*, 2012; Zhang *et al.*, 2016; Yu *et al.*, 2021]. These differences suggest that induced earthquakes might not have the same underlying physical causes as natural earthquakes. The evolution of stress and strength on inactive faults has to be characterized to understand induced earthquakes and to better assess and ultimately forecast seismic hazard.

Earthquake nucleation, propagation and arrest are widely understood to be governed by a fault’s resistance to slip, which is quantified using fault friction and its velocity or displacement dependence [Ida, 1972; Dieterich, 1979; Ruina, 1983; Scholz, 1998]. Velocity-weakening (VW,  $a < b$ ) and velocity-strengthening (VS,  $a > b$ ) are two types of frictional properties in the popular rate- and state-dependent friction formulation, where  $a$  and  $b$  are the two frictional parameters (Fig. 4.1B). This single phenomenological law, originally revealed by velocity step experiments in the laboratory (with typical loading velocity ranging from 1  $\mu\text{m/s}$  to 1 m/s), provides a powerful tool to model the complete earthquake sequences. During slip acceleration, VS faults become stronger while VW faults weaken, which leads to further acceleration of slip. Therefore, classical instability analysis indicates that instabilities (and thus earthquakes) only nucleate

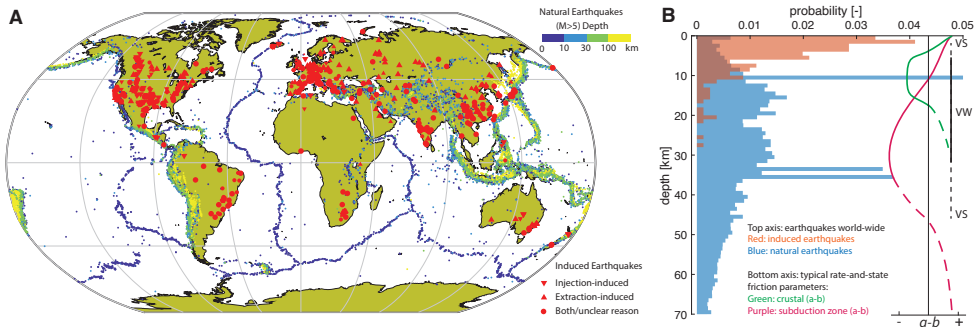


**Figure 4.1: Distribution of natural and induced earthquakes.** (A) Global distribution of natural and induced seismicity. Natural earthquakes with moment magnitude higher than 5 are color-coded according to their hypocenter depth (upper right colorbar, USGS catalog, year 2021) [U.S. Geological Survey]. Induced earthquakes are plotted with red markers. Injection-induced, extraction-induced, and events with unclear causes are marked by different markers (bottom right legend, HiQuake catalog, till 2022, note that the catalog is not exhaustive) [HiQuake; Wilson *et al.*, 2017]. (B) Corresponding depth distribution of natural and induced seismicity. The data are from the same sources as (A). The irregular peaks in natural seismicity data are due to the default depth assignment of 10, 33 and 35 km to low-accuracy earthquakes in the USGS catalog. Only the induced earthquakes reported with a depth estimate from the HiQuake catalog are plotted. The typical distributions of the rate-and-state frictional parameter ( $a - b$ ) with depth in crustal and subduction zone settings are plotted using the bottom axis for comparison [Scholz, 2019].

under VW friction, while VS friction favors stable sliding and thus inhibits earthquake nucleation [Ruina, 1983; Rice and Ruina, 1983; Rubin and Ampuero, 2005]. Nucleation conditions and patterns under VW friction have been thoroughly explored with numerical simulations and laboratory experiments, where the simulated characteristics of nucleation and rupture propagation are in accordance with observations of natural earthquakes [Ellsworth and Beroza, 1995; Olson and Allen, 2005]. It is verified that earthquake nucleation includes a transition from aseismic slip to seismic slip that requires a critical length, termed as the nucleation length, to be reached [Lapusta *et al.*, 2000; Barbot *et al.*, 2012; Guérin-Marthe *et al.*, 2019; McLaskey and Lockner, 2014]. In these studies, any VS portions on a fault function as barriers that slow down or arrest the rupture [Kaneko *et al.*, 2010; Perfettini *et al.*, 2010].

Numerous fault rocks at shallow depths consistently exhibit VS behavior in low temperature and pressure experiments [Marone and Scholz, 1988; Scholz, 2019; Kang *et al.*, 2019; Ruggieri *et al.*, 2021; Miyamoto *et al.*, 2022; Zhong *et al.*, 2023]

(Fig. 4.1B). The observed induced seismicity at such depths thus contradicts the classical prediction of the absence of earthquake nucleation in VS rocks. Evidence from the well-studied Groningen gas field in the Netherlands, the largest natural gas field in Europe and one of the largest in the world, augments this paradox. Damaging earthquakes are located within or close to the depth of the gas reservoir [*van Thienen-Visser et al.*, 2015; *Spetzler and Dost*, 2017; *Willacy et al.*, 2019; *Smith et al.*, 2020] and are believed to be the consequence of the reactivation of pre-existing faults resulting from stress changes due to gas production [*Buijze et al.*, 2019]. Peculiarly, laboratory experiments on the simulated gouges of the reservoir rocks, taken from the borehole, show mainly VS behavior under in-situ pressure-temperature and fluid chemistry conditions [*Hunfeld et al.*, 2017]. This combined evidence indicates a need to clarify whether earthquakes can nucleate on VS faults or not. Previous studies suggest that VS faults can exhibit aseismic slip pulses after an external perturbation of the fault stress state [*Dieterich*, 1979; *Rice and Gu*, 1983; *Perfettini and Ampuero*, 2008]. However, it is unknown whether such pulses could grow into an earthquake or whether they remain aseismic. In addition, the origin of such stress perturbation is not defined in nature.

Slip takes place when stress on a fault overcomes its strength. The fact that a fault restrengthens during periods of inactivity could contribute to explaining why areas devoid of natural earthquakes are not safe in induced scenarios. Healing is a well-established phenomenon describing the time-dependent recovery of fault strength observed in slide-hold-slide (SHS) experiments, where the peak stress of the subsequent slip ('slide') after fault reactivation increases with the time of inactivity ('hold') [*Beeler et al.*, 1994; *Olsen et al.*, 1998; *Marone*, 1998; *Nakatani and Scholz*, 2004; *Chen et al.*, 2015; *Carpenter et al.*, 2016]. In this way larger stress drops are obtained after a longer healing period. The observed strength increase originates from the microphysical growth of grain contacts (asperities) as well as the development of cohesion [*Tenthorey and Cox*, 2006]. Processes such as cementation are evidenced to be involved in cohesion development by microscopic imaging [*Hunfeld et al.*, 2017]. This behavior is confirmed also for the specific VS lithologies in Groningen [*Hunfeld et al.*, 2020]. Our numerical model has quantitatively reproduced the healing behavior in these SHS experiments and supports the origin of aseismic slip events (fig. 4.7). Given that the Groningen region and many other human activity sites have been tectonically inactive for millions of years [*van Oeveren et al.*, 2017], we will eval-



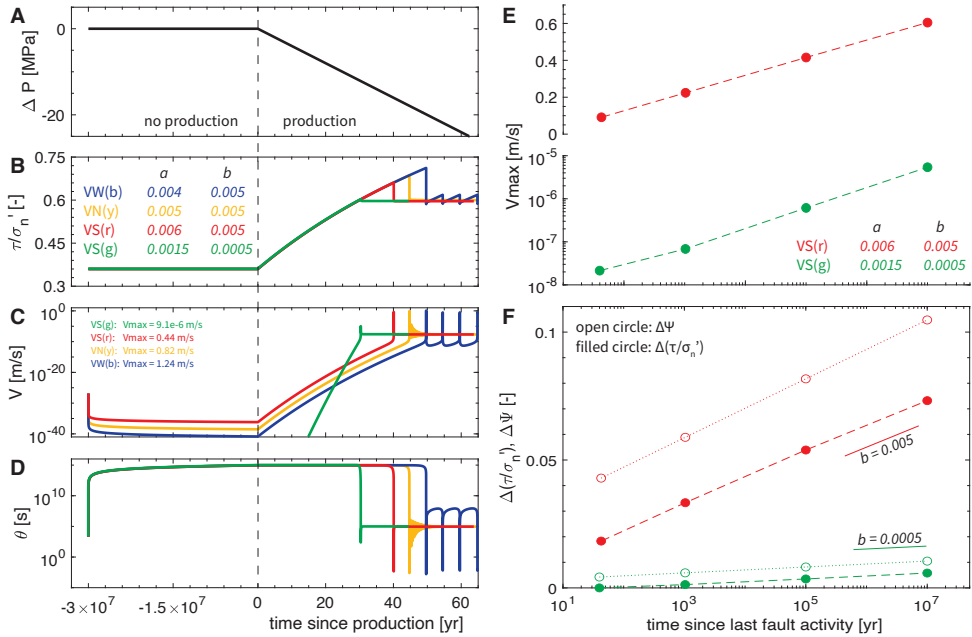


Figure 4.2: *Earthquake sequence after healing over geologic time scales.* (A-D) Simulation of earthquake sequences in 0-D in VS (red:  $a = 0.005, b = 0.004$ ; green:  $a = 0.0015, b = 0.0005$ ), VW (blue:  $a = 0.005, b = 0.006$ ) and VN (yellow:  $a = 0.005, b = 0.005$ ) scenarios with a healing time of 30 Ma, with fixed  $D_{RS} = 2$  mm. (A) The pore pressure change, (B) the ratio of shear stress and effective normal stress  $\tau/\sigma'_n$ , (C) the slip rate, and (D) the state variable are plotted with respect to time since production starts. Negative time refers to the time before production. Different scales are used in the positive and negative parts of the axis. (E-F) Simulation of earthquake sequences in VS scenarios ( $a - b = 0.001$ ) with different lengths of healing time from 10 yr to 10 Ma. (E) The maximum slip rate  $V_{\max}$  of the induced events is plotted with respect to the time of the event since the last fault activity, i.e., where healing starts. (F) The friction drop  $\Delta(\tau/\sigma'_n)$  (i.e., change in the ratio of shear stress to effective normal stress) and the gained interface strength  $\Delta\Psi$  during healing are plotted with respect to the time of the event since the last fault activity.

uate if it is possible to nucleate earthquakes (i.e., fast slips) on VS rocks after healing over geological timescales. Moreover, we aim to understand to what extent the seismic potential for induced seismicity is increased by healing globally, as it is universal for both VS and VW friction. Even though healing is inherent in rate-and-state friction, it has not been used to explain the occurrence of induced earthquakes. In this study, we simulate a typical gas production site configuration in 0-D and 2-D numerically to investigate the role of fault healing in induced seismicity and to understand earthquake nucleation under VS friction (see Methods 4.5 and parameters in table 3.1).

## 4.2 Results

### 4.2.1 Healing: from laboratory to tectonic timescales

We extended the healing period from laboratory experiments to hundreds of millions of years to match natural scenarios (Fig. 4.2 and 4.8). We simulated two types of fault rocks: one with a high healing rate ( $b = 0.005$ ) and one with a low healing rate ( $b = 0.0005$ ). The rapidly healing fault first experiences a period of inactivity during which its stress level is far from failure. This simulates the period after the last fault activity millions of years ago (Fig. 4.2A-B). The slip rate quickly decays to practically zero, which matches observations in the laboratory [Nakatani, 2001] (Fig. 4.2C). After this period of quiescence, we prescribe a sudden, continuous pore pressure change mimicking human activities such as gas production (Fig. 4.2A). During depletion, poroelasticity causes the shear stress to increase faster than the effective normal stress accumulates, pushing the fault towards failure (Fig. 4.2B). The yield or failure point is reached after a certain period of time, i.e., the aseismic waiting period between the start of human perturbation and the seismicity, as observed both in the field [Richter *et al.*, 2020] and in the laboratory [Nakatani, 2001; Hunfeld *et al.*, 2020]. The fault accelerates quickly to seismic slip rates (cm/s to m/s) after failure, generating an earthquake. Afterwards, recurring earthquake sequences are observed on VW faults, where earthquakes with growing slip rates and recurrence intervals occur in sequence (Fig. 4.2C). This is due to the increasing effective normal stress when human activities continue. In contrast, no subsequent earthquakes are expected on VS faults, although several slow-slip events still occur when the fault

is close to velocity-neutral (VN,  $a = b$ ). After a single earthquake, the VS fault reaches a steady state in which it moves at a slow constant slip rate defined by the rate of human activity. Since the ruptured fault segment is not re-locked on human timescales, that portion cannot nucleate future earthquakes, nor can it be ruptured in adjacent earthquakes. In this simulation tuned to the Groningen configuration with a healing time of 30 Ma [*de Jager and Visser, 2017*], the first earthquake with a maximum slip rate of  $\sim 0.4$  m/s occurs about 40 years after the onset of gas production, which is the same order of time span as observed [*Richter et al., 2020*]. The simulated stress drop is about 1.2 MPa, which is similar to the  $\sim 1$  MPa reported for Groningen seismicity [*Kraaijpoel and Dost, 2013; Dost et al., 2016; Bommer et al., 2016*]. In comparison, the slowly healing fault does not become seismogenic after 30 Ma of healing (green lines in Fig. 4.2A-D). Despite its state variable following the same logarithmic increase in the no-production period as the rapidly healing fault (Fig. 4.2D), its yield stress is not elevated to the same level (Fig. 4.2B). Therefore the stress drop is very minor and the associated slip rate only reaches  $9 \mu\text{m/s}$ . This kind of slow slip event occurs earlier after the onset of gas production and thus might occur frequently in natural fault networks.

We activate the human perturbation to the VS faults at different times since the last fault activity to study the effect of the healing time (Fig. 4.2E-F). On the rapidly healing fault, an earthquake with a higher slip rate is recorded when the healing time increases (Fig. 4.2E). Specifically, the maximum slip rate grows logarithmically with the applied healing time. This is accompanied by a larger stress drop (Fig. 4.2F), which comes from an increased yield stress with respect to an unchanged dynamic stress. Comparably, the maximum slip rate recorded in the slow slip events also increases with the healing time on the slowly healing fault, although that follows a linear relationship (Fig. 4.2E). The growth of the stress drop with healing time is also logarithmic, but at a lower rate (Fig. 4.2F). The concept of interface strength

$$\Psi = \mu_0 + b \ln \left( \frac{\theta V_0}{D_{RS}} \right) \quad (4.1)$$

defined in *Nakatani [2001]* (see also Methods) can explain this logarithmic growth of the stress drop (Fig. 4.2F). In the healing phase with a near-zero slip rate, rate-and-state friction predicts a linear growth of the state variable with time ( $\theta = \theta_i + t$ ) and thus a logarithmic growth of the interface strength [ $\Psi = \Psi_i + b \ln(1 + t/\theta_i)$ ], where  $\Psi_i$  and  $\theta_i$  are the initial values of interface

strength and state. We find that the growth of the interface strength predicted by the equation is the same amount as the growth of the simulated stress drop. This observation indicates that the concept of interface strength can indeed be used as an indicator of fault strength. The rate-and-state parameter  $b$  controls the healing rate [Nakatani, 2001; Nakatani and Scholz, 2004]. A rapidly healing fault could achieve a reasonable stress drop and thus a seismic slip rate after a geological timescale of healing, whereas a slowly healing fault remains aseismic after a similar amount of healing time. Given that healing is logarithmic, the slowly healing fault will not become seismogenic until after an exponentially longer healing time.

## 4.2.2 Nucleation on velocity-strengthening faults

Whether a fault is VS or VW not only influences the long-term recurrence of earthquakes, but also affects the spatial evolution of slip on the fault in the period between fault reactivation and seismic rupture – the nucleation (Fig. 4.3 and 4.9). In a 2-D model representing a Groningen fault (model setup in fig. 4.11), the shallowest point of the fault inside the reservoir reaches the yield point first, after the fault has been activated due to gas production (Fig. 4.3A). The nucleation process starts here and expands within the depth interval of the gas reservoir and beyond. The whole process can be separated into three stages according to the slip rate reached at the nucleation front: (i) fault activation, when the maximum slip rate rises from near-zero to a background rate (controlled by the pressure depletion rate); (ii) nucleation, when the maximum slip rate is between the background rate and the seismic rate determined by the dominance of wave radiation [Rubin and Ampuero, 2005]; and (iii) rupture propagation, when the maximum slip rate is above the seismic rate.

We compare the nucleation pattern on VW and VS faults by gradually increasing the value of  $a/b$ , while keeping  $b$  fixed. We find that stage (i) does not rely on  $a/b$  and the nucleation zone reaches the same length of  $L_I$  after this stage (Fig. 4.3 and 4.9). However, the nucleation length before stage (iii), named  $L_{III}$ , varies according to  $a/b$ . For  $a/b \leq 0.5$ , the nucleation process quickly completes at a small  $L_{III}$ , leaving the remainder of the fault to be ruptured seismically ( $a/b = 0.5$  in fig. 4.9C).  $L_{III}$  increases as  $a/b$  increases ( $a/b = 0.7$  in Fig. 4.3E). When  $a/b$  is close to 1, nucleation terminates at the fault boundary without reaching

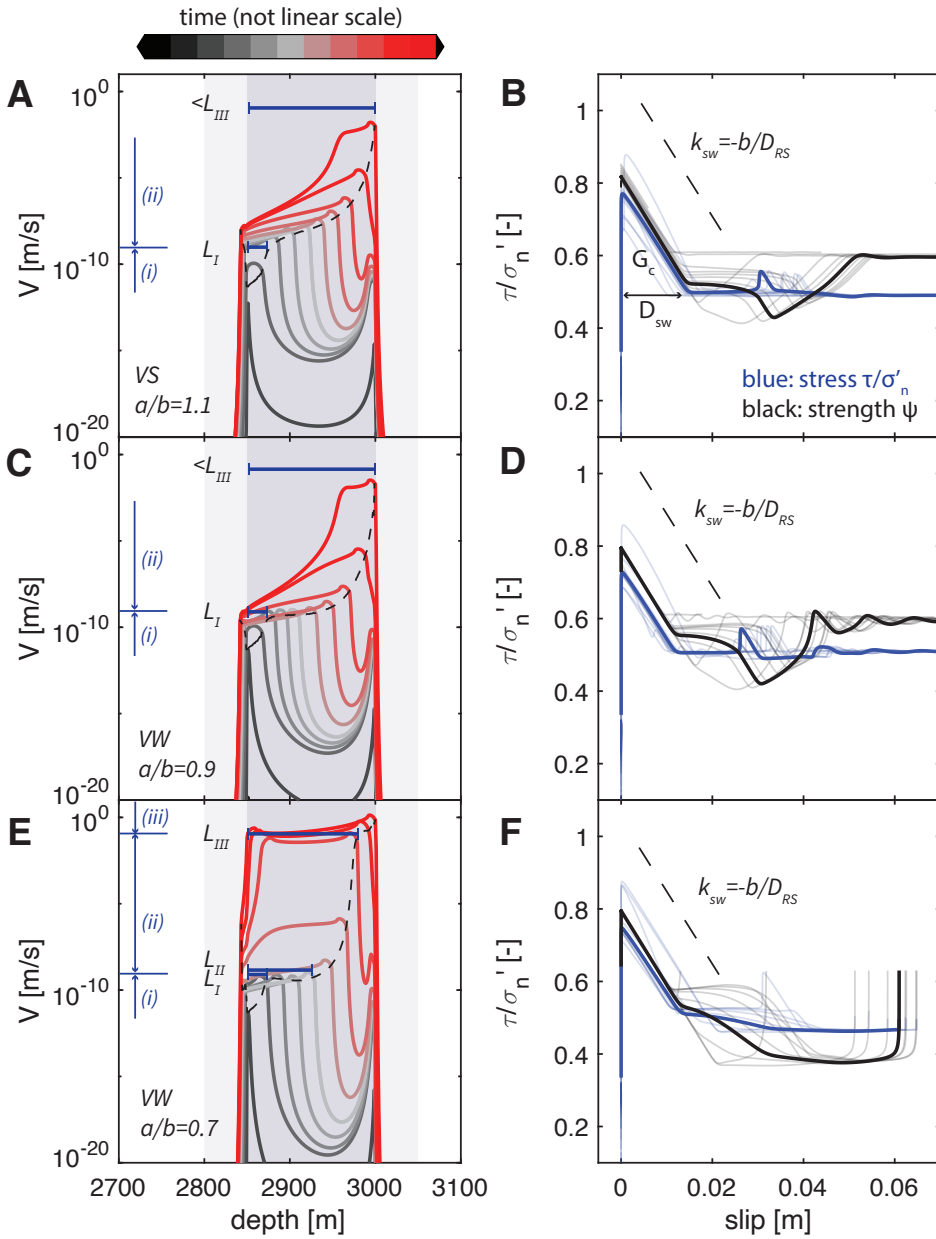


Figure 4.3: (Caption next page.)

Figure 4.3: (Previous page.) *Simulation of the first induced earthquake in 2-D in VS and VW scenarios with several  $a/b$  ratios: (A-B) VS,  $a/b = 1.1$ , (C-D) VW,  $a/b = 0.9$ , (E-F) VW,  $a/b = 0.7$  with fixed  $b = 0.01$  and  $D_{RS} = 0.5$  mm,  $\mu_0 = 0.5$ , healing time  $t_h = 100$  Ma. (A, C, E) The temporal evolution of slip rate. The interseismic and nucleation phases are plotted in black and gray, with gradual transition to the coseismic phase in red (colorbar above). The plotted lines are not in regular time intervals. The nucleation stages (i)-(iii) are indicated by blue arrows next to the vertical axes, separated by the maximum slip rate achieved (stage iii only exists in E). The measured nucleation lengths  $L_I$ ,  $L_{II}$  and  $L_{III}$  are shown as blue bars on the top ( $L_{II}$  only measured in E). The dashed black lines track the temporal-spatial evolution of the nucleation front, characterized as the propagation of the local stress peaks. The blue shadows in the background specify the range of the reservoir depth on the hanging wall side (2850-3050 m) and the footwall side (2800-3000 m). The detailed model setup is depicted in fig. 4.11. (B, D, F) The evolution of friction  $\tau/\sigma'_n$  with respect to slip (blue). The evolution of interface strength  $\Psi$  (Eq. 4.1) is plotted in black for reference. The multiple semi-transparent lines in the background are the observations from different locations (every 20 m between 2800 m and 3050 m depth) on the fault. The bold lines are the observation at the center of the reservoir (2950 m depth). The dashed line indicates the slip-weakening slope of  $k_{sw} = -b/D_{RS}$  for reference. The slip-weakening distance  $D_{sw}$  and the fracture energy  $G_c$  are labeled in (B).*

seismic rate due to the finite fault size, leaving the stage (iii) unobserved ( $a/b = 0.9$  in Fig. 4.3C). A similar pattern of the expansion of the nucleation zone is found on VS faults ( $a/b = 1.1$  in Fig. 4.3A,  $a/b = 1.3$ & $1.5$  in fig. 4.9A-B). Actually, there is no distinct change at ( $a = b$ ), which has conventionally been assumed to be the boundary between instability and stable creep (Fig. 4.3A vs. C).

The nucleation stage (ii) is when VS and VW faults exhibit the most dissimilarity. For VW faults, this stage can be separated into two sections (ii-a) and (ii-b) (Fig. 4.4A). The nucleation zone first expands its length from  $L_I$  to  $L_{II}$  in section (ii-a). During this section, the slip rate at the nucleation front stays at the background rate. The rate of the nucleation expansion also remains approximately constant (fig. 4.10A&C). The nucleation front accelerates rapidly to sub-Rayleigh speeds together with its expansion to  $L_{III}$  in section (ii-b). A larger  $a/b$  corresponds to slower acceleration, and consequently a larger  $L_{III}$ . However, the transitional length scale  $L_{II}$  is not observed on VS faults (Fig. 4.4A). There immediate acceleration of nucleation expansion is observed as soon as  $L_I$  is reached. The nucleation front keeps accelerating during stage (ii) (fig. 4.10B&C). The acceleration is fast at the beginning, then slows down, and speeds up in the end. More velocity-strengthening faults (with a larger  $a/b$ ) have a higher slip rate at the beginning, but its slip rate will be caught up by less VS faults before the end of stage (ii). Here we mainly use the slip rate at the nucleation front to separate different

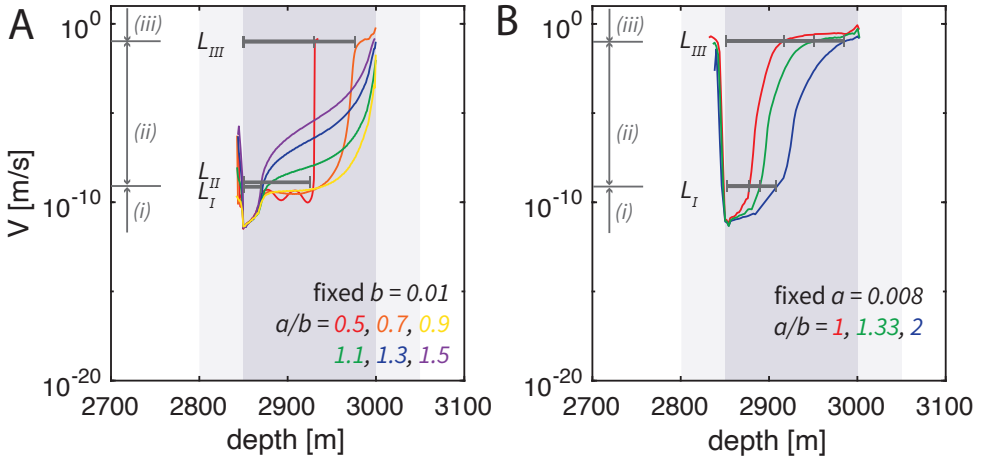


Figure 4.4: **Nucleation front propagation.** (A) The temporal-spatial propagation of the nucleation front extracted from Fig. 4.3 and 4.9. The nucleation stages (i)-(iii) are indicated by gray arrows next to the vertical axes, separated by the maximum slip rate achieved. The measured nucleation lengths  $L_I$ ,  $L_{II}$  and  $L_{III}$  are shown as gray bars on the top ( $L_{II}$  and  $L_{III}$  only measured in some scenarios). (B) The temporal-spatial propagation of the nucleation front in another set of experiments with fixed  $\mu_0 = 0.3$ ,  $a = 0.008$  and varied  $b = 0.008, 0.006, 0.004$ , see fig. 4.12.

nucleation stages since its variation is proportional to the propagation speed of the nucleation front, the more commonly used indicator (Fig. 4.4A vs. 4.10C).

We use these three length scales to clarify various analytical expressions of nucleation length scales derived in previous studies [Rubin and Ampuero, 2005; Ampuero and Rubin, 2008; Day et al., 2005]. The cohesive zone length  $\Lambda_0 = \frac{9\pi}{32} \frac{GD_{RS}}{b\sigma(1-\nu)}$  [Day et al., 2005], also known as the process zone length, matches our simulated length scale  $L_I$ . It is the smallest length scale during nucleation, and appears to apply to both VW and VS faults (Fig. 4.4). This length scale is independent of  $a/b$  but proportional to  $b$  (Fig. 4.4B). The nucleation length  $2L_b = 2 \frac{GD_{RS}}{b\sigma(1-\nu)}$  [Rubin and Ampuero, 2005] matches our simulated length scale  $L_{II}$ . We have only observed this length scale on VW faults, although the expression is independent of  $a/b$ . However, this length scale (or multiplied by a geometrical constant about 1), sometimes also referred to as the minimum nucleation length, is not always present in previous numerical models [Rubin and Ampuero, 2005; Ziv, 2007; Fang et al., 2010; He et al., 2023]. Whether it can be observed or not also relies on the initial and loading conditions. Thus the applicability of this length scale to VS faults needs further exploration under dif-

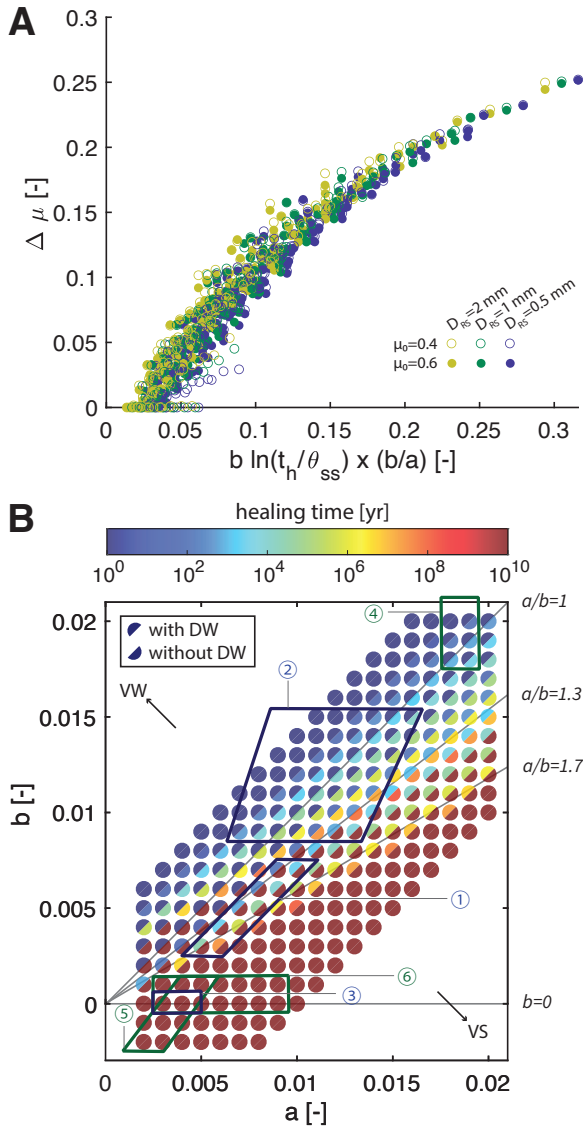
ferent conditions. The suggested nucleation length  $2L_c = \frac{2}{\pi} \left(\frac{b}{b-a}\right)^2 L_b$  [Rubin and Ampuero, 2005] matches our simulated  $L_{III}$  when  $L_{III}$  is smaller than the reservoir thickness. This nucleation length is not measured in full when nucleation terminates at the reservoir or seismogenic zone limit (Fig. 4.4A). Despite that, we find an  $L_{III}$  has to increase with  $a/b$ , even in the VS domain (Fig. 4.4B). The original expression is no longer meaningful when  $a \geq b$ . We have to take the healing-induced strength increase into account to revise the expression of  $L_{III}$  for induced earthquakes. Our revised expression (see Methods) is valid for both VS and VW faults.

The (slip-) weakening mechanism after failure defines the energy budget, which determines whether failure can grow into an earthquake or not. Earthquake energy budgets and slip weakening mechanisms on VS and VW faults show much similarity (Fig. 4.3B, D, F). Independent of the  $a/b$  ratio, the evolution of stress on the fault largely follows the same linear slip-weakening behavior after failure. Shear stress drops from the yield stress to a dynamic stress almost linearly with a similar weakening slope or rate  $k_{sw} = -b/D_{RS}$ , until a similar amount of slip usually referred to as the slip-weakening distance  $D_{sw}$  (Fig. 4.3B). This is valid for observations at different locations on the fault (semi-transparent lines in Fig. 4.3B, D, F). Previous studies have revealed this dependence of  $k_{sw}$  on  $b$  under VW friction [Cocco and Bizzarri, 2002; Lapusta and Liu, 2009]. We find it can be extended to VS friction as well. As long as  $b$  is positive, this slip-weakening behavior always guarantees a positive fracture energy  $G_c$ , which is defined as the area under the stress-slip curve [Ohnaka, 2013] (Fig. 4.3B). Opposite to the classical point of view, VS faults with  $a > b$  thus do not limit failure from growing into earthquakes.

### 4.2.3 Seismic potential quantified

A larger energy release from the source usually translates to a larger ground motion, for a given region where wave attenuation and building responses are fixed [Aki et al., 1978]. We study the influence of frictional parameters on the size of the induced earthquake and therefore the seismic hazard. We use the maximum slip rate and stress drop as proxies to avoid using additional assumptions to empirically upscale our simulation results to 3-D. We systematically explore the parameter space of  $a, b$ , characteristic length  $D_{RS}$  and reference friction  $\mu_0$





Groningen lithologies, (Hunfeld et al, 2017, 2020),

$\sigma'_n = 40 \text{ MPa}$ ,  $100 \text{ }^\circ\text{C}$ , wet condition:

① Slochteren sandstone, ② Basal Zechstein,

③ Ten Boer claystone & Carboniferous shale (same range)

Other reservoir rocks, room temperature, wet condition:

④ Carbonate, (Carpenter et al., 2014), Monte Maggio Fault (Italy),  $\sigma'_n = 10 \text{ MPa}$

⑤ Shale (clay-rich), (Ruggieri et al., 2021), Rochester Shale (U.S.)  $\sigma'_n = 100 \text{ MPa}$

⑥ Basalt, (Zhong et al., 2023), Xiashan Landslide (China),  $\sigma'_n = 5 \text{ MPa}$

Figure 4.5: (Caption next page.)

Figure 4.5: (Previous page.) *Parameter study of the impact of frictional properties and healing time on earthquake stress drop and slip rate.* (A) The friction drop  $\Delta\mu = \Delta(\tau/\sigma'_n)$  as a function of healing time  $t_h$  and  $a/b$ , in 0-D simulations with other parameters such as static friction  $\mu_0$  and characteristic length  $D_{RS}$  also varying. The horizontal axis is the product of the effect of healing  $[b \ln(t_h/\theta_{ss})]$  and the effect of frictional property ( $b/a$ ), where  $\theta_{ss}$  is the state variable at steady state after the earthquake. (B) The required healing time for the first induced earthquake to reach a slip rate of 1 m/s. The simulation results without dynamic weakening (DW) mechanism taken into consideration are shown by the color of the bottom right half of the circle, and the results with DW are shown by the color of the top left half of the circle. The blue quadrilateral labeled as "1" encloses the parameter range of the typical Groningen reservoir rock, the Slochteren sandstone. The other quadrilaterals enclose the parameter range of the typical lithologies above or below Groningen reservoirs (blue) and other reservoir rocks (green) documented in the laboratory experiments listed below.

within the range indicated by laboratory experiments (table 3.1, except for  $D_{RS}$  which is 1-2 orders of magnitude larger, as suggested by [Marone and Kilgore, 1993]). The stress drop appears to be a function of healing time and  $a/b$ , but independent of  $D_{RS}$  and  $\mu_0$  in 0-D simulations (Fig. 4.5A). Larger stress drops are achieved after longer healing times (also in Fig. 4.2E-F), or on less VS faults (also in Fig. 4.2B-C), which is usually reflected in higher slip rates. For both VS and VW faults, a longer healing time increases the seismic potential and encourages the transition from aseismic events to earthquakes.

In hazard assessment, it is common to assess the probability of occurrence of an earthquake of a certain magnitude to evaluate the risk. We quantify how much healing time would be required to make the first induced earthquake *large enough* under given frictional properties (e.g., to reach 1 m/s slip rate as shown in Fig. 4.5B, 4.13). We find that a large variety of VS faults ( $a/b < 1.3$ ) are capable of generating earthquakes after healing over geological timescales, as long as they have moderate to high healing rates ( $b > 0.005$ ). This range is extended further ( $a/b < 1.7$  and  $b > 0$ ) when we also consider enhanced dynamic weakening (DW) mechanisms, which might be activated due to frictional heating when slip rates exceed 1 cm/s. Several DW mechanisms have been proposed and we included flash heating in our model, as this theory is well-supported and easy to use [Tullis and Goldsby, 2003; Beeler et al., 2008] (see Methods). Flash heating further reduces the dynamic frictional strength and thus amplifies the stress drop. It consequently allows higher slip rates, which in turn helps shorten the required healing time before an earthquake of the same slip rate could occur

(Fig. 4.5B).

## 4.3 Discussion

### 4.3.1 Application to Groningen sandstone and other reservoir rocks

The quantification in Fig. 4.5 can be used to forecast the occurrence of future induced earthquakes on specific rock types. This is exemplified through labeling the measured frictional properties of different rock types in Fig. 4.5B. The reservoir rocks hosting earthquakes in Groningen (Slochteren sandstone, [Hunfeld *et al.*, 2017]) needs a healing time of 25 Ma at most before an earthquake of slip rate higher than 1 m/s can occur, when enhanced dynamic weakening is considered (Fig 4.5B). This explains the observed seismicity, since the last fault activities occurred ca. 30-65 Ma ago according to geological studies [de Jager and Visser, 2017; Strozzyk *et al.*, 2017]. On top of the Slochteren sandstone layer, there is a layer of Basal Zechstein caprock (mostly anhydrite) that is weakly VW under specific salinity conditions [Hunfeld *et al.*, 2017], indicating its seismic potential (Fig. 4.5B). At the same time, the Ten Boer claystone and Carboniferous shale layers around the reservoir are VS with negligible or even negative healing [Hunfeld *et al.*, 2020], suggesting their inability of hosting nucleation (Fig. 4.5B). We find this prediction is in good agreement with seismological studies, which have located the hypocenters either in the Slochteren sandstone or Basal Zechstein caprock layers [Spetzler and Dost, 2017; Willacy *et al.*, 2019; Smith *et al.*, 2020]. Our methodology is also applicable to more complicated scenarios where several rock layers of mixed frictional properties exist in the seismogenic zone. In that case if one rock layer is thinner than its  $L_{III}$  such that it cannot accommodate the full nucleation process, the nucleation starting from this layer will still extend to the surrounding rock layers. The whole process will then depend on the healing history and slip-weakening behavior of each layer the nucleation front goes through.

Besides sandstone, we also explore the seismic potential of other representative reservoir rocks across the globe. Carbonate rocks (e.g., limestone), containing

half of the known conventional oil reserves and hosting a great number of natural and induced earthquakes [Scuderi and Collettini, 2016], often show VW behavior and high healing rates in experimental studies [Verberne et al., 2014; Scuderi and Collettini, 2016] (Fig. 4.5B). Earthquakes are thus expected based on classical instability theory and healing will further promote their occurrence. As a representative of unconventional reservoirs, shales are hydraulically fractured for “shale gas”, commonly in North America, and are believed to attribute to the largest induced earthquakes in many regions [Schultz et al., 2018]. At the same time, basalts are explored as an alternative CO<sub>2</sub> storage solution, based on their mineral carbonation ability [Gislason and Oelkers, 2014]. Laboratory studies on both types of rocks report a wide range of frictional properties and healing rates. Some of them are measured as VS with a near-zero or sometimes negative healing rate, such as clay-rich or phyllosilicate-rich shales [Ikari et al., 2009; Kohli and Zoback, 2013; Ruggieri et al., 2021] and basalts [Zhang et al., 2017; Zhong et al., 2023] (Fig. 4.5B). Although the low static friction of shales ( $\sim 0.3$  in wet condition) might allow them to be activated by fast pore pressure change [Scuderi and Collettini, 2018], it is yet to be confirmed whether such instability will grow to an earthquake or whether aseismic slip will prevail as proposed by [Shreedharan et al., 2023]. Also for basalts, given that CO<sub>2</sub> storage involves chemical reactions that change the mineral composition, whether the carbonate precipitates will increase the seismic potential due to their high healing rate is yet poorly investigated [Giacometti et al., 2018].

### 4.3.2 Healing and cohesion

Both healing and slip-weakening, the mechanisms that reshape fault failure criterion and the subsequent weakening mechanism, are activated by a positive rate-and-state parameter  $b$ . Since both mechanisms are unrelated to the value of  $(a - b)$ , our methodology to explain induced earthquakes is generally applicable to both VS and VW faults. However, it is still surprising to see that the healing rate and the slip-weakening rate share the same phenomenological parameter, with its physical meaning unexplained. In fact, experimental studies show that the rate-and-state parameters obtained from SHS experiments are different from those obtained in velocity-step experiments on the same material under identical conditions [Marone, 1998]. Considering that SHS experiments mainly measure healing whereas velocity-step experiments exhibit stick-slip events,

where coseismic weakening is more crucial, we could speculate that the two mechanisms might not share the same set of parameter values. In addition, numerous experimental studies have demonstrated a velocity-dependence of the frictional parameters [Blanpied *et al.*, 1995; He *et al.*, 2013; Niemeijer *et al.*, 2016]. It would be insightful to consider how healing affects subsequent earthquake nucleation using microphysics-based models such as the “CNS model” [Chen and Spiers, 2016] or the “Aharonov & Scholz model” [Aharonov and Scholz, 2018]. Such models would also allow for a different healing behavior (e.g., ‘power-law healing’ observed in the experiments in [Chen and Spiers, 2016]) and a natural way to incorporate dynamic weakening by different mechanisms such as thermal pressurization [Aharonov and Scholz, 2018].

On the other hand, healing has its microphysical mechanism, which is reflected in the macroscopic development of cohesion [Tenthorey and Cox, 2006]. Unlike the classical Mohr-Coulomb criterion, cohesion is implicitly included in the rate-and-state friction, and appears to be dependent on normal stress. In our studied reservoir setup, 30 Ma of healing increases the interface strength  $\Psi$  by 0.23 (assuming  $b = 0.01$ ), which is equivalent to about 4 MPa of cohesion (Eq. 4.1, using the effective normal stress during nucleation). An experimental study of the same type of sandstone shows 12-32 MPa cohesion in bulk rock failure experiment [Naderloo *et al.*, 2023]. This difference implies that the healed fault gouges is yet weak. On the contrary, inversion from seismicity data indicates a considerably low cohesion [Heimisson *et al.*, 2022]. The authors updated the Coulomb criterion by adding a failure threshold, whose existence is justified by healing or cohesion. The best estimate for fitting the seismicity rate in Groningen since gas production is 0.17 MPa, with a 95% confidential interval between 0.07 and 0.18 MPa. Meanwhile, the authors inverted an effective normal stress of 0.6 MPa (assuming  $a = 0.01$ ). Both estimates may fit a heavily injected scenario, but seem to mismatch the increasing effective normal stress due to gas production. Despite that, their ratio ( $0.28 = 0.17 \text{ MPa} / 0.6 \text{ MPa}$ ) is comparable to our simulated interface strength increase  $\Delta\Psi$ .

### 4.3.3 Induced vs. natural seismicity

The role of healing is decisive for intra-plate faults, where tectonic loading rate is slow, to gain enough strength that can be converted to large stress drops and

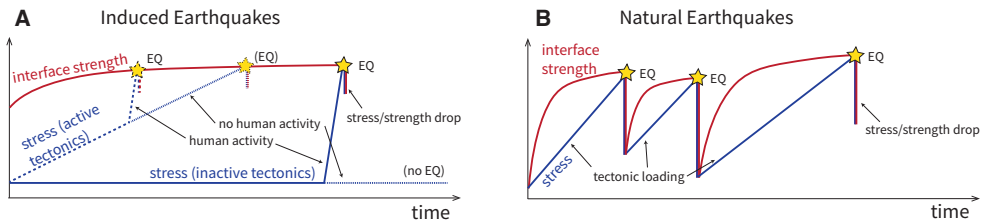


Figure 4.6: *Mechanisms of natural and induced earthquakes.* Schematic explanation of stress (blue) and interface strength (red) evolution for induced and natural earthquakes. Panel (A) explains the induced earthquake occurrence in scenarios of active (dashed lines) and inactive (solid lines) tectonics. The dotted lines are scenarios without human activities. Panel (B) explaining natural earthquake occurrence is modified from [Di Toro et al., 2012].

fast slips. Given its logarithmic growth with time, an exponentially longer healing time would be required to successively increase the stress drop of the subsequent (a-)seismic event by the same amount (Fig 4.5A). For this reason, a fault's potential to generate earthquakes (instead of aseismic events) will not change much during the timescale of human life. The quantification in Fig. 4.5B thus highlights our ability to forecast the occurrence of future induced earthquakes in a region, if good constraints on the fault properties and time since the last fault activity are available. Natural earthquakes, however, have relatively short recurrence intervals. Hence fast coseismic and postseismic healing mechanisms should be more decisive in tectonically active regions [Heaton, 1990; Bedford et al., 2023]. Interseismic Dieterich-type healing, as discussed in this work, could well be negligible.

Another difference between induced and natural earthquakes is whether the stress accumulation is due to tectonic loading or human perturbation [Di Toro et al., 2012] (Fig 4.6). It is necessary to reiterate that stress accumulation is the cause of earthquakes and aseismic events. Even though healing is used to explain the observed fast slips, no earthquakes will eventually occur if the stress change due to subsurface engineering remains small. In the absence of tectonic loading, like the Groningen gas field focused on in this study and many intracontinental settings, all the processes that bring the fault closer to failure and prepare enough energy to achieve fast slip only begin after human interference. If the fault is being tectonically loaded at the same time, then human activities will speed up the (already existing) stress accumulation and eventually bring forward the earthquake nucleation of a later natural event. This scenario

explains the earthquakes in many fluid injection sites in North America [Huang *et al.*, 2017]. Figure 4.6 serves as a conceptual comparison between induced and natural seismicity.

## 4.4 Summary

We showed that, in contrast to current theory and operational strategies, earthquakes can nucleate on VS fault segments, as long as they have been able to heal in an inactive tectonic environment on a historical to geological timescale. Fault strength gained during fault healing allows for adequate stress drop and fracture energy for the subsequent induced event. This means that earthquakes, rather than aseismic events, can occur in reservoir rocks that are being targeted for their safety in sustainable explorations, making them more dangerous than currently anticipated. However, VS fault portions will not be re-locked. They cannot nucleate future earthquakes on human timescales, nor can they be ruptured by adjacent seismic events. This effect of healing that increases seismic potential also applies to VW faults. Our explanation highlights the importance of a better understanding and quantification of fault healing in terms of healing rates as well as duration. This is critical in order to correctly assess induced seismic hazard in all reservoir settings. Considering recent political and societal unrest, reliable hazard assessments may well be a key factor in deciding how much the shallow subsurface can contribute to transiting towards a society driven by sustainable energy.

## 4.5 Methods

### 4.5.1 Model and solver

**Reservoir** We simulate earthquake sequences on a normal fault governed by rate-and-state friction, crosscutting a depleting gas reservoir (Fig. 4.11). The setup and parameters follow preceding studies on the Zeerijp region in the Groningen gas field [Orlic and Wassing, 2013; Van den Bogert, 2015; Buijze *et al.*, 2019]. We restrict the research area to be between 2000 and 4000 m depth with a reservoir of 200 m thickness centered at 2950 m depth. The reservoir is crosscut

by a plane fault with a dip angle of 70 degrees. The fault offsets both sides of the reservoir by 50 m. We cut the horizontal direction at 2000 m distance away from both sides of the fault plane. The setup is modeled in 2-D with the plane-strain assumption. The parameters are summarized in Table 4.1.

The medium is assumed to be poroelastic. Under the quasi-dynamic approximation, we write out the momentum balance equations

$$\begin{aligned}\frac{\partial \sigma_{xx}}{\partial x} + \frac{\partial \sigma_{xz}}{\partial z} &= 0 \\ \frac{\partial \sigma_{xz}}{\partial x} + \frac{\partial \sigma_{zz}}{\partial z} &= 0\end{aligned}\quad (4.2)$$

where subscripts  $x$  and  $z$  are the horizontal and vertical coordinates, respectively.  $\sigma_{ij}(i, j = x, z)$  are the components of the total stress tensor denoting the total stress acting along the  $j$  axis on the plane that is normal to the  $i$  axis. Hooke's law relates the effective stress tensor to the displacement vector  $(u_x, u_z)$  by

$$\begin{aligned}\sigma'_{xx} &= (\lambda + 2G) \frac{\partial u_x}{\partial x} + \lambda \frac{\partial u_z}{\partial z} \\ \sigma'_{xz} &= \lambda \left( \frac{\partial u_x}{\partial z} + \frac{\partial u_z}{\partial x} \right) \\ \sigma'_{zz} &= \lambda \frac{\partial u_z}{\partial z} + (\lambda + 2G) \frac{\partial u_x}{\partial x}\end{aligned}\quad (4.3)$$

with Lamé's two constants  $\lambda$  and  $G$ . The pore pressure  $P$  connects the total stress and the effective stress via

$$\begin{aligned}\sigma'_{xx} &= \sigma_{xx} - \alpha P \\ \sigma'_{xz} &= \sigma_{xz} \\ \sigma'_{zz} &= \sigma_{zz} - \alpha P\end{aligned}\quad (4.4)$$

where  $\alpha$  is the Biot coefficient. We prescribe constant stress boundary at the top of the model that satisfies the lithostatic pressure. The other three boundaries are left to be free-slip to mimic the far-away boundary.

For simplicity, we assume a homogeneous pressure change inside the reservoir due to gas extraction instead of modeling the corresponding fluid flow. No pore pressure change exists outside of the reservoir. During each timestep, the pressure change

$$\delta P = \dot{P} \delta t \quad (4.5)$$



where the pressure rate  $\dot{P}$  is zero before gas production starts. It is assumed to be a constant that matches the average pressure change rate during the past sixty years of production in Groningen [Richter *et al.*, 2020]. This simplification is justified based on the observation of relatively uniform depletion and little pressure difference across the faults [van Oeveren *et al.*, 2017]. In this way, we have applied a one-way coupling between pressure change and rock deformation, meaning that no feedback of rock deformation on pressure change is modeled, as gas is very compressible compared to the reservoir rock [Buijze *et al.*, 2019]. By assuming a homogeneous pressure change within the reservoir we ignore (i) the diffusion and convection taking place within the reservoir and (ii) the permeability of the fault interface and over- and under-burden. This approximation makes the instantaneous traction of the pressure front not possible. The interaction of the fluid pressure front and the rupture front is addressed in previous numerical and experimental works on induced seismicity [Garagash and Germanovich, 2012; Dublanchet, 2019]. Their methodologies and conclusions can be included in our models to obtain a further understanding of earthquake physics of this type.

The initial conditions are chosen according to the geological survey in Groningen ([Buijze *et al.*, 2019] and reference therein). The stress condition follows the lithostatic pressure gradient with hydrostatic fluid and gas pressure. Gas is only present within the reservoir and this results in an overpressure of 3 MPa, which agrees with the commonly observed value in Northern Netherlands [Verweij *et al.*, 2012].

**Fault** The fault is assumed to be governed by rate-and-state friction [Dieterich, 1979; Ruina, 1983]. We use the regularized version to avoid near-zero singularity

$$\tau_s = a\sigma'_n \operatorname{arcsinh} \left\{ \frac{V}{2V_0} \exp \left[ \frac{\mu_0}{a} + \frac{b}{a} \ln \left( \frac{\theta V_0}{D_{RS}} \right) \right] \right\} + \eta V. \quad (4.6)$$

The evolution of the state variable  $\theta$  is governed by one among several different evolution descriptions, the aging law [Ruina, 1983]

$$\dot{\theta} = 1 - \frac{V\theta}{D_{RS}}. \quad (4.7)$$

$\mu_0$  is the reference friction coefficient at the reference slip rate  $V_0$ , the characteristic slip distance is  $D_{RS}$ , and  $a$  and  $b$  are parameters that describe the

relative influence of direct and evolutionary effects, respectively. The parameter  $\eta = G/(2c_s)$  used in (4.6) refers to the “radiation damping term” used in the quasi-dynamic approximation of inertia [Rice, 1993; Cochard and Madariaga, 1994]. The fault functions as an additional interface condition on top of the boundary conditions mentioned above. Namely, the traction on either side of the fault needs to be equal and opposite so that the shear stress  $\tau_s$  and effective normal stress  $\sigma'_n$  can be solely defined on the fault plane as its projection. The slip rate  $V$  is defined by the difference in tangential motion across the fault whereas difference in normal motion is fixed at zero as no fault opening is allowed. That is

$$\begin{aligned}\tau_s &= \hat{n} \cdot \boldsymbol{\sigma}'|_{\Gamma^+} \cdot \hat{t} = \hat{n} \cdot \boldsymbol{\sigma}'|_{\Gamma^-} \cdot \hat{t} \\ \sigma'_n &= -\hat{n} \cdot \boldsymbol{\sigma}'|_{\Gamma^+} \cdot \hat{n} = -\hat{n} \cdot \boldsymbol{\sigma}'|_{\Gamma^-} \cdot \hat{n} \\ V &= \mathbf{u}|_{\Gamma^+} \cdot \hat{t} - \mathbf{u}|_{\Gamma^-} \cdot \hat{t} \\ 0 &= \mathbf{u}|_{\Gamma^+} \cdot \hat{n} - \mathbf{u}|_{\Gamma^-} \cdot \hat{n}\end{aligned}\tag{4.8}$$

where  $\Gamma^+$  and  $\Gamma^-$  refers to two sides of the fault interface,  $\hat{n}$  and  $\hat{t}$  are the unit vectors perpendicular and parallel to the fault, respectively. The second equation gets a negative sign because we use the convention that compressive normal stress is positive.

The initial stress on the fault matches the initial stress condition in the medium. The initial slip rate is set to be near zero due to the absence of tectonic activity before gas production. The state variable is calculated accordingly.

In Fig. 4.5 we introduced dynamic weakening due to flash heating into the model. This is realized by reformulating the rate-and-state friction to incorporate a further reduction in frictional coefficient at high slip rates. We adopted the expression used in [Rice and Ben-Zion, 1996; Goldsby and Tullis, 2011]

$$\tau_s = \frac{a\sigma'_n \operatorname{arcsinh} \left\{ \frac{V}{2V_0} \exp \left[ \frac{\mu_0}{a} + \frac{b}{a} \ln \left( \frac{\theta V_0}{D_{RS}} \right) \right] \right\}}{1 + \frac{L}{\theta V_w}} + \eta V.\tag{4.9}$$

where  $V_w$  is the velocity threshold when flash heating causes 50% reduction in steady-state friction coefficient. Namely, the effect of flash heating becomes notable (causes 1% reduction) at  $0.01V_w$ .

**0-D model** We also use a simplified 0-D model, in which only the shallowest point on the fault inside the reservoir (marked in orange in Fig. 4.11) is modeled, for

our parameter study. The effective normal stress and shear stress on the fault are a result of the poroelastic effect that is defined by the Biot coefficient, Poisson ratio and fault dipping angle

$$\begin{aligned}\tau_s &= \tau_{s0} + \gamma_s P \\ \sigma'_n &= \sigma'_{n0} + \gamma_n P.\end{aligned}\tag{4.10}$$

where  $\tau_{s0}$  and  $\sigma'_{n0}$  are the initial stresses,  $\gamma_s$  and  $\gamma_n$  are the two stress path parameters, which can be extracted from the loading curve in our 2D simulations [Hettema *et al.*, 2000; Jansen *et al.*, 2019]. This equation (4.10) and rate-and-state friction (4.6) and (4.7) are the controlling equations of the 0-D model.

**Solver** We use the MATLAB backslash direct solver for the PDEs stated above [The MathWorks Inc., 2019]. Spatial accuracy is satisfied by fully resolving the minimum nucleation length with  $\sim 20$  grid elements [Lapusta *et al.*, 2000; Rubin and Ampuero, 2005]. Among the several nucleation length definitions [Dieterich, 1992; Rubin and Ampuero, 2005], we have chosen the definition

$$\Lambda_0 = \frac{9\pi}{32} \frac{GD_{RS}}{b\sigma(1-\nu)}\tag{4.11}$$

because this definition is the smallest one under VW friction and is the only meaningful one under VS friction (Fig. 4.4). The size of  $\Lambda_0$  is also called the cohesive zone length or the process zone length.

We use adaptive time stepping to handle the large variation of the slip velocity. Temporal accuracy is satisfied by restricting timestep size to be inversely proportional to slip rate [Lapusta *et al.*, 2000]

$$\delta t = \zeta \frac{D_{RS}}{V_{\max}}\tag{4.12}$$

where  $V_{\max}$  is the maximum slip rate on the fault and  $\zeta$  is a factor controlled by the material and frictional parameters. The derivation of  $\zeta$  can be found in [Lapusta *et al.*, 2000].

## 4.5.2 Interface strength

For readers' convenience, we rewrite the definition of interface strength in [Nakatani, 2001]. The original definition was written with the help of the capital  $\Theta$ , here we rewrite it with the state variable  $\theta$  for better readability. The relation between the two expressions is  $\Theta = b \ln \frac{V_0 \theta}{D_{RS}}$ .

The rate-and-state friction defines the ratio between shear and normal stress  $\tau/\sigma$  by slip velocity  $V$  and the state variable  $\theta$  [Dieterich, 1979; Ruina, 1983]

$$\mu = \tau_s/\sigma_n = \mu_0 + a \ln \left( \frac{V}{V_0} \right) + b \ln \left( \frac{\theta V_0}{D_{RS}} \right). \quad (4.13)$$

Rewriting rate-and-state friction by solving for slip rate we obtain

$$\frac{V}{V_0} = \exp \left[ \frac{\frac{\tau_s}{\sigma_n} - \left( \mu_0 + b \ln \frac{V_0 \theta}{D_{RS}} \right)}{a} \right]. \quad (4.14)$$

In this way, the slip rate is defined by the relative amplitude of the applied shear force  $\frac{\tau_s}{\sigma_n}$  compared to a state-dependent variable  $\Psi = \mu_0 + b \ln \frac{V_0 \theta}{D_{RS}}$ . When the shear force is much higher than  $\Psi$ , a high slip rate is achieved, simulating the coseismic phase. If the shear force is much lower, a locked phase is simulated with a near-zero slip rate. Therefore the term  $\Psi$  in the equation behaves just as well as a description of the fault strength and thus was termed as “interface strength” by Nakatani [2001]. The first term of the aging law (4.7) describes the healing behavior since the second term can be ignored when slip rate is near zero. In this case, we can integrate equation (4.7) and substitute  $\theta$  in the definition of interface strength (4.1), which yields

$$\begin{aligned} \theta &= \theta_i + t \\ \Psi &= \Psi_i + b \ln \left( 1 + \frac{t}{\theta_i} \right) \end{aligned} \quad (4.15)$$

where  $\Psi_i$  and  $\theta_i$  are the initial values of interface strength and state. The linear growth of the state variable and thus the logarithmic growth of the interface strength with time is therefore inherent in rate-and-state friction.

Interface strength is only dependent on the state variable, which provides a memory of the fault loading and slip history via the aging law (4.7). It is not to be confused with the steady-state friction

$$\mu_{ss} = \mu_0 + (a - b) \ln \frac{V}{V_0} \quad (4.16)$$

which is only meaningful when a steady state is achieved.

### 4.5.3 Theoretical derivation of nucleation length $L_{III}$

We derive the theoretically predicted nucleation length  $L_{III}$  in the scenario with a long healing time. This length scale is similar to what has been measured and

defined as  $2L_c$  in *Rubin and Ampuero* [2005]. We follow the derivation there and demonstrate how the healing-induced fault strength increase makes nucleation under VS friction possible and how large the corresponding nucleation length is. The balance of fracture energy  $G_c$  and consumed energy per crack growth  $G_{mec}$  is used in *Rubin and Ampuero* [2005] to estimate the nucleation length. For  $0.5 < a/b < 1$ , they predict that an aseismic growth to  $2L_c$  is expected during nucleation (referred to as stage ii in this article). The fracture energy is estimated from the slip-weakening curve (Fig. 4.3)

$$G_c = \frac{\sigma b D_{RS}}{2} \left( \ln \frac{V_f \theta_i}{D_{RS} \Omega_f} \right)^2, \quad (4.17)$$

where  $V_f$  and  $\theta_f$  are slip rate and state after the crack front arrival, respectively.  $\Omega = V\theta/D_{RS}$  is a measure of how far the fault is from steady state. The consumed energy per crack length is estimated from the ambient-to-residual stress drop

$$G_{mec}(\mathcal{L}) = \frac{\pi \mathcal{L}}{2G'} \Delta\tau^2 \quad (4.18)$$

where  $\mathcal{L}$  is the current crack length,  $G' = G/(1-\nu)$  is the equivalent shear modulus and  $\Delta\tau$  is the ambient-to-residual stress drop, i.e. the difference between the ambient stress before crack arrival and the residual stress after stress drop. In *Rubin and Ampuero* [2005], this was given as

$$\Delta\tau = -\sigma b \ln \Omega_f + \sigma(b-a) \ln \frac{V_f}{V_i} \quad (4.19)$$

where  $V_i$  is the background slip rate which is controlled by the loading condition. This expression can only be positive if  $a < b$ , given  $\Omega_f \sim 1$ . This is reasonable and explains why natural earthquakes do not occur on VS faults. However, for induced seismicity, the reactivated fault did not experience a postseismic and interseismic phase and thus the initial stress is higher than the steady-state ambient stress used in *Rubin and Ampuero* [2005]. Taken this into consideration, the deviation from steady-state  $\Omega_i = V_i \theta_i / L$  before nucleation should be added to (4.19), therefore

$$\Delta\tau = \sigma b \ln \Omega_i + Eq.(19) = \sigma b \ln \frac{\Omega_i}{\Omega_f} - \sigma(a-b) \ln \frac{V_f}{V_i}. \quad (4.20)$$

Since  $\theta_i$  is large after a long period of healing, this expression can become positive even when  $a > b$ . This explains from another perspective why induced

earthquakes are possible on VS faults. By equating  $G_c$  and  $G_{mec}$ , we have

$$L_{III} = 2L_c = \frac{2}{\pi} L_b \left[ \frac{\ln \Omega_i / \Omega_f + \ln V_f / V_i}{\ln \Omega_i / \Omega_f - \frac{a-b}{b} \ln V_f / V_i} \right]^2 \quad (4.21)$$

which is the length of aseismic nucleation growth.

For a better understanding of this expression, we look at several limit cases. We assume  $\ln \Omega_i / \Omega_f$  and  $\ln V_f / V_i$  are positive for simplicity. If  $\ln \Omega_i / \Omega_f \ll \ln V_f / V_i$  and  $a < b$ , this is exactly the assumption [Rubin and Ampuero, 2005] made. The limiting value of  $L_{III}$  is  $L_\infty = \frac{2}{\pi} (\frac{b}{b-a})^2 L_b$ . Otherwise, we notice that the value in the bracket in (4.21) is always larger than 1 and increases as  $a/b$  increases. This indicates that, similar as Rubin and Ampuero [2005], an aseismic growth of nucleation length to  $L_{III}$  should also be expected when  $a > b$ . Even when  $0.5 < a/b < 1$ , the not-to-be-ignored  $\Omega_i$  of induced seismicity makes the value of  $L_{III}$  different than [Rubin and Ampuero, 2005] suggested.

Due to the limited spatial extension of the reservoir width in our study, the nucleation might not be able to achieve its maximum length as  $L_{III}$  predicts. If this is the case, the maximum nucleation length will be the reservoir width (Fig. 4.3). This incomplete nucleation often results in a lower maximum slip rate. Additional simulations are conducted to show the dependence of  $L_{III}$  on frictional parameters. For example, the nucleation length increases when  $b$  is decreased, as shown in Fig. 4.12.

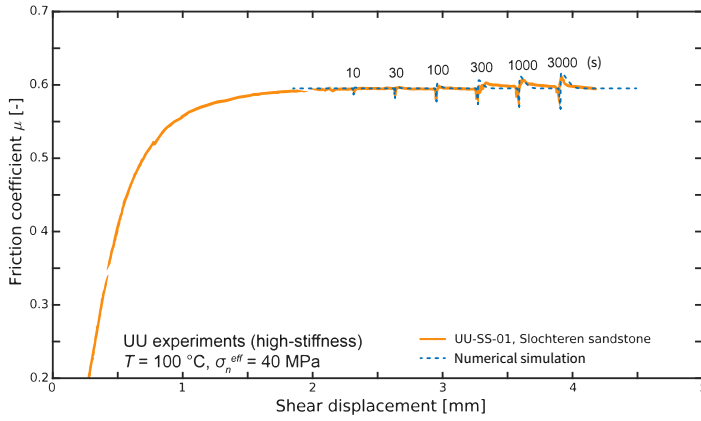


Figure 4.7: Comparison of numerical simulation and laboratory healing of different durations. Laboratory data are from the experiment UU-SS-01 using Groningen Slochteren sandstone in [Hunfeld et al., 2020], numerical results are from the 0-D model explained in this study. Healing durations of 10 to 3000 s were tested.

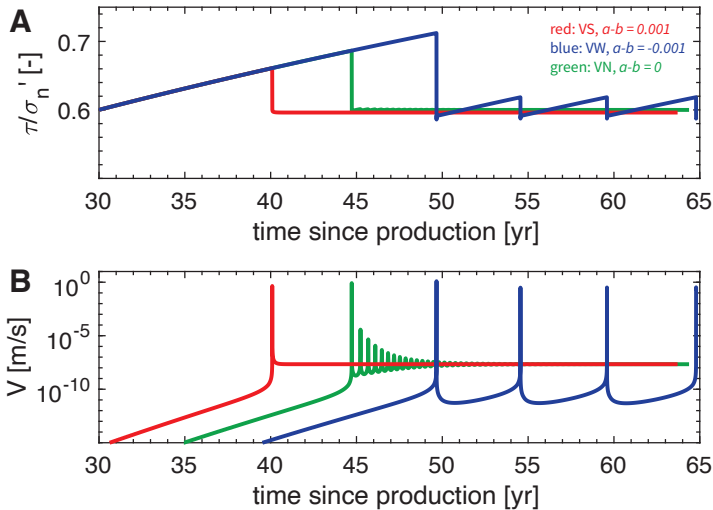


Figure 4.8: Earthquake sequence after healing of 30 Ma. Simulation of (A) the ratio of shear stress and effective normal stress  $\tau/\sigma'_n$  and (A) the slip rate in 0-D in VS (red,  $a = 0.005$ ,  $b = 0.004$ ,  $D_{RS} = 2$  mm), VW (blue,  $b = 0.006$ ) and VN (green,  $b = 0.005$ ) scenarios.

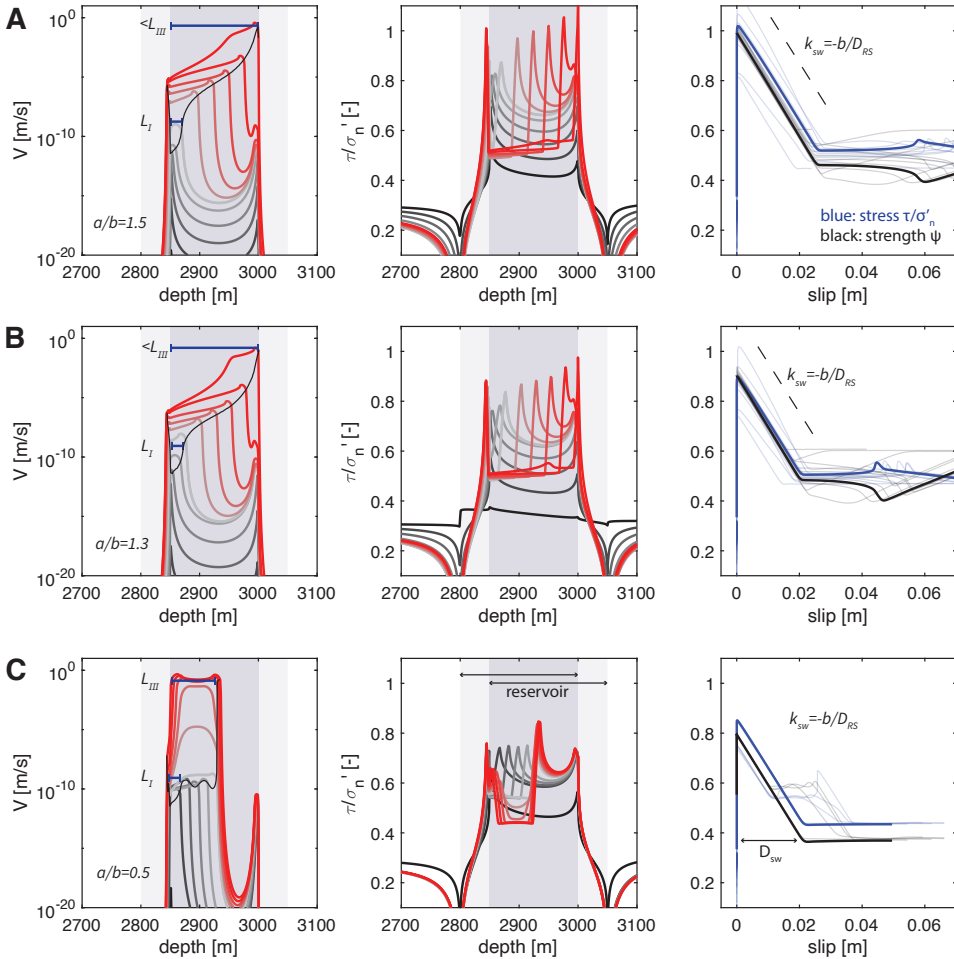


Figure 4.9: *Simulation of the first induced earthquake in 2-D in VS and VW scenarios with several  $a/b$  ratios: (A)  $a/b = 1.5$ , (B)  $a/b = 1.3$ , (C)  $a/b = 0.5$  with fixed  $b = 0.01$  and  $D_{RS} = 0.5$  mm,  $\mu_0 = 0.5$ , healing time  $t_h = 100$  Ma. The temporal evolution of slip rate, the ratio between the shear stress and the effective normal stress, and its evolution with respect to slip are plotted. The interseismic and nucleation phases are plotted in black and gray, with gradual transit to the coseismic phase in red. The plotted lines are not picked up in regular time intervals. The measured nucleation lengths  $L_I$ ,  $L_{II}$  and  $L_{III}$  are shown as blue bars on the top. The dashed black lines track the temporal-spatial evolution of the nucleation front. The purple shadows in the background specify the range of the reservoir depth, on the hanging wall side and the footwall side, respectively. The detailed model setup is depicted in fig. 4.11. The evolution of interface strength  $\Psi$  (Eq. 4.1) is plotted in black for reference. The multiple transparent lines in the background are the observations from different locations (every 20 m between 2800 m and 3050 m depth) on the fault. The bold lines are the observation at the center of the reservoir (2950 m depth).*



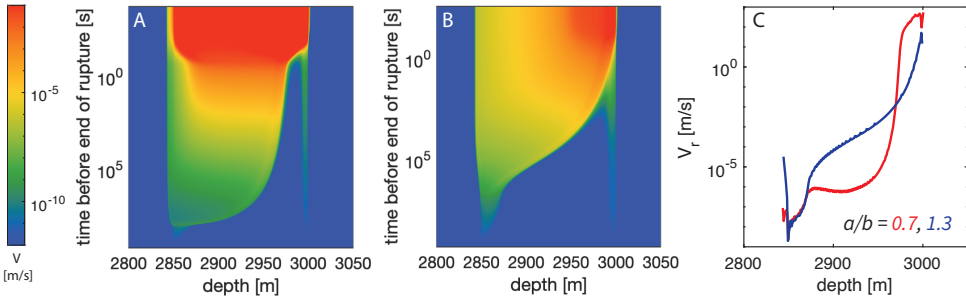


Figure 4.10: *Nucleation of the first induced earthquake in 2-D in VS and VW scenarios with (A)  $a/b = 0.7$ , (B)  $a/b = 1.3$ , with fixed  $b = 0.01$  and  $D_{RS} = 0.5$  mm,  $\mu_0 = 0.5$ , healing time  $t_h = 100$  Ma. The spatial-temporal evolution of slip rate is shown in color. (C) Measured propagation speed of the nucleation front for  $a/b = 0.7$  (red) and  $a/b = 1.3$  (blue).*

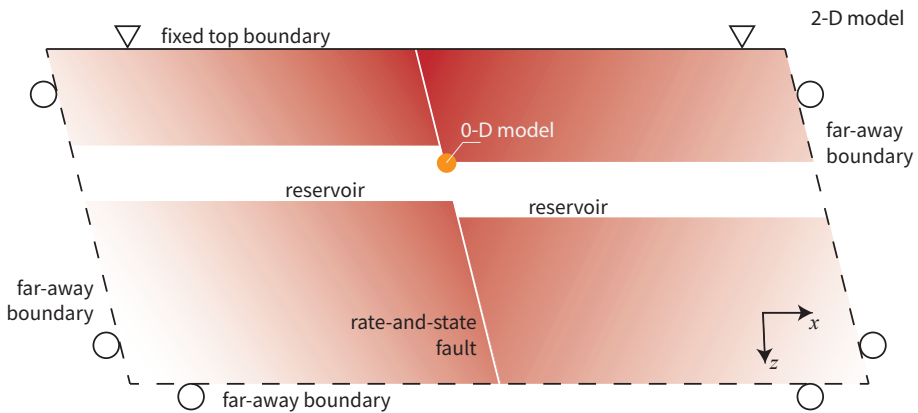


Figure 4.11: *Model setup of a normal fault crosscutting a depleting gas reservoir. The setup is modeled in 2-D with plane-strain assumption. The simplified 0-D model, in which only the top inner corner of the reservoir is modeled, is marked in orange. See the Methods for the explanations of the boundary conditions.*

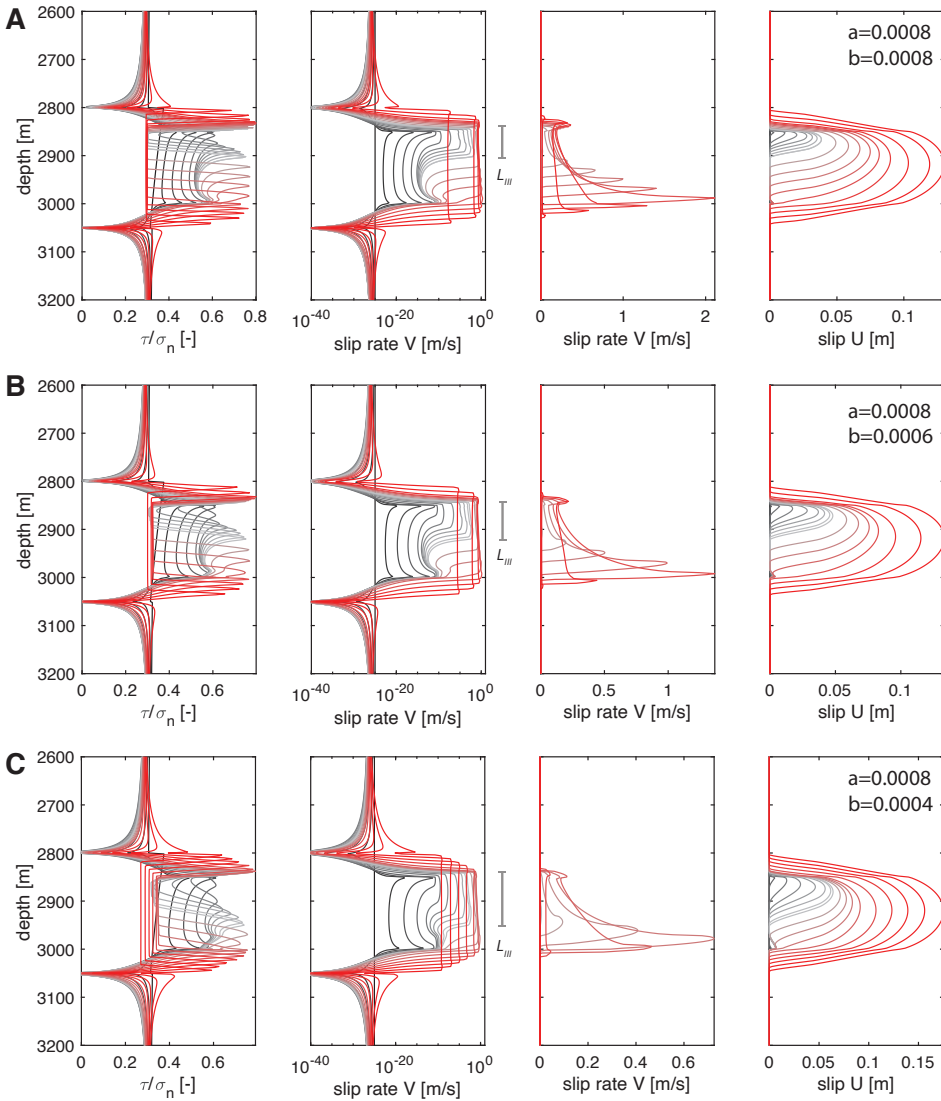


Figure 4.12: *Simulation of the first induced earthquake in 2-D with different  $b$  values.  $a = 0.0008$ ,  $\mu_0 = 0.3$  and other parameters are kept fixed. The interseismic and nucleation phases are plotted in black and gray, with gradual transit to the coseismic phase in red. The plotted lines are not picked up in regular time intervals. The nucleation zones are highlighted by the gray bars.*

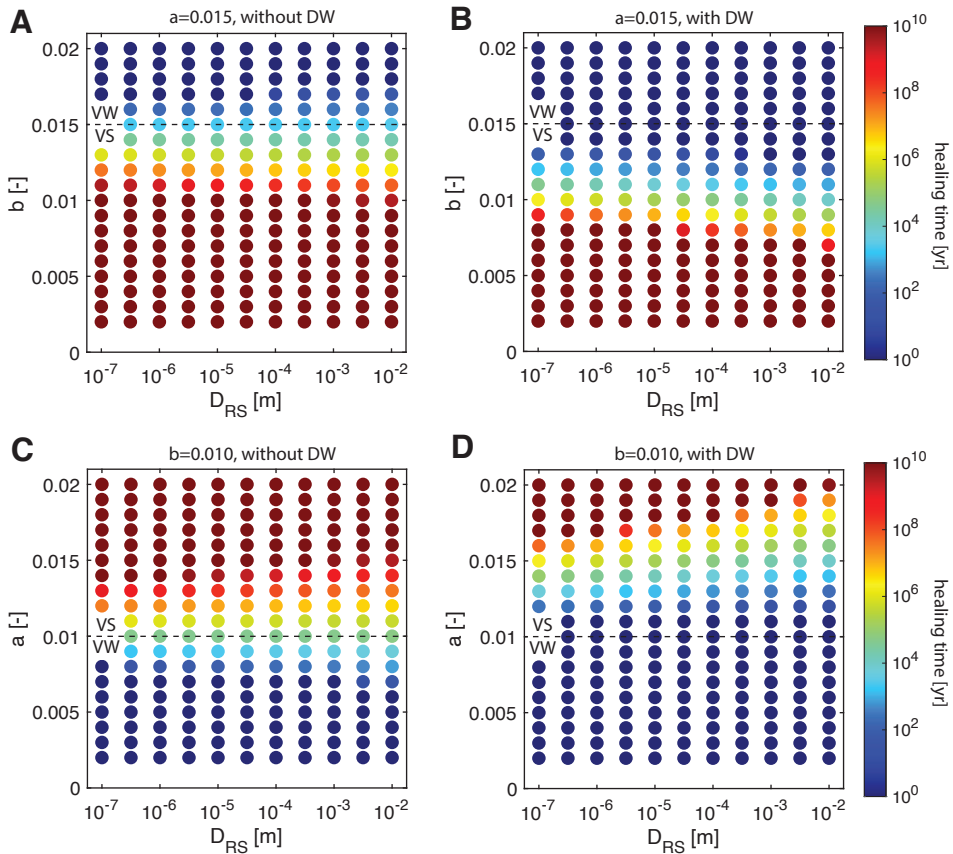


Figure 4.13: *Parameter study of frictional properties and healing time: (A-B) the parameter study on  $b$  and  $D_{RS}$ , (C-D) the parameter study on  $a$  and  $D_{RS}$ , (A, C) without dynamic weakening, (B, D) with dynamic weakening. The colored circles show the required healing time so that the first earthquake, after fault reactivation, can reach a slip rate of 1 m/s.*

Table 4.1: *Physical and numerical parameters*

| Parameter                                    | Symbol     | Value                   |
|----------------------------------------------|------------|-------------------------|
| Density                                      |            |                         |
| - rock (sandstone)                           | $\rho_r$   | 2400 kg/m <sup>3</sup>  |
| - fluid                                      | $\rho_f$   | 1150 kg/m <sup>3</sup>  |
| - gas                                        | $\rho_g$   | 200 kg/m <sup>3</sup>   |
| Shear wave speed in rock                     | $c_s$      | 1.645 km/s              |
| Poisson ratio of rock                        | $\nu$      | 0.15                    |
| Biot coefficient                             | $\alpha$   | 1                       |
| Reference friction coefficient               | $\mu_0$    | 0.3- <u>0.6</u>         |
| Reference slip rate                          | $V_0$      | 10 <sup>-6</sup> m/s    |
| Characteristic slip distance <sup>a</sup>    | $D_{RS}$   | 0.1- <u>0.5</u> -100 mm |
| Rate-and-state direct effect <sup>a</sup>    | $a$        | 0.002-0.02              |
| Rate-and-state evolution effect <sup>a</sup> | $b$        | -0.002-0.02             |
| Dynamic weakening velocity (Eq. 4.9)         | $V_w$      | 1 m/s                   |
| Far-field loading rate                       | $V_p$      | 0 m/s                   |
| Pressure depletion rate <sup>b</sup>         | $\dot{P}$  | -0.0127 Pa/s            |
| Loading path factor (0-D model) <sup>c</sup> |            |                         |
| - on normal stress                           | $\gamma_n$ | -0.2818                 |
| - on shear stress                            | $\gamma_s$ | -0.4469                 |

<sup>a</sup> The parameter range used in this study, underlined values are the default unless specified in figure captions.

<sup>b</sup> Based on the average production rate of Groningen gas field since 1961 [*Richter et al., 2020*].

<sup>c</sup> Simulated values extracted from the 2-D model.



# 5

## Earthquake nucleation and arrest in a heterogeneous earthquake sequence model for Groningen

In preparation for submission as: *Li, M., Niemeijer, A. R., Vossepoel, F. C., & van Dinther, Y. (2024). Earthquake nucleation and arrest in a heterogeneous earthquake sequence model for Groningen. Solid Earth.*

## Abstract

To assess the seismic hazard in Groningen, it is crucial to understand the source processes, including the location of earthquake nucleation and the rupture length. However, these fundamental questions are not well answered by seismological observations due to the uncertainties in measurements and inversions. Here, we apply the theory and model of Chapter 4 to the Groningen gas field and newly take lithology-specific elastic and frictional parameters into account. Using parameters obtained from in-situ and laboratory measurements, we simulated earthquakes nucleating from the velocity-strengthening sandstone reservoir layer that rupture throughout the whole reservoir thickness. The nucleation and rupture processes are generally similar to the homogeneous model used in Chapter 4, with a nucleation starting from the top corner of the hanging wall side of the reservoir. However, a larger pore pressure change is needed due to the less efficient loading, which is caused by the heterogeneous elastic modulus. We did not find evidence that earthquakes can nucleate from the velocity-weakening Basal Zechstein layer inside the caprock, nor that this layer can be ruptured seismically. The rupture in our simulations did not propagate into the underburden Carboniferous shale layer either. The low strength and low healing rate of this layer only allows it to creep in an aseismic manner. This finding is very important in estimating the maximum earthquake magnitude and defining the seismic hazard in Groningen. Given uncertainties in parameters and fault geometry, we will build on our latest model with high likelihood to rupture into the Carboniferous underburden and test whether other factors, such as reservoir thickness and fault offset, will allow seismic propagation into the underburden.

## 5.1 Introduction

On August 16, 2012, at 22:31 local time, an earthquake of magnitude ML 3.6 occurred near Huizinge village, Groningen province, the Netherlands. This earthquake was a result of gas extraction from the Groningen gas field, Europe's largest gas field. While not the first recorded earthquake in the area, it was the most powerful one up to now, causing damage to buildings and spreading fear among locals [Dost and Kraaijpoel, 2013]. The Groningen gas field was discovered in 1959 and soon became one of the largest onshore reservoirs in the world [de Jager and Visser, 2017]. Production started in 1963 and the first earthquake was recorded in 1991 with a magnitude of 2.5. The increasing number of felt earthquakes since a decade ago marked a turning point in the public perception of induced seismicity in the Netherlands and impacted the future of Dutch gas production. Before the Huizinge event, it was believed that seismic events in the gas fields would remain small, but the earthquake showed otherwise, causing a reevaluation of gas production and the potential risks associated. Following the Zeerijp earthquake in 2018 (ML 3.4), the Dutch government decided to completely halt gas production by 2030, later moving up the timeline to 2022. However, the public concern about induced seismicity, perhaps even after field closure, remains unsettled. A comprehensive understanding of the earthquake processes helps to better estimate the seismic hazard and may ultimately alleviate social concerns. One of the central questions is where the earthquake nucleates and how large earthquake ruptures can become.

The recent advancements in the seismological instrumentation network in the Groningen field have significantly enhanced earthquake location accuracy [Dost *et al.*, 2017]. Improvements in the seismic network since 2014 and the introduction of a 3D velocity model by NAM in 2017 reduced the uncertainties of the earthquake location to 0.1 to 0.3 km horizontally and 0.3 km vertically [Dost *et al.*, 2017]. The relocation of seismic events between 2014 and 2016 highlighted two key observations: the relocated events often clustered around known faults, and a majority occurred within the reservoir formation [Spetzler and Dost, 2017; Willacy *et al.*, 2019]. This aligns with data from deep borehole arrays [Zhou and Paulssen, 2020] and full waveform inversion results [Willacy *et al.*, 2019]. Moment tensor inversions of larger events, such as the 2012 Huizinge, and 2018 Zeerijp earthquakes, indicated a normal faulting mechanism on NW-SE faults, consistent with the regional stress field where the maximum horizontal stress aligns



NNW-SSE [Van Eijs, 2015].

However, even the 0.3 km uncertainty in hypocenter inversion is not good enough, compared to the average reservoir thickness, which is between 50 and 300 m. This raised the inconsistency in the inversions and their interpretations. *Spetzler and Dost* [2017]; *Willacy et al.* [2019] agree that most (100% and 70% respectively in the two studies) earthquakes nucleate within the depth range of the reservoir, while *Smith et al.* [2020] could locate only 28% hypocenters within the reservoir domain and rather located about 60% in the caprock layer. This debate cannot be resolved when considering results from laboratory experiments on the frictional properties of the simulated gouges of the reservoir rocks taken from the borehole. The reservoir rocks show mainly velocity-strengthening (VS) behavior, a frictional behavior that favors stable aseismic slips instead of earthquakes, under in-situ pressure-temperature and fluid chemistry conditions [*Hunfeld et al.*, 2017]. Based on these experiments, the key candidate for earthquake nucleation is a 50 m thick layer in the caprock. This anhydrite- and carbonate-rich Basal Zechstein (BZ) layer was measured to be velocity-weakening (VW) under specific conditions. If nucleation occurs in this layer, it may or may not have a chance to rupture into the reservoir, which has a consequences on the earthquake magnitude. In this study, we constructed a numerical model to explore in which of the lithological layers Groningen earthquakes might nucleate. In Chapter 4 we have demonstrated how fault healing contributes to earthquake nucleation within the reservoir. Here, we center our research on whether the nucleation may also occur outside the reservoir, for example, in the BZ layer.

Another crucial question to answer is how large earthquake rupture can become. Rupture length directly links to seismic moment and thus can be a proxy to estimate earthquake magnitude. If the rupture is restricted to the reservoir layer, then the rupture width in the dip direction is limited. In that case, the reservoir thickness can be used to estimate the maximum magnitude,  $M_{max}$ . Seismological studies sometimes adopt a simple Brune model with a Heaviside source time function to describe earthquake rupture [*Brune*, 1970; *Madariaga and Ruiz*, 2016]. This model assumes a circular crack with a sudden stress drop at the tip to build the relationship between the rupture radius, slip, and stress drop to the seismic moment [*Kraaijpoel and Dost*, 2013]. Adopting this model, the 2012 Huizinge earthquake is estimated to have a rupture radius of about 390

m, a stress drop of 2.5 MPa, and an average slip of 50 mm. It should be noted that these computations rely on assumptions regarding rupture shape and kinematics. Moreover, considering the reservoir thickness (50-300 m), the circular crack assumption might no longer be valid. The horizontal extent of the rupture inside the reservoir might be much larger compared to its vertical extent. Therefore, it is not yet clear whether the rupture finally goes to the over- and underburdens and how large  $M_{max}$  will be. To avoid making large assumptions about the source behaviors, we model earthquakes with its associated aseismic slips in sequence and then utilize quasi-dynamic models to simulate the entire earthquake process. Since a large extent above the reservoir, up to 1000 m thick, is occupied by Zechstein rock salts (ZR) that deform in an aseismic manner due to viscous relaxation of stresses, here we center our research on whether the rupture may propagate into the underburden.

Rapid progress has been made in understanding the in-situ geomechanical and rheological properties of the rocks, thought to be present in faults in the Groningen gas field. Benefiting from the newly available findings and laboratory data [Lele *et al.*, 2015; Hunfeld *et al.*, 2017, 2020; Arts *et al.*, 2023], we build heterogeneous models that include the dominant lithological layers in Groningen. Several models have been proposed to understand the mechanics and spatio-temporal characteristics of induced seismicity in the Groningen field, including models that focus on seismicity rates in the fault network in response to static stress changes [Candela *et al.*, 2019, 2022; Smith *et al.*, 2022; Heimisson *et al.*, 2022; Acosta *et al.*, 2023], models that focus on modeling the time-dependent stress change on a single fault and the induced fault failure [Van Wees *et al.*, 2014, 2017; van Wees *et al.*, 2018; Jansen *et al.*, 2019; Jansen and Meulenbroek, 2022; Cornelissen and Jansen, 2023], and models that focus on modeling the earthquake processes of a single earthquake using quasi-dynamic or dynamic approaches [Zbinden *et al.*, 2017; Buijze *et al.*, 2019; Buijze, 2020; Weng *et al.*, 2021; Ruan *et al.*, 2023]. For example, Jansen *et al.* [2019]; Jansen and Meulenbroek [2022]; Cornelissen and Jansen [2023] derived analytical and semi-analytical expressions of the fluid-induced stress changes on displaced vertical and inclined faults and the associated aseismic slips. Buijze *et al.* [2019]; Buijze [2020] used a 2-D quasi-static reservoir depletion model to simulate until fault activation coupled to a dynamic rupture model for the subsequent dynamic rupture. Ruan *et al.* [2023] applied a similar approach in 3-D and confirmed the aforementioned findings. Despite rate-and-state friction formulation being adopted in some seismicity models,

most models used a combination of the Mohr-Coulomb failure criterion and linear slip-weakening friction to describe earthquakes. Those models ignore the slip rate dependence of friction and thus the physical nucleation process and the post-seismic healing process cannot be incorporated into the same model to simulate the whole earthquake sequence continuously. Moreover, these models did not consider the heterogeneous elastic and frictional properties due to the presence of lithological layers [Hunfeld *et al.*, 2017, 2020]. Yet these properties govern static and dynamic fault strength and stress state and thus define fault criticality to failure. With considerable variations in rate-and-state friction parameters across lithologies as measured, yet never accounted for, velocity-strengthening behavior and absence of healing in the clay-rich rocks occupying the underburden, these heterogeneous properties could critically affect the key questions we pose. In this study, we integrate the knowledge from seismological studies of lithostratigraphy and laboratory studies of fault frictional properties to simulate lithology-dependent elastic and frictional properties in a single earthquake sequence model, which we used in Chapter 4 to evaluate how fault healing affects seismicity in general. We use this heterogeneous model to understand fault slip in a more realistic setting and aim to complete the answer to where earthquakes nucleate (i.e., inside or outside of the reservoir) and whether the rupture could propagate beyond the reservoir thickness.

## 5.2 Methods

We build forth on the model of Chapter 4 by introducing lithology-dependent elastic parameters in the medium and friction coefficients derived from fault gouges of each lithology combination (i.e. 50-50 mixtures). We simulate earthquake sequences on a normal fault governed by rate-and-state friction, crosscutting a depleting gas reservoir. The setup is modeled in 2-D in a quasi-dynamic manner, with the plane-strain assumption. The medium is assumed to be poroelastic. The assumptions on the fault friction and medium rheology, the controlling mechanical equations and the fault geometry are provided in Chapters 6 and 4. To best accommodate the fault geometry and the heterogeneous parameters, we have developed a new numerical code with staggered grid on an affine computing space, as explained in Chapter 6.

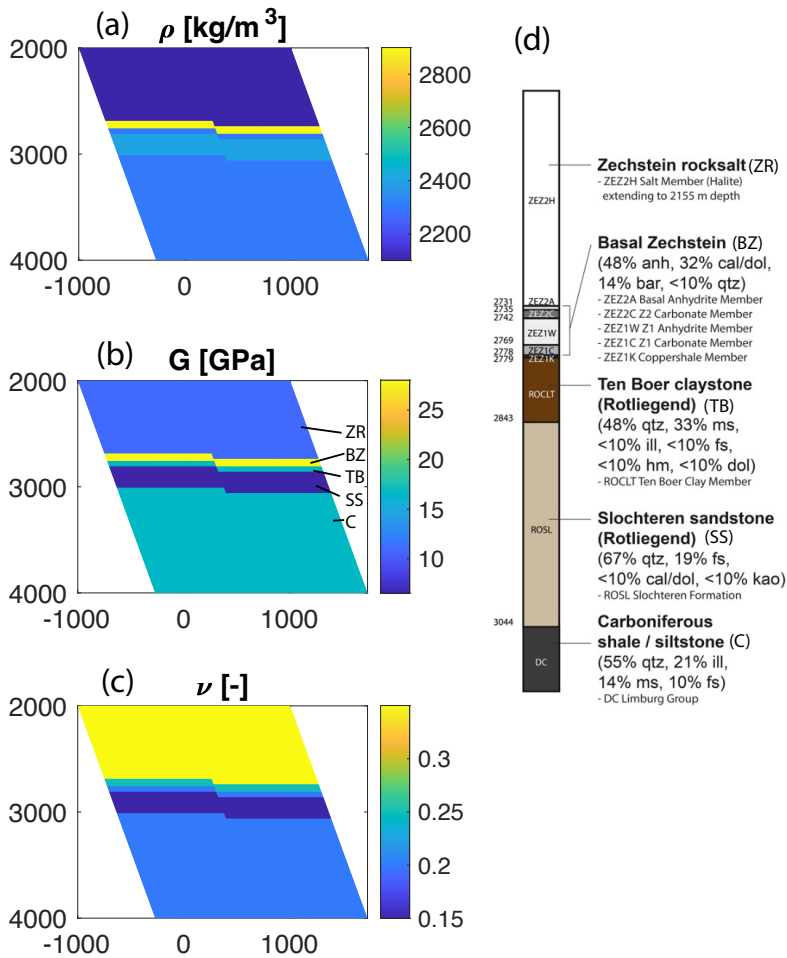


Figure 5.1: Model setup for heterogeneous reference model based on well logging. (a-c) Numerical model with stratification for (a) density, (b) shear modulus, and (c) Poisson ratio (top to bottom). (d) Lithological layers from well logging of borehole SDM-1 [Hunfeld et al., 2017].

Table 5.1: *Fault geometry and background parameters [Buijze et al., 2019; Li et al., 2023]*

| Parameter                            | Symbol    | Value                  |
|--------------------------------------|-----------|------------------------|
| Density gas in reservoir             | $\rho_g$  | 200 kg/m <sup>3</sup>  |
| Density fluid over- and underburden  | $\rho_f$  | 1150 kg/m <sup>3</sup> |
| Initial gas pressure                 | $P_0$     | 35 MPa                 |
| Dip angle                            | $\varphi$ | 70 degrees             |
| Stress ratio $\sigma_h/\sigma_v$     | $K_0$     | 0.75                   |
| Biot coefficient                     | $\alpha$  | 1                      |
| Far-field loading rate               | $V_p$     | 0 m/s                  |
| Pressure depletion rate <sup>a</sup> | $\dot{P}$ | -0.0127 Pa/s           |

<sup>a</sup> Based on the average production rate of Groningen gas field since 1961 [Richter et al., 2020].

Table 5.2: *Elastic [Lele et al., 2015] and frictional parameters [Hunfeld et al., 2017, 2020]*

| Rock type                                            | ZR               | BZ               | TB               | SS               | C                |
|------------------------------------------------------|------------------|------------------|------------------|------------------|------------------|
| Starts at [m] <sup>a</sup>                           | 2000             | 2730             | 2800             | 2850             | 3050             |
| Ends at [m] <sup>a</sup>                             | 2730             | 2800             | 2850             | 3050             | 4000             |
| Density $\rho$ [kg/m <sup>3</sup> ]                  | 2.1              | 2.9              | 2.3              | 2.4              | 2.3              |
| Young's modulus $E$ [10 <sup>9</sup> MPa]            | 30               | 70               | 40               | 15               | 40               |
| Poisson ratio of rock $\nu$ [-]                      | 0.35             | 0.25             | 0.2              | 0.15             | 0.2              |
| <b>Fault segment at juxtaposition of<sup>b</sup></b> | <b>ZR/ZR</b>     | <b>BZ/BZ</b>     | <b>TB/TB</b>     | <b>SS/SS</b>     | <b>C/C</b>       |
| Reference friction coefficient $\mu_0$ [-]           | 0.5              | 0.6              | 0.4              | 0.6              | 0.5              |
| Reference slip rate $V_0$ [m/s]                      | 10 <sup>-6</sup> | 10 <sup>-6</sup> | 10 <sup>-6</sup> | 10 <sup>-6</sup> | 10 <sup>-6</sup> |
| Characteristic slip distance $D_{RS}$ [mm]           | 0.5              | 0.5              | 0.5              | 0.5              | 0.5              |
| Rate-and-state direct effect $a$ [-]                 | 0.003            | 0.018            | 0.003            | 0.012            | 0.003            |
| Rate-and-state evolution effect $b$ [-]              | 0.001            | 0.02             | 0.001            | 0.01             | 0.001            |
| DW threshold velocity $V_w$ [m/s]                    | 1                | 1                | 1                | 1                | 1                |

<sup>a</sup> On the hanging wall side.

<sup>b</sup> See methods for the fault frictional properties of the juxtaposition of different rock types.

Our model setup follows the stratigraphy logged in the SDM1-well (Fig 5.1, Table 5.1, 5.2). Five stratigraphic units are considered. From top to bottom, these formations constitute the Zechstein rocksalt (ZR), Basal Zechstein formation (BZ), Ten Boer claystone (TB), Slochteren sandstone reservoir (SS), and Carboniferous shale/siltstone (C). The gas extraction from the Groningen field primarily targets the Slochteren formation within the upper Rotliegend group of Permian age. This geological layer is predominantly composed of fluvial and Aeolian sandstones [de Jager and Visser, 2017]. The reservoir's depth varies across the field, lying at about 2400 m in the southern region and deepening to approximately 2900 m towards the northern areas. The reservoir also thickens northward, ranging from around 50 m to exceeding 300 m. Overlying the Slochteren Formation is the Ten Boer Claystone, part of the upper Rotliegend group, with a thickness varying from several tens of meters to over 80 m. Further above lies the Triassic Zechstein formation, characterized by a 50-m thick basal sequence of anhydrite and carbonates known as the Basal Zechstein formation, succeeded by a rocksalt (Halite) formation spanning 100-1000 meters in thickness. Beneath the Slochteren Reservoir lies the Carboniferous underburden, consisting of siltstones and shales. In this study, we use the layer thicknesses recorded in the SDM-1 well log for the heterogeneous reference model and change their values to study the influence of layer thickness.

The medium properties (density, elastic modulus, Poisson's ratio) of the rock layers are assigned after the NAM 2015 report (Fig 5.1, Table 5.2) [Lele et al., 2015]. With the presence of gas and water, the Slochteren sandstone layer has a porosity ranging from 10% to 24% and a permeability from 1 to 1000 mD [de Jager and Visser, 2017]. This results in variable density, elastic modulus, and Poisson's ratio and consequently variable loading behavior due to pressure change [Buijze et al., 2019]. We use an averaged porosity value of 0.15 and the corresponding medium properties from the report.

We assign the fault parameters (dip angle, fault offset) that best represent the Groningen faults. An extensive network of over a thousand normal faults has been identified through 3D seismic interpretations [Kortekaas and Jaarsma, 2017]. These faults exhibit a steep dip [Wentinck, 2016]. We choose a dip angle of 70 degrees in the heterogeneous reference model, as most faults fall around this value [Buijze, 2020]. These faults are characterized by offsets (i.e., the vertical distance of the same lithology at both sides of the fault) typically ranging

between 20 to 100 meters and occasionally up to around 300 meters, resulting in the juxtaposition of various stratigraphic units. We choose to use 50 m in the heterogeneous reference model and change the value to study the influence of fault offset. The absolute layer depths recorded in the well log of SDM-1 are used as the stratigraphy of the hanging wall. The foot wall of the fault is shifted upward with the offset (Fig 5.1, Table 5.1).

The rate-and-state frictional properties come from numerous laboratory experiments executed under in-situ pressure-temperature conditions on simulated fault gouges, derived from rocks directly from the Groningen field [Hunfeld *et al.*, 2017, 2020]. According to the experiments, the Basal Zechstein anhydrite and the Slochteren sandstone have a large evolution parameter  $b$  in the rate-and-state friction formulation. This means they have a relatively high healing rate, indicating their seismic potential after healing during millions of years of tectonic quiescence (Chapter 4). The other fault gouges have a near zero or even negative  $b$  parameter showing almost no healing. The Basal Zechstein anhydrite is found to be velocity-weakening. The fault segments cross-cutting the other layers, including the sandstone reservoir, are weakly velocity-strengthening. For the fault portions at lithological juxtapositions, the frictional properties depend strongly on how well the gouges are mixed [Bedford *et al.*, 2022]. However, the formation of the fault gouges is changed simultaneously by fault slips. It is probably not optimal to define an interface friction in this case. Recent experiments proposed several hypotheses to approximate the frictional behavior at those bi-material faults. Arts *et al.* [2023] proposed that an interface between VW and VS materials tends to show similar velocity-dependence of friction as the VS side does, whereas the interface between statically strong and weak materials tends to be strong. Based on this hypothesis we, in the heterogeneous reference model, use the values of  $a, b, D_{RS}$  parameters from the more velocity-strengthening material while using the value of  $\mu_0$  from the stronger material. We also explore other possibilities to combine friction properties of bi-material faults such as suggested by Hunfeld *et al.* [2017]. Finally, we also include dynamic weakening due to flash heating into the model, which is activated at a slip rate threshold  $V_w$  to describe the reduction in frictional coefficient in experiments at seismic slip rates [Hunfeld, 2020]. The initial conditions (such as the pre-production stress state) and boundary conditions are the same as introduced in Chapter 4.

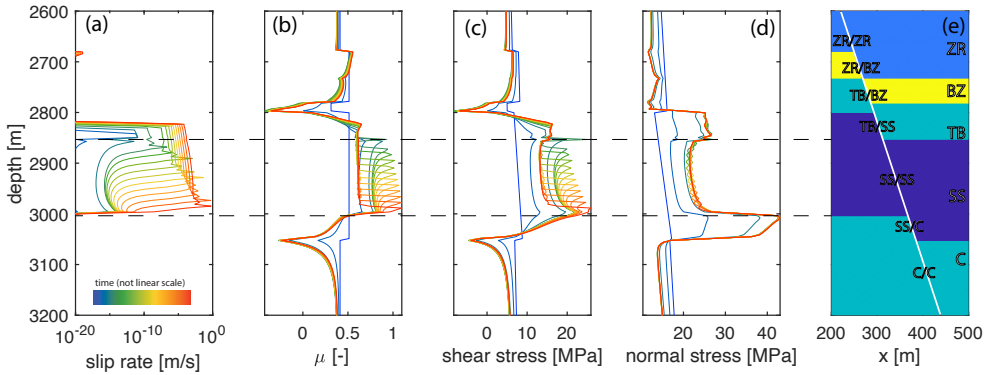


Figure 5.2: Heterogeneous reference model M1. The temporal evolutions of (a) the slip rate, (b) the frictional coefficient, (c) the shear stress, and (d) the effective normal stress are plotted. The interseismic and nucleation phases are plotted in blue and green, with a gradual transition to the coseismic phase in red. The time intervals between the plotted lines are not regular. The reservoir thickness is between the dashed black lines. The model setup is depicted in (e). From top to bottom, these formations constitute the Zechstein rocksalt (ZR), Basal Zechstein formation (BZ), Ten Boer claystone (TB), Slochteren sandstone reservoir (SS), and Carboniferous shale/siltstone (C). The usage of frictional parameters depends on the rock types on both sides (see methods).

## 5.3 Results and Analysis

### 5.3.1 Heterogeneous reference model M1

We first build a heterogeneous reference model (M1) by adding the lithological layers to the geometrical setup used in Chapter 4 (Fig 5.2). Since the gas production started after a geological timescale of tectonic inactivity, increasing shear and (effective) normal stress have been observed on the fault segment inside the reservoir (blue lines). The shallowest point of the fault completely inside the reservoir (2850 m depth) experiences the largest increase in the *frictional coefficient* ( $\mu$ , the ratio between shear and effective normal stress) and reaches the failure point after a pore pressure change of 27 MPa. As explained in Chapter 4, the failure point of the fault in the sandstone is elevated due to the tectonic timescale of healing. Fault segments close to but outside the reservoir thickness experience a slight decrease in normal stress and a sharp decrease in shear stress due to the pore pressure change. The nucleation process starts at this depth and expands downward into the gas reservoir (green lines). During this process,  $\mu$  drops about 0.4 inside the nucleation zone, accompanied by an



accelerating slip rate. The slip rate goes above the seismic rate (about 1 cm/s [Rubin and Ampuero, 2005]), where nucleation turns into rupture propagation (red lines), and finally reaches a maximum of 1 m/s at the lower boundary of the reservoir on the footwall side (3000 m depth). The pore pressure change below this depth raises the normal stress substantially but does not increase shear stress. A decrease in the frictional coefficient means no fault failure and thus cannot support the rupture to expand any further. However, at the top end of the reservoir, nucleation is allowed to propagate a small distance into the overburden due to the smaller normal stress increase. The penetration distance or arrest location is controlled by the frictional property of the Ten Boer claystone because TB is more velocity-strengthening at the TB/SS interface. Since the fault in this layer gains no strength during the long period of healing, it is easy to fail and slip subsequently (Figure 5.2). However, it is unclear why the slip rate in TB goes seismic without an accompanied stress drop. The Basal Zechstein anhydrite and the Zechstein rocksalt layers on top of it are not activated because of decreased shear stress due to reservoir depletion. Moreover, in this heterogeneous reference model M1, Basal Zechstein layers on both sides of the fault do not juxtapose. Both the BZ/ZR and the BZ/TB fault segments are controlled by the frictional properties of the other side (ZR or TB), which are velocity-strengthening with no healing. The velocity-weakening and healing properties of BZ are thus not activated in this setup (Fig 5.2). After the first earthquake, the fault segment inside the reservoir is not re-locked but continuous to creep. A second earthquake is thus not observed.

We compare the heterogeneous reference model (M1) with the model without heterogeneity (M0) as introduced in (Chapter 4) (Fig 5.3a-e). There is only one earthquake in both models. The earthquake in the heterogeneous reference model (M1) is comparable to the earthquake in the homogeneous model (M0) in terms of slip rate, stress drop and rupture behavior (Fig 5.3). However, there are several notable differences. First, the earthquake in M1 requires a larger pore pressure change before failure: 27 versus 23 MPa in M0. This means a longer period of gas production, which is probably due to the less efficient loading caused by the stratification of elastic properties. Due to the poroelastic effect, a low Poisson's ratio leads to a more efficient loading path towards the failure criterion, as shown also in Zbinden *et al.* [2017]; Buijze [2020]. In the homogeneous model M0, all lithologies had the elastic properties of the reservoir sandstone. The Poisson's ratio of the sandstone is dependent on the porosity, but is gen-

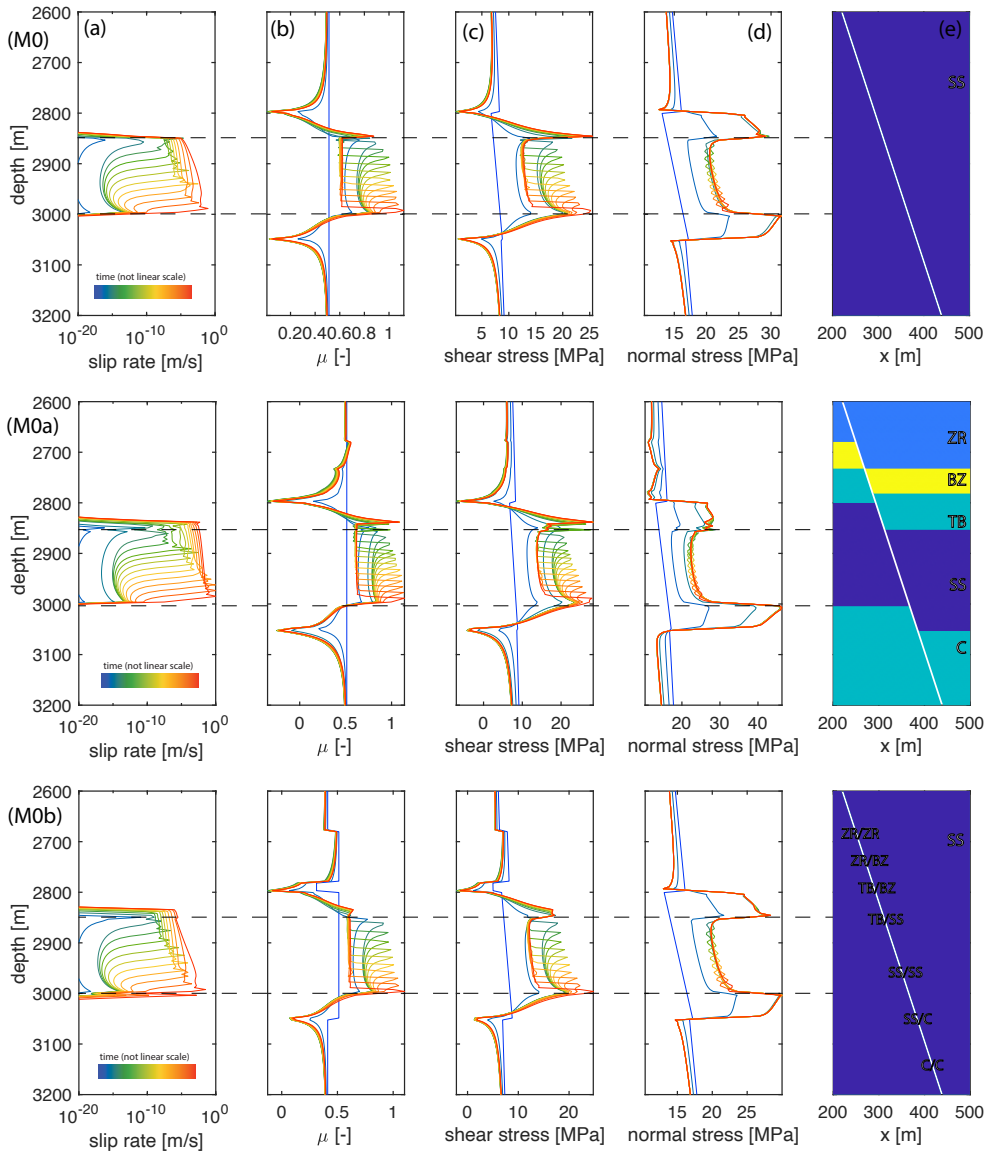


Figure 5.3: Simulations of homogeneous models  $M_0$ ,  $M_{0a}$  and  $M_{0b}$ . (Top panel) the model  $M_0$  used in Chapter 4 with homogeneous medium and frictional properties. The temporal evolutions of (a) the slip rate, (b) the frictional coefficient, (c) the shear stress, and (d) the effective normal stress are plotted. The interseismic and nucleation phases are plotted in blue and green, with a gradual transition to the coseismic phase in red. The time intervals between the plotted lines are not regular. The reservoir thickness is between the dashed black lines. The model setup is depicted in (e). (Middle panel) the model  $M_{0a}$  with heterogeneous medium property and homogeneous frictional property. (Bottom panel) the model  $M_{0b}$  with homogeneous medium property and heterogeneous frictional property.

erally lower than that of the other layers (Fig 5.1) [Lele *et al.*, 2015]. Therefore, when the elastic parameters are updated to their lithology-dependent values, the less efficiently loaded surrounding materials will indirectly slow down the stress change inside the reservoir. We did two additional simulations to separate the effects of heterogeneous frictional and elastic properties. We ran a simulation that only has mechanical heterogeneity (M0a) and another simulation that only has frictional heterogeneity (M0b) (Fig 5.3). The temporal evolution profiles of slip rate and stress in M0a are similar to the heterogeneous model M1 whereas the temporal evolution profiles in M0b are similar to the homogeneous model M0. This demonstrates that the slower loading is not caused by the heterogeneous frictional property but by the heterogeneous elastic property. Interestingly, M0a needs 30 MPa pore pressure change before failure and M0b 21 MPa, indicating that the presence of frictional heterogeneity even brings the induced earthquake forward in time. Second, the rupture in M0 is restricted to the depth where two sides of the reservoir are connected. We do not observe the nucleation or rupture to go above 2850 m in this model. Despite a very limited amount, we do see the nucleation expansion into the TB/SS segment in both M0a and M0b, similar to M1. It is yet to be clarified how this phenomenon results from both types of heterogeneities.

### 5.3.2 Can the velocity-weakening Basal Zechstein fault segment be activated?

One of the key questions to answer is whether the velocity-weakening Basal Zechstein anhydrite can be activated during nucleation or rupture or not. We did not observe seismic slips in this layer in the heterogeneous reference model (M1). However, this is probably because there was no BZ/BZ interface (Fig 5.2). Borehole surveys and seismic studies at other locations in Groningen have shown that the Ten Boer claystone layer can become relatively thin at some locations, while Basal Zechstein can be as thick as up to 700 m (Fig 5.4) [Kettermann *et al.*, 2017; Green *et al.*, 2020]. In these scenarios, the BZ layer is closer to the reservoir depth and can even have direct contact with the sandstone reservoir across the fault. We simulated earthquakes in two setups with a thicker BZ layer and a thinner TB layer, which we respectively term as M2a and M2b. In M2b, we removed the TB completely to put the BZ directly next to the region of pore pressure change.

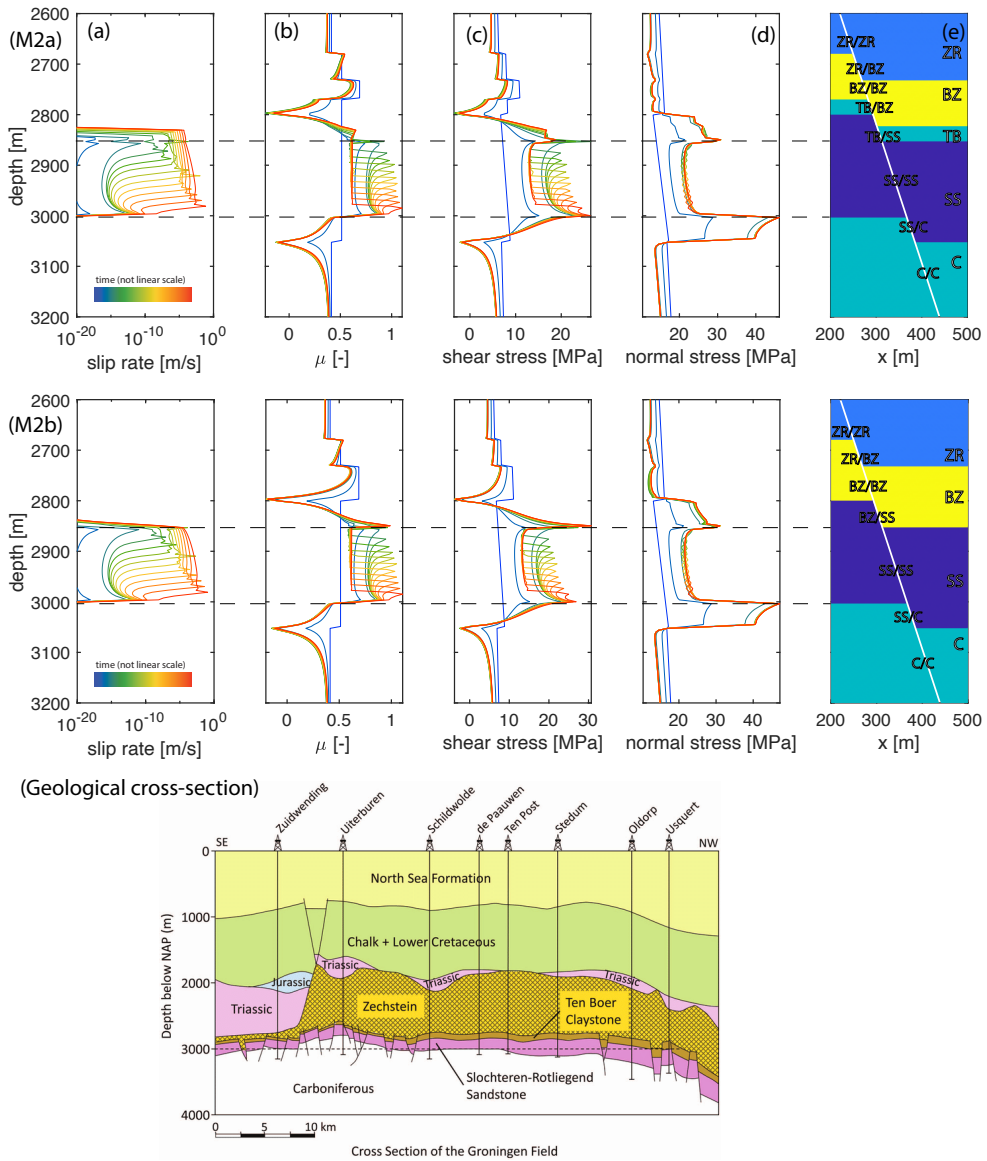


Figure 5.4: Simulations with various Basal Zechstein layer thicknesses: M2a and M2b. (Top panel) the model M2a with a 90 m thick BZ layer. The temporal evolutions of (a) the slip rate, (b) the frictional coefficient, (c) the shear stress, and (d) the effective normal stress are plotted. The interseismic and nucleation phases are plotted in blue and green, with a gradual transition to the coseismic phase in red. The time intervals between the plotted lines are not regular. The reservoir thickness is between the dashed black lines. The model setup is depicted in (e). (Middle panel) the model M2b with a 120 m thick BZ layer. (Bottom panel) Geological cross-section through the Groningen gas field from [Green et al., 2020].

The earthquakes in both simulations are comparable to the earthquake in the heterogeneous reference model M1. The earthquake ruptures the fault at the same time after production starts (67 yr) and experiences the same amplitude of slip rate and stress drop (Fig 5.4). In M2a, the thickened BZ is juxtaposed with ZR, TB layers and itself. We do not observe a slip rate increase on these fault segments. Similar to the reference model M1, this is because of the decreased shear stress. The nucleation does expand upwards into the TB caprock, the same as in M1, but only for a few meters. Even the BZ/BZ segment, which is velocity-weakening, is not activated. The same results are observed in M2b. In this simulation, both BZ/BZ and BZ/SS fault segments, which sum up to 120 m in thickness, have gained strength due to healing (Fig 5.4). However, they are not re-activated during nucleation and rupture because the shear stress is not increased on these segments. In all these simulations, the seismic slip is restricted to the reservoir. This is different from the case when the TB layer is present (models M1 and M2a), where the TB/SS fault segment shows the frictional property of the TB side. As we explained in the M1 model, the first few meters of the TB/SS fault segment do fail due to the low strength. In summary, our simulations thus do not provide support for the hypothesis that earthquake hypocenters can be located in the caprock.

### 5.3.3 Can the rupture propagate into the underburden?

Since all our simulations, including our models M0-M2, suggest seismic slip can only propagate into the overburden to a negligible extent, a second question most relevant for seismic hazard is whether the rupture can significantly propagate into the underburden. Propagation into the underburden is limited in our models, because the underburden experiences a decrease in shear stress. We find this observation in good agreement with natural observations and other numerical studies [Buijze, 2020; van der Heiden *et al.*, 2022]. To challenge the findings for our limited set of parameters, we simulate a geometrical and parameteric setup (model M3) that a-prior has a high likelihood of rupture propagation into the underburden according to the broad parameter analysis of Buijze [2020]. In this setup, we use a stress ratio  $K_0$  of 0.7 and stick to our fault dip angle of 70 degrees. We increase the reservoir thickness to 250 m and decrease the fault offset to 10 m. Our simulation shows similar results compared to the reference model M1, because it does not propagate into the underburden (Fig

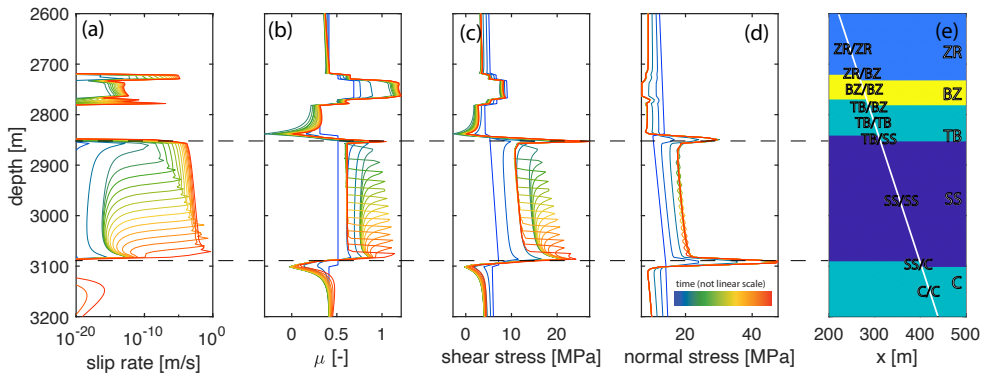


Figure 5.5: Simulations with a set of parameters with high likelihood of rupture propagation into the underburden: M3. The temporal evolutions of (a) the slip rate, (b) the frictional coefficient, (c) the shear stress, and (d) the effective normal stress are plotted. The interseismic and nucleation phases are plotted in blue and green, with a gradual transition to the coseismic phase in red. The time intervals between the plotted lines are not regular. The reservoir thickness is between the dashed black lines. The model setup is depicted in (e).

5.5). In this scenario slip rates in the Carboniferous do increase and reach almost  $10^{-15}$  m/s, but this is still many orders of magnitude below tectonic plate velocities. One striking difference is high slip rates (up to  $10^{-5}$  m/s) observed in the fault segment where Zechstein rocksalt and Basal Zechstein interface. However, it is not yet clear why this fault segment is activated as it is expected to be a strong velocity-strengthening segment. We will continue to test more scenarios with high potential for propagation into the underburden to provide better support for this important question and the impact lithology-dependent properties have, including using a thicker reservoir and a smaller fault offset, as indicated by *Buijze et al.* [2019].

### 5.3.4 Uncertainty in frictional parameters

The mechanical and frictional parameters both have uncertainties. Together with the uncertainty in fault geometry, some simulation results may not be able to apply generally to everywhere in the gas field. To demonstrate the robustness of the conclusions, we would have to repeat the simulations with parameters that are varied within their confidence intervals. However, when considering lithology-dependent fault properties, it becomes even more complicated. One

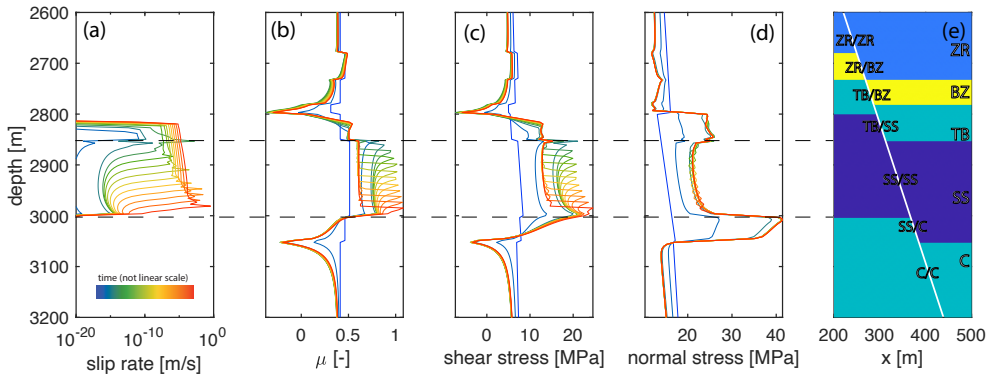


Figure 5.6: Simulation with parameters of homogeneous mixtures from Hunfeld *et al.* [2017].

of the main complexities comes from the fault rheology where two different materials are juxtaposed. As slip continues, two materials form a heterogeneous mixture whose rheology evolves with time and slip [Bedford *et al.*, 2022; Arts *et al.*, 2023]. Arts *et al.* [2023] performed laboratory experiments on mixtures of gouge derived from the Groningen gas field. Arts *et al.* [2023] proposed that, after a certain amount of slip, the fault friction stabilizes to have the  $(a - b)$  value from the VS side, but the static friction coefficient from the stronger side. We adopted this hypothesis in our simulations. However, according to Hunfeld *et al.* [2017], a well-mixed fault gouge of both velocity-weakening and velocity-strengthening materials shows both  $(a - b)$  and  $\mu_0$  around the average of the two individual materials. We conducted a simulation using the  $\mu_0$  values from Hunfeld *et al.* to test if applying this modification would change the results. We find that there is no clear difference when results are compared with the heterogeneous reference model M1 (Fig 5.6). This indicates that the static frictional coefficient, within its confidence interval, does not play an important role in the nucleation process.

## 5.4 Discussion

Our preliminary simulations, employing lithology-dependent frictional and elastic parameters derived from in-situ and laboratory measurements, aim to identify the lithological layer from which nucleation starts and which layers undergo rupture. These questions cannot be answered by seismological in-



versions due to the lack the resolution. Debates have centered whether nucleation can also take place in the thin velocity-weakening Basal Zechstein layer in the caprock and whether the rupture can also propagate into the velocity-strengthening Carboniferous shale underburden. Our preliminary simulation results do not provide evidence supporting positive answers to these questions. Simulated earthquakes only nucleate from the velocity-strengthening sandstone reservoir and rupture across its entire thickness. Two primary mechanisms contribute to this behavior. First, from a mechanical perspective, minimal pore pressure change outside the reservoir leads to a slight increase or a sharp decrease in shear stress, insufficient to trigger fault failure. Second, from a frictional perspective, fault segments outside the reservoir, mainly velocity-strengthening and lacking healing (negligible  $b$ ), do not accumulate sufficient strength to release large stresses upon activation. Consequently, earthquake nucleation is not expected, and dynamic rupture should be readily arrested in these areas.

While acknowledging the simplified treatment of fluid pressure diffusion in the current model, we speculate that the results will likely persist even with a more realistic representation of stress change due to fluid pressure diffusion. The expectation is based on the assumption that the pore pressure change in the Basal Zechstein is unlikely to be enough for activation, given the predominantly low-permeability nature of the layer. Additional factors, not considered in the current study, may play a role but require further confirmation. Two hypotheses regarding the frictional behavior of a heterogeneous fault gouge, one involving not-well-mixed materials [Arts *et al.*, 2023] and the other with well-mixed materials [Hunfeld *et al.*, 2017], were adopted. The simulations, incorporating different static friction ( $\mu_0$ ) values from these hypotheses, show no clear difference in results (M1 and M3). This suggests that, within its confidence interval, the static frictional coefficient does not play a significant role in the nucleation process. Despite a great number of laboratory measurements on ( $a - b$ ), the values of  $a$  and  $b$  separately have not been systematically reported. We plan to further test these parameters when more data become available through experiments on heterogeneous fault gouges with all combinations of rock mixtures and involving both slow and fast velocities.

This finding holds significant importance in estimating the maximum earthquake magnitude and defining seismic hazard in Groningen. Given the uncer-



tainties in parameters and fault geometry, further simulations will be conducted to validate or refute these findings. Emphasis will be placed on key geometric factors such as reservoir thickness, fault dip angle, and fault offset. These factors modify the stress loading rate before and during earthquake nucleation and may alter the criticality of each fault segment.

## 5.5 Conclusions

We applied the theory and model of Chapter 4 to the Groningen gas field, using lithology-dependent friction and elastic parameters obtained from in-situ and laboratory measurements. After millions of years of inactivity, we simulated various models in which a single earthquake nucleates from the top inner corner of the velocity-strengthening sandstone reservoir, which ruptures across the whole reservoir thickness. The nucleation and rupture processes are generally similar to the homogeneous model described in Chapter 4. However, a larger pore pressure change is needed due to the less efficient loading, which is caused by the heterogeneous elastic modulus and Poisson's ratio. We did not find evidence that earthquakes can nucleate from the velocity-weakening Basal Zechstein layer, nor can this layer be ruptured to slip seismically. The ruptures in our simulations did not propagate into the underburden, i.e., the Carboniferous shale layer, either.

# 6

Methods and code validation

The results in this thesis are obtained through developing, validating and applying two code packages. *Garnet* is used in Chapters 2 and 3. In Chapters 4 and 5, I employed a MATLAB code that I developed from scratch. In this chapter I first validate *Garnet* for the simulation of fully dynamic and quasi-dynamic sequences of earthquakes and aseismic slip in 2D and 3D, which may also involve fluid diffusion along the fault. Then I describe the fundamental of a completely new code that is developed to accurately accommodate the dipping fault used in Groningen, including the realization of heterogeneous stress state, frictional properties and mechanical properties, the implementation of frictional healing and controlled pore pressure change due to gas production.

## 6.1 Validation of *Garnet*

*Garnet* is a recently developed C++ code library designed for the parallel resolution of coupled non-linear multi-physics problems within the field of earth sciences [Pranger, 2020]. This versatile tool allows users to formulate problems in a dimension-independent manner by defining a generic set of symbolic differential operators, such as `div` and `grad`. These operators are then realized at compile-time in the appropriate number of dimensions as efficient compute kernels. The library implements a classical second-order accurate staggered grid finite difference discretization of partial differential equations (PDEs) in space, alongside adaptive time-stepping schemes of various orders of accuracy and other characteristics based on the linear multistep family of time discretizations. *Garnet* interfaces with PETSc [Balay et al., 1997, 2019a,b] for linear and nonlinear solvers and preconditioners, MPI [MPI Forum, 2015] for coarse-scale distributed memory parallelism, and Kokkos [Edwards et al., 2014] (and subsequently OpenMP, POSIX threads, or CUDA) for fine-scale concurrency. With this code package offering flexible usage of fundamental functions and solvers, I constructed the model setups and algorithms used in the thesis chapters. The workflow in Chapter 2, as an illustration of the algorithms, is depicted in Fig 6.1. I executed *Garnet*'s validation and benchmarking through the South California Earthquake Center (SCEC) benchmark problems, confirming its reliability and applicability [Erickson et al., 2020; Jiang et al., 2022; Erickson et al., 2023].

Numerical simulations of Sequences of Earthquakes and Aseismic Slip (SEAS) have seen remarkable progress in addressing critical questions in earthquake

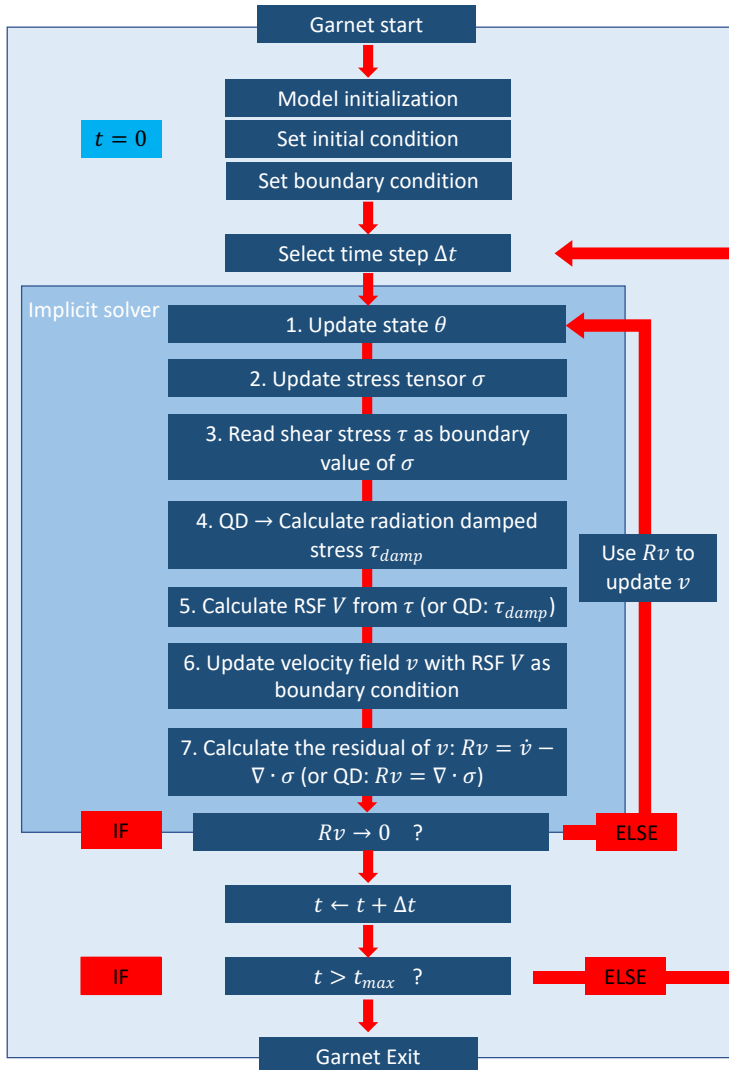


Figure 6.1: Flowchart of the numerical algorithm used in Chapter 2: Quasi-dynamic (QD) models share most steps with fully dynamic (FD) models in common, steps peculiar for the QD approach are labeled with “QD” closed in the parentheses (steps 4, 5 and 7).

physics over the past decades. Despite these advancements, significant challenges persist in capturing the multiscale interactions between earthquake nucleation, dynamic rupture, and aseismic slip. The growing complexity of SEAS modeling necessitates concerted efforts to validate codes and advance these simulations with reproducibility and broadened impact. Over the last decade, the SCEC has supported various code comparison projects to verify numerical simulations on dynamic earthquake ruptures [e.g. [Harris et al., 2009, 2018](#)]. The SEAS benchmark project, initiated in 2018 [[Erickson et al., 2020](#); [Jiang et al., 2022](#)], represents an extension of these efforts, aiming to evaluate the accuracy of numerical models simulating earthquake cycles. These exercises involve comparing different computational methods to assess our capacity to accurately resolve detailed fault slip histories across various time scales. These endeavors demand a deeper understanding of the dependence of fault slip history on initial conditions, model spin-up, fault properties, and friction laws.

I used this SEAS benchmark initiative to successfully verify the earthquake cycle implementation in *Garnet*. This verification included the 2-D benchmarks BP1-QD/FD [[Erickson et al., 2020, 2023](#)], 3-D benchmarks BP4/5-QD [[Jiang et al., 2022](#)], and a 2-D fluid injection benchmark BP6-A/S [[Lambert et al., 2023](#)]. In the following I briefly summarize the main results from these co-authored papers to showcase the accuracy and effectiveness of *Garnet* in solving these benchmark problems.

### 6.1.1 2-D benchmarks: BP1-QD/FD

\*Partly published in a co-authored paper as [Erickson, B. A., Jiang, J., Lambert, V., ..., Li, M., ... \(2023\). Incorporating full elastodynamic effects and dipping fault geometries in community code verification exercises for simulations of earthquake sequences and aseismic slip \(SEAS\). \*Bulletin of the Seismological Society of America\*, 113\(2\), 499-523.](#)

BP1-QD/FD represents two versions of the same benchmark problem: quasi-dynamic (QD) and fully dynamic (FD). The scenario involves a 2-D anti-plane problem with a 1-D planar vertical strike-slip fault governed by rate-and-state friction embedded in a 2-D homogeneous, linear elastic half-space (Fig 6.2a). The simulation focuses on sequences of earthquakes with periodic occurrences

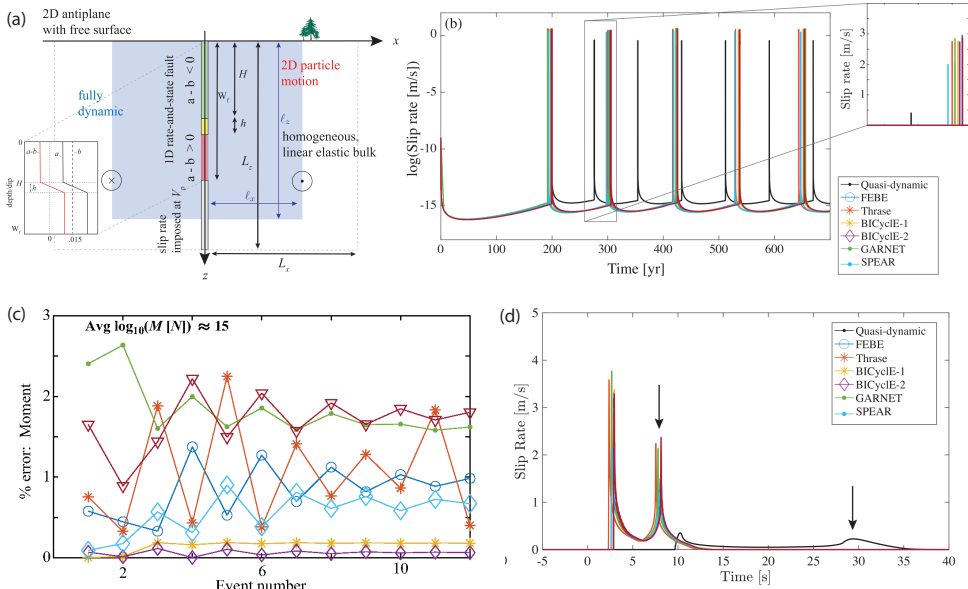


Figure 6.2: (a) Model setup of BP1-QD/FD. (b) Long-term behavior of BP1-FD models: slip rates at the depth of 7.5 km. (c) Long-term metric comparisons for BP1-FD show percent errors in moment plotted against event number, in which error is relative to the reference solution using the boundary element code BICyCLE. (d) Coseismic behavior of BP1-FD during the eighth event: slip rates at 7.5 km depth. Time (in seconds) is relative to the time at which the slip rate near the nucleation depth ( $z = 12.5$  km) first exceeds 0.1 m/s. The surface reflection phase is marked by a black arrow. Modified from Erickson et al. [2023].

and their interactions with aseismic slips. In this benchmark, 11 groups employing different numerical methods, including *Garnet*, are compared. The results demonstrate excellent agreement in both long-term and coseismic fault behavior. In the long term, there is outstanding quantitative alignment among the codes in terms of earthquake interevent times and event moments (Fig 6.2b). Specifically, the difference in simulated seismic moment between *Garnet* and the reference solution, which utilizes a boundary element code, falls below 2% (Fig 6.2c). In the short term, reasonable agreements are achieved in peak slip rates and rupture arrival times. The arrival times of rupture and surface reflection at 7.5 km depth in *Garnet* fall within the range observed in other models (Fig 6.2d). This comprehensive comparison underscores the accuracy and reliability of *Garnet*.

### 6.1.2 3-D benchmarks: BP4/5-QD

\*Partly published in a co-authored paper as Jiang, J., Erickson, B. A., Lambert, V., ..., Li, M., ... (2022). *Community-driven code comparisons for three-dimensional dynamic modeling of sequences of earthquakes and aseismic slip*. *Journal of Geophysical Research: Solid Earth*, 127(3), e2021JB023519.

BP4/5-QD comprises two benchmark problems with similar definitions. BP4 involves a planar vertical strike-slip fault governed by rate- and state-dependent friction in a 3D homogeneous, linear elastic whole-space (Fig 6.3a). On the other hand, BP5 features a fault with a narrower vertical dimension in a 3D half-space (Fig 6.3b). Both problems allow for periodic earthquakes instead of smaller irregular ones. Quasi-dynamic simulations from 10 modeling groups, including *Garnet*, exhibit excellent quantitative agreement among simulated outputs. Key properties of individual earthquakes, such as rupture style, duration, total slip, peak slip rate, and stress drop, show comparability even in marginally resolved simulations. Both the long-term and coseismic behaviors modeled in *Garnet* align well with those of other modeling groups. Three different numerical methods: finite difference method [*Garnet*, Pranger, 2020], finite element method [EQsimu, Liu et al., 2020], and boundary element method [BICycle, Lapusta et al., 2000; Lapusta and Liu, 2009] display strong agreement in long-term slip rate time series (Fig 6.3c). The comparison of the coseismic phase, in terms of the stress drop and the rupture propagation, also reveals consistency among the groups (Fig 6.3d,e). Slight difference is observed in the rupture contour curvature (Fig 6.3e), which suggests that *Garnet* has a slightly larger horizontal rupture speed compared to BICycle but smaller than EQsimu. This discrepancy may arise from variations in boundary conditions applied in each numerical model. The discrepancy becomes stronger for later earthquakes, due to error accumulation and other factors. Similarly, the off-fault observations have a good qualitative agreement of surface velocity time series and displacement histories at various distances away from the fault (Fig 6.3f). Overall, the discrepancies in coseismic off-fault deformation appear larger than all the on-fault properties that have been examined. This is likely due to multiple factors, including inaccurate representations of surface observation points (e.g., grid points offset from the surface) and domain truncation in the fault-normal direction. In summary, the comparison places *Garnet*'s results centrally among all models, affirming its validity for earthquake cycle modeling.

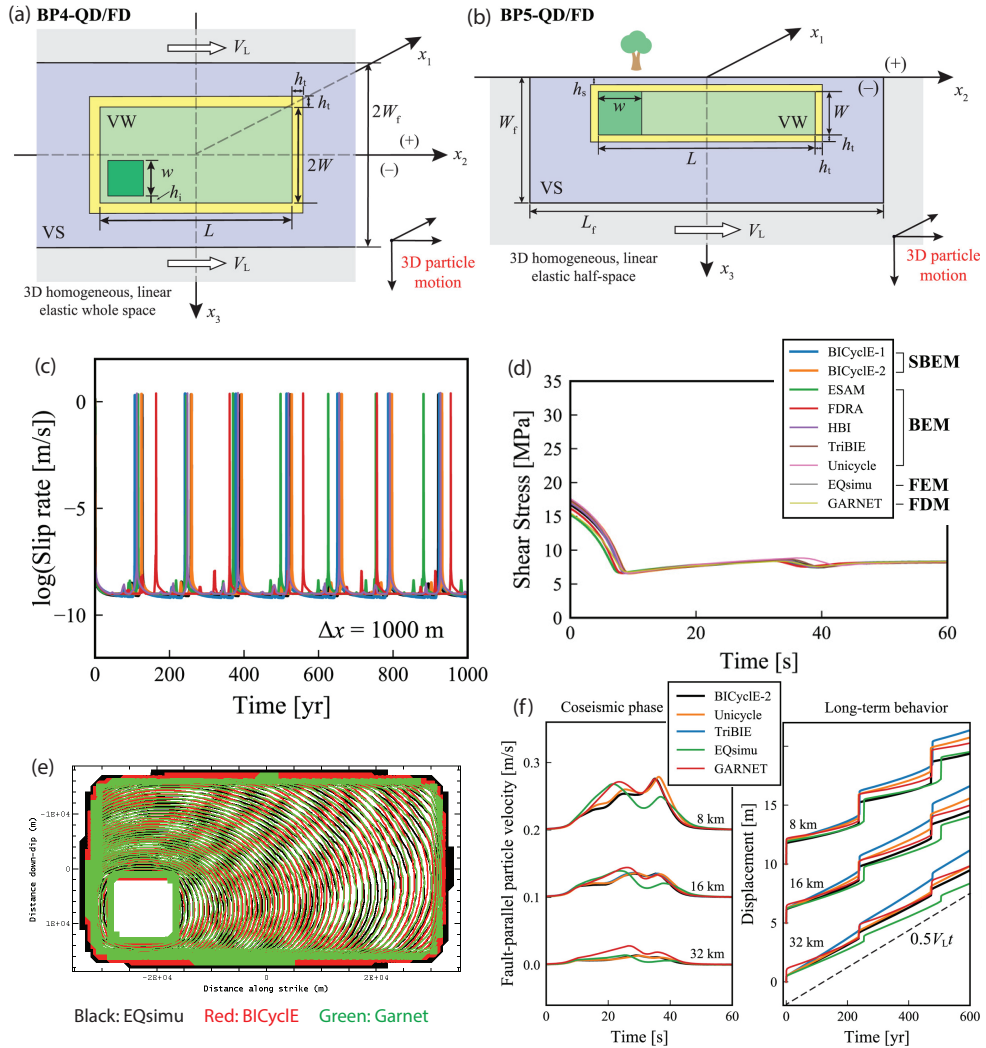


Figure 6.3: (a,b) Model setups of BP4-QD and BP5-QD. (c) Time evolution of maximum slip rates within the seismogenic zone in BP4-QD simulations. (d) Coseismic rupture of the first event in BP5-QD simulations. Time evolution of shear stress during the first earthquake is shown at a point within the initial nucleation zone ( $x_2 = -24$  km;  $x_3 = 10$  km). (e) Rupture fronts of the first earthquake in BP4-QD simulations. The contours of rupture fronts are plotted every second after the earthquake initiation. (f) Off-fault ground displacements in BP5-QD simulations. Fault-parallel displacement rates  $v_2$  during the first event (left) and long-term displacement history (right) are shown at three off-fault locations on the surface ( $x_1 = 8, 16, \text{ or } 32$  km;  $x_2 = 0$  km;  $x_3 = 0$  km). The dashed line indicates the far-field surface displacement. The time series corresponding to different locations are vertically offset for visualization purpose. Modified from Jiang et al. [2022].



### 6.1.3 Fluid injection benchmark: BP6-A/S

BP6 represents the most recent benchmark problem, specifically addressing fluid injection [Lambert *et al.*, 2023]. In this scenario, BP6 examines an aseismic transient induced by fluid injection and 1-D diffusion along a planar fault in a 2-D homogeneous, linear elastic whole space. The fault is governed by velocity-strengthening friction, using either the aging (-A) or slip (-S) law for the evolution of the state variable (Fig 6.4a). This benchmark focuses on aseismic processes and earthquake nucleation, including the influence of (a) changes in effective normal stress and pore fluid pressure due to fluid injection and diffusion and (b) different evolution laws for fault friction. Excellent quantitative agreement is achieved among simulations. Results are all within 1% from the analytic solution (Fig 6.4b-e), although the slip law version shows slightly more variation. This benchmark is still ongoing, more results and analysis come in the future. Yet it demonstrates *Garnet* can be successfully used for fluid diffusion along a fault.

## 6.2 Code for modeling induced earthquakes in Groningen

The chapters with specific results about the Groningen gas field (Chapters 4 and 5), are completed with a MATLAB code that I developed from scratch. The motivation for developing this code arose from the challenges encountered in implementing boundary conditions for a dipping fault setup in *Garnet*. As of now, this code is tailored specifically for solving the induced earthquakes in the Groningen setup. While its extension to cover a broader range of scenarios is feasible, it has not been implemented yet. Similar to *Garnet*, this code relies on the finite difference method on a staggered grid to achieve optimal spatial accuracy. To enhance temporal efficiency, an adaptive time-stepping scheme is incorporated. Unlike *Garnet*, this code employs the MATLAB “backslash” direct solver for the discretized partial differential equations (PDEs). Leveraging MATLAB’s robust capabilities in matrix calculations and matrix-level parallelization, the “backslash” direct solver typically outperforms iterative methods for moderately resolved grids. However, it comes with the drawback of high computational

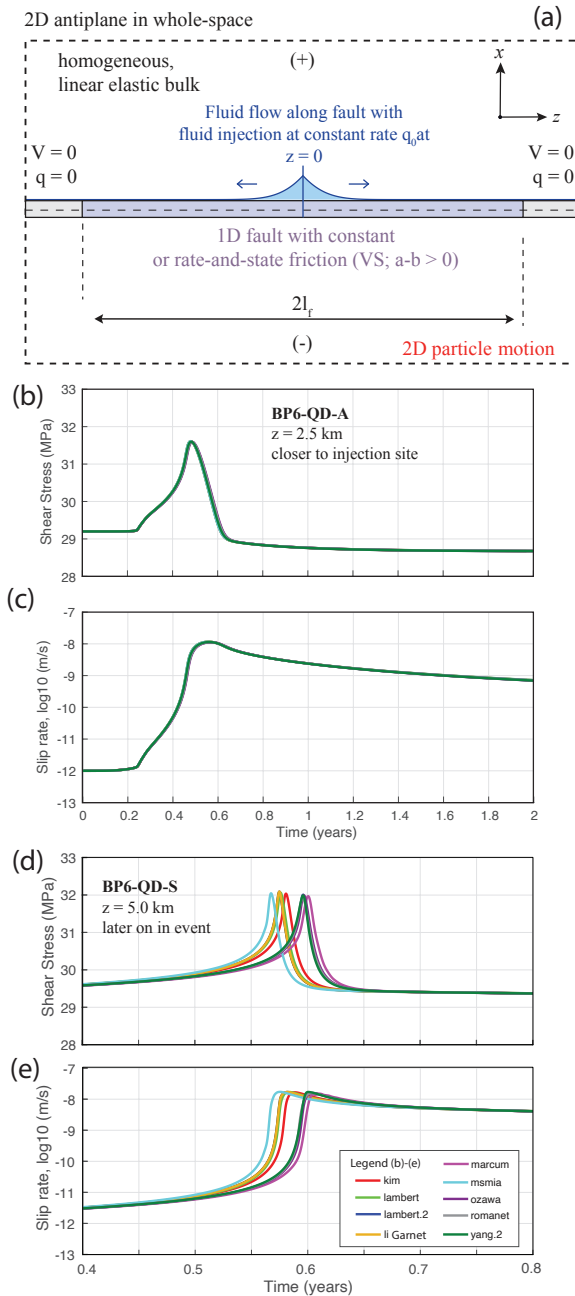


Figure 6.4: (a) Model setups of BP6-A/S. (b,c) Time evolution of shear stress and slip rate at  $z = 2.5$  km in BP6-A. (d,e) Time evolution of shear stress and slip rate at  $z = 5.0$  km in BP6-S. Modified from Lambert et al. [2023] with permission.

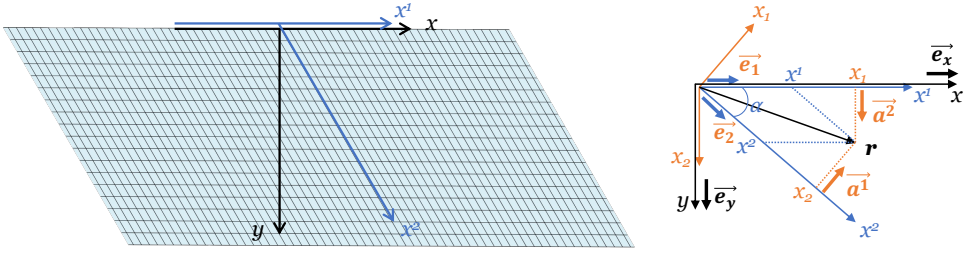


Figure 6.5: Illustration of a skewed coordinate system. The skewed physical grid is shown with the blue covariant bases and the orange contravariant bases. The orthogonal computational grid is shown with the black axes.

complexity ( $O(N^3)$ ), causing a rapid increase in computing time as the grid size decreases.

To accommodate the dipping fault within the rectangular finite difference grid, an affine transformation is implemented between the physical grid and the computational grid. This allows the physical grid to take on various curvilinear forms, while the computational grid remains orthogonal and homogeneous. In the following section, I begin with a tensor analysis in a general curvilinear coordinate system, introducing relevant terminology and conventions. To avoid redundancy with standard textbooks (such as *Simmonds* [1994]) and provide the readers with simpler formulae, I swiftly go into the skewed coordinate system I adopted in this thesis, which is a special curvilinear coordinate system (Fig 6.5). Despite having non-orthogonal axes, the coordinates remain homogeneous and time-independent.

### 6.2.1 Skewed coordinates

A skewed coordinate system is a non-orthogonal curvilinear system, with one basis not perpendicular to the corresponding coordinate surface (Fig 6.5). I define a 2-D skewed coordinate system with covariant bases ( $\mathbf{e}_1, \mathbf{e}_2$ ), with an angle of  $\alpha$  between them. A vector  $\mathbf{r}$  can be expressed with its contravariant components ( $x^1, x^2$ ) as

$$\mathbf{r} = x^1 \mathbf{e}_1 + x^2 \mathbf{e}_2, \quad (6.1)$$

or with its covariant components ( $x_1, x_2$ ) as

$$\mathbf{r} = x_1 \mathbf{e}^1 + x_2 \mathbf{e}^2, \quad (6.2)$$

with the contravariant bases  $(\mathbf{e}^1, \mathbf{e}^2)$ . Note that usually  $(\mathbf{e}_1, \mathbf{e}_2)$  are defined as unit bases, then  $(\mathbf{e}^1, \mathbf{e}^2)$  are not normalized. They are related to the unit bases  $(\hat{\mathbf{e}}^1, \hat{\mathbf{e}}^2)$  by  $\mathbf{e}^1 = \frac{\hat{\mathbf{e}}^1}{\sin \alpha}$  and  $\mathbf{e}^2 = \frac{\hat{\mathbf{e}}^2}{\sin \alpha}$ .

The vector  $\mathbf{r}$  can also be expressed in an orthogonal coordinate system with bases  $(\mathbf{e}_x, \mathbf{e}_y)$  as

$$\mathbf{r} = x\mathbf{e}_x + y\mathbf{e}_y. \quad (6.3)$$

In the orthogonal coordinate system, there is no need to distinguish between the covariant and contravariant components. I use only subscripts without ambiguity. The transformation between the skewed coordinates  $(x^1, x^2)$  and the orthogonal coordinates  $(x, y)$  can be expressed via the basis transformation

$$\begin{aligned} \mathbf{e}_1 &= \mathbf{e}_x \\ \mathbf{e}_2 &= \cos \alpha \mathbf{e}_x + \sin \alpha \mathbf{e}_y. \end{aligned} \quad (6.4)$$

The coefficients form the transformation matrix

$$[\beta_{ij}] = \mathbf{e}_i \mathbf{e}_j = \begin{pmatrix} 1 & \cos \alpha \\ 0 & \sin \alpha \end{pmatrix} \quad (6.5)$$

and the (covariant) metric tensor

$$[g_{ij}] = [\mathbf{e}_i \cdot \mathbf{e}_j] = \begin{pmatrix} 1 & \cos \alpha \\ \cos \alpha & 1 \end{pmatrix}. \quad (6.6)$$

The contravariant metric tensor is

$$[g^{ij}] = [g_{ij}]^{-1} = \frac{1}{\sin^2 \alpha} \begin{pmatrix} 1 & -\cos \alpha \\ -\cos \alpha & 1 \end{pmatrix}. \quad (6.7)$$

## 6.2.2 Controlling equations in skewed coordinates

Controlling equations in the elastic mechanics are expressed in the skewed coordinates with the help of the metric tensor. Here I derive the formulae of the most commonly used equations, the Hooke's law and the momentum balance equation, in this coordinate system.

### Displacement and strain

Let displacement  $\mathbf{u} = u^i \mathbf{e}_i = u_i \mathbf{e}^i$ , ( $i = 1, 2$ ), the covariant components and the contravariant components are linked via the metric tensor, I have

$$u_i = g_{ij} u^j, \quad u^i = g^{ij} u_j. \quad (6.8)$$

I use the covariant components ( $u^1, u^2$ ) as solution variables. Infinitesimal strain  $\boldsymbol{\varepsilon} = \varepsilon_{ij} \mathbf{e}^i \mathbf{e}^j$  is defined with the gradient of displacement. In curvilinear coordinates, I need to introduce the Levi-Civita connection when calculating the vector gradient

$$\nabla \mathbf{u} = (\partial_i u_j - \Gamma_{ij}^k u_k) \mathbf{e}^i \mathbf{e}^j \quad (6.9)$$

where  $\partial_i \equiv \frac{\partial}{\partial x^i}$  is the partial derivative in the direction  $\mathbf{e}_i$ . The Christoffel symbols  $\Gamma_{ij}^k = (\partial_j \mathbf{e}_i) \cdot \mathbf{e}^k$  come from the gradient of the bases. When the grid is homogeneous and thus the bases are spatially invariant, as in the used skewed coordinates, I have  $\Gamma_{ij}^k \equiv 0$ . In this case

$$\varepsilon_{ij} = \frac{1}{2} (\partial_i u_j + \partial_j u_i). \quad (6.10)$$

From now on, I do not write out the zero  $\Gamma_{ij}^k$  for simplicity. The readers can refer to textbooks (such as *Simmonds [1994]*) for the complete derivation in general curvilinear coordinate systems.

Therefore the strain can be written, using the solution variables, as

$$\begin{aligned} \varepsilon_{11} &= \partial_1 u_1 = \partial_1 u^1 + \partial_1 u^2 \cos \alpha \\ \varepsilon_{12} &= \frac{1}{2} (\partial_1 u_2 + \partial_2 u_1) \\ &= \frac{1}{2} [(\partial_1 u^2 + \partial_2 u^1) + (\partial_1 u^1 + \partial_2 u^2) \cos \alpha] \\ \varepsilon_{22} &= \partial_2 u_2 = \partial_2 u^2 + \partial_2 u^1 \cos \alpha. \end{aligned} \quad (6.11)$$

### Elasticity and stress

For linear elastic materials, the constitutive equation describing the strain-stress relation can be written as

$$\boldsymbol{\sigma} = \mathbf{C} : \boldsymbol{\varepsilon} \quad (6.12)$$

where  $\mathbf{C}$  is the fourth-rank elasticity tensor. For mathematical and physical convenience, I express strain in its contravariant form and stress in its covariant form, the constitutive equation can be expressed in the index form

$$\sigma^{ij} = C^{ijkl} \varepsilon_{kl}. \quad (6.13)$$

For homogeneous isotropic materials, two independent Lamé constants  $\lambda$  and  $G$  are enough to describe the elasticity

$$C^{ijkl} = \lambda g^{ij} g^{kl} + G(g^{ik} g^{jl} + g^{il} g^{jk}). \quad (6.14)$$

In the skewed coordinate system I have

$$\begin{aligned} C^{1111} &= \frac{\lambda + 2G}{\sin^4 \alpha} \\ C^{1112} &= \frac{-(\lambda + 2G) \cos \alpha}{\sin^4 \alpha} \\ C^{1122} &= \frac{\lambda + 2G \cos^2 \alpha}{\sin^4 \alpha} \\ C^{1212} &= \frac{(\lambda + G) \cos^2 \alpha + G}{\sin^4 \alpha}, \end{aligned} \quad (6.15)$$

the other 12 components are left out given the symmetry of  $\mathbf{C}$  and  $\mathbf{g}$ .

Therefore the stress can be written, using the solution variables, as

$$\begin{aligned} \sigma^{11} &= \frac{1}{\sin^2 \phi} [(\lambda + 2G) \partial_1 u^1 + \lambda \partial_2 u^2 - 2G \cos \phi \partial_2 u^1] \\ \sigma^{12} &= \frac{1}{\sin^2 \phi} [G (\partial_1 u^2 + \partial_2 u^1) - (\lambda + G) \cos \phi (\partial_1 u^1 + \partial_2 u^2)] \\ \sigma^{22} &= \frac{1}{\sin^2 \phi} [(\lambda + 2G) \partial_2 u^2 + \lambda \partial_1 u^1 - 2G \cos \phi \partial_1 u^2]. \end{aligned} \quad (6.16)$$

### Momentum conservation

The momentum balance equation writes as

$$\rho \ddot{u}^i = \partial_j \sigma^{ij} \quad (6.17)$$

where  $\rho$  is the material density and  $\ddot{\mathbf{u}}$  is the second derivative of displacement with respect to time, i.e., the acceleration. The terms with  $\Gamma_{ij}^k$  are omitted to keep the expression concise.

Expanding the expression by replacing the terms with the solution variables  $u^i$ , I obtain the equation for  $u^1$

$$\begin{aligned} \rho \ddot{u}^1 &= \frac{1}{\sin^2 \phi} [(\lambda + 2G) (\partial_1^2 - \cos \phi \partial_1 \partial_2) u^1 \\ &\quad + G (\partial_2^2 - \cos \phi \partial_1 \partial_2) u^1 + (\lambda + G) (\partial_1 \partial_2 - \cos \phi \partial_2^2) u^2], \end{aligned} \quad (6.18)$$

and the equation for  $u^2$

$$\begin{aligned} \rho \ddot{u}^2 = & \frac{1}{\sin^2 \phi} [(\lambda + 2G) (\partial_2^2 - \cos \phi \partial_1 \partial_2) u^2 \\ & + G (\partial_1^2 - \cos \phi \partial_1 \partial_2) u^2 + (\lambda + G) (\partial_1 \partial_2 - \cos \phi \partial_1^2) u^1]. \end{aligned} \quad (6.19)$$

These equations, together with the boundary conditions and the fault friction formation, define the problems to be solved.

### 6.2.3 Fault as an interface

In the model setup of Chapters 4 and 5, fault friction is assigned as an interface condition at the surface of  $x^1 = 0$ . The fault stress state is described as

$$\begin{aligned} \tau &= \sin \alpha (\sigma^{12} + \sigma^{11} \cos \alpha) \\ &= \frac{G}{\sin \phi} [\partial_1 u^2 + (1 - 2 \cos^2 \phi) \partial_2 u^1 + \cos \phi (\partial_1 u^1 - \partial_2 u^2)] \\ \sigma_n &= \sigma^{11} \sin^2 \alpha \\ &= (\lambda + 2G) \partial_1 u^1 + \lambda \partial_2 u^2 - 2G \cos \phi \partial_2 u^1 \end{aligned} \quad (6.20)$$

where  $\tau$  is the shear stress and  $\sigma_n$  is the normal stress on the fault plane. The fault slip  $d$  is the difference of the displacements on the two sides of the fault

$$\begin{aligned} d &= [u^2] + [u^1] \cos \alpha \\ &= [u^2] \end{aligned} \quad (6.21)$$

where  $[ ]$  is used to denote the difference  $[u] = u|_{x=0+} - u|_{x=0-}$ . The difference of the  $u^1$  is zero as no fault opening is assumed. The stresses  $\tau$  and  $\sigma_n$ , together with the slip rate  $V \equiv \dot{d}$ , follow the rate-and-state friction formulation.

### 6.2.4 Boundary conditions

The top surface is prescribed with constant stress due to the gravity of the overburden, which is equivalent to a free surface boundary condition. The stress

state is expressed as

$$\begin{aligned}
 \sigma^{yy} &= \sigma^{22} \sin^2 \alpha \\
 &= (\lambda + 2G) \partial_2 u^2 + \lambda \partial_1 u^1 - 2G \cos \phi \partial_1 u^2 \\
 \sigma^{xy} &= \sin \alpha (\sigma^{12} + \sigma^{22} \cos \alpha) \\
 &= \frac{G}{\sin \phi} [\partial_2 u^1 + (1 - 2 \cos^2 \phi) \partial_1 u^2 + \cos \phi (\partial_2 u^2 - \partial_1 u^1)].
 \end{aligned} \tag{6.22}$$

Both the shear stress  $\sigma_{xy}$  and the normal stress  $\sigma_{yy}$  are constant. The other boundaries are prescribed with free-slip boundary condition.





# 7

Conclusions: summary and outlook

## 7.1 Main findings in the previous chapters

Recent developments in instrumentation and methodology are advancing our understanding of earthquake processes. However, despite the fact that some medium to large earthquakes have been witnessed to revisit the same fault (e.g. the Parkfield earthquakes [Roeloffs and Langbein, 1994]), observations on the repetitive occurrence of significant, destructive earthquakes in nature remains highly exceptional [Segall and Harris, 1987; Chlieh *et al.*, 2004; Prawirodirdjo *et al.*, 2010]. This limits the continuous monitoring of whole earthquake sequences, from interseismic loading to nucleation, seismic rupture, until post-seismic relaxation. Moreover, these natural observations are usually confined to the Earth's surface, distant from the earthquake source. These indirect measurements often demand the use of inverse modeling methods for interpretation. To compensate for this limitation, laboratory experiments are conducted with the rock samples collected from outcrops or boreholes, with some of them using the in-situ temperature and pressure conditions [Verberne *et al.*, 2014; Chen *et al.*, 2015; Hunfeld *et al.*, 2017]. These experiments generate a diverse slip spectrum from earthquakes in a quasi-regular sequence to complex nucleation and rupture patterns [McLaskey and Lockner, 2014; Passelègue *et al.*, 2020]. However, these experiments analyze samples on a confined millimeter to meter scale, posing challenges in extrapolating their findings to a larger, natural scale. To supplement these observations, it's essential to understand the multi-physics, multi-scale mechanisms that drive fault slip. Numerical models serve as a crucial link to overcome the inherent limitations of natural and experimental observations in terms of their spatial and temporal coverage. They significantly contribute to our comprehension of earthquake sequences and ultimately aid in refining long-term seismic hazard assessments. In this thesis, I simulate fault behaviors under various conditions and scenarios, such as in laboratory experiments (Chapter 3), tectonic environments (Chapter 2), and induced conditions in a gas reservoir (Chapter 4 & 5). My numerical models aim to substantially enhance our understanding of earthquake processes, bridging the gap between laboratory experiments and natural occurrences.

A common concern among numerical modelers is determining the appropriate model complexity for addressing their research objectives. They often ponder how dimension reduction might affect their results both qualitatively and

quantitatively. In Chapter 2, I systematically examine the advantages and limitations of simplifications that eliminate spatial dimensions in quasi-dynamic earthquake sequence models, from 3-D models with a 2-D fault plane down to 0-D or 1-D models with a 0-D fault point. My analysis shows that 2-D or 3-D models exhibiting quasi-periodic characteristic earthquakes display qualitatively similar behavior to lower-dimensional models. Certain coseismic characteristics like stress drop and fracture energy are largely controlled by local frictional parameters and are hence comparable. Nevertheless, dimension reduction quantitatively affects other observations. I note increased recurrence intervals, coseismic slip, peak slip velocities, and rupture speeds. These changes are primarily due to the elimination of velocity-strengthening patches that transmit tectonic loading onto the velocity-weakening fault patch. The reduced presentation of these velocity-strengthening patches reduces the interseismic stress rates inside the nucleation zone and thus amplifies the slip deficit, which results in a larger coseismic slip. The impact of dimension elimination from 3-D to 2-D is also reflected in a smaller nucleation length. A concise theoretical framework is developed to support this explanation quantitatively. By incorporating an equivalent stressing rate at the nucleation length  $h^*$  of 2-D and 3-D models, 0-D or 1-D models can also effectively reproduce the recurrence intervals of higher-dimensional models. Given the computational efficiency of lower-dimensional models that run over a million times faster, dimension reduction not only alleviates energy-consuming simulations but also enhances the efficiency of projects that require monotonous repetitions of forward models. This chapter provides the first qualitative and quantitative guidance on economical model design and interpretation of modeling studies.

Recent large-scale laboratory experiments exhibit varying nucleation locations with changing nucleation lengths, which is analogous to natural observations. It is hypothesized that fault heterogeneity plays an important role. Considering the significant impact of effective normal stress on fault strength and fracture energy, in Chapter 3, I employ an earthquake sequence model to quantitatively investigate the influence of normal stress heterogeneity on earthquake nucleation and the subsequent sequences. My model features a stochastically variable, spatially heterogeneous normal stress field, analogous to a 2-meter scale laboratory experiment. My analysis identifies five regimes of earthquake nucleation and slip behaviors governed by the ratio of the heterogeneity wavelength ( $\lambda$ ) to the nucleation length ( $L_c$ ). For instance, full ruptures are observed when  $\lambda$

is significantly smaller than  $L_c$ , displaying slips and recurrence intervals akin to those on homogeneous faults with the same averaged normal stress (termed the homogenized nucleation regime). However, frequent occurrences of slow slip events and partial ruptures prevail when  $\lambda$  is much larger than  $L_c$ , wherein each earthquake's nucleation length depends on the local stress level (localized nucleation regime). Interestingly, as  $\lambda$  approaches the magnitude of  $L_c$ , nucleation locations migrate between low normal stress regions (LSR) and high normal stress regions (HSR). When  $\lambda$  is larger than  $L_c$ , earthquakes nucleate in LSRs, and HSRs function as barriers (LSR-preferred nucleation regime). However, HSRs and LSRs exchange their roles when  $\lambda$  is smaller than  $L_c$  (HSR-preferred nucleation regime). Nucleation can also migrate from an LSR to its neighboring HSR in a single earthquake, when  $\lambda$  is between the minimum and maximum nucleation length of the heterogeneous fault (migratory nucleation regime). In this case, a large amount of aseismic slip and the associated stress drop are observed in the initial LSR, which can be linked to the migration of foreshocks documented in natural and laboratory observations. Identifying these five regimes holds significance in estimating the seismic potential of natural faults. Given that the stress state of most natural faults remains unknown, my findings are of particular interest in induced seismicity settings where human activities significantly impact (or even control) the effective normal stress. Additionally, my study offers an explanation for the observed aseismic slips during earthquake nucleation, foreshocks, and their spatial migration using fault stress heterogeneity, shedding light on understanding fault stress levels based on geodetic observations of foreshocks and preslips.

Current knowledge suggests that faults in the shallow subsurface should resist earthquake nucleation, because their frictional strength increases as slip accelerates. Yet, these supposedly stable faults frequently experience earthquakes induced by human exploration of the subsurface. In Chapter 4, I simulate earthquake sequences on a normal fault governed by rate-and-state friction, crosscutting a depleting gas reservoir, for millions of years since its last tectonic activity. I solve the paradox by demonstrating that single earthquakes can indeed nucleate on velocity-strengthening faults following long-term *fault healing* over millions of years. Subsequent slip on ruptured segments over human lifetimes is stable and aseismic. These ruptured segments thus form a barrier inhibiting future, larger, and more destructive earthquakes. The spatiotemporal evolution of fault slip on velocity-strengthening faults during nucleation and the subsequent

co-seismic phases is qualitatively similar to the scenario on velocity-weakening faults, but with a different nucleation length. To describe this, I extend the current analytical expression of nucleation length to the velocity-strengthening domain with the contribution of frictional healing taken into consideration. The mechanism causing a single earthquake relates to the healing during the tectonic inactivity that increases fault strength and the slip weakening after fault failure caused by induced stress accumulation. Together this leads to fault failure with a subsequent adequate stress drop. Both mechanisms relate closely to the evolution parameter  $b$  in rate-and-state friction. This revelation emphasizes that velocity-strengthening rocks, previously deemed safe in sustainable explorations, can unexpectedly host earthquakes, making them potentially riskier than previously presumed. I therefore quantify the potential of any fault to experience induced seismicity in terms of the required healing time and sufficient stress drop upon fault reactivation. With a geological timescale of healing, the conventional divide between seismogenic and non-seismogenic frictional properties at velocity-neutral ( $a/b = 1$ ) is shifted substantially to the velocity-strengthening side:  $a/b = 1.3$ , and at most  $a/b = 1.7$  with dynamic weakening mechanisms taken into consideration. My explanation and quantification of how earthquakes occur on conventionally stable, velocity-strengthening faults illustrates the importance of a better understanding and quantification of fault healing and its implications on seismic hazard. This is critical to correctly assess induced seismic hazard in all traditional and sustainable settings. Considering recent political and societal unrest, reliable hazard assessments may well be a key factor in deciding how much the shallow subsurface can contribute to transiting towards sustainable energy.

A closer look at the Groningen reservoir reveals that there are five major layers, from the top to the bottom: the Zechstein rocksalt, the Basal Zechstein anhydrite/carbonate, the Ten Boer claystone, the Slochteren sandstone reservoir, and the carboniferous shale/siltstone. According to Chapter 4, the velocity-weakening Basal Zechstein layer is seismogenic and the velocity-strengthening Slochteren sandstone becomes seismogenic with a geological timescale of healing due to a large rate-and-state parameter  $b$ , while the other layers of claystone or shale are non-seismogenic due to their low or even negative  $b$  parameter. This speculation raises more critical questions about whether the seismogenic layers will be actually activated to nucleate earthquakes and whether the seismic rupture can propagate into other layers. Addressing seismic hazard in Groningen

necessitates a good understanding of locations of earthquake nucleation and arrest. Despite advancements in instrumentation in recent years, seismological observations fail to sufficiently answer these fundamental questions due to measurement and inversion uncertainties. In Chapter 5, I applied the theory and model from earlier chapters to build a more realistic Groningen earthquake sequence model using lithology-dependent friction and elastic parameters obtained from in-situ and laboratory measurements. The simulations indicate that earthquakes originate from the velocity-strengthening sandstone reservoir and rupture across the entire reservoir width. However, compared to the homogeneous model used in Chapter 4, a larger pore pressure change is required due to the less efficient loading resulting from heterogeneous elastic properties. I found no evidence of earthquakes nucleating within the velocity-weakening Basal Zechstein layer, nor did this layer rupture seismically. Additionally, the rupture in our simulations did not extend into the underburden, represented by a velocity-strengthening Carboniferous shale layer. I find that the pore pressure change outside the reservoir is minimal, such that the stress state at the fault is far from critical. This strong stress valley forms an efficient barrier inhibiting propagation to larger depths. On top of that, the fault segments that are velocity-strengthening and do not exhibit healing (negligible size of  $b$ ) did not build up strength during the geological timescale, which is required to trigger a large stress drop upon activation. Consequently, earthquake nucleation should not be expected, and dynamic rupture should be arrested in these areas. Hence rupture propagation is mostly restricted to within the reservoir. Its reduced possibility of propagating into the under- and overburden reduces the total seismic energy release and thus the anticipated moment magnitude. This finding holds substantial implications for estimating the maximum earthquake magnitude and defining seismic hazards in Groningen. Given uncertainties in parameters and fault geometry, I will build on our latest model with a high likelihood to rupture into the Carboniferous underburden and test whether other factors, such as reservoir thickness and fault offset, will allow seismic propagation into the underburden.

The development and validation of the two code packages used in this thesis are introduced in Chapter 6. *Garnet* is used in Chapters 2 and 3. Validation of *Garnet* includes employing the benchmark problems BP1-BP6 from Southern California Earthquake Center (SCEC) to compare my simulation of fully dynamic and quasi-dynamic sequences of earthquakes and aseismic slip in 2-D and 3-D, which may

also involve fluid diffusion along the fault, with the participating codes from the community. Besides these developments based on the existing code package *Garnet* to model various dimensions, scales, and heterogeneous fault stress, a completely new code is developed to accurately accommodate the dipping fault used in Groningen, including the realization of heterogeneous stress state, frictional properties and mechanical properties, the implementation of frictional healing, and controlled pore pressure change due to gas production. This MATLAB code that I developed from scratch is employed in Chapters 4 and 5.

## 7.2 Outlook

In this section, I will discuss overarching issues within the thesis and propose future avenues for research. This includes ongoing projects and challenges that require community attention. This work is also part of NWO's DeepNL project InFocus which aims at building physics-based forward models and understanding the physics of earthquakes in Groningen, at building and testing data assimilation tools to forecast laboratory and ultimately natural earthquakes, and eventually at helping to minimize the effects of earthquakes for society. I build forward models that provide the physics-based input for the assimilation of limited and uncertain observations. My collaborator Diab-Montero uses data assimilation techniques to combine my models with observations to obtain a better forecastability of earthquakes and slow slip events.

### 7.2.1 Using data assimilation for earthquake forecasting

\*Partly published as: Diab-Montero, H. A., Li, M., van Dinther, Y., & Vossepoel, F. C. (2023). *Estimating the occurrence of slow slip events and earthquakes with an ensemble Kalman filter. Geophysical Journal International*, 234(3), 1701-1721.

Our ability to forecast future earthquakes is hindered by the very limited information on fault states. The current state of stress, strength, and frictional parameters governing fault slip are highly uncertain. Ensemble data-assimilation methods offer a way to estimate these variables by combining physics-based models, proposed in this thesis, with observations while considering uncertainties [Van Dinther *et al.*, 2019a]. However, Van Dinther *et al.* [2019a] is limited to



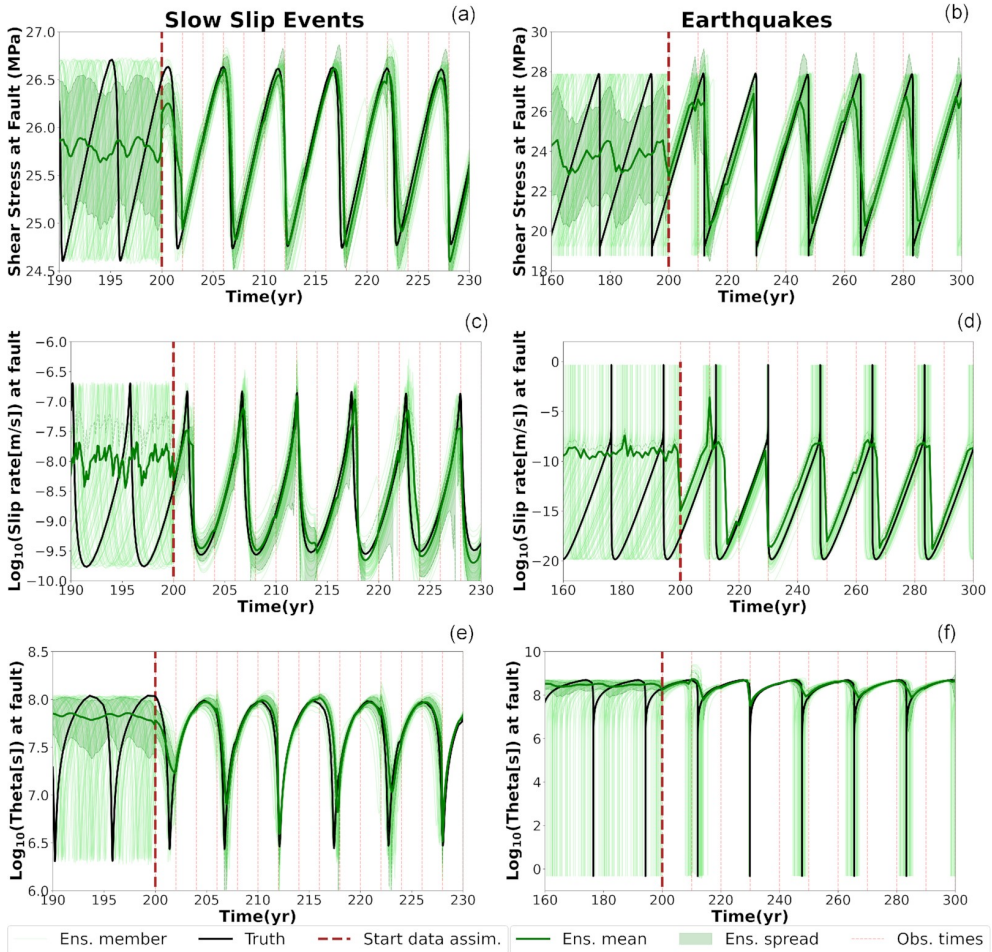


Figure 7.1: Estimated evolution of on-fault (a, b) shear stress, (c, d) slip rate, and (e, f) state  $\theta$  for (a, c, e) slow slip events and (b, d, f) earthquakes. The red dashed lines indicate the start of data assimilation. The solid black line represents the true model, the green solid line is the ensemble mean and the light green lines represent the ensemble members. The ensemble spread is shown as the light green hatched area, which is one standard deviation below and above the ensemble mean and corresponds to the ensemble members between the percentiles P16 and P84 of the ensemble distribution. Cited from Figure 5 in Diab-Montero et al. [2023].

assimilating observations from a single point in synthetic experiments. Within the DeepNL InFocus project my collaborators and I aim to enhance the estimates of the recurrence of slow slip events and earthquakes using limited observational data of low frequency and accuracy, from both synthetic and laboratory experiments. In this section, the main findings of this work, published in a co-authored paper, are summarized with a focus on using data assimilation methods to expedite fault slip forecasts. I conduct perfect model tests to assess the effectiveness of data assimilation.

An ensemble Kalman filter (EnKF) is employed to estimate the fault state, including shear stresses, slip rates, and the state  $\theta$  of rate-and-state friction in a 1-D model. Noised shear stress and velocity are acquired at a short distance to the laboratory fault and then assimilated. Before data assimilation, ensemble members provide random estimates of earthquake occurrence and stress loading. The mean value of these members is almost constant thus I cannot distinguish between interseismic and coseismic phases (Fig 7.1). Following data assimilation, there is a significant reduction in the spread of the ensemble for all hidden states, evident after assimilating the first observation. This synchronization of ensemble members is clear from the occurrence of the first slow slip event, which is forecasted even after only assimilating a single observation (Fig 7.1a). The first earthquake takes place after the assimilation of the second observation. Despite introducing uncertainties in shear stress estimates, the ensemble accurately predicted the timing of the stress drop (Fig 7.1b). Subsequent earthquake sequences demonstrate that the EnKF estimates are well synchronized with the truth. Data assimilation substantially improves the estimates of the temporal occurrence of slow slip events and, to a large extent, earthquakes (Fig 7.1). There is a very low forecasting failure rate of about 10% when using short alarms of just 10% of the recurrence interval. In other words, most slow slip events could be forecast half a year before their occurrence, and most earthquakes around 2 years in advance. These results affirm that data assimilation is a promising approach for combining uncertain physics with indirect, noisy observations in forecasting both slow slip events and earthquakes. The capacity of data assimilation to improve estimates of fault slips suggests its potential to advance the field of earthquake forecasting.

The method is being extended to 2-D and 3-D earthquake models to further demonstrate its ability to estimate state variables and will be eventually applied

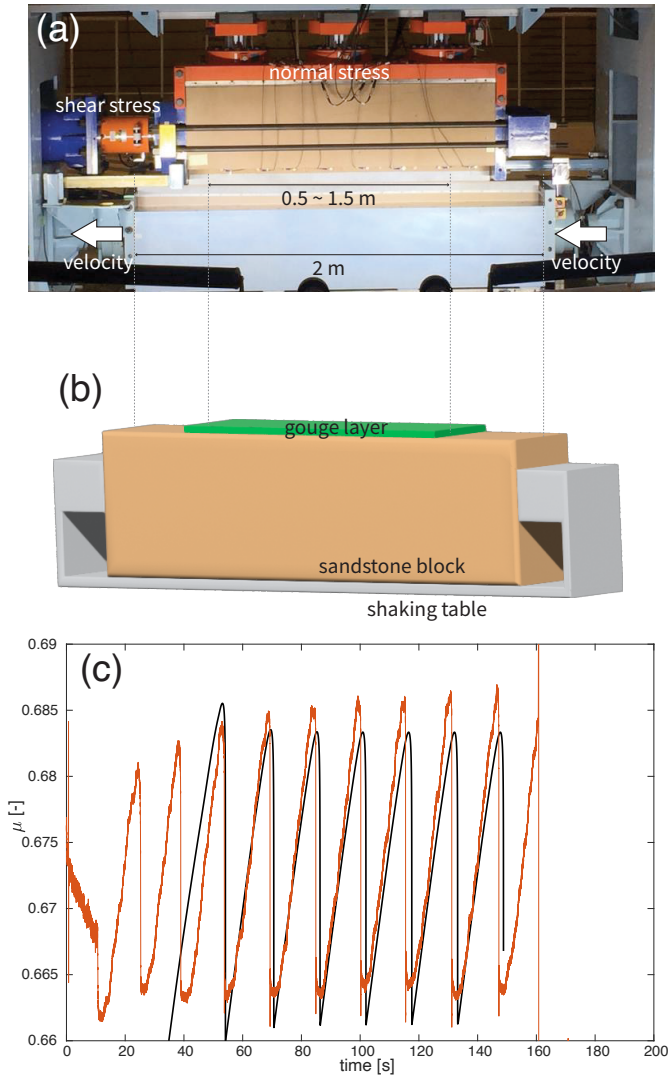


Figure 7.2: (a) The 2-m fault model in the NIED laboratory in Japan [Ji *et al.*, 2023]. Fine-ground material (gouge) is spread between two sandstone blocks to simulate a gouge layer, with a variable extent between 0.5 and 1.5 m. (b) Numerical model simulating the laboratory experiment. We only model the bottom half of the model while taking the system stiffness into account. The gouge layer is assumed to deform elastically with its infinitely thin surface following rate-and-state friction. (c) Comparison between numerical simulation (black) and laboratory experiment (orange) results. Figure shows the evolution of the frictional coefficient since a loading velocity switch from 0.1 to 0.01 mm/s.

to forecast laboratory earthquakes introduced in Chapter 3. To achieve this, I developed forward models in 2-D and 3-D that represent a 2-m direct-shear laboratory setup, featuring an array of shear-strain gauges and piezoelectric transducers located at a short distance from the fault. By tuning the model stiffness, I generated earthquake sequences qualitatively comparable to what are observed in the experiments (Fig 7.2). These models are being used to test the data assimilation tool in forecasting the labquakes. By assimilating the data collected from the strain gauges, we expect to realize a quantitatively better forecast quality. Comparisons between the models in different dimensions will also provide insights into the challenges associated with this space-time system and uncover the most important variables to assimilate.

## 7.2.2 Unaddressed physical processes

Throughout this thesis, I constructed models for diverse scenarios, ranging from laboratory experiments to both natural and induced earthquakes. The primary framework employed was a rate-and-state-friction (RSF)-controlled planar fault embedded in an elastic medium. However, this approach limited the ability to address crucial physical processes influencing fault slip behavior. Notably, the effect of heat. High temperatures in tectonic settings like subduction zones, are well-known for their influence on the viscous and plastic deformations [Van Dinther *et al.*, 2013b,a]. Even for induced seismicity at shallower depths, the temperature already exceeds 100 degrees Celsius. This high temperature, together with the high pressure, has a major influence on the frictional properties of most rocks. For example, an experimental study shows a transition of carbonates from slight velocity-strengthening to velocity-weakening at the reservoir temperature [Verberne *et al.*, 2014]. These impacts are more or less reflected in the parameter choices I made, but not simulated directly. Besides the background temperature, fast slip itself can generate a huge amount of heat in a short time, which increases the temperature of the fault gouge significantly [Tullis and Goldsby, 2003; Goldsby and Tullis, 2011]. The flash heating formulation utilized in this thesis reflects its impact on reducing the friction coefficient at high slip rates. However, my methodology did not account for the thermal pressurization effect, not to mention the changes in the mechanical properties of rocks and fluids. My future research will explore the impact of heat on all these related processes.

The use of rate-and-state friction to describe the plastic behavior of fault gouge marked a significant departure from the traditional *Mohr-Coulomb failure criterion + slip-weakening law* combination, since RSF accounts for the velocity dependence of the plastic deformation. However, RSF remains a phenomenological law based on an infinitely thin fault assumption. Recent studies propose extending this framework into the inelastic medium by using the strain rate to replace the slip rate in the classic RSF formulation [Herrendörfer et al., 2018] or exploring alternative plasticity descriptions [Pranger, 2020; Pranger et al., 2022; Goudarzi et al., 2023]. Some of these alternatives introduce a viscous component to the plastic flow law to make up for the inherent shortcomings of the RSF formulation, particularly its lack of a localization length scale. Stepping one step beyond RSF is crucial when modeling shear bands instead of infinitely thin fault surfaces. My Groningen model already encountered this challenge in dealing with the ductile Zechstein rocksalt layer. This layer, positioned at the top of the Groningen fault system, terminates the faults due to its inherently creeping nature (see Fig 5.4c). The creep behavior of the Zechstein rocksalt significantly influences stress distribution, resulting in a notable reduction of fault normal stress in all underlying formations, including the reservoir sandstone. The juxtaposition of rocksalt with other rock types further impacts the horizontal stress state across the fault [Buijze, 2020]. As a result, the fault failure requires a smaller pore pressure change. To simplify the model, I have assumed the rocksalt fault segment to be velocity-strengthening, allowing it to predominantly experience creeping behavior. However, this simplistic approach does not adequately capture the ductile deformation after faults terminate. There is a clear need for future research to surpass the limitations of the rate-and-state friction framework to better represent the dynamics of the fault core.

Another unexplored aspect is the influence of fluid presence and flow, a topic gaining attention in the scientific community for its impact on earthquake-related processes [Zhu et al., 2020]. The Southern California Earthquake Center (SCEC) benchmark project is actively developing challenges to evaluate various groups' abilities in modeling fluid flow. I participated in the most recent challenge, BP6, which focuses on an aseismic transient driven by fluid injection and 1-D diffusion along a planar velocity-strengthening fault in a 2-D homogeneous, linear elastic whole space [Lambert et al., 2023]. However, in this thesis, I did not incorporate fluid flow into the models. In the Groningen model, I assumed the pore pressure change to be homogeneous within the reservoir, based on obser-

vations of relatively uniform depletion and minimal pressure differences across faults [van Oeveren *et al.*, 2017]. This approach established a one-way coupling between pressure changes and rock deformation, neglecting any feedback from rock deformation on pressure changes due to the compressibility of gas [Buijze *et al.*, 2019]. Additionally, I neglected the pore pressure diffusion outside the reservoir. Observations in the Ten Boer claystone layer indicate depletion, albeit lagging behind the depletion observed in the sandstone reservoir by 7 MPa [Burkitov *et al.*, 2016]. The Ten Boer's lower static friction coefficient led to reactivation at lower pressure changes compared to the Slochteren sandstone, potentially resulting in aseismic slip due to inefficient stress drop. On top of the Ten Boer is the velocity-weakening Basal Zechstein layer. It is speculated that the pore pressure change in this layer may not be enough to activate it due to its composition of low-permeability materials and its increased strength from healing features. In short, the inclusion of fluid diffusion may not significantly alter current conclusions. However, all these speculations are to be justified by future numerical and laboratory studies. Nevertheless, assuming homogeneous pressure changes within the reservoir ignores the diffusion and convection within the reservoir, as well as the permeability of fault interfaces. This approximation precludes the instantaneous traction of the pressure front. The interaction between the fluid pressure front and the rupture front emerges as a crucial factor in controlling rupture dynamics, as evident in previous numerical and experimental studies [Garagash and Germanovich, 2012; Dublanchet, 2019]. Future work should carefully consider the presence of fluids.

These identified gaps underscore the importance of extending the current models to address heat effects, improve plasticity descriptions, and incorporate the influence of fluid presence for a more comprehensive understanding of earthquake-related processes.

### 7.2.3 Heterogeneity in laboratory and Groningen

The definition of heterogeneity within the scientific community lacks consistency, primarily because the concept is inherently multi-faceted and can be approached differently at various length scales. This nature is also reflected in laboratory experiments and numerical simulations. Some models identify themselves as heterogeneous with just a single anomaly, be it in numerical simula-



tions [Dong *et al.*, 2022] or laboratory experiments [Cebry *et al.*, 2023]. Others incorporate periodic or binary anomaly sequences to represent heterogeneity in both numerical [Luo and Liu, 2021] and experimental settings [Gounon *et al.*, 2022]. However, the true nature of heterogeneity is far from straightforward, and its randomness deviates from simple descriptions like a Gaussian distribution. Laboratory observations suggest a bimodal Gaussian distribution of fault roughness [Selvadurai *et al.*, 2023]. This distribution, featuring two characteristic roughness scales, finds support in the tribology community for its fitting representation of wear processes during friction [Adachi and Kato, 2000; Hu *et al.*, 2019]. As the slip-weakening distance concept is linked to the renewal of contact surfaces at the microscopic scale, these two roughness length scales could potentially reflect two slip-weakening distances. An updated version of the rate-and-state friction formulation introduces another state variable and another set of  $b$  and  $D_c$  parameters based on experiments showing a two-stage evolution of fault friction [Blanpied and Tullis, 1987], prompting a possibility to relate the two phenomena. Natural observations further complicate the heterogeneity landscape, suggesting that fault heterogeneity may exhibit fractal characteristics [Brown and Scholz, 1985; Okubo and Aki, 1987; Ohnaka, 2003; Candela *et al.*, 2012]. In this scenario, structures exist at any wavelength, challenging the notion of a characteristic length scale [Ide and Aochi, 2005].

Within this thesis, I employed the term *heterogeneity* to denote non-uniformity at two distinct length scales. At a larger scale, I modeled a heterogeneous fault in a gas reservoir due to the cross-cutting of different lithological layers (Chapter 5). Here, lithology-specific elastic and frictional properties remain fixed and constant. On this scale, there are also heterogeneities caused by large-scale mechanics such as overburden gravity, tectonic folding and bending, and stress perturbation of large seismic slips. They can be measured and studied in a deterministic fashion [Yang *et al.*, 2012; Michel *et al.*, 2021; Taufiqurrahman *et al.*, 2023]. However, heterogeneity arises also within each lithological layer. For example, the Basal Zechstein layer in Groningen comprises staggered anhydrite-rich and carbonate-rich sublayers (Fig 5.1b). The changes in mineral components with depth and location influence macroscopic properties. Statistical methods may better capture these smaller-scale features. Fault roughness is another example. At this length scale, I modeled a heterogeneous fault in the laboratory with a random normal stress distribution (Chapter 3). The heterogeneity is characterized by wavelength and amplitude. Here, exploring the collective behavior of multi-

ple stochastic realizations to find their common characteristics becomes more meaningful. I elaborated on how this wavelength of heterogeneity comes into play with other physical length scales to shape the fault dynamics. The interplay between these different scales, particularly when heterogeneity becomes fractal, poses a significant challenge in incorporating multiscale heterogeneities into a unified framework. This challenge underscores the need for continued research to develop comprehensive models that can account for the rich variety of heterogeneity observed across different length scales.

## 7.2.4 Maximum earthquake magnitude and model dimension

Earthquake magnitude is a commonly discussed parameter due to its direct understandability and comparability for scientists across various subfields of earth science. The most commonly used magnitude is the moment magnitude  $M_w$ , which is defined directly from the seismic moment  $M_0$  by  $M_w = \frac{2}{3} \log_{10} M_0 - 10.7$  [Kanamori, 1977]. Seismic moment is a measure of the energy released during an earthquake, with a physics-based definition as  $M_0 = \mu Ad$ , where  $\mu$  is the shear modulus,  $A$  is the rupture area, and  $d$  is the average seismic slip. Understanding the maximum magnitude  $M_{max}$  to be expected is crucial for hazard assessment. Yet,  $M_{max}$  can have different interpretations. Firstly, it may refer to a statistical estimate of the maximum earthquake size within a given time frame, such as the largest earthquake in the next 50 years with 90% confidence. In this context, a longer time frame and a lower confidence may result in a larger  $M_{max}$ . Secondly, it can mean the physically achievable earthquake size. Considering the entire fault is ruptured thus I have the maximum rupture area  $A_{max}$  equal to the fault area. Using an empirical scaling law between seismic moment and rupture area [Wells and Coppersmith, 1994],  $M_{max}$  can be estimated. However, natural earthquakes often exhibit confined ruptures where earthquakes do not rupture the whole fault area. Therefore it is questionable whether this theoretical limit could be achieved.

Numerous hypotheses have been proposed on the topic of why rupture arrests [Galis *et al.*, 2017]. This thesis has presented a few scenarios such as rupture arrest due to the change in frictional property from velocity-weakening to velocity-strengthening (Chapter 2), due to normal stress heterogeneity (Chapter 3), due



to dynamic changes in stress state due to fluid extraction (Chapter 4), and a combination of these factors (Chapter 5). Taking Chapter 5 as an example, the study in Groningen reveals that ruptures are predominantly confined to the reservoir depth, which averages 200 m in thickness. Other numerical studies support this observation, suggesting that ruptures larger than 400 m are exceedingly rare (less than 3% as suggested by *Buijze [2020]*). However, this is not yet enough to estimate  $M_{max}$ , as the rupture area depends on the length in another dimension. Let's do a quick calculation. *Kraaijpoel and Dost [2013]* reported that the Huizinge earthquake (ML 3.6), the largest induced earthquake in Groningen, has a rupture radius of around 400 m with around 5 centimeters of slip. This estimate is based on a very simple Brune model, which assumes circular rupture. Assuming a 200 m rupture length along dip, this implies a horizontal rupture length exceeding 800 m or an aspect ratio of 4:1 or higher. Such horizontal length is plausible but requires more geophysical evidence to confirm. Actually, recent 3-D rupture models for Groningen do indicate substantial horizontal content [*van der Heiden et al., 2022*]. Therefore it is still reasonable to say such an earthquake could be accommodated within the reservoir. However, to validate this hypothesis, 3-D models are essential since the rupture arrest mechanism in the horizontal direction must be clarified. One may propose that this is due to the horizontal length of each reservoir chamber, or the regions far away from production wells experience less pressure change and thus remain stable. Testing these hypotheses would involve incorporating fluid diffusion into the current code.

Even disregarding these considerations, the third dimension is still crucial and should not be neglected for accurate modeling and forecasts of future earthquake sizes. A comparison in Chapter 2 highlighted the significantly shorter recurrence interval in a 3-D model compared to in its 2-D counterpart along the vertical dimension of the fault. The rupture speed in the 3-D model is also slower. Interestingly, the vertical rupture speed can be changed if the horizontal fault length is modified. Consequently, interpreting results from 2-D simulations in a 3-D context needs delicate treatment. The same principle holds for using models in 1-D and 0-D, as discussed in Chapters 2 and shown in the comparison between 0-D and 2-D reservoir models in 4. Yet, 2-D simulations accounting for accurate loading and frictional behavior already provide first-order constraints on the possibility to propagate outside the reservoir.

### 7.2.5 Quasi-dynamic approximation

Models use different approximations for modeling the dynamic of an earthquake rupture, such as a quasi-static approach [e.g., *Aochi and Ide, 2017*], a quasi-dynamic (QD) approach [e.g., *Rice, 1993; Ben-Zion and Rice, 1995; Liu and Rice, 2007; Van den Ende et al., 2018*] and a fully dynamic (FD) approach [e.g., *Lapusta and Liu, 2009; Kaneko et al., 2010; Thomas et al., 2017; Herrendörfer et al., 2018*]. Quasi-static models solve a series of kinetic problems during interseismic loading. They cannot simulate desirable fast seismic slip since no dynamic physics is considered. QD models use the radiation damping term to approximate the energy release due to seismic waves emitted perpendicular to the fault, which are not explicitly simulated [e.g., *Rice, 1993; Cochard and Madariaga, 1994; Crupi and Bizzarri, 2013*]. This approximation helps to relieve the restriction in time stepping to simulate wave propagation and reduces the computational demands and time for many models. However, it is known to introduce qualitative and quantitative differences compared to FD modeling results [e.g., *Thomas et al., 2014; Chen and Lapusta, 2019*]. One important consequence is that seismic wave reflections from the free surface or lithological layers with high impedance contrasts cannot be simulated. Since this approximation is widely used in the community, it is worth discussing the impact it introduces.

In a comparison between the 3-D QD and 3-D FD models, FD models exhibit larger total slip, longer recurrence intervals, higher maximum slip rates, and shorter coseismic durations compared to QD models (Fig 7.3a,b). In contrast to the periodic events observed in QD models, FD events display more non-periodic features, with small creeps occurring between significant seismic slips (Fig 7.3b). These local failures suggest a more efficient stress concentration during loading. In the coseismic rupture, FD rupture is twice to three times faster than QD rupture (Fig 7.3c,d,f). Consequently, the maximum peak slip velocity in FD models is four times higher than in QD models (Fig 7.3e). FD events are thus slightly more pulse-like rather than crack-like. *Thomas et al. [2014]* suggests that FD events can be fully pulse-like with enhanced coseismic weakening. In other words, FD models generate higher stress concentrations at the rupture tip. This higher local energy consumption in FD models also indicates that if I reduce the wave-emitted energy in QD models, I might obtain stronger slip acceleration and higher peak slip velocity, which is closer to what is in FD models. Therefore, I conducted a 3-D QD model with a modified radiation damping factor  $\eta^*$  to inves-

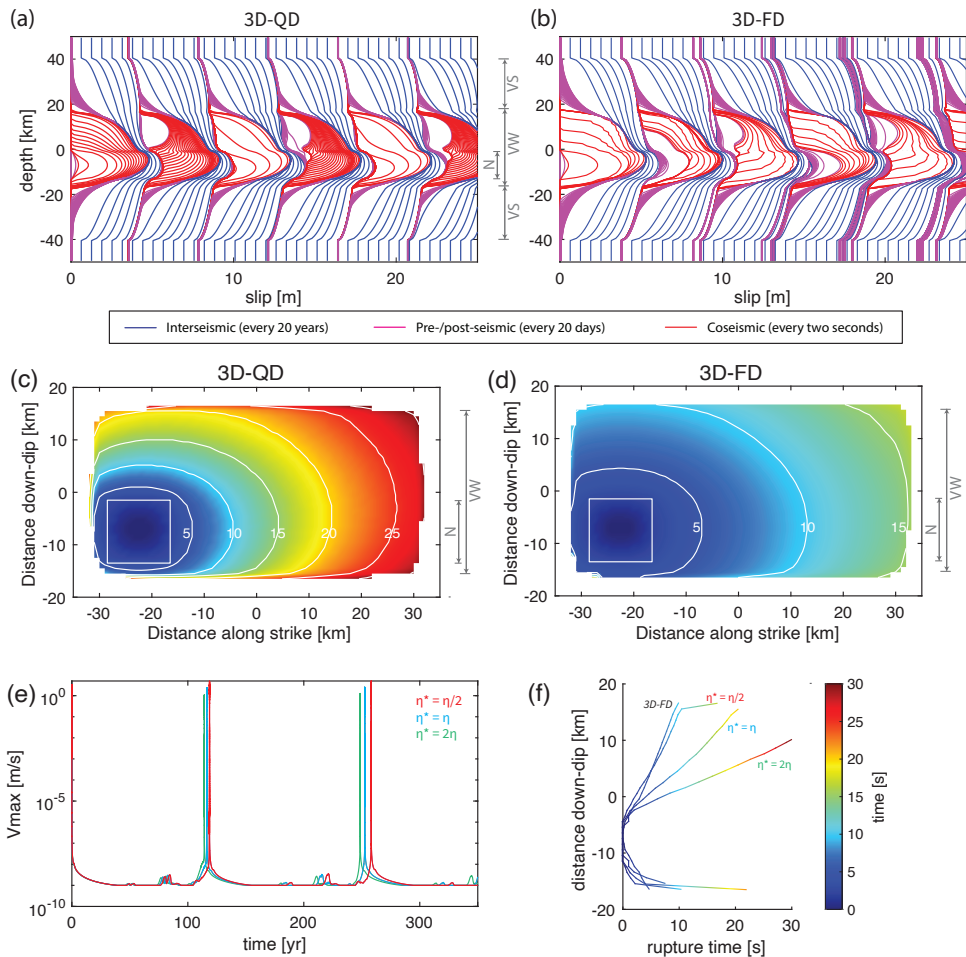


Figure 7.3: Comparison of the 3-D QD and 3-D FD models. The cumulative slip profile of (a) the 3-D QD model BP4-qd, and (b) the 3-D FD model, along the dip direction ‘EF’ cutting across the predefined nucleation zone ‘N’ are plotted. ‘VW’, ‘VS’, and ‘N’ label the range of VW, VS, and predefined nucleation zones (see Fig 2.1). The blue lines indicating the interseismic loading are plotted every 20 years, the magenta lines every 20 days and the red lines the coseismic rupture every two seconds. Note that the slip contour distortions around the depths of 0 and -12 km are introduced into these cumulative patterns by the predefined nucleation zone, whose properties increased the amount of slip in that zone for the first event only. (c, d) The arrival time of the coseismic rupture front of the first event in 3-D, which is measured when slip velocity reaching the seismic limit. The two panels show the central part of the fault plane, where white color means no seismic slip is observed. Contours are plotted every five seconds. (e) The maximum slip velocity in multiple earthquake cycles in 3-D QD model using three different radiation damping factors. (f) The coseismic rupture front arrival time along the vertical line ‘EF’. Lines end at where no seismic slip is observed. The rupture time of the corresponding 3-D FD model is plotted as reference.

tigate the impact of the radiation damping approximation. While interseismic characteristics remain consistent across different  $\eta^*$  values, coseismic characteristics vary significantly (Fig 7.3e,f). As I expected, smaller radiation damping values result in larger rupture speeds, shorter coseismic durations, and higher peak slip velocities. Specifically, the case with  $\eta^* = \eta/2$  shows similar rupture speed and coseismic duration to 3-D FD simulations, suggesting the possibility of fine-tuning a smaller  $\eta^*$  value for better comparability.

However, in QD with  $\eta^* = \eta/2$ , the slip velocity increased 210% from its initial value inside the nucleation zone to the maximum. Whereas in FD, this accelerating factor is 420%. This indicates that QD models still fall short in accurately modeling the energy concentration at the rupture tip. In summary, a strong stress concentration is missing in both the interseismic loading and the coseismic rupture when the quasi-dynamic approximation is used. The impact of omitting the inertia term cannot be fully compensated with a radiation damping term even if the factor  $\eta$  is fine-tuned. This feature should be respected when adopting QD models and interpreting the results. For example, when using FD models in Groningen, the energy concentration at rupture tip might allow the rupture to propagate further into the over- and underburden.

## 7.2.6 Uncertainties in model input and output

Every modeler aspires for their model to accurately represent the research subject, but uncertainties inevitably exist, influencing the reliability of the results. This includes how uncertain the parameters are and how representative the model setup is. In the context of the Groningen reservoir discussed in Chapter 5, two primary sources of uncertainty are identified. Firstly, uncertainties arise from frictional parameters, which are highly dependent on experimental configuration and conditions [Hunfeld *et al.*, 2017]. Especially the dynamic friction, when dynamic weakening mechanisms come into play, can undergo rapid changes, posing challenges to measurement accuracy and the reliability of current frictional theories [Hunfeld, 2020]. Secondly, the model setup may not be fully representative of the complex fault systems in Groningen. Considering the known and unknown faults with varying fault lengths, dipping and striking angles, offsets, and stratigraphy, finding a representative model setup is challenging. In addition, the background pre-production stress field is highly

ill-constrained. All these factors could change fault criticality and thus the potential of fault activation [Buijze, 2020]. These two sources of uncertainty challenge the representativeness of the model output.

While efforts should be continued to reduce uncertainties in input parameters and enhance knowledge of the model setup variations, there are practical steps that modelers can take. First, one should compare model outputs to natural observations. This helps establish consistency and build confidence. For example, the modeled earthquake magnitudes should align with the earthquake catalog, and in the scenario of Groningen induced seismicity, the modeled pressure change should match the waiting period between production commencement and the onset of seismic activity (Fig 4.2). Second, one should conduct parameter studies to explore the possible parameter space, such as illustrated in a study on frictional parameters  $a, b, D_{RS}$  for seismic potential (Fig 4.5). This helps to justify the representativeness of a model and to identify which parameters influence specific outcomes and the robustness. A third approach involves self-convergence tests and benchmarking. Self-convergence tests refer to employing mesh refinements to ensure that a converged result is attained (Fig 2.2). It is also common to report the convergence rate in other computational science disciplines such as computational fluid dynamics. However, these tests may not detect errors in model setup and solvers. Model output can nonetheless converge to an incorrect result. This is where benchmarking comes into play. Benchmarking involves comparing model outputs with exercises featuring known (often analytical) solutions or comparing with other groups within the community solving the same exercise (Fig 6.2, 6.3, 6.4). Implementing these methods collectively would provide modelers and all model users with greater confidence in their model outputs and a better interpretation.

# Bibliography

Abercrombie, R. E., and Mori, J., Occurrence patterns of foreshocks to large earthquakes in the western united states, *Nature*, 381(6580), 303–307, 1996. Cited on page 87.

Acosta, M., Avouac, J.-P., Smith, J. D., Sirorattanakul, K., Kaveh, H., and Bourne, S. J., Earthquake nucleation characteristics revealed by seismicity response to seasonal stress variations induced by gas production at groningen, *Geophysical Research Letters*, 50(19), e2023GL105,455, 2023. Cited on pages 30 and 157.

Adachi, K., and Kato, K., Formation of smooth wear surfaces on alumina ceramics by embedding and tribo-sintering of fine wear particles, *Wear*, 245(1-2), 84–91, 2000. Cited on pages 116 and 202.

- Aharonov, E., and Scholz, C. H., A physics-based rock friction constitutive law: Steady state friction, *Journal of Geophysical Research: Solid Earth*, 123(2), 1591–1614, 2018. Cited on pages 29 and 136.
- Aki, K., Bouchon, M., Chouet, B., and Das, S., Quantitative prediction of strong motion for a potential earthquake fault, in *Strong Ground Motion. NSF Seminar Workshop, San-Diego*, pp. 3–5, 1978. Cited on page 131.
- Allison, K. L., and Dunham, E. M., Earthquake cycle simulations with rate-and-state friction and power-law viscoelasticity, *Tectonophysics*, 733, 232–256, 2018. Cited on pages 44 and 82.
- Ampuero, J.-P., and Rubin, A. M., Earthquake nucleation on rate and state faults—aging and slip laws, *Journal of Geophysical Research: Solid Earth*, 113(B1), 2008. Cited on pages 72 and 130.
- Andrews, D., Hanks, T. C., and Whitney, J. W., Physical limits on ground motion at yucca mountain, *Bulletin of the Seismological Society of America*, 97(6), 1771–1792, 2007. Cited on page 60.
- Aochi, H., and Ide, S., Role of multiscale heterogeneity in fault slip from quasi-static numerical simulations, *Earth, Planets and Space*, 69(1), 1–18, 2017. Cited on page 205.
- Arts, J., Niemeijer, A., Drury, M., Willingshofer, E., and Matenco, L., Mechanical and microstructural characterization of spatially heterogeneous simulated fault gouges, derived from the groningen gas field stratigraphy, *Tech. rep.*, Copernicus Meetings, 2023. Cited on pages 157, 162, 170, and 171.
- Arts, J. P., Niemeijer, A. R., Drury, M. R., Willingshofer, E., and Matenco, L. C., The frictional strength and stability of spatially heterogeneous fault gouges, *Earth and Planetary Science Letters*, 628, 118,586, 2024. Cited on page 87.
- Atkinson, G. M., Eaton, D. W., and Igonin, N., Developments in understanding seismicity triggered by hydraulic fracturing, *Nature Reviews Earth & Environment*, 1(5), 264–277, 2020. Cited on page 121.
- Balay, S., Gropp, W. D., McInnes, L. C., and Smith, B. F., Efficient management of parallelism in object oriented numerical software libraries, in *Modern Software Tools in Scientific Computing*, edited by E. Arge, A. M. Bruaset, and H. P. Langtangen, pp. 163–202, Birkhäuser Press, 1997. Cited on pages 46 and 174.
- Balay, S., et al., PETSc Web page, <https://www.mcs.anl.gov/petsc>, 2019a. Cited on pages 46 and 174.
- Balay, S., et al., PETSc users manual, *Tech. Rep. ANL-95/11 - Revision 3.12*, Argonne National Laboratory, 2019b. Cited on pages 46 and 174.

- Barbot, S., Slow-slip, slow earthquakes, period-two cycles, full and partial ruptures, and deterministic chaos in a single asperity fault, *Tectonophysics*, 768, 228,171, 2019. Cited on pages 43, 58, 80, and 102.
- Barbot, S., Lapusta, N., and Avouac, J.-P., Under the hood of the earthquake machine: Toward predictive modeling of the seismic cycle, *Science*, 336(6082), 707–710, 2012. Cited on pages 44 and 122.
- Barcheck, G., Brodsky, E., Fulton, P., King, M., Siegfried, M., and Tulaczyk, S., Migratory earthquake precursors are dominant on an ice stream fault, *Science Advances*, 7(6), eabd0105, 2021. Cited on page 114.
- Bedford, J. D., Faulkner, D. R., and Lapusta, N., Fault rock heterogeneity can produce fault weakness and reduce fault stability, *Nature Communications*, 13(1), 326, 2022. Cited on pages 35, 87, 162, and 170.
- Bedford, J. D., Hirose, T., and Hamada, Y., Rapid fault healing after seismic slip, *Journal of Geophysical Research: Solid Earth*, 128(6), e2023JB026,706, 2023. Cited on page 137.
- Bedford, J. R., Moreno, M., Deng, Z., Oncken, O., Schurr, B., John, T., Báez, J. C., and Bevis, M., Months-long thousand-kilometre-scale wobbling before great subduction earthquakes, *Nature*, 580(7805), 628–635, 2020. Cited on page 87.
- Beeler, N., Tullis, T., and Weeks, J., The roles of time and displacement in the evolution effect in rock friction, *Geophysical research letters*, 21(18), 1987–1990, 1994. Cited on pages 29, 33, and 123.
- Beeler, N., Tullis, T., and Goldsby, D., Constitutive relationships and physical basis of fault strength due to flash heating, *Journal of Geophysical Research: Solid Earth*, 113(B1), 2008. Cited on page 133.
- Behr, W. M., and Bürgmann, R., What's down there? the structures, materials and environment of deep-seated slow slip and tremor, *Philosophical Transactions of the Royal Society A*, 379(2193), 20200,218, 2021. Cited on pages 35 and 87.
- Ben-Zion, Y., and Rice, J. R., Slip patterns and earthquake populations along different classes of faults in elastic solids, *Journal of Geophysical Research: Solid Earth*, 100(B7), 12,959–12,983, 1995. Cited on pages 47 and 205.
- Ben-Zion, Y., and Rice, J. R., Dynamic simulations of slip on a smooth fault in an elastic solid, *Journal of Geophysical Research: Solid Earth*, 102(B8), 17,771–17,784, 1997. Cited on pages 47 and 93.
- Ben-Zion, Y., and Sammis, C. G., Characterization of fault zones, *Pure and applied geophysics*, 160, 677–715, 2003. Cited on pages 35 and 87.



- Blanpied, M. L., and Tullis, T. E., The stability and behavior of a frictional system with a two state variable constitutive law, *Friction and Faulting*, pp. 415–444, 1987. Cited on page 202.
- Blanpied, M. L., Lockner, D. A., and Byerlee, J. D., Frictional slip of granite at hydrothermal conditions, *Journal of Geophysical Research: Solid Earth*, 100(B7), 13,045–13,064, 1995. Cited on page 136.
- Bommer, J. J., Dost, B., Edwards, B., Stafford, P. J., van Elk, J., Doornhof, D., and Ntinalexis, M., Developing an application-specific ground-motion model for induced seismicity, *Bulletin of the Seismological Society of America*, 106(1), 158–173, 2016. Cited on page 126.
- Bourne, S., and Oates, S., Extreme threshold failures within a heterogeneous elastic thin sheet and the spatial-temporal development of induced seismicity within the groningen gas field, *Journal of Geophysical Research: Solid Earth*, 122(12), 10–299, 2017. Cited on pages 29, 30, and 34.
- Breckels, I., and Van Eekelen, H., Relationship between horizontal stress and depth in sedimentary basins, *Journal of Petroleum Technology*, 34(09), 2191–2199, 1982. Cited on page 21.
- Brown, S. R., and Scholz, C. H., Broad bandwidth study of the topography of natural rock surfaces, *Journal of Geophysical Research: Solid Earth*, 90(B14), 12,575–12,582, 1985. Cited on pages 116 and 202.
- Brune, J. N., Tectonic stress and the spectra of seismic shear waves from earthquakes, *Journal of geophysical research*, 75(26), 4997–5009, 1970. Cited on page 156.
- Buijze, A. J. L., Numerical and experimental simulation of fault reactivation and earthquake rupture applied to induced seismicity in the groningen gas field, Ph.D. thesis, Utrecht University, 2020. Cited on pages 30, 157, 161, 164, 168, 200, 204, and 208.
- Buijze, L., van den Bogert, P. A., Wassing, B. B., Orlic, B., and ten Veen, J., Fault reactivation mechanisms and dynamic rupture modelling of depletion-induced seismic events in a rotliegend gas reservoir, *Netherlands Journal of Geosciences*, 96(5), s131–s148, 2017. Cited on page 18.
- Buijze, L., Van den Bogert, P., Wassing, B., and Orlic, B., Nucleation and arrest of dynamic rupture induced by reservoir depletion, *Journal of Geophysical Research: Solid Earth*, 124(4), 3620–3645, 2019. Cited on pages 30, 32, 33, 34, 123, 138, 140, 157, 160, 161, 169, and 201.
- Burkitov, U., Van Oeveren, H., Valvatne, P., van Elk, J., and Doornhof, D., Groningen field review 2015 subsurface dynamic modelling report, *Report No. EP201603238100, Assen: NAM*, 2016. Cited on pages 22 and 201.
- Burridge, R., and Knopoff, L., Model and theoretical seismicity, *Bulletin of the seismological society of america*, 57(3), 341–371, 1967. Cited on pages 43 and 79.

- Candela, T., Renard, F., Klinger, Y., Mair, K., Schmittbuhl, J., and Brodsky, E. E., Roughness of fault surfaces over nine decades of length scales, *Journal of Geophysical Research: Solid Earth*, 117(B8), 2012. Cited on pages 88, 116, and 202.
- Candela, T., Osinga, S., Ampuero, J.-P., Wassing, B., Pluymaekers, M., Fokker, P. A., van Wees, J.-D., de Waal, H. A., and Muntendam-Bos, A. G., Depletion-induced seismicity at the groningen gas field: Coulomb rate-and-state models including differential compaction effect, *Journal of Geophysical Research: Solid Earth*, 124(7), 7081–7104, 2019. Cited on pages 29, 30, and 157.
- Candela, T., Pluymaekers, M., Ampuero, J.-P., Van Wees, J.-D., Buijze, L., Wassing, B., Osinga, S., Grobde, N., and Muntendam-Bos, A. G., Controls on the spatio-temporal patterns of induced seismicity in groningen constrained by physics-based modelling with ensemble-smoother data assimilation, *Geophysical Journal International*, 229(2), 1282–1308, 2022. Cited on pages 29, 30, 33, and 157.
- Cannon, M., and Kole, P., The first year of distributed strain sensing (dss) monitoring in the groningen gas field, *NAM report*, 2017. Cited on page 22.
- Carpenter, B. M., Ikari, M. J., and Marone, C., Laboratory observations of time-dependent frictional strengthening and stress relaxation in natural and synthetic fault gouges, *Journal of Geophysical Research: Solid Earth*, 121(2), 1183–1201, 2016. Cited on pages 33 and 123.
- Catalli, F., Meier, M.-A., and Wiemer, S., The role of coulomb stress changes for injection-induced seismicity: The basel enhanced geothermal system, *Geophysical Research Letters*, 40(1), 72–77, 2013. Cited on page 87.
- Cattania, C., Complex earthquake sequences on simple faults, *Geophysical Research Letters*, 46(17-18), 10,384–10,393, 2019. Cited on pages 43, 44, 58, and 80.
- Cattania, C., and Segall, P., Precursory slow slip and foreshocks on rough faults, *Journal of Geophysical Research: Solid Earth*, 126(4), e2020JB020,430, 2021. Cited on pages 35, 36, and 88.
- Cebry, S. B., Sorhaindo, K., and McLaskey, G. C., Laboratory earthquake rupture interactions with a high normal stress bump, *Journal of Geophysical Research: Solid Earth*, 128(11), e2023JB027,297, 2023. Cited on page 202.
- Cebry, S. B. L., Ke, C.-Y., Shreedharan, S., Marone, C., Kammer, D. S., and McLaskey, G. C., Creep fronts and complexity in laboratory earthquake sequences illuminate delayed earthquake triggering, *Nature communications*, 13(1), 6839, 2022. Cited on page 89.
- Cesca, S., Rohr, A., and Dahm, T., Discrimination of induced seismicity by full moment tensor inversion and decomposition, *Journal of Seismology*, 17, 2012. Cited on page 121.

- Chemenda, A. I., Cavalié, O., Vergnolle, M., Bouissou, S., and Delouis, B., Numerical model of formation of a 3-d strike-slip fault system, *Comptes Rendus Geoscience*, 348(1), 61–69, 2016. Cited on page 44.
- Chen, J., and Spiers, C. J., Rate and state frictional and healing behavior of carbonate fault gouge explained using microphysical model, *Journal of Geophysical Research: Solid Earth*, 121(12), 8642–8665, 2016. Cited on pages 29 and 136.
- Chen, J., Verberne, B. A., and Spiers, C. J., Effects of healing on the seismogenic potential of carbonate fault rocks: Experiments on samples from the longmenshan fault, sichuan, china, *Journal of Geophysical Research: Solid Earth*, 120(8), 5479–5506, 2015. Cited on pages 33, 123, and 190.
- Chen, T., and Lapusta, N., Scaling of small repeating earthquakes explained by interaction of seismic and aseismic slip in a rate and state fault model, *Journal of Geophysical Research: Solid Earth*, 114(B1), 2009. Cited on page 45.
- Chen, T., and Lapusta, N., On behaviour and scaling of small repeating earthquakes in rate and state fault models, *Geophysical Journal International*, 218(3), 2001–2018, 2019. Cited on pages 44, 45, 58, 68, 70, 72, 80, and 205.
- Chen, X., Carpenter, B. M., and Reches, Z., Asperity failure control of stick-slip along brittle faults, *Pure and Applied Geophysics*, 177, 3225–3242, 2020. Cited on page 115.
- Chlieh, M., De Chabaliér, J., Ruegg, J., Armijo, R., Dmowska, R., Campos, J., and Feigl, K., Crustal deformation and fault slip during the seismic cycle in the north chile subduction zone, from gps and insar observations, *Geophysical Journal International*, 158(2), 695–711, 2004. Cited on pages 36, 43, and 190.
- Cocco, M., and Bizzarri, A., On the slip-weakening behavior of rate-and state dependent constitutive laws, *Geophysical Research Letters*, 29(11), 11–1, 2002. Cited on pages 70 and 131.
- Cochard, A., and Madariaga, R., Dynamic faulting under rate-dependent friction, *pure and applied geophysics*, 142(3), 419–445, 1994. Cited on pages 47, 141, and 205.
- Corbi, F., Funicicello, F., Moroni, M., Van Dinther, Y., Mai, P. M., Dalguer, L., and Faccenna, C., The seismic cycle at subduction thrusts: 1. insights from laboratory models, *Journal of Geophysical Research: Solid Earth*, 118(4), 1483–1501, 2013. Cited on page 37.
- Cornelissen, P., and Jansen, J.-D., Steady-state flow through a subsurface reservoir with a displaced fault and its poro-elastic effects on fault stresses, *Transport in Porous Media*, 150(3), 709–734, 2023. Cited on pages 30 and 157.
- Crupi, P., and Bizzarri, A., The role of radiation damping in the modeling of repeated earthquake events, *Annals of Geophysics*, 56(1), 0111, 2013. Cited on pages 47 and 205.

- Day, S. M., Dalguer, L. A., Lapusta, N., and Liu, Y., Comparison of finite difference and boundary integral solutions to three-dimensional spontaneous rupture, *Journal of Geophysical Research: Solid Earth*, 110(B12), 2005. Cited on pages 54 and 130.
- de Jager, J., and Visser, C., Geology of the groningen field –an overview, *Netherlands Journal of Geosciences*, 96(5), s3–s15, 2017. Cited on pages 16, 19, 21, 126, 134, 155, and 161.
- Di Toro, G., Mittempergher, S., Ferri, F., Mitchell, T. M., and Pennacchioni, G., The contribution of structural geology, experimental rock deformation and numerical modelling to an improved understanding of the seismic cycle: Preface to the special volume ‘physico-chemical processes in seismic faults’, *Journal of Structural Geology*, 38, 3–10, 2012. Cited on page 137.
- Diab-Montero, H. A., Li, M., van Dinther, Y., and Vossepoel, F. C., Ensemble kalman filter estimates shear stress and seismic slip rates in synthetic laboratory experiment, in *EGU General Assembly*, 2021. Cited on page 80.
- Diab-Montero, H. A., Li, M., van Dinther, Y., and Vossepoel, F. C., Estimating the occurrence of slow slip events and earthquakes with an ensemble kalman filter, *Geophysical Journal International*, 234(3), 1701–1721, 2023. Cited on pages 19, 40, and 196.
- Diehl, T., Kraft, T., Kissling, E., and Wiemer, S., The induced earthquake sequence related to the st. gallen deep geothermal project (switzerland): Fault reactivation and fluid interactions imaged by microseismicity, *Journal of Geophysical Research: Solid Earth*, 122(9), 7272–7290, 2017. Cited on page 17.
- Dieterich, J., Preseismic fault slip and earthquake prediction, *Journal of Geophysical Research: Solid Earth*, 83(B8), 3940–3948, 1978. Cited on pages 87 and 112.
- Dieterich, J. H., Modeling of rock friction: 1. experimental results and constitutive equations, *Journal of Geophysical Research: Solid Earth*, 84(B5), 2161–2168, 1979. Cited on pages 26, 27, 29, 47, 91, 93, 121, 123, 140, and 143.
- Dieterich, J. H., Earthquake nucleation on faults with rate-and state-dependent strength, *Tectonophysics*, 211(1-4), 115–134, 1992. Cited on pages 28 and 142.
- Dieterich, J. H., and Kilgore, B., Implications of fault constitutive properties for earthquake prediction, *Proceedings of the National Academy of Sciences*, 93(9), 3787–3794, 1996. Cited on page 27.
- Dong, P., Xu, R., Yang, H., Guo, Z., and Xia, K., Fault slip behaviors modulated by locally increased fluid pressure: Earthquake nucleation and slow slip events, *Journal of Geophysical Research: Solid Earth*, p. e2022JB024612, 2022. Cited on pages 36, 88, 89, and 202.
- Dost, B., and Kraaijpoel, D., The august 16, 2012 earthquake near huizinge (groningen), *KNMI, de Bilt, the Netherlands*, 2013. Cited on pages 16 and 155.

- Dost, B., Edwards, B., and Bommer, J., Local and moment magnitudes in the groningen field, *NAM, Report*, 2016. Cited on page 126.
- Dost, B., Ruigrok, E., and Spetzler, J., Development of seismicity and probabilistic hazard assessment for the groningen gas field, *Netherlands Journal of Geosciences*, 96(5), s235–s245, 2017. Cited on pages 22 and 155.
- Dragert, H., Wang, K., and James, T. S., A silent slip event on the deeper cascadia subduction interface, *Science*, 292(5521), 1525–1528, 2001. Cited on page 23.
- Duan, B., and Oglesby, D. D., Heterogeneous fault stresses from previous earthquakes and the effect on dynamics of parallel strike-slip faults, *Journal of Geophysical Research: Solid Earth*, 111(B5), 2006. Cited on pages 35, 36, and 88.
- Dublanchet, P., Fluid driven shear cracks on a strengthening rate-and-state frictional fault, *Journal of the Mechanics and Physics of Solids*, 132, 103,672, 2019. Cited on pages 140 and 201.
- Edwards, H. C., Trott, C. R., and Sunderland, D., Kokkos: Enabling manycore performance portability through polymorphic memory access patterns, *Journal of Parallel and Distributed Computing*, 74(12), 3202–3216, domain-Specific Languages and High-Level Frameworks for High-Performance Computing, 2014. Cited on pages 46 and 174.
- Ellsworth, W., and Beroza, G., Seismic evidence for an earthquake nucleation phase, *Science*, 268(5212), 851–855, 1995. Cited on pages 87 and 122.
- Ellsworth, W. L., Injection-induced earthquakes, *science*, 341(6142), 1225,942, 2013. Cited on page 16.
- Ellsworth, W. L., and Bulut, F., Nucleation of the 1999 izmit earthquake by a triggered cascade of foreshocks, *Nature Geoscience*, 11(7), 531–535, 2018. Cited on page 87.
- Erickson, B. A., and Dunham, E. M., An efficient numerical method for earthquake cycles in heterogeneous media: Alternating subbasin and surface-rupturing events on faults crossing a sedimentary basin, *Journal of Geophysical Research: Solid Earth*, 119(4), 3290–3316, 2014. Cited on page 44.
- Erickson, B. A., Birnir, B., and Lavallée, D., A model for aperiodicity in earthquakes, *Nonlinear processes in geophysics*, 15(1), 1–12, 2008. Cited on page 43.
- Erickson, B. A., et al., The community code verification exercise for simulating sequences of earthquakes and aseismic slip (seas), *Seismological Research Letters*, 91(2A), 874–890, 2020. Cited on pages 44, 45, 49, 174, and 176.
- Erickson, B. A., et al., Incorporating full elastodynamic effects and dipping fault geometries in community code verification exercises for simulations of earthquake sequences and aseismic slip (seas), *Bulletin of the Seismological Society of America*, 113(2), 499–523, 2023. Cited on pages 38, 92, 174, 176, and 177.

- Eyre, T. S., Samsonov, S., Feng, W., Kao, H., and Eaton, D. W., Insar data reveal that the largest hydraulic fracturing-induced earthquake in Canada, to date, is a slow-slip event, *Scientific reports*, 12(1), 2043, 2022. Cited on page 23.
- Fagereng, Å., and Sibson, R. H., Mélange rheology and seismic style, *Geology*, 38(8), 751–754, 2010. Cited on page 87.
- Fang, Z., Dieterich, J. H., and Xu, G., Effect of initial conditions and loading path on earthquake nucleation, *Journal of Geophysical Research: Solid Earth*, 115(B6), 2010. Cited on page 130.
- Freund, L., The mechanics of dynamic shear crack propagation, *Journal of Geophysical Research: Solid Earth*, 84(B5), 2199–2209, 1979. Cited on page 26.
- Fukuyama, E., Ellsworth, W. L., Waldhauser, F., and Kubo, A., Detailed fault structure of the 2000 western Tottori, Japan, earthquake sequence, *Bulletin of the Seismological Society of America*, 93(4), 1468–1478, 2003. Cited on page 37.
- Galis, M., Ampuero, J. P., Mai, P. M., and Cappa, F., Induced seismicity provides insight into why earthquake ruptures stop, *Science advances*, 3(12), eaap7528, 2017. Cited on page 203.
- Galvez, P., Ampuero, J.-P., Dalguer, L. A., Somala, S. N., and Nissen-Meyer, T., Dynamic earthquake rupture modelled with an unstructured 3-d spectral element method applied to the 2011 M9 Tohoku earthquake, *Geophysical Journal International*, 198(2), 1222–1240, 2014. Cited on page 74.
- Garagash, D. I., and Germanovich, L. N., Nucleation and arrest of dynamic slip on a pressurized fault, *Journal of Geophysical Research: Solid Earth*, 117(B10), 2012. Cited on pages 140 and 201.
- Geertsma, J., Land subsidence above compacting oil and gas reservoirs, *Journal of Petroleum Technology*, 25(06), 734–744, 1973. Cited on page 32.
- Geller, R. J., Jackson, D. D., Kagan, Y. Y., and Mulargia, F., Earthquakes cannot be predicted, *Science*, 275(5306), 1616–1616, 1997. Cited on page 17.
- Giacomel, P., Spagnuolo, E., Nazzari, M., Marzoli, A., Passelegue, F., Youbi, N., and Di Toro, G., Frictional instabilities and carbonation of basalts triggered by injection of pressurized H<sub>2</sub>O- and CO<sub>2</sub>-rich fluids, *Geophysical Research Letters*, 45(12), 6032–6041, 2018. Cited on page 135.
- Gislason, S. R., and Oelkers, E. H., Carbon storage in basalt, *Science*, 344(6182), 373–374, 2014. Cited on page 135.
- Goldsby, D. L., and Tullis, T. E., Flash heating leads to low frictional strength of crustal rocks at earthquake slip rates, *Science*, 334(6053), 216–218, 2011. Cited on pages 141 and 199.

- Goudarzi, M., Gerya, T., and Dinther, Y. v., A comparative analysis of continuum plasticity, viscoplasticity and phase-field models for earthquake sequence modeling, *Computational Mechanics*, pp. 1–19, 2023. Cited on page 200.
- Gounon, A., Latour, S., Letort, J., and El Arem, S., Rupture nucleation on a periodically heterogeneous interface, *Geophysical Research Letters*, 49(20), e2021GL096,816, 2022. Cited on pages 35, 88, 89, 114, and 202.
- Green, R. A., et al., Liquefaction hazard in the groningen region of the netherlands due to induced seismicity, *Journal of Geotechnical and Geoenvironmental Engineering*, 146(8), 04020,068, 2020. Cited on pages 166 and 167.
- Gu, Y., and Wong, T.-f., Effects of loading velocity, stiffness, and inertia on the dynamics of a single degree of freedom spring-slider system, *Journal of Geophysical Research: Solid Earth*, 96(B13), 21,677–21,691, 1991. Cited on page 43.
- Guérin-Marthe, S., Nielsen, S., Bird, R., Giani, S., and Di Toro, G., Earthquake nucleation size: Evidence of loading rate dependence in laboratory faults, *Journal of Geophysical Research: Solid Earth*, 124(1), 689–708, 2019. Cited on page 122.
- Harris, R. A., et al., The sceec/usgs dynamic earthquake rupture code verification exercise, *Seismological Research Letters*, 80(1), 119–126, 2009. Cited on pages 49 and 176.
- Harris, R. A., et al., Verifying a computational method for predicting extreme ground motion, *Seismological Research Letters*, 82(5), 638–644, 2011. Cited on page 45.
- Harris, R. A., et al., A suite of exercises for verifying dynamic earthquake rupture codes, *Seismological Research Letters*, 89(3), 1146–1162, 2018. Cited on pages 49 and 176.
- Hawthorne, J., and Rubin, A., Laterally propagating slow slip events in a rate and state friction model with a velocity-weakening to velocity-strengthening transition, *Journal of Geophysical Research: Solid Earth*, 118(7), 3785–3808, 2013. Cited on page 72.
- He, C., Luo, L., Hao, Q.-M., and Zhou, Y., Velocity-weakening behavior of plagioclase and pyroxene gouges and stabilizing effect of small amounts of quartz under hydrothermal conditions, *Journal of Geophysical Research: Solid Earth*, 118(7), 3408–3430, 2013. Cited on page 136.
- He, C., Zhang, L., Liu, P., and Chen, Q.-F., Characterizing the final stage of simulated earthquake nucleation governed by rate-and-state fault friction, *Journal of Geophysical Research: Solid Earth*, 128(5), e2023JB026,422, 2023. Cited on page 130.
- Heaton, T. H., Evidence for and implications of self-healing pulses of slip in earthquake rupture, *Physics of the Earth and Planetary Interiors*, 64(1), 1–20, 1990. Cited on page 137.

- Heimisson, E. R., Crack to pulse transition and magnitude statistics during earthquake cycles on a self-similar rough fault, *Earth and Planetary Science Letters*, 537, 116,202, 2020. Cited on page 88.
- Heimisson, E. R., Smith, J. D., Avouac, J.-P., and Bourne, S. J., Coulomb threshold rate-and-state model for fault reactivation: application to induced seismicity at groningen, *Geophysical Journal International*, 228(3), 2061–2072, 2022. Cited on pages 30, 34, 136, and 157.
- Helmstetter, A., and Sornette, D., Foreshocks explained by cascades of triggered seismicity, *Journal of Geophysical Research: Solid Earth*, 108(B10), 2003. Cited on pages 87 and 112.
- Herrendörfer, R., Gerya, T., and Van Dinther, Y., An invariant rate-and state-dependent friction formulation for viscoelastoplastic earthquake cycle simulations, *Journal of Geophysical Research: Solid Earth*, 123(6), 5018–5051, 2018. Cited on pages 43, 80, 81, 200, and 205.
- Hettema, M., Schutjens, P., Verboom, B., and Gussinklo, H., Production-induced compaction of a sandstone reservoir: the strong influence of stress path, *SPE Reservoir Evaluation & Engineering*, 3(04), 342–347, 2000. Cited on pages 32 and 142.
- Hillers, G., and Miller, S. A., Dilatancy controlled spatiotemporal slip evolution of a sealed fault with spatial variations of the pore pressure, *Geophysical Journal International*, 168(1), 431–445, 2007. Cited on pages 35, 36, and 88.
- HiQuake, Induced earthquakes. Cited on page 122.
- Hough, S. E., Shaking from injection-induced earthquakes in the central and eastern united states, *Bulletin of the Seismological Society of America*, 104(5), 2619–2626, 2014. Cited on page 17.
- Hu, S., Huang, W., Shi, X., Peng, Z., and Liu, X., Bi-fractal feature of bi-gaussian stratified surfaces, *Tribology International*, 134, 427–434, 2019. Cited on pages 116 and 202.
- Huang, Y., Earthquake rupture in fault zones with along-strike material heterogeneity, *Journal of Geophysical Research: Solid Earth*, 123(11), 9884–9898, 2018. Cited on pages 35, 36, 87, and 88.
- Huang, Y., Ellsworth, W. L., and Beroza, G. C., Stress drops of induced and tectonic earthquakes in the central united states are indistinguishable, *Science Advances*, 3(8), e1700,772, 2017. Cited on page 138.
- Hunfeld, L., Niemeijer, A., and Spiers, C., Frictional properties of simulated fault gouges from the seismogenic groningen gas field under in situ p–t-chemical conditions, *Journal of Geophysical Research: Solid Earth*, 122(11), 8969–8989, 2017. Cited on pages 33, 93, 97, 123, 134, 156, 157, 158, 159, 160, 162, 170, 171, 190, and 207.



- Hunfeld, L. B., Frictional properties of simulated fault gouges from the groningen gas field and implications for induced seismicity., Ph.D. thesis, Utrecht University, 2020. Cited on pages 18, 162, and 207.
- Hunfeld, L. B., Chen, J., Hol, S., Niemeijer, A. R., and Spiers, C. J., Healing behavior of simulated fault gouges from the groningen gas field and implications for induced fault reactivation, *Journal of Geophysical Research: Solid Earth*, 125(7), e2019JB018,790, 2020. Cited on pages 33, 123, 125, 134, 146, 157, 158, 160, and 162.
- Hunfeld, L. B., Chen, J., Niemeijer, A. R., Ma, S., and Spiers, C. J., Seismic slip-pulse experiments simulate induced earthquake rupture in the groningen gas field, *Geophysical Research Letters*, 48(11), e2021GL092,417, 2021. Cited on page 20.
- Ida, Y., Cohesive force across the tip of a longitudinal-shear crack and griffith's specific surface energy, *Journal of Geophysical Research*, 77(20), 3796–3805, 1972. Cited on page 121.
- Ida, Y., The maximum acceleration of seismic ground motion, *Bulletin of the Seismological Society of America*, 63(3), 959–968, 1973. Cited on page 72.
- Ide, S., and Aochi, H., Earthquakes as multiscale dynamic ruptures with heterogeneous fracture surface energy, *Journal of Geophysical Research: Solid Earth*, 110(B11), 2005. Cited on pages 116 and 202.
- Ikari, M. J., Saffer, D. M., and Marone, C., Frictional and hydrologic properties of clay-rich fault gouge, *Journal of Geophysical Research: Solid Earth*, 114(B5), 2009. Cited on page 135.
- Im, K., Saffer, D., Marone, C., and Avouac, J.-P., Slip-rate-dependent friction as a universal mechanism for slow slip events, *Nature Geoscience*, 13(10), 705–710, 2020. Cited on page 80.
- Jansen, J., Singhal, P., and Vossepoel, F., Insights from closed-form expressions for injection- and production-induced stresses in displaced faults, *Journal of Geophysical Research: Solid Earth*, 124(7), 7193–7212, 2019. Cited on pages 30, 32, 33, 142, and 157.
- Jansen, J.-D., and Meulenbroek, B., Induced aseismic slip and the onset of seismicity in displaced faults, *Netherlands Journal of Geosciences*, 101, e13, 2022. Cited on pages 30 and 157.
- Ji, Y., Niemeijer, A., Baden, D. H., Yamashita, F., Xu, S., Hunfeld, L. B., Pijenburg, R., and Spiers, C. J., Bridging laboratory and field-scale friction in earthquake nucleation: Insights from m-scale experiments, *AGU23*, 2023. Cited on pages 90, 97, and 198.
- Jiang, J., and Lapusta, N., Deeper penetration of large earthquakes on seismically quiescent faults, *Science*, 352(6291), 1293–1297, 2016. Cited on page 44.
- Jiang, J., et al., Community-driven code comparisons for three-dimensional dynamic modeling of sequences of earthquakes and aseismic slip, *Journal of Geophysical Research: Solid Earth*, 127(3), e2021JB023,519, 2022. Cited on pages 38, 44, 45, 47, 49, 50, 80, 82, 92, 174, 176, and 179.

- Jordan, T., et al., Operational earthquake forecasting: State of knowledge and guidelines for implementation., *Annals of Geophysics*, 2011. Cited on page 17.
- Kammer, D. S., Radiguet, M., Ampuero, J.-P., and Molinari, J.-F., Linear elastic fracture mechanics predicts the propagation distance of frictional slip, *Tribology letters*, 57, 1–10, 2015. Cited on page 26.
- Kanamori, H., The energy release in great earthquakes, *Journal of geophysical research*, 82(20), 2981–2987, 1977. Cited on page 203.
- Kanamori, H., and Rivera, L., *Energy Partitioning During an Earthquake*, pp. 3–13, American Geophysical Union (AGU), 2006. Cited on page 62.
- Kaneko, Y., Lapusta, N., and Ampuero, J.-P., Spectral element modeling of spontaneous earthquake rupture on rate and state faults: Effect of velocity-strengthening friction at shallow depths, *Journal of Geophysical Research: Solid Earth*, 113(B9), 2008. Cited on pages 28, 29, and 34.
- Kaneko, Y., Avouac, J.-P., and Lapusta, N., Towards inferring earthquake patterns from geodetic observations of interseismic coupling, *Nature Geoscience*, 3(5), 363, 2010. Cited on pages 44, 122, and 205.
- Kaneko, Y., Ampuero, J.-P., and Lapusta, N., Spectral-element simulations of long-term fault slip: Effect of low-rigidity layers on earthquake-cycle dynamics, *Journal of Geophysical Research: Solid Earth*, 116(B10), 2011. Cited on page 81.
- Kang, J.-Q., Zhu, J.-B., and Zhao, J., A review of mechanisms of induced earthquakes: from a view of rock mechanics, *Geomechanics and Geophysics for Geo-Energy and Geo-Resources*, 5, 171–196, 2019. Cited on pages 28 and 122.
- Kato, A., Fukuda, J., Kumazawa, T., and Nakagawa, S., Accelerated nucleation of the 2014 Iquique, Chile Mw 8.2 earthquake, *Scientific reports*, 6(1), 24,792, 2016. Cited on page 87.
- Kato, N., and Tullis, T. E., A composite rate-and state-dependent law for rock friction, *Geophysical research letters*, 28(6), 1103–1106, 2001. Cited on page 29.
- Keilis-borok, V., On estimation of displacement in an earthquake source and of source dimension, *Ann. Geofis.*, 12, 1959. Cited on pages 68 and 70.
- Kettermann, M., Abe, S., Raith, A. F., de Jager, J., and Urai, J. L., The effect of salt in dilatant faults on rates and magnitudes of induced seismicity—first results building on the geological setting of the Groningen rotliegend reservoirs, *Netherlands Journal of Geosciences*, 96(5), s87–s104, 2017. Cited on page 166.
- Kilb, D., Gomberg, J., and Bodin, P., Aftershock triggering by complete Coulomb stress changes, *Journal of Geophysical Research: Solid Earth*, 107(B4), ESE-2, 2002. Cited on page 87.

- King, G. C., Stein, R. S., and Lin, J., Static stress changes and the triggering of earthquakes, *Bulletin of the Seismological Society of America*, 84(3), 935–953, 1994. Cited on page 87.
- Knopoff, L., Energy release in earthquakes, *Geophysical Journal International*, 1(1), 44–52, 1958. Cited on pages 68 and 70.
- Kohli, A. H., and Zoback, M. D., Frictional properties of shale reservoir rocks, *Journal of geophysical research: solid earth*, 118(9), 5109–5125, 2013. Cited on page 135.
- Kortekaas, M., and Jaarsma, B., Improved definition of faults in the groningen field using seismic attributes, *Netherlands Journal of Geosciences*, 96(5), s71–s85, 2017. Cited on pages 21 and 161.
- Kostrov, B. V., and Das, S., *Principles of earthquake source mechanics*, Cambridge University Press, 1988. Cited on page 60.
- Kraaijpoel, D., and Dost, B., Implications of salt-related propagation and mode conversion effects on the analysis of induced seismicity, *Journal of Seismology*, 17, 95–107, 2013. Cited on pages 23, 126, 156, and 204.
- Lambert, V., and Lapusta, N., Resolving simulated sequences of earthquakes and fault interactions: implications for physics-based seismic hazard assessment, 2021. Cited on page 44.
- Lambert, V., et al., Community code verification exercises for simulations of earthquake sequences and aseismic slip (seas): Effects from dipping faults and full elastodynamics to fluids and fault friction evolution, *AGU23*, 2023. Cited on pages 176, 180, 181, and 200.
- Lapusta, N., Elastodynamic analyses of sliding with rate and state friction, Ph.D. thesis, Harvard University, 2001. Cited on page 44.
- Lapusta, N., and Liu, Y., Three-dimensional boundary integral modeling of spontaneous earthquake sequences and aseismic slip, *Journal of Geophysical Research: Solid Earth*, 114(B9), 2009. Cited on pages 44, 131, 178, and 205.
- Lapusta, N., and Rice, J. R., Nucleation and early seismic propagation of small and large events in a crustal earthquake model, *Journal of Geophysical Research: Solid Earth*, 108(B4), 2003. Cited on pages 29 and 44.
- Lapusta, N., Rice, J. R., Ben-Zion, Y., and Zheng, G., Elastodynamic analysis for slow tectonic loading with spontaneous rupture episodes on faults with rate-and state-dependent friction, *Journal of Geophysical Research: Solid Earth*, 105(B10), 23,765–23,789, 2000. Cited on pages 29, 34, 43, 55, 94, 122, 142, and 178.
- Lapusta, N., et al., Modeling earthquake source processes: from tectonics to dynamic rupture, in *Report to the National Science Foundation*, 2019. Cited on pages 44 and 74.

- Latour, S., Schubnel, A., Nielsen, S., Madariaga, R., and Vinciguerra, S., Characterization of nucleation during laboratory earthquakes, *Geophysical Research Letters*, 40(19), 5064–5069, 2013. Cited on pages 87 and 112.
- Lebihain, M., Roch, T., Violay, M., and Molinari, J.-F., Earthquake nucleation along faults with heterogeneous weakening rate, *Geophysical Research Letters*, 48(21), e2021GL094,901, 2021. Cited on page 94.
- Leeman, J., Marone, C., and Saffer, D., Frictional mechanics of slow earthquakes, *Journal of Geophysical Research: Solid Earth*, 123(9), 7931–7949, 2018. Cited on page 80.
- Lele, S., Garzon, J., Hsu, S., DeDontney, N., Searles, K., and Sanz, P., Groningen 2015 geomechanical analysis, *Exxon Mobil Upstream Research Company, Spring, TX, USA, Final Report. Nederlandse Aardolie Maatschappij (Assen)*, 2015. Cited on pages 92, 157, 160, 161, and 166.
- Li, M., Pranger, C., and van Dinther, Y., Characteristics of earthquake sequences: comparison from 0d to 3d, in *EGU General Assembly Conference Abstracts*, 2021. Cited on page 81.
- Li, M., Pranger, C., and van Dinther, Y., Characteristics of earthquake cycles: A cross-dimensional comparison of 0d to 3d numerical models, *Journal of Geophysical Research: Solid Earth*, 127(8), e2021JB023,726, 2022. Cited on page 92.
- Li, M., Niemeijer, A., and Van Dinther, Y., Why induced earthquakes occur on conventionally stable faults: frictional healing explains, 2023. Cited on page 160.
- Li, T., Cai, M., and Cai, M., A review of mining-induced seismicity in china, *International Journal of Rock Mechanics and Mining Sciences*, 44(8), 1149–1171, 2007. Cited on page 17.
- Liu, D., Duan, B., and Luo, B., Eqsimu: a 3-d finite element dynamic earthquake simulator for multicycle dynamics of geometrically complex faults governed by rate-and state-dependent friction, *Geophysical Journal International*, 220(1), 598–609, 2020. Cited on page 178.
- Liu, Y., and Rice, J. R., Spontaneous and triggered aseismic deformation transients in a subduction fault model, *Journal of Geophysical Research: Solid Earth*, 112(B9), 2007. Cited on pages 34, 47, 80, and 205.
- Lotto, G. C., Jeppson, T. N., and Dunham, E. M., Fully coupled simulations of megathrust earthquakes and tsunamis in the japan trench, nankai trough, and cascadia subduction zone, *Pure and Applied Geophysics*, 176(9), 4009–4041, 2019. Cited on page 44.
- Luo, Y., and Liu, Z., Fault zone heterogeneities explain depth-dependent pattern and evolution of slow earthquakes in cascadia, *Nature communications*, 12(1), 1959, 2021. Cited on pages 88, 89, and 202.

- Madariaga, R., Study of an oscillator of single degree of freedom with dieterich-ruina rate and state friction, laboratoire de géologie, école normale supérieure, *Unpublished Notes*, 1998. Cited on page 43.
- Madariaga, R., and Ruiz, S., Earthquake dynamics on circular faults: A review 1970–2015, *Journal of Seismology*, 20, 1235–1252, 2016. Cited on page 156.
- Madden, E. H., et al., Linked 3-d modelling of megathrust earthquake-tsunami events: from subduction to tsunami run up, *Geophysical Journal International*, 224(1), 487–516, 2021. Cited on page 74.
- Magnani, M. B., Blanpied, M. L., DeShon, H. R., and Hornbach, M. J., Discriminating between natural versus induced seismicity from long-term deformation history of intraplate faults, *Science Advances*, 3(11), e1701,593, 2017. Cited on page 121.
- Marone, C., The effect of loading rate on static friction and the rate of fault healing during the earthquake cycle, *Nature*, 391(6662), 69–72, 1998. Cited on pages 27, 28, 33, 123, and 135.
- Marone, C., and Kilgore, B., Scaling of the critical slip distance for seismic faulting with shear strain in fault zones, *Nature*, 362(6421), 618–621, 1993. Cited on pages 29 and 133.
- Marone, C., and Scholz, C., The depth of seismic faulting and the upper transition from stable to unstable slip regimes, *Geophysical Research Letters*, 15(6), 621–624, 1988. Cited on pages 28 and 122.
- Mavrommatis, A. P., Segall, P., and Johnson, K. M., A decadal-scale deformation transient prior to the 2011 mw 9.0 tohoku-oki earthquake, *Geophysical Research Letters*, 41(13), 4486–4494, 2014. Cited on page 114.
- McGarr, A., Simpson, D., Seeber, L., and Lee, W., Case histories of induced and triggered seismicity, *International Geophysics Series*, 81(A), 647–664, 2002. Cited on page 16.
- McLaskey, G. C., Earthquake initiation from laboratory observations and implications for foreshocks, *Journal of Geophysical Research: Solid Earth*, 124(12), 12,882–12,904, 2019. Cited on pages 37, 87, and 113.
- McLaskey, G. C., and Kilgore, B. D., Foreshocks during the nucleation of stick-slip instability, *Journal of Geophysical Research: Solid Earth*, 118(6), 2982–2997, 2013. Cited on pages 87 and 112.
- McLaskey, G. C., and Lockner, D. A., Preslip and cascade processes initiating laboratory stick slip, *Journal of Geophysical Research: Solid Earth*, 119(8), 6323–6336, 2014. Cited on pages 37, 43, 87, 112, 122, and 190.
- Michel, S., Jolivet, R., Rollins, C., Jara, J., and Dal Zilio, L., Seismogenic potential of the main himalayan thrust constrained by coupling segmentation and earthquake scaling, *Geophysical Research Letters*, 48(13), e2021GL093,106, 2021. Cited on pages 97 and 202.

- Mitchell, T., and Faulkner, D., The nature and origin of off-fault damage surrounding strike-slip fault zones with a wide range of displacements: A field study from the atacama fault system, northern chile, *Journal of Structural Geology*, 31(8), 802–816, 2009. Cited on page 87.
- Miyamoto, T., et al., Characteristics of fault rocks within the aftershock cloud of the 2014 orkney earthquake (m5.5) beneath the moab khotsong gold mine, south africa, *Geophysical Research Letters*, 49(14), e2022GL098745, e2022GL098745 2022GL098745, 2022. Cited on pages 28 and 122.
- Morad, D., Sagy, A., Tal, Y., and Hatzor, Y. H., Fault roughness controls sliding instability, *Earth and Planetary Science Letters*, 579, 117,365, 2022. Cited on pages 35, 88, and 114.
- MPI Forum, Mpi: A message-passing interface standard. version 3.1, 2015. Cited on pages 46 and 174.
- Naderloo, M., Kumar, K. R., Hernandez, E., Hajibeygi, H., and Barnhoorn, A., Experimental and numerical investigation of sandstone deformation under cycling loading relevant for underground energy storage, *Journal of Energy Storage*, 64, 107,198, 2023. Cited on page 136.
- Nakatani, M., Conceptual and physical clarification of rate and state friction: Frictional sliding as a thermally activated rheology, *Journal of Geophysical Research: Solid Earth*, 106(B7), 13,347–13,380, 2001. Cited on pages 33, 67, 125, 126, 127, 142, and 143.
- Nakatani, M., and Scholz, C. H., Frictional healing of quartz gouge under hydrothermal conditions: 1. experimental evidence for solution transfer healing mechanism, *Journal of Geophysical Research: Solid Earth*, 109(B7), 2004. Cited on pages 33, 123, and 127.
- Nielsen, S., Taddeucci, J., and Vinciguerra, S., Experimental observation of stick-slip instability fronts, *Geophysical Journal International*, 180(2), 697–702, 2010. Cited on page 87.
- Niemeijer, A., Boulton, C., Toy, V., Townend, J., and Sutherland, R., Large-displacement, hydrothermal frictional properties of dfdp-1 fault rocks, alpine fault, new zealand: Implications for deep rupture propagation, *Journal of Geophysical Research: Solid Earth*, 121(2), 624–647, 2016. Cited on page 136.
- Obara, K., and Kato, A., Connecting slow earthquakes to huge earthquakes, *Science*, 353(6296), 253–257, 2016. Cited on page 87.
- Ohnaka, M., A constitutive scaling law and a unified comprehension for frictional slip failure, shear fracture of intact rock, and earthquake rupture, *Journal of Geophysical Research: Solid Earth*, 108(B2), 2003. Cited on pages 116 and 202.
- Ohnaka, M., *The physics of rock failure and earthquakes*, Cambridge University Press, 2013. Cited on page 131.

- Ohnaka, M., Kuwahara, Y., and Yamamoto, K., Constitutive relations between dynamic physical parameters near a tip of the propagating slip zone during stick-slip shear failure, *Tectonophysics*, 144(1-3), 109–125, 1987. Cited on page 72.
- Ohtani, M., Kame, N., and Nakatani, M., Synchronization of megathrust earthquakes to periodic slow slip events in a single-degree-of-freedom spring-slider model, *Scientific reports*, 9(1), 1–9, 2019. Cited on page 44.
- Ohtani, M., Nakatani, M., and Kame, N., Time to seismic failure induced by repeating sses in a single-degree-of-freedom spring-slider model, *Geophysical Journal International*, 224(2), 1242–1255, 2020. Cited on page 43.
- Okubo, P. G., Dynamic rupture modeling with laboratory-derived constitutive relations, *Journal of Geophysical Research: Solid Earth*, 94(B9), 12,321–12,335, 1989. Cited on page 44.
- Okubo, P. G., and Aki, K., Fractal geometry in the san andreas fault system, *Journal of Geophysical Research: Solid Earth*, 92(B1), 345–355, 1987. Cited on pages 116 and 202.
- Olsen, M. P., Scholz, C. H., and Léger, A., Healing and sealing of a simulated fault gouge under hydrothermal conditions: Implications for fault healing, *Journal of Geophysical Research: Solid Earth*, 103(B4), 7421–7430, 1998. Cited on pages 33 and 123.
- Olson, E. L., and Allen, R. M., The deterministic nature of earthquake rupture, *Nature*, 438(7065), 212–215, 2005. Cited on page 122.
- Orlic, B., and Wassing, B., A study of stress change and fault slip in producing gas reservoirs overlain by elastic and viscoelastic caprocks, *Rock mechanics and rock engineering*, 46(3), 421–435, 2013. Cited on page 138.
- Passelègue, F. X., Almakari, M., Dublanchet, P., Barras, F., Fortin, J., and Violay, M., Initial effective stress controls the nature of earthquakes, *Nature communications*, 11(1), 5132, 2020. Cited on pages 36, 88, and 190.
- Perfettini, H., and Ampuero, J.-P., Dynamics of a velocity strengthening fault region: Implications for slow earthquakes and postseismic slip, *Journal of Geophysical Research: Solid Earth*, 113(B9), 2008. Cited on page 123.
- Perfettini, H., et al., Seismic and aseismic slip on the central peru megathrust, *Nature*, 465(7294), 78–81, 2010. Cited on page 122.
- Perrin, C., Manighetti, I., Ampuero, J.-P., Cappa, F., and Gaudemer, Y., Location of largest earthquake slip and fast rupture controlled by along-strike change in fault structural maturity due to fault growth, *Journal of Geophysical Research: Solid Earth*, 121(5), 3666–3685, 2016. Cited on pages 24 and 87.

- Petrillo, G., Lippiello, E., Landes, F. P., and Rosso, A., The influence of the brittle-ductile transition zone on aftershock and foreshock occurrence, *Nature communications*, 11(1), 1–10, 2020. Cited on page 43.
- Petrini, C., Gerya, T., Yarushina, V., van Dinther, Y., Connolly, J., and Madonna, C., Seismo-hydro-mechanical modelling of the seismic cycle: methodology and implications for subduction zone seismicity, *Tectonophysics*, 791, 228,504, 2020. Cited on page 44.
- Pijnenburg, R. P. J., et al., Deformation behavior of reservoir sandstones from the seismogenic groningen gas field: An experimental and mechanistic study, Ph.D. thesis, UU Dept. of Earth Sciences, 2019. Cited on page 20.
- Pranger, C., Unstable physical processes operating on self-governing fault systems, improved modeling methodology, Ph.D. thesis, ETH Zurich, 2020. Cited on pages 38, 46, 55, 92, 174, 178, and 200.
- Pranger, C., Sanan, P., May, D. A., Le Pourhiet, L., and Gabriel, A.-A., Rate and state friction as a spatially regularized transient viscous flow law, *Journal of Geophysical Research: Solid Earth*, 127(6), e2021JB023,511, 2022. Cited on pages 79 and 200.
- Prawirodirdjo, L., McCaffrey, R., Chadwell, C. D., Bock, Y., and Subarya, C., Geodetic observations of an earthquake cycle at the sumatra subduction zone: Role of interseismic strain segmentation, *Journal of Geophysical Research: Solid Earth*, 115(B3), 2010. Cited on pages 36, 43, and 190.
- Preuss, S., Herrendörfer, R., Gerya, T., Ampuero, J.-P., and van Dinther, Y., Seismic and aseismic fault growth lead to different fault orientations, *Journal of Geophysical Research: Solid Earth*, 124(8), 8867–8889, 2019. Cited on page 87.
- Preuss, S., Ampuero, J. P., Gerya, T., and Dinther, Y. v., Characteristics of earthquake ruptures and dynamic off-fault deformation on propagating faults, *Solid Earth*, 11(4), 1333–1360, 2020. Cited on pages 35 and 44.
- Pritchard, M. E., et al., New opportunities to study earthquake precursors, *Seismological Research Letters*, 91(5), 2444–2447, 2020. Cited on pages 17 and 87.
- Radiguet, M., et al., Triggering of the 2014 m w 7.3 papanao earthquake by a slow slip event in guerrero, mexico, *Nature Geoscience*, 9(11), 829–833, 2016. Cited on page 114.
- Ray, S., and Viesca, R. C., Earthquake nucleation on faults with heterogeneous frictional properties, normal stress, *Journal of Geophysical Research: Solid Earth*, 122(10), 8214–8240, 2017. Cited on pages 95 and 114.
- Reasenber, P. A., Foreshock occurrence before large earthquakes, *Journal of Geophysical Research: Solid Earth*, 104(B3), 4755–4768, 1999. Cited on page 17.



- Renard, F., and Candela, T., Scaling of fault roughness and implications for earthquake mechanics, *Fault zone dynamic processes: Evolution of fault properties during seismic rupture*, pp. 195–215, 2017. Cited on page 89.
- Rice, J. R., Spatio-temporal complexity of slip on a fault, *Journal of Geophysical Research: Solid Earth*, 98(B6), 9885–9907, 1993. Cited on pages 47, 92, 93, 141, and 205.
- Rice, J. R., and Ben-Zion, Y., Slip complexity in earthquake fault models, *Proceedings of the National Academy of Sciences*, 93(9), 3811–3818, 1996. Cited on pages 47, 93, and 141.
- Rice, J. R., and Gu, J.-c., Earthquake aftereffects and triggered seismic phenomena, *Pure and applied geophysics*, 121, 187–219, 1983. Cited on page 123.
- Rice, J. R., and Ruina, A. L., Stability of steady frictional slipping, *Journal of Applied Mechanics*, 50(2), 343–349, 1983. Cited on pages 28 and 122.
- Richter, G., Hainzl, S., Dahm, T., and Zöller, G., Stress-based, statistical modeling of the induced seismicity at the groningen gas field, the netherlands, *Environmental Earth Sciences*, 79, 2020. Cited on pages 125, 126, 140, 151, and 160.
- Roeloffs, E., and Langbein, J., The earthquake prediction experiment at parkfield, california, *Reviews of Geophysics*, 32(3), 315–336, 1994. Cited on page 190.
- Romanet, P., Sato, D. S., and Ando, R., Curvature, a mechanical link between the geometrical complexities of a fault: application to bends, kinks and rough faults, *Geophysical Journal International*, 223(1), 211–232, 2020. Cited on pages 44 and 89.
- Rosenau, M., Lohrmann, J., and Oncken, O., Shocks in a box: An analogue model of subduction earthquake cycles with application to seismotectonic forearc evolution, *Journal of Geophysical Research: Solid Earth*, 114(B1), 2009. Cited on pages 37 and 43.
- Ruan, J., Ghose, R., and Mulder, W. A., 3d geomechanical modeling of induced seismic slips considering realistic reservoir geometry with intersecting faults, *Authorea Preprints*, 2023. Cited on pages 30 and 157.
- Rubin, A. M., Episodic slow slip events and rate-and-state friction, *Journal of Geophysical Research: Solid Earth*, 113(B11), 2008. Cited on page 80.
- Rubin, A. M., and Ampuero, J.-P., Earthquake nucleation on (aging) rate and state faults, *Journal of Geophysical Research: Solid Earth*, 110(B11), 2005. Cited on pages 28, 29, 54, 65, 70, 94, 104, 122, 127, 130, 131, 142, 144, 145, and 164.
- Ruggieri, R., et al., The role of shale content and pore-water saturation on frictional properties of simulated carbonate faults, *Tectonophysics*, 807, 228,811, 2021. Cited on pages 28, 122, and 135.

- Ruina, A., Slip instability and state variable friction laws, *Journal of Geophysical Research: Solid Earth*, 88(B12), 10,359–10,370, 1983. Cited on pages 26, 27, 29, 47, 91, 93, 121, 122, 140, and 143.
- Sathiakumar, S., Barbot, S., and Hubbard, J., Earthquake cycles in fault-bend folds, *Journal of Geophysical Research: Solid Earth*, 125(8), e2019JB018,557, 2020. Cited on page 44.
- Scholz, C. H., Earthquakes and friction laws, *Nature*, 391(6662), 37–42, 1998. Cited on page 121.
- Scholz, C. H., *The mechanics of earthquakes and faulting*, Cambridge university press, 2019. Cited on pages 28 and 122.
- Schultz, R., Atkinson, G., Eaton, D. W., Gu, Y. J., and Kao, H., Hydraulic fracturing volume is associated with induced earthquake productivity in the duvernay play, *Science*, 359(6373), 304–308, 2018. Cited on page 135.
- Scuderi, M. M., and Collettini, C., The role of fluid pressure in induced vs. triggered seismicity: Insights from rock deformation experiments on carbonates, *Scientific reports*, 6(1), 1–9, 2016. Cited on page 135.
- Scuderi, M. M., and Collettini, C., Fluid injection and the mechanics of frictional stability of shale-bearing faults, *Journal of Geophysical Research: Solid Earth*, 123(10), 8364–8384, 2018. Cited on page 135.
- Segall, P., Earthquakes triggered by fluid extraction, *Geology*, 17(10), 942–946, 1989. Cited on page 16.
- Segall, P., and Harris, R., Earthquake deformation cycle on the san andreas fault near parkfield, california, *Journal of Geophysical Research: Solid Earth*, 92(B10), 10,511–10,525, 1987. Cited on pages 36, 43, and 190.
- Selvadurai, P. A., Galvez, P., Mai, P. M., and Glaser, S. D., Modeling frictional precursory phenomena using a wear-based rate-and state-dependent friction model in the laboratory, *Tectonophysics*, 847, 229,689, 2023. Cited on pages 114, 115, and 202.
- Shreedharan, S., Saffer, D., Wallace, L. M., and Williams, C., Ultralow frictional healing explains recurring slow slip events, *Science*, 379(6633), 712–717, 2023. Cited on page 135.
- Simmonds, J., *A Brief on Tensor Analysis*, Undergraduate Texts in Mathematics, Springer New York, 1994. Cited on pages 55, 182, and 184.
- Smith, J. D., White, R. S., Avouac, J.-P., and Bourne, S., Probabilistic earthquake locations of induced seismicity in the groningen region, the netherlands, *Geophysical Journal International*, 222(1), 507–516, 2020. Cited on pages 123, 134, and 156.

- Smith, J. D., Heimisson, E. R., Bourne, S. J., and Avouac, J.-P., Stress-based forecasting of induced seismicity with instantaneous earthquake failure functions: Applications to the groningen gas reservoir, *Earth and Planetary Science Letters*, 594, 117,697, 2022. Cited on pages 30, 34, and 157.
- Socquet, A., et al., An 8 month slow slip event triggers progressive nucleation of the 2014 chile megathrust, *Geophysical Research Letters*, 44(9), 4046–4053, 2017. Cited on page 114.
- Spetzler, J., and Dost, B., Hypocentre estimation of induced earthquakes in groningen, *Geophysical Journal International*, 209(1), 453–465, 2017. Cited on pages 22, 123, 134, 155, and 156.
- Strozyk, F., Reuning, L., Scheck-Wenderoth, M., and Tanner, D., The tectonic history of the zechstein basin in the netherlands and germany, in *Permo-Triassic salt provinces of Europe, North Africa and the Atlantic Margins*, pp. 221–241, Elsevier, 2017. Cited on page 134.
- Sykes, L. R., Shaw, B. E., and Scholz, C. H., Rethinking earthquake prediction, *Pure and Applied Geophysics*, 155, 207–232, 1999. Cited on page 87.
- Tabrez, A. S., Freed, A. M., Calais, E., Manaker, D. M., and McCann, W. R., Coulomb stress evolution in northeastern caribbean over the past 250 years due to coseismic, postseismic and interseismic deformation, *Geophysical Journal International*, 174(3), 904–918, 2008. Cited on page 87.
- Tada, H., Paris, P. C., and Irwin, G. R., The stress analysis of cracks, *Handbook, Del Research Corporation*, 34, 1973. Cited on page 70.
- Takeuchi, C. S., and Fialko, Y., Dynamic models of interseismic deformation and stress transfer from plate motion to continental transform faults, *Journal of Geophysical Research: Solid Earth*, 117(B5), 2012. Cited on page 82.
- Tal, Y., Hager, B. H., and Ampuero, J. P., The effects of fault roughness on the earthquake nucleation process, *Journal of Geophysical Research: Solid Earth*, 123(1), 437–456, 2018. Cited on pages 35 and 88.
- Tang, R., Zhu, S., and Gan, L., Dynamic rupture simulations of the 2008 7.9 wenchuan earthquake: Implication for heterogeneous initial stress and complex multifault geometry, *Journal of Geophysical Research: Solid Earth*, 126(12), e2021JB022,457, 2021. Cited on pages 36 and 89.
- Taufiqurrahman, T., Gabriel, A.-A., Li, D., Ulrich, T., Li, B., Carena, S., Verdecchia, A., and Gallovič, F., Dynamics, interactions and delays of the 2019 ridgecrest rupture sequence, *Nature*, pp. 1–8, 2023. Cited on pages 36, 89, 97, and 202.

- Tenthorey, E., and Cox, S. F., Cohesive strengthening of fault zones during the interseismic period: An experimental study, *Journal of Geophysical Research: Solid Earth*, 111(B9), 2006. Cited on pages 33, 123, and 136.
- The MathWorks Inc., Matlab version: 9.7.0 (r2019b), 2019. Cited on page 142.
- Thomas, M. Y., Lapusta, N., Noda, H., and Avouac, J.-P., Quasi-dynamic versus fully dynamic simulations of earthquakes and aseismic slip with and without enhanced coseismic weakening, *Journal of Geophysical Research: Solid Earth*, 119(3), 1986–2004, 2014. Cited on pages 47 and 205.
- Thomas, M. Y., Bhat, H. S., and Klinger, Y., Effect of brittle off-fault damage on earthquake rupture dynamics, *Fault zone dynamic processes: Evolution of fault properties during seismic rupture*, 227, 255, 2017. Cited on page 205.
- Tullis, T., and Goldsby, D., Laboratory experiments on fault shear resistance relevant to coseismic earthquake slip, *SCEC Ann. Prog. Rep., Southern California Earthquake Center*, 2003. Cited on pages 29, 133, and 199.
- Ulrich, T., Vater, S., Madden, E. H., Behrens, J., van Dinther, Y., Van Zelst, I., Fielding, E. J., Liang, C., and Gabriel, A.-A., Coupled, physics-based modeling reveals earthquake displacements are critical to the 2018 palu, sulawesi tsunami, *Pure and Applied Geophysics*, 176(10), 4069–4109, 2019. Cited on page 74.
- Uphoff, C., Rettenberger, S., Bader, M., Madden, E. H., Ulrich, T., Wollherr, S., and Gabriel, A.-A., Extreme scale multi-physics simulations of the tsunamigenic 2004 sumatra megathrust earthquake, in *Proceedings of the international conference for high performance computing, networking, storage and analysis*, pp. 1–16, 2017. Cited on page 44.
- U.S. Geological Survey, Earthquake lists, maps, and statistics. Cited on page 122.
- Van den Bogert, P., Impact of various modelling options on the onset of fault slip and fault slip response using 2-dimensional finite-element modelling, *Restricted, Report No. SR, 15*, 2015. Cited on page 138.
- Van den Ende, M., Chen, J., Ampuero, J.-P., and Niemeijer, A., A comparison between rate-and-state friction and microphysical models, based on numerical simulations of fault slip, *Tectonophysics*, 733, 273–295, 2018. Cited on page 205.
- van der Heiden, V., Ulrich, T., van de Wiel, L., Gabriel, A.-A., Buijze, L., and van Dinther, Y., Physics-based constraints on the moment magnitudes for induced seismicity in the groningen gas field through 3d dynamic earthquake rupture modelling, in *AGU Fall Meeting Abstracts*, vol. 2022, pp. S22A-03, 2022. Cited on pages 168 and 204.

- Van Dinther, Y., Gerya, T., Dalguer, L. A., Corbi, F., Funicello, F., and Mai, P. M., The seismic cycle at subduction thrusts: 2. dynamic implications of geodynamic simulations validated with laboratory models, *Journal of Geophysical Research: Solid Earth*, 118(4), 1502–1525, 2013a. Cited on pages 44 and 199.
- Van Dinther, Y., Gerya, T. V., Dalguer, L., Mai, P. M., Morra, G., and Giardini, D., The seismic cycle at subduction thrusts: Insights from seismo-thermo-mechanical models, *Journal of Geophysical Research: Solid Earth*, 118(12), 6183–6202, 2013b. Cited on pages 43 and 199.
- Van Dinther, Y., Künsch, H. R., and Fichtner, A., Ensemble data assimilation for earthquake sequences: probabilistic estimation and forecasting of fault stresses, *Geophysical Journal International*, 217(3), 1453–1478, 2019a. Cited on pages 19, 37, 44, and 195.
- Van Dinther, Y., Preiswerk, L. E., and Gerya, T. V., A secondary zone of uplift due to megathrust earthquakes, *Pure and Applied Geophysics*, 176(9), 4043–4068, 2019b. Cited on page 44.
- Van Eijs, R., Neotectonic stresses in the permian slochteren formation of the groningen field, *KNMI Scientific Report. Report No. EP201510210531. NAM (Assen)*, 2015. Cited on pages 22 and 156.
- van Oeveren, H., Valvatne, P., Geurtsen, L., and van Elk, J., History match of the groningen field dynamic reservoir model to subsidence data and conventional subsurface data, *Netherlands Journal of Geosciences*, 96(5), s47–s54, 2017. Cited on pages 21, 34, 123, 140, and 201.
- van Thienen-Visser, K., and Breunese, J., Induced seismicity of the groningen gas field: History and recent developments, *The Leading Edge*, 34(6), 664–671, 2015. Cited on page 16.
- van Thienen-Visser, K., Pruiksma, J., and Breunese, J., Compaction and subsidence of the groningen gas field in the netherlands, *Proceedings of the International Association of Hydrological Sciences*, 372, 367–373, 2015. Cited on page 123.
- Van Wees, J., Buijze, L., Van Thienen-Visser, K., Nepveu, M., Wassing, B., Orlic, B., and Fokker, P., Geomechanics response and induced seismicity during gas field depletion in the netherlands, *Geothermics*, 52, 206–219, 2014. Cited on pages 22, 30, and 157.
- Van Wees, J.-D., Fokker, P. A., Van Thienen-Visser, K., Wassing, B. B., Osinga, S., Orlic, B., Ghouri, S. A., Buijze, L., and Pluymaekers, M., Geomechanical models for induced seismicity in the netherlands: Inferences from simplified analytical, finite element and rupture model approaches, *Netherlands Journal of Geosciences*, 96(5), s183–s202, 2017. Cited on pages 30 and 157.
- van Wees, J.-D., Osinga, S., Van Thienen-Visser, K., and Fokker, P. A., Reservoir creep and induced seismicity: inferences from geomechanical modeling of gas depletion in the groningen field, *Geophysical Journal International*, 212(3), 1487–1497, 2018. Cited on pages 30, 33, and 157.

- Verberne, B., Spiers, C. J., Niemeijer, A. R., De Bresser, J., De Winter, D., and Plümpner, O., Frictional properties and microstructure of calcite-rich fault gouges sheared at sub-seismic sliding velocities, *Pure and Applied Geophysics*, 171, 2617–2640, 2014. Cited on pages 135, 190, and 199.
- Verweij, J., Simmelink, H., Underschultz, J., and Witmans, N., Pressure and fluid dynamic characterisation of the dutch subsurface, *Netherlands Journal of Geosciences*, 91(4), 465–490, 2012. Cited on page 140.
- Wang, X., Dal Zilio, L., Morgan, J. K., and Kammer, D. S., Non-precursory accelerating aseismic slip during rupture nucleation, *Journal of Geophysical Research: Solid Earth*, 128(6), e2022JB026,066, 2023. Cited on pages 87 and 112.
- Weiss, J. R., et al., Illuminating subduction zone rheological properties in the wake of a giant earthquake, *Science Advances*, 5(12), eaax6720, 2019. Cited on pages 37 and 44.
- Wells, D. L., and Coppersmith, K. J., New empirical relationships among magnitude, rupture length, rupture width, rupture area, and surface displacement, *Bulletin of the seismological Society of America*, 84(4), 974–1002, 1994. Cited on page 203.
- Weng, H., and Ampuero, J.-P., The dynamics of elongated earthquake ruptures, *Journal of Geophysical Research: Solid Earth*, 124(8), 8584–8610, 2019. Cited on page 44.
- Weng, H., and Ampuero, J.-P., Integrated rupture mechanics for slow slip events and earthquakes, *Nature Communications*, 13(1), 7327, 2022. Cited on pages 26, 36, and 88.
- Weng, H., Huang, J., and Yang, H., Barrier-induced supershear ruptures on a slip-weakening fault, *Geophysical Research Letters*, 42(12), 4824–4832, 2015. Cited on pages 36, 88, and 89.
- Weng, H., Ampuero, J.-P., and Buijze, L., Physics-based estimates of the maximum magnitude of induced earthquakes in the groningen gas field, in *EGU General Assembly Conference Abstracts*, pp. EGU21–6144, 2021. Cited on pages 30, 78, and 157.
- Wentinck, R., Induced seismicity in the groningen field: Second statistical assessment of tremors along faults in a compacting reservoir, *Assen: Nederlandse Aardolie Maatschappij BV*, 2016. Cited on pages 21 and 161.
- Wesnousky, S. G., Displacement and geometrical characteristics of earthquake surface ruptures: Issues and implications for seismic-hazard analysis and the process of earthquake rupture, *Bulletin of the Seismological Society of America*, 98(4), 1609–1632, 2008. Cited on page 78.
- Willacy, C., van Dedem, E., Minisini, S., Li, J., Blokland, J.-W., Das, I., and Droujinine, A., Full-waveform event location and moment tensor inversion for induced seismicity, *Geophysics*, 84(2), KS39–KS57, 2019. Cited on pages 22, 23, 123, 134, 155, and 156.

- Wilson, M., Foulger, G., Gluyas, J., Davies, R., and Julian, B., Hiquake: The human-induced earthquake database, *Seismological Research Letters*, 88(6), 1560–1565, 2017. Cited on page 122.
- Wollherr, S., Gabriel, A.-A., and Mai, P. M., Landers 1992 “reloaded” : Integrative dynamic earthquake rupture modeling, *Journal of Geophysical Research: Solid Earth*, 124(7), 6666–6702, 2019. Cited on page 74.
- Wyss, M., Evaluation of proposed earthquake precursors, 1991. Cited on page 87.
- Xu, S., Fukuyama, E., Yamashita, F., Kawakata, H., Mizoguchi, K., and Takizawa, S., Fault strength and rupture process controlled by fault surface topography, *Nature Geoscience*, pp. 1–7, 2023. Cited on pages 35 and 88.
- Yamashita, F., Fukuyama, E., Xu, S., Mizoguchi, K., Kawakata, H., and Takizawa, S., Rupture preparation process controlled by surface roughness on meter-scale laboratory fault, *Tectonophysics*, 733, 193–208, 2018. Cited on pages 35, 88, 89, and 114.
- Yang, H., Liu, Y., and Lin, J., Effects of subducted seamounts on megathrust earthquake nucleation and rupture propagation, *Geophysical Research Letters*, 39(24), 2012. Cited on pages 36, 88, 89, 97, and 202.
- Yu, H., Harrington, R. M., Kao, H., Liu, Y., and Wang, B., Fluid-injection-induced earthquakes characterized by hybrid-frequency waveforms manifest the transition from aseismic to seismic slip, *Nature communications*, 12(1), 6862, 2021. Cited on page 121.
- Zbinden, D., Rinaldi, A. P., Urpi, L., and Wiemer, S., On the physics-based processes behind production-induced seismicity in natural gas fields, *Journal of Geophysical Research: Solid Earth*, 122(5), 3792–3812, 2017. Cited on pages 30, 33, 34, 157, and 164.
- Zhang, H., Eaton, D. W., Li, G., Liu, Y., and Harrington, R. M., Discriminating induced seismicity from natural earthquakes using moment tensors and source spectra, *Journal of Geophysical Research: Solid Earth*, 121(2), 972–993, 2016. Cited on page 121.
- Zhang, L., He, C., Liu, Y., and Lin, J., Frictional properties of the south china sea oceanic basalt and implications for strength of the manila subduction seismogenic zone, *Marine Geology*, 394, 16–29, 2017. Cited on page 135.
- Zhang, L., Liu, Y., Li, D., Yu, H., and He, C., Geometric control on seismic rupture and earthquake sequence along the yingxiu-beichuan fault with implications for the 2008 wenchuan earthquake, *Journal of Geophysical Research: Solid Earth*, p. e2022JB024113, 2022. Cited on pages 36 and 89.
- Zhong, Z., Xu, C., Wang, L., Hu, Y., and Zhang, F., Experimental investigation on frictional properties of stressed basalt fractures, *Journal of Rock Mechanics and Geotechnical Engineering*, 2023. Cited on pages 28, 122, and 135.

- Zhou, W., and Paulssen, H., Compaction of the groningen gas reservoir investigated with train noise, *Geophysical Journal International*, 223(2), 1327–1337, 2020. Cited on pages 22 and 155.
- Zhu, W., Allison, K. L., Dunham, E. M., and Yang, Y., Fault valving and pore pressure evolution in simulations of earthquake sequences and aseismic slip, *Nature communications*, 11(1), 4833, 2020. Cited on page 200.
- Zielke, O., Galis, M., and Mai, P. M., Fault roughness and strength heterogeneity control earthquake size and stress drop, *Geophysical Research Letters*, 44(2), 777–783, 2017. Cited on pages 35 and 88.
- Ziv, A., On the nucleation of creep and the interaction between creep and seismic slip on rate-and state-dependent faults, *Geophysical research letters*, 34(15), 2007. Cited on page 130.





# Acknowledgements

Completing this PhD thesis has been a long and rewarding journey, made even more challenging by the unprecedented global COVID-19 pandemic. I never imagined that I would be away from my parents for five full years. A lot has changed in the meantime, and this realization hit me profoundly when I returned to my hometown right after dropping the last period in this thesis. The pandemic brought about unexpected hurdles and disruptions, but it also underscored the resilience and support of the incredible people around me.

First, I am extremely grateful to my promoters, Liviu, Ylona, and Andre, for your continuous support and invaluable advice. Without you opening the door to the Dutch scientific community for me, I would have never thought about finishing my PhD here. Ylona, I have known you the longest, since I did my master thesis at ETH Zurich under the supervision of you, Taras, and Casper. It was then that I decided to continue in this discipline for a longer time. I cannot say for my lifetime, but my passion endures. Without your efforts, the whole project would not have been possible. You strike a good balance between scientific rigor and allowing the freedom for me to develop as an independent researcher. We have achieved what we planned despite the obstacles. Liviu, thank you for always being ready to provide me the just-right support whenever I needed it—no more, no less. Andre, your inspiring discussions and instructive comments have broadened my perspective. Both of you helped me transition from a pure seismology background to appreciating longer timescales in geology and smaller spatial scales in laboratory experiments. Special thanks to Casper, whose mathematical sense has influenced me greatly. I have been using your code library since my master thesis. Though I often complained about its mysterious wrapping, I am pleased with its elegant completeness and tidiness. I cherish that our friendship extends beyond science. I wish you a fulfilling journey outside academia. My gratitude extends to all the professors and scientists who have provided direct help to this PhD project—Femke, Ernst, Fred, Fadi,

Jan-Diederik, Loes, Luuk, Chris and Yuntao; all co-authors and collaborators—Brittany, Junle, Valere; and the doctoral examination committee for taking the time to read, evaluate and attend the defence of this thesis.

Next, I would like to express my thanks to all my colleagues in the DeepNL project. The NWO team—Ajita, Cindy, Niels—thank you for organizing all the wonderful events, including annual meetings, summer schools, and other gatherings. Aleks, Aukje, Eddy, Faezeh, Iban, Jingming, Milad, Samantha, I enjoyed our chats and lunches during my non-regular visits to TU Delft. You made me feel connected to a big family. Chien-Cheng and Taka, we started almost simultaneously at Utrecht University, and thus had many opportunities to attend scientific gatherings together. Though we did not get a chance to work together, I wish you both fruitful careers ahead. Hamed, you are my closest collaborator in the InFocus project. I can't count how many days we have spent together in Delft and Utrecht. I can't thank you enough for making the most use of my models. I am really happy that you are now titled as Doctor.

Despite the pandemic and work-from-home boom, I managed to spend most of my working hours in the office. There, I could meet my colleagues from the Tectonics group and the HPT lab. Antoine, Kristof, Istvan, Rens, Job, Vincent, Nemanja, Jasper, Mohsen, Arjan, Jianye, Hadi, Mark, Huiru, Bowen, Mike, Qiang, Wenzhuo—I enjoyed our pleasant coffee chats and hope we have more chances to lunch together. Despite being isolated from the other colleagues working in the VMA building, I actually enjoyed pretty much the working environment with you all in this small but warm ESL building. Yuqi and Sandra, you were the master students who worked with me for several months each. I learned a lot from our collaboration and wish you good futures beyond science. Alexander, thank you for sharing the office with me in the last year of my PhD. It is hard to believe, but you are the person with whom I shared and will be sharing an office the longest. I probably have also talked with you the most, thanks to the long pandemic period. Yuntao and Wen, you are the best people to share my scientific and non-scientific thoughts with, particularly in my mother tongue. I remember our discussions on the sofa, covering everything from earthquakes to life attitudes. We disagreed, quarreled, and got to know each other better.

I should not avoid mentioning my friends outside of the campus. Without you, I do not know how I could have endured the pandemic alone. Yuanyuan, Sheng,

Yang, Yibo—we met at the pre-pandemic new PhD event. Your outgoing personalities made it a great relief for me to share emotions with you. Cooking and dining with you provided the routine entertainment that saved me from boring days. Binhao, Jinhui, Joseph, Lifei, Mingqi, Wenjin, Wei, Weijia, Weiwei, Yuji—we met at various social events and conferences, online and offline. Although we do not see each other often, I am sure we always have plenty to chat about the next time we meet. We also extended our relationships beyond professional interactions to our private lives. Jinhui, Weiwei and Yuji, I appreciate having met you all in Corsica. You are both my close colleagues and friends. With you we discuss scientific issues, but also share feelings and moods. My reserved thanks go to Fuda and Mingjie, whom I have known since middle school. We keep each other updated through regular online meetings, sharing happiness and sorrow, regardless of whether we are in the UK, the Netherlands, Japan, or China. The same goes to Yun and Chenxu, whom I have known since high school. Going hiking and outing with you is always full of fun. I wish you a successful career in the Netherlands.

My final paragraph is reserved for my family. We don't often talk about my future plans, but I feel your emotional support no matter where I decide to go, from my hometown to Zhengzhou and Beijing, to Switzerland and here. Thank you for your endless love and encouragement throughout this journey. You have been a pillar of strength for me, even from afar. My dear sister, I'm sorry to have been absent during your growth. I left home to attend high school when you were three. Next year, you will be leaving home to attend university. You will become an adult and start a more colorful new life yourself. It is my promise to give you the support whenever you need it. I also promise to come back home more frequently and make up for the lost time.

Thank you all.

*Meng Li*  
*June 2, Utrecht*



# Curriculum vitae

## Meng LI / 李蒙

Researcher at *Utrecht University, Utrecht, Netherlands*

### Education

|                                                                         |                |
|-------------------------------------------------------------------------|----------------|
| <b>Ph.D</b><br><i>Utrecht University, Utrecht, Netherlands</i>          | 2019.10-2024.7 |
| <b>M.Sc in Earth Sciences</b><br><i>ETH Zürich, Zürich, Switzerland</i> | 2017.9-2019.9  |
| <b>B.Sc in Geophysics</b><br><i>Peking University, Beijing, China</i>   | 2013.9-2017.7  |

### Publication list

1. Li, M., Niemeijer, A. R., & van Dinther, Y. (submitted). Earthquake nucleation altered by stochastic normal stress heterogeneity. *Journal of Geophysical Research: Solid Earth*.
2. Li, M., Niemeijer, A. R., Vossepoel, F. C., & van Dinther, Y. (submitted). Earthquake nucleation and arrest in a heterogeneous earthquake sequence model for Groningen. *Solid Earth*.
3. Li, M., Niemeijer, A., & Van Dinther, Y. (in review). Why induced earthquakes occur on conventionally stable faults: frictional healing explains. Available at *Research Square*. <https://doi.org/10.21203/rs.3.rs-3317840/v1>.

4. Diab-Montero, H. A., **Li, M.**, van Dinther, Y., & Vossepoel, F. C. (2023). Estimating the occurrence of slow slip events and earthquakes with an ensemble Kalman filter. *Geophysical Journal International*, 234(3), 1701-1721.
5. Erickson, B. A., Jiang, J., Lambert, V., ..., **Li, M.**, ... (2023). Incorporating full elastodynamic effects and dipping fault geometries in community code verification exercises for simulations of earthquake sequences and aseismic slip (SEAS). *Bulletin of the Seismological Society of America*, 113(2), 499-523.
6. **Li, M.**, Pranger, C., & van Dinther, Y. (2022). Characteristics of earthquake cycles: A cross-dimensional comparison of 0-D to 3-D numerical models. *Journal of Geophysical Research: Solid Earth*, 127(8), e2021JB023726.
7. Jiang, J., Erickson, B. A., Lambert, V., ..., **Li, M.**, ... (2022). Community-driven code comparisons for three-dimensional dynamic modeling of sequences of earthquakes and aseismic slip. *Journal of Geophysical Research: Solid Earth*, 127(3), e2021JB023519.

